



HAL
open science

Investigations of highly oxygenated organic molecules (HOMs) in the laboratory and in the real atmosphere: ACROSS project

Stéphanie Alage

► **To cite this version:**

Stéphanie Alage. Investigations of highly oxygenated organic molecules (HOMs) in the laboratory and in the real atmosphere: ACROSS project. Environmental Engineering. Université Paris-Est Créteil Val-de-Marne - Paris 12, 2023. English. NNT : 2023PA120004 . tel-04627663

HAL Id: tel-04627663

<https://theses.hal.science/tel-04627663>

Submitted on 27 Jun 2024

HAL is a multi-disciplinary open access archive for the deposit and dissemination of scientific research documents, whether they are published or not. The documents may come from teaching and research institutions in France or abroad, or from public or private research centers.

L'archive ouverte pluridisciplinaire **HAL**, est destinée au dépôt et à la diffusion de documents scientifiques de niveau recherche, publiés ou non, émanant des établissements d'enseignement et de recherche français ou étrangers, des laboratoires publics ou privés.

THÈSE DE DOCTORAT



Investigations of Highly Oxygenated organic Molecules (HOMs) in the laboratory and in the real atmosphere: ACROSS project

Thèse de doctorat de l'Université Paris-Est Créteil

École doctorale n° 531, Sciences, Ingénierie et Environnement – SIE
Sciences de l'Univers et de l'Environnement

Thèse préparée dans le **Laboratoire Interuniversitaire des Systèmes Atmosphériques**
sous la direction de **Christopher CANTRELL**, Professeur,
le co-encadrement de **Vincent MICHOU**D, Maître de conférences,

Thèse soutenue à l'Université Paris-Est Créteil, le 4 décembre 2023, par

Stéphanie ALAGE

Composition du jury

Membres du jury avec voix délibérative :

Matthieu RIVA, Chargé de Recherche, IRCELYON, CNRS
Anne MONOD, Professeure, LCE, UAM
Valérie GROS, Directrice de Recherche, LSCE, CNRS
Alexandre KUKUI, Chargé de Recherche, LPC2E, CNRS
Bénédicte PICQUET-VARRAULT, Professeure, LISA, UPEC

Rapporteur
Rapportrice
Examinatrice
Examinateur
Examinatrice

Acknowledgments

I would like express my sincere thankful to all those who have contributed to the successful completion of my thesis. This journey has been truly remarkable, and I appreciate the unwavering support and assistance I have received from each of you.

First, my sincere thanks to the head of the Laboratoire Inter-universitaire des Systèmes Atmosphériques (LISA), Patrice Coll, for welcoming me to this laboratory.

I extend my appreciation to the esteemed members of my thesis jury, who agreed to evaluate this work. Special thanks to Pr. Bénédicte PICQUET-VARRAULT, the president of the jury and a member of the MEREIA team and my thesis committee, for her invaluable expertise that significantly shaped this research. Thank you to my reviewers, Pr. Anne MONOD and Dr. Matthieu RIVA, for your critical insights that have greatly enriched my work. Much appreciation extends to Dr. Alexandre KUKUI for the honor of being one of the examiners of my thesis.

A special mention goes to Dr. Valérie GROS for accepting to examine this work, for your wise advices and enduring support, from supervising my master's training to providing valuable insights as a dedicated member of my Thesis Committee throughout my years as a Ph.D. student. I also extend my gratitude to Stéphane SAUVAGE for his invaluable contributions as a Thesis Committee Member.

I am deeply thankful to my supervisors, Pr. Christopher CANTRELL and Dr. Vincent MICHOU, for their invaluable guidance, expertise, mentorship and unwavering support throughout this research. Your trust in my work and the confidence you placed in me have been instrumental in my growth as a researcher.

Special thanks to Mathieu, Edouard, and Antonin for their indispensable presence during the CESAM experimental campaigns, without which completing this work wouldn't have been possible.

Heartfelt appreciation to my MEREIA colleagues: Layal, Elie, Camilo, Diana, Chenjie, Lucy, Aline, Claudia, Paola, Anil, François, Johannes, Francesco and Ludovico. A particular thank you to Manuela for the nice moments we shared, especially during the ACROSS field campaign, and for the assistance provided during my chamber experiments.

Most importantly, my deepest thanks to my dearest friend and office neighbor, Sergio, a.w with whom I shared all my worries and laughter. Thank you for everything!

Thanks to Mathilde for the friendly times we spent together from the beginning of my thesis.

I extend my appreciation to the administrative and IT teams.

Lastly, I wouldn't be here today without the unconditional support and love of my fiancé, Joe, my friends, Charbel and Roy, and my family, Hamid, Ibtissam, Rania, Marie-Rose, and Iyad. They knew how to support me when I needed them the most and always cheered me up. I love you all and hope you're proud of me!

Table of Contents

Introduction	1
Chapter 1 Introduction to atmospheric chemistry of the troposphere	4
1.1. Properties of the earth's atmosphere	4
1.1.1. Atmospheric vertical structure and composition.....	4
1.1.2. Tropospheric characteristics.....	6
1.2. Tropospheric chemistry	8
1.2.1. Volatile Organic Compounds.....	8
1.2.1.1. Anthropogenic VOCs (AVOCs)	12
1.2.1.2. Biogenic VOCs (BVOCs).....	12
1.2.2. Oxidants in the troposphere.....	15
1.2.2.1. OH radicals	15
1.2.2.2. Ozone	16
1.2.2.3. Nitrate radical.....	19
1.2.3. Oxidation processes.....	21
1.2.3.1. The initial attack on VOC by one of the oxidants	21
1.2.3.2. The evolution of RO ₂ · radicals.....	22
1.2.3.3. The evolution of RO· radicals.....	24
1.2.4. Urban tropospheric chemistry	24
1.2.5. Rural/forested tropospheric chemistry	26
1.2.6. Effects of biogenic-anthropogenic interactions on atmospheric organic chemistry	27
1.2.6.1. Laboratory studies.....	28
1.2.6.2. Field campaigns	29
1.3. Highly Oxygenated Organic Molecules (HOMs): VOC autoxidation products	31
1.3.1. Definition and formation pathways.....	31
1.3.2. Laboratory studies of formation of HOMs from BVOC oxidation.....	33
1.3.3. Laboratory studies of formation of HOMs from AVOC oxidation	36
1.3.4. Observations of HOMs in ambient air	38
Thesis objectives.....	39
Chapter 2 Instrumentation: A Chemical Ionization Atmospheric Pressure interface Time-of-Flight mass spectrometer (ToFCIMS)	40
2.1. Instrumental Configuration.....	40
2.1.1. Chemical Ionization inlet: Nitrate Reagent Ion Production and Reaction	40

2.1.2.	Nitrate Reagent Ion Production.....	41
2.1.3.	Ion-Molecule Reaction.....	42
2.1.4.	Ion Quantification.....	44
2.1.5.	Data Analysis: Tofware.....	45
2.2.	Tuning ToFCIMS parameters in the laboratory.....	47
2.2.1.	Inlet flows.....	47
2.2.2.	Effect of ion trajectory guiding voltages.....	49
2.2.2.a.	Oxalic acid signals with different sets of voltages.....	50
2.2.2.b.	Succinic acid signals with different sets of voltages.....	53
2.2.3.	Single-ion-signal setup.....	56
2.2.4.	Discussion.....	56
2.3.	Instrument Sensitivity and calibration.....	57
2.3.1.	Conventional methods and challenges.....	58
2.3.2.	Experimental protocol and results.....	60
2.3.2.1.	Experimental protocol.....	60
2.3.2.2.	Outcomes from the Approach 1.....	66
2.3.2.3.	Outcomes from Approach 2.....	70
2.3.3.	Conventional calibration protocol and results.....	72
2.3.4.	Discussion.....	75
Chapter 3 Formation of HOMs from simulation chamber studies of VOC oxidation.....		77
3.1.	CESAM Chamber: General description.....	77
3.2.	Experimental Configuration Employed in Chamber Studies.....	78
3.3.	Analytical Instruments and Quantities Measured.....	79
3.3.1.	Additional Gas-phase instruments.....	80
3.3.1.1.	Fourier Transform Infrared spectrometer (FTIR).....	80
3.3.1.2.	Proton Transfer Reaction Time of Flight Mass Spectrometer (PTR-MS).....	81
3.3.1.3.	Ozone, NO _x , NO ₂ and SO ₂ analyzers.....	82
3.3.2.	Particulate phase analysis.....	82
3.3.2.1.	Scanning Mobility Particle Sizer (SMPS).....	82
3.4.	Chamber Experiments.....	83
3.5.	Data Corrections in Chamber Studies.....	85
3.5.1.	Correction from dilution.....	85
3.5.2.	Correction due to particle wall losses.....	86
3.6.	HOMs formation from monoterpene ozonolysis.....	86

3.6.1.	Ozone-initiated reactions of α -pinene, limonene and 3-carene.....	86
3.6.2.	General scheme for HOM Formation from monoterpene ozonolysis.....	88
3.7.	Results from chamber experiments	90
3.7.1.	Ozonolysis reaction of α -pinene.....	90
3.7.2.	Limonene Ozonolysis experiments	95
3.7.3.	3-carene Ozonolysis experiments.....	98
3.7.4.	Ozonolysis experiments of BVOC mixtures.....	101
3.7.5.	α,β -phellandrene + $\text{NO}_3\cdot$ reactions.....	102
3.8.	Discussion.....	105
Chapter 4 Characterization of HOMs in a forested region during an atmospheric measurement field campaign: ACROSS.....		107
4.1.	The ACROSS Project.....	107
4.2.	Ambient measurement site description.....	107
4.3.	Instrumentation Deployed for Ambient Measurements at the Rambouillet supersite...	110
4.3.1.	Deployment of NO_3^- ToFCIMS during ACROSS campaign.....	110
4.3.2.	Additional Instruments Positioned atop of the tower.....	111
4.4.	Campaign Data Overview	112
4.5.	Results of ACROSS Measurements	116
4.5.1.	Overview of Spectral analysis for HOMs	116
4.5.2.	HOM Classification via PCA Analysis.....	117
4.5.2.1.	Terpene-Isoprene HOMs	123
4.5.2.2.	Terpene nitrates I	126
4.5.2.3.	Terpene nitrates II.....	128
4.5.2.4.	Terpene accretions	129
4.5.2.5.	Sunlit component	130
4.5.2.6.	Sunlit terpenes.....	131
4.5.2.7.	Isoprene accretions.....	131
4.5.3.	Case studies	133
4.5.4.	Other measured OVOCs.....	137
4.5.5.	Gas-phase HOMs relationship to Organic Aerosols detected by a Time-of-Flight Aerosol Mass Spectrometer (ToF-AMS).....	140
4.6.	Discussion.....	143
Conclusions and Perspectives		147
References		153

Appendix	185
Supplement–Chapter 2	185
S.2.1. Effect of ion trajectory guiding voltages	185
S.2.1.1. Thuner derived set of voltages initially obtained by Aerodyne	185
S.2.1.2. Oxalic acid sensitivities with different sets of voltages	185
S.2.1.3. Tartaric acid sensitivities with different sets of voltages	187
S.2.1.4. Pyruvic acid sensitivities with different sets of voltages	188
S.2.2. Chemical Structures of Organic Compounds Reviewed in Chapter 2, Section 2.3 ...	190
S.2.3. Data Analysis: Tofware	190
S.2.3.1. Mass calibration	191
S.2.3.2. Baseline determination.....	191
S.2.3.3. Peak shape and width.....	191
S.2.3.4. High resolution peak identification.....	194
Supplement–Chapter 3	197
Supplement-Chapter 4	211
Abstract	220
Résumé	220

Table of Figures

Figure 1.1. Vertical structure of Earth's atmosphere as a function of the global average annual temperature profile (McIlveen, 1991).	5
Figure 1.2. Idealized schematic of the diurnal evolution of the Planetary Boundary Layer (PBL) in clear sky conditions (after Stull, 1988).	7
Figure 1.3. Distribution by sector of VOC emission sources in Ile-de-France Region in 2019 (Airparif, 2022).	9
Figure 1.4. Simplified scheme depicting tropospheric ozone formation from the most important chemical pathways of the troposphere, during daytime (adapted from Jenkin and Clemitshaw, 2000; Liu et al., 2012).	18
Figure 1.5. Ozone isopleth diagram adopted from (National Research Council, 1991).	19
Figure 1.6. General schematic diagram of VOC degradation initiated by OH to form first generation products under atmospheric conditions. The colors blue and black represent the dominant chemical pathways under high and low NO _x conditions, respectively (adapted from Kroll and Seinfeld. (2008)).	23
Figure 1.7. PAN simplified formation mechanism.	26
Figure 1.8. General schematic diagram illustrating the key process of autoxidation, where a molecule undergoes intramolecular H-atom shift and subsequent O ₂ addition to the carbon-centered radical (Ehn et al., 2014). This can be repeated several times leading to HOMs.	33
Figure 2.1. Instrumental configuration of the NO ₃ ⁻ ToFCIMS.	41
Figure 2.2. Schematic illustration of the chemical ionization inlet used in this work (diagram adapted from Jokinen, 2015 and Garmash, 2020).	42
Figure 2.3. The two operation modes of the ToFMS, the V-mode and the W-mode (Jordan et al., 2009).	45
Figure 2.4. An illustrative example of a mass calibration carried out using three reagent ions and several fluorinated organics.	46
Figure 2.5. The two main reagent ions signal stability with different sets of total (T) and Sheath (Sh) flows.	48
Figure 2.6. The ToFwerk APi schematic showing the SSQ, BSQ, and PB regions and their various components. A chemical nitrate ionization inlet replaces the IMR region within the scope of our work.	49
Figure 2.7.a. Percentage contributions of the reagent ions (HNO ₃) _{n=0-2} ·NO ₃ ⁻ and (NO ₃)·H ₂ O ⁻ . b. Percentage ion contributions of the deprotonated form C ₂ HO ₄ ⁻ and the two clusters (NO ₃)·C ₂ H ₂ O ₄ ⁻ and (HNO ₃ NO ₃)·C ₂ H ₂ O ₄ ⁻ for oxalic acid ion products. Numbers represent the ion contribution (%) for the various ions.	50
Figure 2.8.a. Signals of nitrate reagent ions according to the set of voltages tested on the instrument. b. Ratios of various nitrate reagent ion signals to NO ₃ ⁻ as a function of the sets of voltages tested	

on the instrument. c. Signals of oxalic ions (both the deprotonated and the cluster forms) for the sets of voltages tested on the instrument.	51
Figure 2.9. a. Signals of nitrate reagent ions according to the set of voltages tested on the instrument (Table 2.3). b. Ratios of various nitrate reagent ion signals to NO_3^- as a function of the sets of voltages tested on the instrument. c. Signals of succinic ions (both the deprotonated and the cluster forms) for the sets of voltages tested on the instrument.	54
Figure 2.10. a. Percentage contributions of the reagent ions $(\text{HNO}_3)_{n=0-2}\text{NO}_3^-$ and $(\text{NO}_3)\cdot\text{H}_2\text{O}^-$. b. Percentage ion contributions of the deprotonated form $\text{C}_4\text{H}_5\text{O}_4^-$ and the two clusters $(\text{NO}_3)\cdot\text{C}_4\text{H}_6\text{O}_4^-$ and $(\text{HNO}_3\text{NO}_3)\cdot\text{C}_4\text{H}_6\text{O}_4^-$ for succinic acid ion products. Numbers represent the ion contribution (%) for the various ions.	55
Figure 2.11. Experimental set-up used for NO_3^- ToFCIMS calibration with organic compounds. b. Stainless steel grids and tube containing the organic compound.	62
Figure 2.12. Vacuum line for the preparation of the compounds injected into the simulation chamber.	64
Figure 2.13. The experimental setup to deduce the sensitivity of NO_3^- ToFCIMS to an organic compound from its concentration derived by FTIR spectrometry using the CSA chamber.	65
Figure 2.14. NO_3^- ToFCIMS sensitivity (slope) to pyruvic acid derived from the linear curve showing the injected concentration versus the pyruvic ion signals normalized to the total ion count of the reagent ions.	66
Figure 2.15. Oxalic calibration coefficients obtained showing the mean (red line) and 95% confidence intervals (green and gray lines). The red symbols depict the factors obtained from each experiment.	67
Figure 2.16. Succinic acid calibration coefficients obtained. The red symbols depict the factors obtained from each experiment performed.	68
Figure 2.17. Malonic calibration coefficients obtained within a 95% confidence interval. The red symbols depict the factors obtained from each experiment performed.	69
Figure 2.18. Tartaric calibration coefficients obtained within a 95% confidence interval. The red symbols depict the factors obtained from each experiment performed.	69
Figure 2.19. 4-Nitro-catechol calibration coefficients obtained within a 95% confidence interval. The red symbols depict the factors obtained from each experiment performed.	70
Figure 2.20. Time series of pyruvic acid concentrations obtained by FTIR and the corresponding normalized ion signals from the NO_3^- ToFCIMS.	71
Figure 2.21. FTIR pyruvic acid concentration vs normalized pyruvic acid signals of ToFCIMS. The red dashed lines are the fitted trend lines. The slopes equal the calibration factor for each experiment.	72
Figure 3.1. A photograph of the CESAM atmospheric simulation chamber located in the LISA laboratory at the Université Paris-Est Créteil (Maurin, 2013).	77
Figure 3.2. Overview of the experimental setup of CESAM.	80

Figure 3.3. The operating principle of a PTR-ToF-MS (Blake et al., 2009).....	81
Figure 3.4. Schematic of the SMPC-CPC TSI Series 3080 (Series 3080 Operation and Service Manual, 2009).	83
Figure 3.5. α -pinene Ozonolysis initiation reaction (Iyer et al., 2021).	87
Figure 3.6. Limonene ozonolysis initiation reaction following the reaction sequence of one of the major CIs (Wang et al., 2023).	87
Figure 3.7. Example of 3-carene ozonolysis initiation reaction following the reaction sequence of one of the major CIs (Wang et al., 2019).	87
Figure 3.8. Scheme showing the generalized formation mechanism of HOMs from monoterpene $C_{10}H_{16}$ ozonolysis in the absence of NO_x . Formulas highlighted in red and purple are peroxy and alkoxy radicals, respectively, both possessing an odd number of hydrogen atoms ($n=15$), and in black closed-shell products with an even numbers of hydrogen atoms ($n=14,16$). x is the oxygen number with even values initially coming from autoxidation pathway, denoted the RO_2 propagation channel (adapted from Molteni et al., 2019).	88
Figure 3.9. Experiment O1-time series of gas phase precursors, α -pinene (in blue) and O_3 (in red), along with the SOA mass and number concentrations (in black and green, respectively), the gas phase products (in pptv), total HOMs (in purple), the sum of C_{5-10} monomers (in orange) and C_{15-20} dimers (in light blue).	90
Figure 3.10. Visualization of monomer (orange plot) and dimers (blue plot) data sets using Min-Max Normalization.	91
Figure 3.11.a. Averaged mass spectrum of α -pinene ozonolysis experiment-O1 in the monomers mass range (200-400 Th). b. Averaged mass spectrum of α -pinene ozonolysis in the dimers mass range (450-620 Th). The x-axis displays mass to charge ratio (m/z Th) while the y-axis exhibits the normalized signal, as discussed in section 2.3. The m/z values include the mass of the nitrate ion (NO_3^-), but not shown in the chemical formulas. The compounds the highest signals are presented.....	92
Figure 3.12.a. Comparison of average mass spectra obtained from Experiment O1 (red bars) and O2 (blue bars). b. Ratio of peaks detected from Experiment O2 to Experiment O1. The red bar shows the ratio of 1.	95
Figure 3.13. Experiment O3-time series of the gas phase precursors limonene (in blue) and O_3 (in red), along with the SOA mass and number concentrations (in black and green, respectively), the gas phase products (in pptv), total HOMs product (in purple), the sum of C_{8-10} monomer (in orange) and C_{16-20} dimer (in light blue).	96
Figure 3.14. Average mass spectrum of limonene ozonolysis experiment-O3 in the monomer mass range (200-400 Th). b. Average mass spectrum of limonene ozonolysis in the dimer mass range (450-620 Th). The x-axis displays mass to charge ratio (m/z Th) while the y-axis exhibits the normalized signal, as explained in section 2.3. The m/z value include the mass of the nitrate ion (NO_3^-). The compounds with the highest signals are presented.	97
Figure 3.15. a. Comparison of average mass spectrum obtained from Experiments O3 (top) and O4 (bottom). b. Ratio of peaks detected from Experiment O4 to Experiment O3. The red bar points to the ratio equal to 1.	98

Figure 3.16. Experiment O5-time series of gas phase precursors, 3-carene (in blue) and O ₃ (in red), along with the SOA mass and number concentrations (in black and green, respectively), the gas phase normalized total HOMs products (in purple), the sum of C ₇₋₁₀ monomers (in orange) and C ₁₅₋₂₀ dimers (in light blue).	99
Figure 3.17. Average mass spectrum of 3-carene ozonolysis experiment-O5 in the monomers mass range (200-400 Th). b. Average mass spectrum of 3-carene ozonolysis in the dimers mass range (450-620 Th). The x-axis displays mass to charge ratio (m/z Th) while the y-axis exhibits the normalized signal, as explained in section 2.3. The m/z value demonstrated is aligned with the nitrate ion (NO ₃ ⁻). The compounds with relatively higher signals are presented, although some peaks may have overlapping signals, but the dominant one is displayed (* for example).	100
Figure 3.18. Comparison of the average mass spectrum obtained from Experiments O7 (red bars) and O8 (purple bars).	102
Figure 3.19. Averaged Mass Spectrum of Exp. N6 for α-phellandrene + NO ₃ in the monomers mass range (330-390 Th). b. Averaged Mass Spectrum of Exp. N6 for α-phellandrene + NO ₃ in the dimers mass range (500-660 Th). The x-axis displays mass to charge ratio (m/z Th) while the y-axis exhibits the normalized signal. The m/z value include the mass of the nitrate ion (NO ₃ ⁻). The compounds with the highest signals are presented. The averaging is performed for spectra collected during the first 10 min after the addition of N ₂ O ₅	104
Figure 3.20. Comparison of monomers and dimers detected from α-phellandrene + NO ₃ in Exp. N11 (with t-butene) vs Exp. N12 (without t-butene). The values of the normalized signals are averaged for the first 10 min reaction after the addition of N ₂ O ₅ . Symbol ‘+’ refer to the presence of new products in Experiment N11 that are not found in Experiment N12. Symbol ‘×’ refer to the absence of products within the Experiment N11 that were found in Experiment N12.	105
Figure 4.1. Photos of the measurement site in the Rambouillet Forest (from the top of the tower on the left) and a view of the 40-m tower (on the right) during the ACROSS summer campaign. ...	108
Figure 4.2. Map of the main site locations involved in the ACROSS campaign.	109
Figure 4.3. Photos showing, from left to right, the room atop of the tower, the installation of the NO ₃ ⁻ ToFCIMS and the instrument in its acquisition mode during the ACROSS summer campaign.	110
Figure 4.4. Temporal data overview during ToFCIMS operation at the top of the tower. a. T and SR (Météo-France). b. NO and NO ₂ (IMT, LISA). c. O ₃ and SO ₂ (LISA). d. isoprene and sum of MVK/MACR/ISOPOOH (IMT). e. monoterpenes (IMT). f. sesquiterpenes (IMT). g. Total HOMs (break at 20 pptv) and H ₂ SO ₄ (this study, LISA). A color-coded banner at the top of the figure is employed to highlight time intervals corresponding to distinct major wind origins: blue for southwestern winds, green for northwestern winds, light red for northeastern winds and yellow for east-southeastern winds (Figure S.4.1–4.8).	113
Figure 4.5. The average diurnal cycles of: a. isoprene and the sum of MVK/MACR/ISOPOOH frag. b. Monoterpenes, and sesquiterpenes. c. NO, NO ₂ , O ₃ on the right y-axis starting at 30ppbv and SR on the right offset y-axis. d. AOx (tower level) and OH concentrations (ground level). The error bars represent one standard deviation.	115

Figure 4.6. Diurnal profiles of total HOMs and H ₂ SO ₄ mixing ratios throughout the study period. The error bars represent one standard deviation.	115
Figure 4.7.a. Average mass spectra for the daytime period (4:00-19:00) and the nighttime (20:00-03:00) across the study period. The gray shaded area represents the nighttime spectrum (below zero line). The red text reflects suggested formulas for HOM-RO ₂ . The red asterisk on highlights C ₅ H ₁₀ N ₂ O ₈ molecules with mixing ratios not scaled (1x[HOM]). a, b. The expanded mass spectra of the mass ranges 220-300 and 300-400 have peak levels scaled by 5 except for the one marked by an asterisk. c. The expanded mass spectra of the dimer mass range 500-600, all peaks levels remained unchanged. For b, c and d, the major peaks are labeled.....	116
Figure 4.8. Time profiles of PCA-derived components from HOM data collected by the NO ₃ ⁻ ToFCIMS throughout the campaign. The shaded region in red corresponds to a time interval aligned with the red tick labels on the y-axis, positioned to the right to enhance visibility of the lower component levels.....	118
Figure 4.9. The average diurnal cycles of PCA-derived components from HOM data collected by the NO ₃ ⁻ ToFCIMS throughout the campaign. The error bars represent one standard deviation of the bin for which the average is shown by the symbol.	122
Figure 4.10. The average diurnal cycles of PCA-derived Terpene-Isoprene HOMs component from HOM data collected by the NO ₃ ⁻ ToFCIMS throughout the campaign. The error bars represent one standard deviation of the bin for which the average is shown by the symbol.....	123
Figure 4.11. Pearson correlation coefficients between the 7 principal components of the PCA analysis (a-f) and gas-phase tracers (NO, NO ₂ , O ₃ , OH concentration [OH], OH reactivity (OHR), AOx, SO ₂ , H ₂ SO ₄ , Isop. for isoprene, MVK* for MVK/MACR/ISOPOOH Frag, Monoterpenes (MTs), types of MTs such as pinoaldehyde, camphor, and nopinone), and meteorological factors (P, SR, T, WD, WS, and RH). All measurements were taken at the top of the tower except for [OH]. The green labels represent positive values of Pearson correlation, while the red labels represent negative values.	125
Figure 4.12. Examples of diurnal cycles for the major isoprene and monoterpenes nitrate and non-nitrate HOMs in the component Terpene-Isoprene HOMs.....	126
Figure 4.13. The average diurnal cycles of PCA-derived Terpene nitrates I component from HOM data collected by the NO ₃ ⁻ ToFCIMS throughout the campaign. The error bars represent one standard deviation of the bin for which the average is shown by the symbol.....	127
Figure 4.14. The average diurnal cycles of PCA-derived Terpene nitrates II component from HOM data collected by the NO ₃ ⁻ ToFCIMS throughout the campaign. The error bars represent one standard deviation of the bin for which the average is shown by the symbol.....	128
Figure 4.15. The average diurnal cycles of PCA-derived Terpene accretions component from HOM data collected by the NO ₃ ⁻ ToFCIMS throughout the campaign. The error bars represent one standard deviation of the bin for which the average is shown by the symbol.....	129
Figure 4.16. The average diurnal cycles of PCA-derived Sunlit component from HOM data collected by the NO ₃ ⁻ ToFCIMS throughout the campaign. The error bars represent one standard deviation of the bin for which the average is shown by the symbol.	130

Figure 4.17. The average diurnal cycles of PCA-derived Sunlit component from HOM data collected by the NO ₃ ⁻ ToFCIMS throughout the campaign. The error bars represent one standard deviation of the bin for which the average is shown by the symbol.	131
Figure 4.18. The average diurnal cycles of PCA-derived Sunlit component from HOM data collected by the NO ₃ ⁻ ToFCIMS throughout the campaign. The error bars represent one standard deviation of the bin for which the average is shown by the symbol.	132
Figure 4.19. Diurnal variations of measured parameters at the top of the tower: Study-1 (upper panel) and Study-2 (lower panel).	134
Figure 4.20. Diurnal variations of measured parameters at the top of the tower: Study-3.	136
Figure 4.21. Time Series of major Non-HOM species detected by the NO ₃ ⁻ ToFCIMS on the tower level.	138
Figure 4.22.a. Temporal data of total HOMs (dark red trace) and OA-AMS (light red dotted trace). The yellow squared area represents a significant biomass burning event that occurred in the afternoon of July 19 th . Breaks are introduced at 12.5 for the left y-axis and 20 for the right y-axis. b, c. Diurnal cycles of PCA-derived HOM components and OA-AMS data. Data related to biomass burning have been excluded from the diurnal cycle calculations.	141
Figure 4.23. Pearson correlation coefficient between the OA-AMS and the 7 principal components of the PCA analysis. a. throughout the day. b. daylight (6:00–19:00). c. nighttime (21:00–4:00).	142

List of Tables

Table 1.1. Major gaseous constituents of Earth's atmosphere and their mixing ratio, in a dry environment, except for water (Wallace and Hobbs, 2006).....	4
Table 1.2. Estimated Tropospheric lifetimes for Selected VOCs (at 298 K) (from Atkinson, 2000 and Atkinson and Arey, 2003a).....	9
Table 1.3. Classification of major atmospheric VOCs into categories based on their chemical structures.	11
Table 1.4. Classification of VOCs according to their boiling point temperatures (Molhave et al., 1997).....	11
Table 1.5. Selected terpene compounds emitted by terrestrial vegetation giving the chemical names, molecular structure, and molecular weight (Fuentes et al., 2000; Atkinson and Arey, 2003a).	14
Table 1.6. NO ₃ rate coefficients for selected classes of AVOCs and BVOCs and their lifetimes at fixed NO ₃ mixing ratio (Brown and Stutz, 2012).	20
Table 1.7. Vapor pressure changes of an organic compound upon addition of a functional group (Kroll and Seinfeld, 2008). The factors are multiplicative which implies that the addition of a functional group reduces the vapor pressure by the factor given (i.e. the factor is multiplied by the original vapor pressure of the compound).....	24
Table 1.8. Molar HOM Yields (\pm uncertainty) from BVOC oxidation, collected from literature studies for various oxidants and using NO ₃ ⁻ Chemical Ionization Mass Spectroscopy detection.	35
Table 1.9. Molar HOM Yields from AVOC oxidation by OH, and using NO ₃ ⁻ Chemical Ionization reported in the literature.	37
Table 2.1. List of perfluorinated organic compounds chosen for mass calibration covering a wide range of m/z.....	47
Table 2.2. Summary of the RSD% values for the 8 data sets.	48
Table 2.3. Set of Voltage configuration.	53
Table 2.4. Calibration factors obtained for succinic acid for the various sets of applied voltages.	56
Table 2.5. Reported calibration factors in the literature using a NO ₃ ⁻ ToFCIMS.....	59
Table 2.6. Candidate organic compounds used to evaluate the sensitivity of the instrument. The yielding response (+ = detected, - = not detected) is based on the appropriate heating temperature. *Upon heating, this compound exhibits color changes, indicating decomposition.	61
Table 2.7. The calibration factor deriving from three experimental setups, described briefly in the comments column.	73
Table 2.8. Parameters employed in the H ₂ SO ₄ source used during calibration experiments of the NO ₃ ⁻ ToFCIMS.	74

Table 2.9. Summary of the calibration factors resulted for the organic compounds measured with the NO ₃ ⁻ ToFCIMS. *Following Approach 1; **Following Approach 2	75
Table 3.1. The rate coefficients of selected BVOCs for reaction with O ₃ and OH [•] radicals at 298 K	79
Table 3.2. Experimental conditions for the CESAM chamber studies (ppbv±1stdv of signal uncertainty). Experiment numbers starting with the letter ‘O’ refer to VOC reaction with ozone. [VOC] ₀ , [Cyclohexane] ₀ and [O ₃] ₀ are the initial levels of VOC, cyclohexane and ozone, in ppbv.	84
Table 3.3. Experimental conditions of the BVOC + NO ₃ chamber experiments. [VOC] ₀ and [t-C ₄ H ₈] ₀ are the initial levels of α,β-phellandrene and trans-2-butene, in ppbv and ppmv, respectively. The reaction time is defined as the period starting from the initial injection of the oxidant and extending until the end of the experiment. Experiment numbers starting with the letter ‘N’ and ‘N’ refer to α-phellandrene and β-phellandrene reaction with NO ₃ , respectively.	84
Table 3.4. Experimental conditions for the CESAM chamber studies from AVOC + OH reactions. Experiment numbers starts with the letter ‘H’ referring for reaction with hydroxyl radicals. [VOC] ₀ , [NO] ₀ , [seed] and the flow of H ₂ O ₂ are the variables initially injected into the chamber	85
Table 3.5. Summary of the experimental conditions, the BVOC and the reaction time in min. The reaction time is defined as the period starting from the initial injection of the oxidant and extending until the end of the experiment.	101
Table 4.1. The distribution of tree species in the Rambouillet forest (ONF, 2006).....	108
Table 4.2. Measurement techniques deployed during the campaign at the top of the tower.	112
Table 4.3. The molecules contributing to the Terpene-Isoprene HOMs component with molecules sorted in descending order of their contribution to the component.....	120
Table 4.4. The molecules contributing to the Terpene nitrates I component with molecules sorted in descending order of their contribution to the component.	121
Table 4.5. The molecules contributing to the Terpene nitrate II, Terpene accretions and Sunlit factor components, respectively, with molecules sorted in descending order of their contribution to the component.	121
Table 4.6. The molecules contributing to the Sunlit terpenes, and Isoprene accretions, respectively, components with molecules sorted in descending order of their contribution to the component.	122
Table 4.7. Summary of Statistics for the different case studies.	135
Table 4.8. C ₂ -C ₃ nitrates and non-nitrates molecules and C ₆ -C ₇ nitrophenols detected by the ToFCIMS at the tower level, listed in descending order based on their contribution to the overall spectrum. * non-nitrate C ₄	139

List of Acronyms

ACROSS	Atmospheric Chemistry Of The Suburban Forest
APi-ToF	Atmospheric Pressure Interface Time Of Flight Mass Spectrometry
APi	Atmospheric Pressure Interface
AVOC(s)	Anthropogenic Volatile Organic Compound(s)
BSQ	Big Segmented Quadrupole
BSQB	Big Segmented Quadrupole Back
BSQF	Big Segmented Quadrupole Front
BVOC(s)	Biogenic Volatile Organic Compound(s)
CCN	Cloud Condensation Nuclei
CD	Collisional Dissociation
CESAM	Chambre Expérimentale De Simulation Atmosphérique
CI _s	Criegee Intermediates
CI	Chemical Ionization
CI-QMS	Chemical Ionization Coupled To A Quadrupole Mass Spectrometer
CL	Convective Layer
CPC	Condensation Particle Counter
CSA	Chambre de Simulation Atmosphérique
DMA	Differential Mobility Analyzer
ELVOC(s)	Extremely Low Volatile Organic Compound(s)
EZ	Entrainment Zone
FT	Free Troposphere
FTIR	Fourier Transform Infrared Spectrometer
FWHM	Full Width at Half Maximum
GHG	GreenHouse Gases
HC(s)	HydroCarbon(s)
HDF5	Hierarchical Data Format 5
HOM(s)	Highly Oxygenated organic Molecule(s)
HOM-ONs	Highly Oxygenated organic Molecule Organic Nitrates
HOM-RO·	Highly Oxygenated organic Molecule Derived Alkoxy Radicals
HOM-RO ₂ ·	Highly Oxygenated organic Molecule Derived Peroxy Radicals
HR	High Resolution
ID	Internal Diameter
IR	InfraRed
IVOC(s)	Intermediate Volatile Organic Compound(s)
lpm	liter-per-minute
LVOC(s)	Low Volatile Organic Compound(s)

m/z	mass-to-charge
MACR	MethACRolein
MBO	Methyl-3-Buten-2-Ol
MCP	Multi-Channel Plate
MCT	Mercury-Cadmium-Telluride
MEGAN	Model of Emissions of Gases and Aerosols from Nature
MFC	Mass Flow Controller
MVK	MethylVinylKetone
NO ₃ ⁻ CI	Nitrate Chemical Ionization
NO ₃ ⁻ CI-APi-ToF ≡ NO ₃ ⁻	Nitrate Chemical Ionization Atmospheric Pressure Interface
ToFCIMS	Time-Of-Flight Mass Spectrometer
NPF	New Particle Formation
OC	Organic Compounds
OHs	Orgnaic Halides
ONs	Organic Nitrates
OSs	Organic Sulfates
OVOCs	Oxygenated Volatile Organic Compounds
PA	Proton Affinity
PAHs	Polycyclic Aromatic Hydrocarbons
PANs	PeroxyAcyl Nitrates
PB	Primary Beam
PBL	Planetary Boundary Layer
PCBs	PolyChlorinated Biphenyls
PFA	PerFluoroAlkoxy
POZ	Primary OZonide
ppbv	parts per billion by volume
ppmv	parts per million by volume
pptv	parts per trillion by volume
ppqv	parts per quadrillion by volume
PTR-MS	Proton Transfer Reaction Mass Spectrometer
Pvap	vapor Pressure
RD	Relative Difference
RF	RadioFrequency
RH	Relative Humidity
RL	Residual Layer
RSD	Relative Standard Deviation
SAMU	Spectromètre de masse Atmosphérique Multi-espèces
SBL	Stable Boundary Layer
SI	Single Ion
SIS	Single Ion Signal
SMPS	Scanning Mobility Particle Sizer
SOA	Secondary Organic Aerosols
SSQ	Small Segmented Quadrupole

ST	Source Tube
Stdv	Standard deviation
SVOC(s)	Semi Volatile Organic Compound(s)
T	Temperature
ITE	Ion Transmission Efficiency
ToF	Time-of-Flight
ToFMS	Time-of-Flight Mass Spectrometer
ULVOC(s)	Ultra Low Volatile Organic Compound(s)
UMR	Unit Mass Resolution
UV	UltraViolet
VHP	Vinyl HydroPeroxide
VOCs	Volatile Organic Compounds

Introduction

Since the beginning of the industrial revolution in the 17th century, the world's population has continued to increase to its current level of 8 billion. This growth is strongly linked to technological advancements, especially in the area of healthcare, which has resulted in a decline in the mortality rate and thus an upsurge in the population size (Roser et al., 2013). Furthermore, this massive and continuous increase and the swift urbanization of cities are responsible for immense use of burning of fuels for creation of energy that results in the release of a wide variety of trace gases and particulate species into the troposphere, thereby degrading ambient air quality, impacting climate and damaging public health. The pollution of air, whether outdoor or indoor, is recognized as one of the greatest environmental health threat to human beings as it accounts for an estimated 7 million deaths annually predominantly in developing countries (WHO, 2020).

Among the most reactive trace species, volatile organic compounds (VOCs) play a significant role in the chemistry of the troposphere. Although they represent only a small component of air (pptv to ppbv levels), they control a large part of its chemistry. These molecules are involved in many chemical reactions, and the resulting transformations can result in the formation or destruction of a variety of oxidants and secondary products which could be more harmful than the molecules from which they are derived. VOCs are well-known for their involvement in the production of ground-level ozone (O₃) and the formation of secondary organic aerosols (SOA) known to significantly affect air quality, human health and climate (Seinfeld and Pandis, 2016).

VOCs can be emitted into the air in large amounts by both anthropogenic (human activity emissions) and natural sources (biogenic emissions), or may be the product of chemical transformations occurring during transport of air masses (Guenther et al., 2012; Baudic et al., 2016).

The pathways that control the chemical evolution of VOCs are driven by various oxidation regimes that depend on environment in which the oxidation takes place:

- Urban plumes: marked by high levels of nitrogen oxides (NO_x), the sum of nitrogen monoxide (NO) and nitrogen dioxide (NO₂), mainly emitted from combustion related to transportation and energy production, and dominated by anthropogenic VOCs (AVOCs).
- Rural/Forested areas: characterized by lower levels of NO_x and dominated by biogenic VOCs (BVOCs) (Guenther et al., 2012; Freney et al., 2014).

- Urban/forested mixed environments: characterized by moderate NO_x levels and a combination of AVOCs and BVOCs.

Recently, AVOCs and BVOCs have been shown to serve as key precursors for the gas-phase formation of Highly Oxygenated organic Molecules (HOMs), initially designated as Extremely Low Volatile Organic Compounds (ELVOCs) (Schobesberger et al., 2013; Ehn et al., 2014). The term HOM is defined as the name for the class of products formed in the gas phase chemical process called autoxidation (Bianchi et al., 2019). Because of their low volatility, it is expected that they efficiently partition into the particle phase, thereby having the potential to condense onto pre-existing aerosols or contribute to new particle formation (NPF) (Riccobono et al., 2014; Kirkby et al., 2016). Incorporation of organic compounds, including HOMs, into aerosols creates what is known as SOA.

The primary focus of this thesis research is to investigate the pathways through which HOMs form as a result of the oxidation of VOC precursors. This investigation is conducted through chamber experiments as well as atmospheric field observation. To detect HOMs as well as other OVOCs, a NO_3^- ToFCIMS (nitrate Chemical Ionization Inlet integrated with an Atmospheric Pressure interface Time of Flight Mass Spectrometry, APi-ToF) instrument is employed.

This thesis manuscript is structured into four major chapters:

- In the first chapter, we provide an overview of the general context of our thesis project, elaborating on the state of the art, particularly the scientific knowledge regarding VOCs, from their emissions to their behavior in the troposphere under various oxidation conditions. The latter illustrates its connection with the gas-phase formation of HOMs.
- The second chapter outlines the operational principles, advantages, and limitations of the NO_3^- ToFCIMS instrument. Additionally, it presents the results obtained from the characterization of this instrument in the laboratory through a series of experiments, which are also described in detail. Approaches for instrument calibration, essential for quantifying HOMs and OVOCs, have been developed and are presented and discussed in this chapter.
- The third chapter describes the experiments conducted in the chamber. The HOMs data generated from the NO_3^- ToFCIMS are interpreted, analyzed, and discussed within the course of this chapter. Lists of HOMs are also established for use as a reference during field observations.

- Finally, Chapter 4 presents the results from the study of HOMs in the forest during a field campaign of the ACROSS project. This project is introduced along with a description of the instrumental set-up, an overview of the data obtained from measurements of key compounds (e.g. O₃, VOCs, NO_x, H₂SO₄) and environmental parameters (e.g. temperature, solar radiation), as well as a comprehensive analysis of the overall HOM measurements.

Chapter 1 Introduction to atmospheric chemistry of the troposphere

1.1. Properties of the earth's atmosphere

1.1.1. Atmospheric vertical structure and composition

The atmosphere of the earth is a complex mixture of gases and particles surrounding the terrestrial globe. The gas phase consists primarily of about 78% of nitrogen (N₂), 21% of molecular oxygen (O₂) and 0.9% of argon (Ar). The remaining 0.1% consists of so-called trace gases that are active in atmospheric chemistry. The major gaseous constituents are presented in Table 1.1 along with their corresponding averaged mixing ratio (Wallace and Hobbs, 2006). Water vapor (H₂O) is most abundant in the lower atmosphere with variable amounts depending on the region (latitude and altitude) and the atmospheric conditions. Small fractions of suspended solid and liquid particles are also present in the atmosphere.

Atmospheric composition has been and continues to be significantly affected by the presence of trace gaseous and particulate substances that originate from both biogenic (natural) and anthropogenic (man-made) sources. Despite their relatively low abundance, they play crucial roles in the radiative balance and in the chemical properties of the atmosphere (Seinfeld and Pandis, 2016).

Table 1.1. Major gaseous constituents of Earth's atmosphere and their mixing ratio, in a dry environment, except for water (Wallace and Hobbs, 2006).

Constituent	Mixing Ratio
Nitrogen (N ₂)	78%
Oxygen (O ₂)	21%
Argon (Ar)	0.93%
Water vapor (H ₂ O)*	0-5.0%
Carbon dioxide (CO ₂)*	420 ppm
Neon (Ne)	18 ppm
Helium (He)	5.2 ppm
Methane (CH ₄)*	1.9 ppm
Krypton (Kr)	1.1 ppm
Hydrogen (H ₂)	0.53 ppm
Nitrous oxide (N ₂ O)*	0.31 ppm
Ozone (O ₃)*	0-0.1 ppm

*Greenhouse gases (GHG)

Earth's atmosphere is composed of four distinct layers: the troposphere, the stratosphere, the mesosphere and the thermosphere (Figure 1.1). Boundaries between layers are caused by changes in the direction of temperature gradients with altitude.

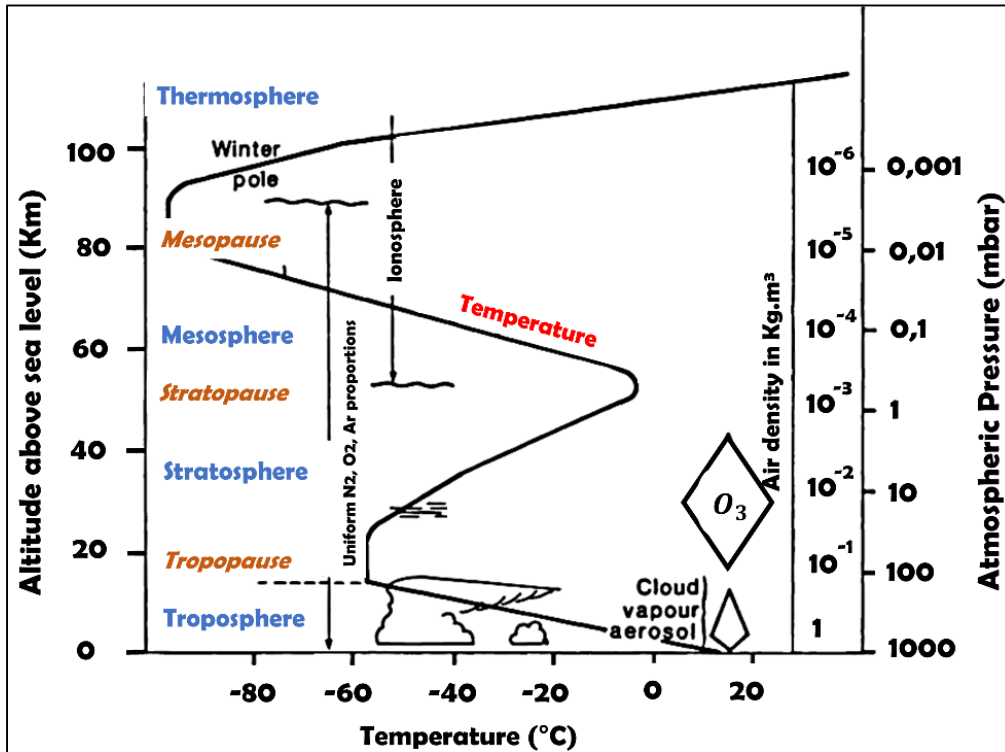


Figure 1.1. Vertical structure of Earth's atmosphere as a function of the global average annual temperature profile (McIlveen, 1991).

These layers are also separated one from the other by sub-layers where the temperature gradients change direction. These sub-layers are designed as: the tropopause, the stratopause and the mesopause.

The lowest layer is the troposphere that extends from the surface to the tropopause, and whose thickness varies between about 7 to 18 km depending on the latitude and the season. The temperature of the troposphere gradually decreases with altitude at a rate of approximately 6.5°C per 1 km, reaching its lowest temperature of about -56°C near the tropopause. The troposphere typically has significant vertical mixing and cloud formation, because of the generally large amounts of H₂O vapor. The troposphere is also the place where compounds released from the surface typically reside.

The stratosphere, situated from the tropopause to altitudes of about 45 to 55 km, contains 90% of atmospheric ozone (O₃), which is formed naturally from the photolysis of O₂ through its interaction with the sun's ultraviolet (UV) radiation that has sufficiently high energy (wavelengths less than 241 nm). The ozone layer is essential in protecting life on Earth by absorbing most of the UV rays that are extremely harmful to all living things. This phenomenon is responsible for the release of heat explaining the increase in temperature with altitude that reduces vertical mixing within this layer.

The mesosphere is located above the stratopause and extends to the mesopause at about 85 to 100 km in altitude (Venkat Ratnam et al., 2010). In this layer, temperature decreases with altitude to a coldest value of about -90°C . In addition, this is generally where dust and particles from space (meteors) ignite.

The highest layer in the atmosphere, the thermosphere, is located above the mesopause and reaches about 600 km in altitude. It is characterized by high temperatures reaching from 500°C up to 2000°C near its maximum altitude due to the presence of N_2 and O_2 and their ions and atoms absorbing the short-wavelength radiation. The ionosphere is considered to be the lower part of the thermosphere where photoionization of N_2 and O_2 occurs leading to bands of brightly colored lights around the poles, known as aurora borealis and aurora australis, or simply the Northern and Southern Lights (UCAR, 2015).

1.1.2. Tropospheric characteristics

The troposphere is the layer that supports life and maintains most of the floral and faunal environments on planet Earth. It holds the bulk of atmospheric mass (about 80%), and as previously mentioned, contains nearly all the water vapor, and thus is the region where most of the meteorological, climatic and chemical processes are located. It is distinguished by two sublayers separated one from the other by an inversion layer where the normal temperature gradient is inverted: the planetary boundary layer (PBL), extending from the surface to various altitudes between a few hundred meters to 2 km (depending on latitude, surface elevation and structure, time of year, and time of day), and the free troposphere (FT), extending upwards from the PBL to the tropopause (Zehnder et al., 2018). The presence of inversion layers depends on the atmospheric conditions, and usually is present at night and in the early morning. During the day, there is typically enough mixing and surface heating to suppress the inversion and lead to an elevation of the PBL height.

The PBL is in direct contact with the earth's surface (land and sea) and is therefore indirectly affected, on timescales ranging from hours to days, by aerodynamic drag caused by its roughness, and by heat transfer that maintains the radiative balance between the surface and the FT. It is therefore often characterized by turbulence and strong winds. The PBL thickness follows a diurnal trend as the earth's surface warms and cools over a 24-hour period as shown in Figure 1.2.

In clear sky daytime conditions, vertical turbulence is generated above the ground as warmer and hence lighter air rises as the surface is heated from solar shortwave radiation. This layer which is

known as the convective layer (CL), is vertically limited by a stable layer above called the entrainment zone (EZ). It is where vertical exchange between the FT and the PBL occur. At sunset, the CL starts to collapse due to the rapid cooling of the surface by infrared (IR) radiation emission, and subsequently transforms into a stable boundary layer (SBL) near the surface that is characterized by limited vertical mixing due to the temperature inversion. A residual layer (RL), marked by the same turbulent properties as the daytime CL, remains present above the SBL and is associated with a stable capping inversion layer (CIL) above. The SBL continues to grow during night as the surface continues to cool. Thus, the turbulence in the RL is limited by the underlying SBL and the aloft CIL, with no additional source of turbulence generation to sustain it. However, it plays a crucial role in the rapid growth of the CL after sunrise, where a new CL is formed that replaces the nighttime SBL and the cycle continues.

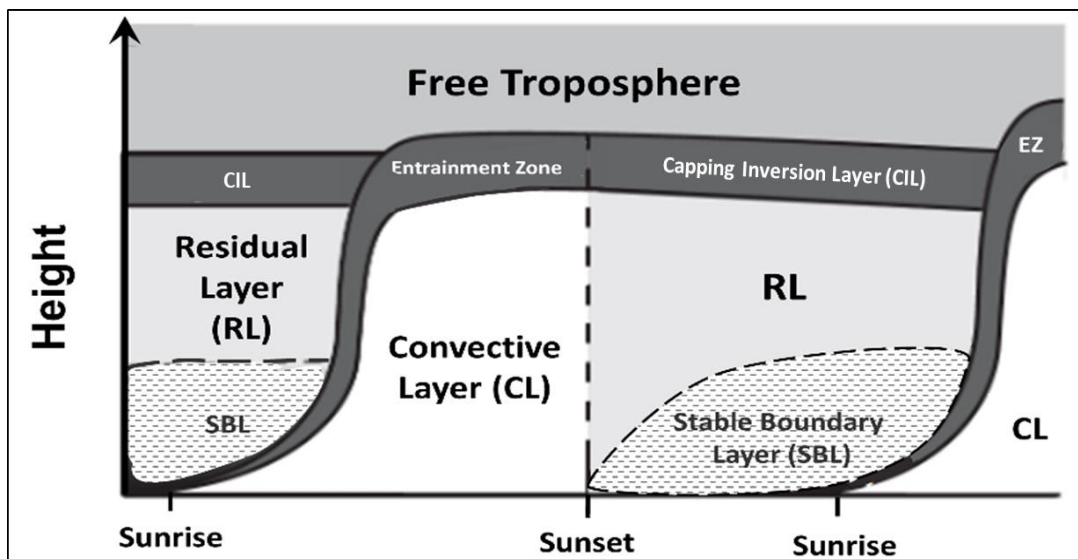


Figure 1.2. Idealized schematic of the diurnal evolution of the Planetary Boundary Layer (PBL) in clear sky conditions (after Stull, 1988).

The PBL serves as an important interface for most direct emissions or transformation of chemical pollutants including VOCs emitted from a variety of anthropogenic and biogenic sources. The PBL plays a key role in the vertical mixing of chemical species and their dispersion, impacting their concentration and thus the composition of the lower atmosphere (Vivone et al., 2021).

Thus, the PBL has a fundamental and crucial role in the vertical transport of heat and pollutants from the surface to the FT, thereby influencing meteorology and air quality on local, regional and global scales.

1.2. Tropospheric chemistry

The troposphere acts as an oxidative chemical reactor in which solar radiation triggers reactions leading to the formation of oxidants for many atmospheric species. Interaction between oxidants and other trace atmospheric components results in their oxidation. Important among the reactants are volatile organic compounds (VOCs) and reactive nitrogen compounds including nitrogen oxides (NO_x) leading to a wide variety of secondary substances. As described earlier, VOCs are involved in many of the chemical reactions occurring in the troposphere. They are important precursors for secondary products such as O₃ and SOA. This section focuses on the current scientific knowledge of VOCs, from their emission to their fate in the troposphere in both urban and rural/forested environments as well as in mixed urban/forested environments. The tropospheric chemistry in various oxidation regimes is described to introduce their connection to the formation of gas-phase HOMs, which is the core of this research work.

1.2.1. Volatile Organic Compounds

Atmospheric VOCs comprise hundreds of thousands of reactive organic species that are present at trace levels (Goldstein and Galbally, 2007). They are marked by at least one carbon (C) atom bound to one or more other atoms such as hydrogen (H), oxygen (O), nitrogen (N), halogens and other heteroatoms. However, the term VOC usually excludes methane (CH₄), and the two inorganic carbon-containing compounds, carbon monoxide (CO) and carbon dioxide (CO₂). VOCs were initially defined as compounds characterized by high vapor pressures under normal atmospheric conditions of temperature and pressure (25°C, 101.325 Pa), exceeding 0.01 kPa at a temperature of 293.15 K with a boiling point of 250°C or less (Directive 1999/13/CE, Article 2).

VOCs are recognized to either be directly emitted into the air through both natural (from land or marine ecosystems, known also as biogenic) and anthropogenic man-made sources (from urban and suburban areas), or formed by chemical transformations during long-range transport of air masses (Atkinson, 1995). On a global scale, VOCs are dominated by emissions from the biosphere (BVOCs) representing approximately 90% of the total emissions (Guenther et al., 2012; Sindelarova et al., 2014). However, the relative abundance varies regionally, especially in urban environments where anthropogenic sources account for the major proportion of VOC emissions (Baudic et al., 2017). For instance, in the Ile-de-France region AVOCs dominate with 75% of total VOC emissions, as shown in Figure 1.3 (Airparif, 2021).

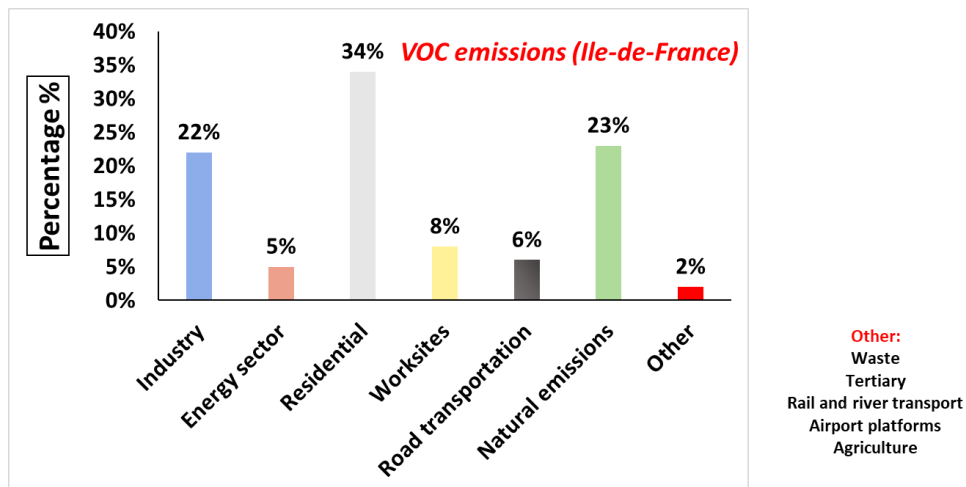


Figure 1.3. Distribution by sector of VOC emission sources in Ile-de-France Region in 2019 (Airparif, 2022).

Table 1.2. Estimated Tropospheric lifetimes for Selected VOCs (at 298 K) (from Atkinson, 2000 and Atkinson and Arey, 2003a).

Compound	Lifetime due to*			
	OH	O ₃	NO ₃	Photolysis
Propane	10 d	>4500 yr	~7 yr	
n-Butane	4.7 d	>4500 yr	2.8 yr	
n-octane	1.3 d		240 d	
Ethene	1.4 d	10 d	225 d	
Propene	5.3 h	1.6 d	4.9 d	
Isoprene	1.4 h	1.3 d	50 min	
α -pinene	2.6 h	4.6 h	5 min	
Limonene	50 min	2 h	3 min	
3-Carene	1.6 h	11 h	3.5 min	
β -Caryophyllene	42 min	2 min	1.5 min	
Benzene	9.4 d	>4.5 yr	>4 yr	
Toluene	1.9 d	>4.5 yr	1.9 yr	
m-Xylene	5.9 h	>4.5 yr	200 d	
Styrene	2.4 h	1 d	3.7 h	
o-Cresol	3.3 h	65 d	2 min	
Formaldehyde	1.2 d	>4.5 yr	80 d	4 h
Acetaldehyde	8.8 h	>4.5 yr	17 d	6 d
Benzaldehyde	11 h		18 d	
Acetone	53 d		>11 yr	60 d
2-Butanone	10 d			
Methylglyoxal	9.3 h	>4.5 yr		2 h
Methanol	12 d		1 yr	
Ethanol	3.5 d		26 d	
Methyl t-butyl ether	3.9 d		72 d	
Methacrolein	4.1 h	15 d	11 d	1 d
Methyl vinyl ketone	6.8 h	3.6 d	>385 d	2 d
Methyl hydroperoxide	2.1 d			5 d
2-Butyl nitrate	13 d			15-30 d

*Lifetime calculated using the following:

- For OH radical reactions, a 12-h daytime average of 2.0×10^6 molecule cm^{-3} ;
- For NO₃ radical reactions, a 12-h nighttime average of 5×10^8 molecule cm^{-3} ;
- For O₃, a 24-h average of 7×10^{11} molecule cm^{-3}

BVOCs are generally found to be more reactive than AVOCs, with typical atmospheric lifetimes of a few hours or less compared to a few days for most AVOCs (Atkinson, 2000; Atkinson and Arey, 2003a). Table 1.2 displays the tropospheric lifetimes of some examples of VOCs including various families (discussed in this section).

Once emitted into the air, VOCs are subject to removal by chemical transformations, including chemical oxidation reactions with the three major oxidants, namely hydroxyl radicals ($\text{OH}\cdot$), nitrate radicals ($\text{NO}_3\cdot$) and ozone (O_3). In marine environments, halogens (chlorine (Cl), bromine (Br), and iodine (I)) may also be important oxidants (Finlayson-Pitts, 2010). Chemical reaction in the troposphere eventually leads to the formation of multifunctional organic vapors that are usually less volatile than the initial compound, except in cases of fragmentation, and that can take part in the formation and growth of SOA (Kanakidou et al., 2005; Riipinen et al., 2011). Furthermore, photolysis may occur for some VOCs, which involves compounds that absorb solar radiation at wavelengths that reach the troposphere. Oxidized VOCs can also undergo physical processes such as dry (on the ground and on surfaces of aerosols or vegetation) or wet deposition (rain) (Goldstein and Galbally, 2007).

VOCs act as key precursors in the formation of SOA as well as the production of ground-level O_3 , which have been shown to cause severe adverse impacts on the health of both humans and ecosystems, and to influence the Earth's radiative balance and therefore impact the overall global climate system (Gryparis et al., 2004; Fiscus et al., 2005). Some VOCs have been shown to have direct chronic effects on human health, which include both carcinogenic and non-carcinogenic impacts. For instance, benzene, an aromatic VOC, is a known carcinogen, while other products, especially those from incomplete combustion of VOCs have deleterious health effects (US EPA, 1990; Ramírez et al., 2012). Generally, VOCs can be classified into categories based on their chemical structure (Seinfeld and Pandis, 2016; M. Wang et al., 2020) (Table 1.3):

- Non-methane hydrocarbons, consisting solely of carbon and hydrogen, and covering four chemical families of species: alkanes, alkenes, alkynes and aromatics (including polycyclic aromatic hydrocarbons (PAHs)).
- Terpenoid compounds, recognized as a dominant class of natural products, including many hydrocarbon chemical species, with the general formula $(\text{C}_5\text{H}_8)_n$, and a variety of oxygenated terpenoids.
- Oxygenated VOCs (OVOCs) are organic compounds containing at least one oxygen atom. They can be classified, depending on the functional groups present, such as aldehydes,

ketones, alcohols, and carboxylic acids (e.g. acetaldehyde, acetone, ethanol, and formic acid).

- Other families of organic compounds containing atoms in addition to C, H and O. Some examples are organic sulfates (OSs), organic nitrates (ONs), organic halides (OHs), polychlorinated biphenyls (PCBs) and peroxyacyl nitrates (PANs). Their properties vary greatly depending on their chemical structure.

Table 1.3. Classification of major atmospheric VOCs into categories based on their chemical structures.

Family	Chemical formulas
Non-methane Hydrocarbons	Alkanes C_nH_{2n+2} Alkene C_nH_{2n} Alkynes C_nH_{2n-2} Aromatics (C_6H_6 benzene and other derivatives) Polycyclic aromatic hydrocarbons (PAHs)
Terpenoids	Isoprene $n=1$ C_5H_8 Monoterpenes $n=2$ $C_{10}H_{16}$ Sesquiterpenes $n=3$ $C_{15}H_{24}$ Oxygenated terpenoids
Oxygenated VOCs	Carbonyl compounds (Ketones $RCOR'$, aldehydes $RCHO$) Carboxylic acids $RCOOH$ Alcohols ROH Peroxides $ROOH$, $ROOR'$
Other VOCs	OC with heteroatoms (S, N, Cl, Br, ...) Organic sulfates, Organic nitrates, Organic halides Pesticides, Polychlorinated biphenyls (PCBs)

Another way to classify VOCs is based on their boiling point that reflects their volatility (Molhave et al., 1997) as shown in Table 1.4.

Table 1.4. Classification of VOCs according to their boiling point temperatures (Molhave et al., 1997).

Description	Abbreviation	Boiling point range (°C)
Very volatile organic compounds	VVOC	$T_b < 50-100$
Volatile organic compounds	VOC	$50-100 < T_b < 240-260$
Semi-volatile organic compounds	SVOC	$240-260 < T_b < 380-400$

Recently in the context of atmospheric chemistry, a naming system for the various organic compounds has evolved based on effective saturation concentration C^* (300 K) expressed in $\mu\text{g}\cdot\text{m}^{-3}$, reflecting the degree of volatility (Donahue et al., 2012; Schervish and Donahue, 2020). In this system, six classes are defined:

- 1- ULVOC ($C^* < 3.10^{-9} \mu\text{g}\cdot\text{m}^{-3}$): Molecules with sufficiently low volatility to efficiently nucleate under typical conditions.
- 2- ELVOC ($3.10^{-9} < C^* < 3.10^{-5} \mu\text{g}\cdot\text{m}^{-3}$): Molecules that can easily condense on pre-existing clusters and may also participate directly in new particle formation.

- 3- LVOC ($3 \cdot 10^{-5} < C^* < 0.3 \mu\text{g}\cdot\text{m}^{-3}$): Molecules that can condense on any sufficiently large particle.
- 4- SVOC ($0.3 < C^* < 300 \mu\text{g}\cdot\text{m}^{-3}$): Molecules that will exist significantly in both condensed and gas phase at equilibrium in the atmosphere.
- 5- IVOC ($300 < C^* < 3 \cdot 10^6 \mu\text{g}\cdot\text{m}^{-3}$): Molecules that are almost exclusively in the gas-phase due to relatively high vapor pressures.
- 6- VOC ($C^* > 3 \cdot 10^6 \mu\text{g}\cdot\text{m}^{-3}$): Molecules that are volatile under any circumstances.

1.2.1.1. Anthropogenic VOCs (AVOCs)

Anthropogenic VOC emissions are the result of a multitude of human activities, but account for approximately 10% of total VOC emissions on a global scale (Guenther et al., 2012).

Typically, human activities are categorized into four predominant sectors:

- (1) Road and airway Transport (combustion and evaporation of fossil fuel),
- (2) Residential/Tertiary sector (domestic heating, cooking, solvent use, household products, etc.),
- (3) Chemical and Industrial (power generation, solvent use, waste treatment facilities, etc.),
- (4) Biomass burning (open fires in forest, cooking fires, burning charcoal, etc.).

Several thousand different organic compounds have been identified in the atmosphere (Nozière et al., 2015), but only a small number of species are present in relatively high abundance. The species that are characteristic of anthropogenic emissions are aromatics such as benzene (C_6H_6), toluene (C_7H_8), xylenes (C_8H_{10}), and ethylbenzene (C_8H_{10}), alkanes such as ethane (C_2H_6), propane (C_3H_8), and butane (C_4H_{10}), carbonyl compounds (acetone, formaldehyde, and acetaldehyde), alcohols (methanol, and ethanol), alkenes (ethene, and propene) and alkynes (acetylene). Nitro-phenols, a family of aromatic compounds with both $-\text{NO}_2$ and $-\text{OH}$ functionalities, linked to a benzene ring, also represent common AVOCs (Yuan et al., 2015). Some VOCs, such as isoprene and ethylene, are emitted by both anthropogenic and biogenic sources (Fenske and Paulson, 1999; Guo and Ecker, 2004; Rissanen, 2021). Secondary VOCs are primarily oxygen-containing compounds that are generated through various atmospheric oxidation processes (Reimann and Lewis, 2007).

1.2.1.2. Biogenic VOCs (BVOCs)

Research suggests that emission of BVOCs by vegetation (trees, crops grass, etc.) allows protection against the damaging effects of some abiotic stresses, such as high temperature (Peñuelas and Llusià, 2002), high light intensity, oxidative stresses (Velikova et al., 2005) and other factors (Vallat et al., 2005; Vickers et al., 2009). For some plants, BVOCs may also be released under biotic stresses, such as the attack by pathogens and herbivores enemies, or while recovering after

a wound damage (Pichersky and Gershenzon, 2002; Peñuelas and Llusà, 2003; Dudareva et al., 2006). Terpenoid emissions are also a mechanism to communicate with other plants, through volatilization, leaching or decomposition of plant debris (Vickers et al., 2014). Furthermore, BVOCs may be released throughout the plant's life cycle or, more commonly, at specific stages of development (e.g. maturation of leaves and foliage, spiraling, blooming, and fruit ripening) (Loreto and Schnitzler, 2010). Overall, the emitted BVOCs depend on the type of the plant.

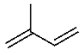
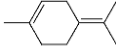
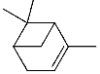
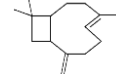
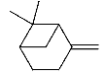
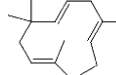
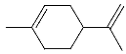
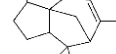
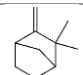
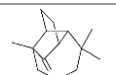
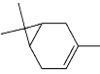
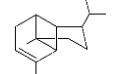
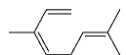
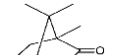
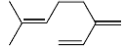
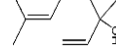
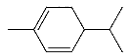
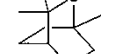
BVOCs are classified into several groups based on the number of carbons:

- **Terpenoid group** which includes isoprene, monoterpenes, and sesquiterpenes (see examples in Table 1.5).
 - Isoprene (C_5H_8) is the BVOC with the largest emissions accounting for nearly 50% of global biogenic emissions (at about 1000 Tg) (Guenther et al., 2012). Other studies report a higher contribution of isoprene with approximately 70% of global emissions (Sindelarova et al., 2014). Isoprene emissions depend significantly on temperature and light intensity, and are also induced by oxidative stress (Fehsenfeld et al., 1992; Vickers et al., 2009). It is commonly emitted by various plant types, such as Salicaceae (e.g. Aspen trees), quercus (e.g. oaks), asplenium (e.g. ferns), and picea (e.g. spruces) (Tingey et al., 1981, 1987; Sharkey et al., 2008).
 - Monoterpenes ($C_{10}H_{16}$) are made up of two isoprene units and are very reactive toward most atmospheric oxidants, which makes this family of compounds interesting to study. They constitute the second largest emitter with about 15% of global BVOC emissions (Guenther et al., 2012). Their structures include endocyclic (inside the ring) and/or exocyclic (outside the ring) double bonds (Steiner and Goldstein, 2007). Monoterpene emissions are dependent on temperature and induced by oxidative stress but do not depend on solar radiation like isoprene emissions (Dement et al., 1975; Vickers et al., 2009). Conifers, Pinaceae (e.g. pine, spruce), and Lamiaceae (e.g. mint, basil) along with a few species of Fagaceae (e.g. oaks, chestnut, beech) are among the plant families with high levels of monoterpenes stored in their tissues (Fuentes et al., 2000; Steiner and Goldstein, 2007).
 - Sesquiterpenes ($C_{15}H_{24}$) are made up of three units of isoprene. Numerous plant species are known for their emission including conifer and broadleaf trees, shrubs, and agricultural crops. The annual estimated emissions are about 2.5% of total BVOC emissions (Duhl et al., 2008; Guenther, 2013). The emissions are found to be dependent on temperature (Duhl et al., 2008). However, due to their low volatility, and the high reactivity of some sesquiterpenes

(e.g. β -caryophyllene and farnesene), they can be difficult to sample, detect, and quantify (Bouvier-Brown et al., 2009).

- **Oxygenated compounds (OVOCs)** can be emitted by plants and formed by oxidation. They include families such as alcohols, aldehydes, ketones, organic acids and esters, including methanol, ethanol, acetaldehyde, acetone, acetic and formic acid (Villanueva-Fierro et al., 2004; Seco et al., 2007; Mellouki et al., 2015). The most common OVOCs in the atmosphere include methanol and acetone. Methanol is the largest biogenic OVOC emission at approximately 100 Tg.yr^{-1} (Jacob et al., 2005; Stavrou et al., 2011). Formic acid and acetic acids are the most prominent volatile organic acids emitted by vegetation.
- Terpenoids also include a small fraction of oxygenated monoterpenes such as camphor, 1,8-cineole, α -terpineol, linalool, methyl-3-buten-2-ol MBO (Guenther et al., 2012). A variety of alkanes, alkenes, organic halides and sulfur as well as benzenoid compounds are also emitted at smaller rates from natural sources (Guenther, 2013). Forests are known for significant emissions of alkenes such as ethene, propene and butene. Moreover, organic halides can be produced by vegetation and include methyl bromide, methyl chloride and methyl iodide.

Table 1.5. Selected terpene compounds emitted by terrestrial vegetation giving the chemical names, molecular structure, and molecular weight (Fuentes et al., 2000; Atkinson and Arey, 2003a).

Compound Name	Chemical Structure	Compound Name	Chemical Structure
isoprene ^a		terpinolene ^b	
α -pinene ^b		β -caryophyllene ^c	
β -pinene ^b		α -humulene ^c	
limonene ^b		a-Cedrene ^c	
camphene ^b		longifolene ^c	
3-carene ^b		α -copaene ^c	
β -ocimene ^b		camphor ^d	
myrcene ^b		linalool ^e	
α -phellandrene ^b		1,8-cineole ^e	

Molecular formula and weight (g.mol^{-1}): ^a C_5H_8 68.18, ^b $\text{C}_{10}\text{H}_{16}$ 136.24, ^c $\text{C}_{15}\text{H}_{24}$ 204.35, ^d $\text{C}_{10}\text{H}_{16}\text{O}$ 152.23 and ^e $\text{C}_{10}\text{H}_{18}\text{O}$ 154.25

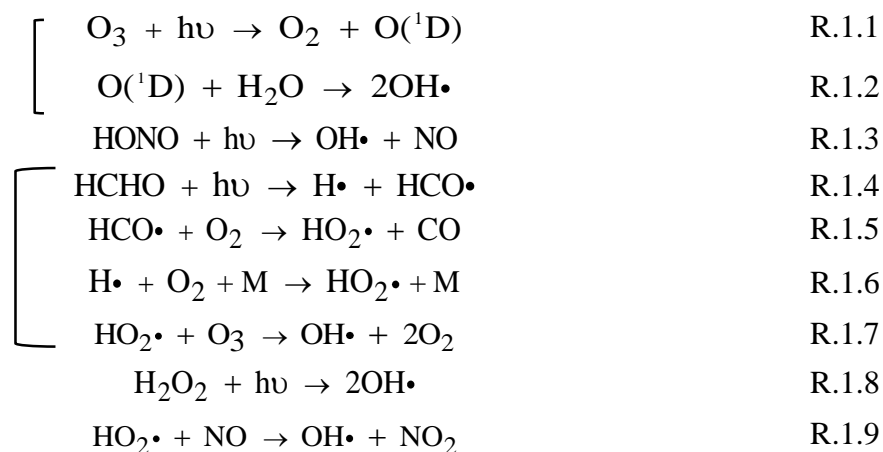
Hence, most of the BVOCs emitted from terrestrial vegetation are unsaturated species or involve oxygen-containing functional groups such as alcohols and organic acids. They are reactive toward common tropospheric oxidants, and thus serve as key components of atmospheric chemistry. Depending on the oxidant, their lifetimes range from seconds to days and up to several years for some BVOC-oxidant combinations (Atkinson and Arey, 2003a). The lifetimes of these compounds depend on the time of the day, ambient conditions (e.g. season, latitude, cloud cover) and the air mass chemical composition.

1.2.2. Oxidants in the troposphere

1.2.2.1. OH radicals

Daytime oxidation in the troposphere primarily involve reactions of OH· radicals. They have pivotal roles in the chemistry of the troposphere by initiating most oxidation reactions of both anthropogenic and biogenic VOCs. Thus, OH· is referred to the cleansing agent of the troposphere. The formation of OH· depends on the region concerned. Under low NO_x conditions, they are predominantly generated through the photolysis of O₃ which produces oxygen atoms in the first excited state (O(¹D)) (R.1.1), which can react with water vapor (R.1.2) (Monks, 2005). Because of the dependence of its production on light and water vapor concentration, OH· production can vary greatly depending on the environment, season, and time of day. For instance, in winter, given the limited sunlight, the contribution of this source is relatively small (Emmerson et al., 2005). However, in the tropics and during the summer season, OH· radical abundances reach the highest concentrations (Lelieveld et al., 2016).

Studies have revealed that in the urban and suburban atmospheres, which are associated with polluted air masses, other important sources of OH· radicals exist involving the photolysis of nitrous acid (HONO) (R.1.3), formaldehyde (HCHO) (R.1.4, R.1.5, R.1.6, R.1.7) and hydrogen peroxide H₂O₂ (R.1.8) (Atkinson and Aschmann, 1993; Finlayson-Pitts and Pitts, 2000; Heard et al., 2004; Harrison et al., 2006; Elshorbany et al., 2009; Mao et al., 2010; Michoud et al., 2012; Harrison, 2018).



In both forested and urban areas, the reaction of $\text{HO}_2\cdot$ with NO (R.1.9), and the decomposition of the Criegee intermediate biradicals, formed by the ozone-alkene reaction, are another important sources of $\text{OH}\cdot$ radicals (Kroll et al., 2002; Ren et al., 2003; Heard et al., 2004; Emmerson et al., 2005). Criegee intermediate biradicals are also important oxidants for a few species in the troposphere.

At night, the level of $\text{OH}\cdot$ radicals tends to greatly decrease, but a small amount can still remain from the nocturnal ozonolysis of alkenes, NO_3 -initiated reaction with alkenes and aldehydes as well as thermal decomposition of PANs ($\text{RC}(\text{O})\text{O}_2\text{NO}_2$) (Orlando et al., 1992; Finlayson-Pitts and Pitts, 2000; Ren et al., 2006).

$\text{OH}\cdot$ radicals are especially reactive towards aldehydes, alkanes, alkenes, and ketones. The reactions often proceed via H-atom abstraction favoring the most weakly bound H atom in the molecule, to produce an alkyl radical $\text{R}\cdot$ (R.1.10), which then rapidly associates with O_2 , through a termolecular reaction with a third body M ($= \text{N}_2$ or O_2), to produce an organic peroxy radical $\text{RO}_2\cdot$ (R.1.11, Lightfoot et al., 1992). $\text{OH}\cdot$ can also react by addition to a carbon-carbon double bond which leads to the formation of hydroxy-alkyl radicals.



1.2.2.2. Ozone

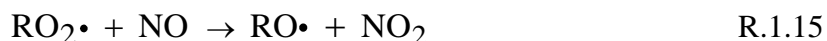
The lifetime of ozone in the troposphere ranges from a few days in the PBL to a few weeks in the FT. It can therefore be transported over long distances thus potentially affecting downwind regions (Wang et al., 1998; Fiore et al., 2002; Wang et al., 2010). Although there is no significant production during nighttime, O_3 can be present and active during both daytime and nighttime.

O₃ is predominately produced via NO₂ photolysis. Indeed, solar radiation ($\lambda < 420$ nm) leads to the photolysis of NO₂ to form NO and O(³P) (R.1.12), followed by association of the ground-state oxygen atoms with O₂ and forming O₃ (R.1.13). The NO that is formed can react with O₃ (R.1.14).



One should note that NO not only occurs as a product of NO₂ photolysis, but can be directly released, especially during combustion processes (e.g. from energy production, transportation).

Reactions 1.12, 1.13, and 1.14 exhibit a net zero-balance cycle between NO₂, O₃, and NO, also known as Leighton cycle (Fishman et al., 1979). However, O₃ production is enhanced in the presence of VOCs and sunlight, that disrupt the equilibrium by consuming NO. Carbon monoxide (CO) and methane (CH₄) also have a significant role in O₃ production. NO-consuming reactions can take place by means of reactions with RO₂· and HO₂· radicals (R.1.9 and R.1.15) (Fishman et al., 1979; Monks et al., 2015). Such reactions constitute NO sinks in competition with consumption by O₃, thereby contributing to the net accumulation and production of O₃ in the troposphere (Stone et al., 2012).



O₃ formation is initiated especially by OH· radicals during daytime through its attack on VOCs leading to formation of RO₂· radicals, as shown in R.1.10 and R.1.11. The organic peroxy radicals oxidize NO to NO₂ (R.1.15). This also leads to the production of RO· radicals that in part react with O₂ yielding OVOCs and HO₂· (R.1.16) (among other products) and subsequently reform OH· radicals, leading to a new oxidation cycle (Jenkin and Clemitshaw, 2000). This may proceed either to form more oxidized products or ultimately lead to production of CO₂ and H₂O. The ensuing chemistry of RO· depends on their chemical structure and reactivity. More details about the chemical oxidation scheme including organic products (Figure 1.4) will be discussed below.

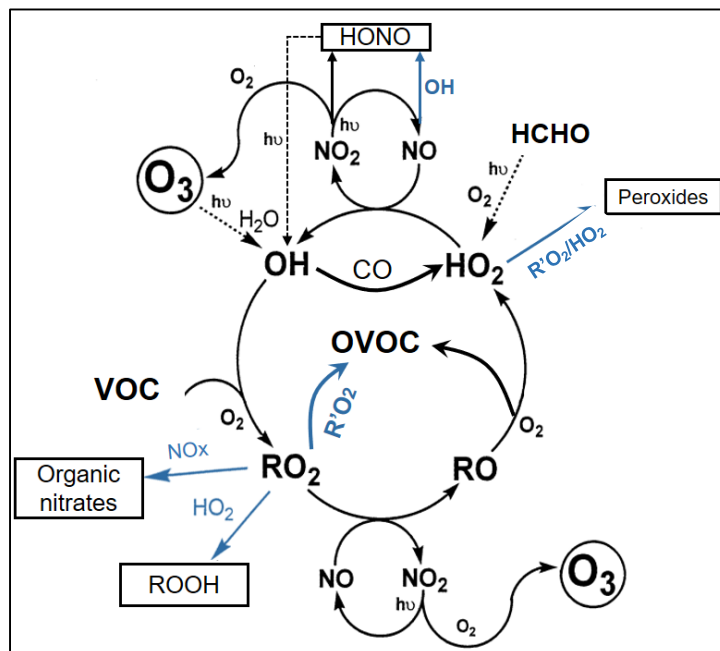


Figure 1.4. Simplified scheme depicting tropospheric ozone formation from the most important chemical pathways of the troposphere, during daytime (adapted from Jenkin and Clemitshaw, 2000; Liu et al., 2012).

In addition, O_3 , along with other urban pollutants, is subject to long range transport downwind of urban areas to rural/forested regions while continuing to mix and react. As a result, rural O_3 concentrations can be elevated, thereby impacting the atmospheric chemistry of those regions (Gilliam et al., 1989; Comrie, 1994; Gilliam and Turrill, 1995; Skelly, 2000).

In suburban or rural regions downwind of urban areas, ozone values may well exceed 100 ppbv (Seinfeld and Pandis, 2016).

Overall, photochemical O_3 formation is a nonlinear chemical process in relation to NO_x and VOC levels in the production region. An isopleth diagram is usually adopted to show the ozone concentrations as a function of the initial NO_x and VOC levels (Figure 1.5). It is derived from modeling investigations.

This diagram allows identification of three main regimes, “ NO_x -limited”, “VOC-limited” and standard.

- The “ NO_x -limited” regime features situations of $VOC/NO_x > 15$ (e.g. rural regions) characterized by relatively low NO_x levels and high VOC concentrations. Hence, when NO_x increases, O_3 production is favored while being relatively insensitive to changing VOC concentrations, as for example following the red arrow in Figure 1.5.
- The “VOC-limited” regime characterizes the region with $VOC/NO_x < 4$ (e.g. urban areas), with relatively high NO_x levels. The blue arrow in Figure 1.5 depicts an example of a decrease in O_3 concentration (0.16 to 0.08 ppm) when NO_x level increases. This can be

explained partly by ozone titration by its reaction with high levels of NO (R.1.14). Under these conditions, O₃ formation is favored when VOC concentrations increase.

- The standard regime marks an intermediate region with $4 < \text{VOC}/\text{NO}_x < 15$ and where ozone formation depends on both species leading to O₃ concentration changes that depend on both NO_x or VOC levels.

Other factors can also affect O₃ production efficiency, such as temperature, transport, solar radiation (photolysis rates), deposition as well as precursor reactivities.

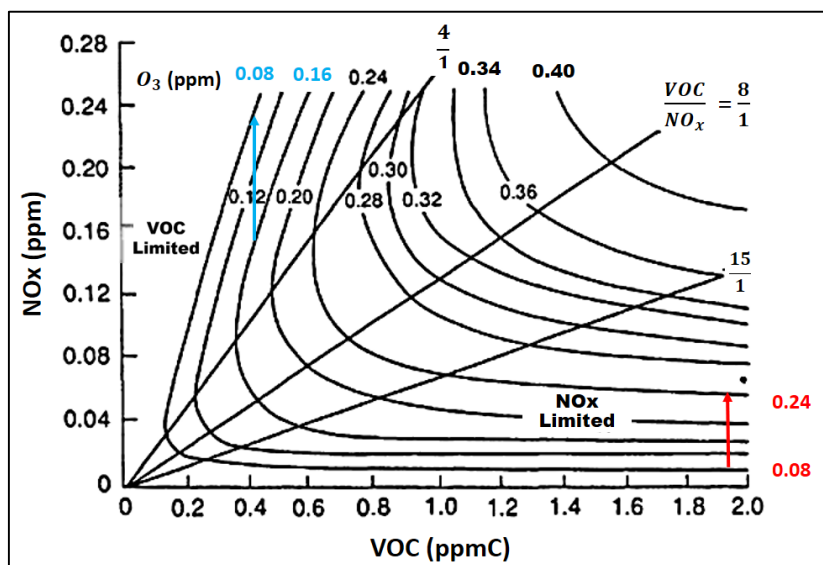
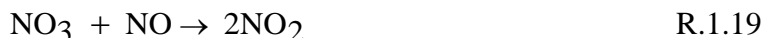


Figure 1.5. Ozone isopleth diagram adopted from (National Research Council, 1991).

1.2.2.3. Nitrate radical

NO₃· radical is one of the major oxidizing agents during nighttime as it is quickly destroyed during daytime by solar photolysis (R.1.17 and R.1.18) and reaction with NO (R.1.19) (Graham and Johnston, 1978; Wayne et al., 1991; Brown and Stutz, 2012; Ng et al., 2017).



NO₃· reacts with a variety of VOCs including aldehydes, alkenes, and OVOCs, as shown in Table 1.6 (Atkinson and Arey, 2003b; Geyer et al., 2003). In addition to oxidation during nighttime, NO₃· has been found to be an oxidant during daylight hours, although to a much less extent than during the night (Geyer et al., 2003).

Table 1.6. NO₃ rate coefficients for selected classes of AVOCs and BVOCs and their lifetimes at fixed NO₃ mixing ratio (Brown and Stutz, 2012).

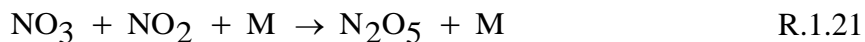
VOC	k(NO ₃) (cm ³ .molecule ⁻¹ .s ⁻¹)	Lifetime for NO ₃ = 20 pptv
<i>Anthropogenic hydrocarbons</i>		
Alkanes	< 5 × 10 ⁻¹⁶	> 46 days
Aromatics	< 2 × 10 ⁻¹⁵	> 11 days
Ethene	2 × 10 ⁻¹⁶	> 116 days
Linear alkenes	1-2 × 10 ⁻¹⁴	28-55 h
Internal, branched alkenes	3-600 × 10 ⁻¹³	0.5 min-1.9 h
<i>Oxygenates</i>		
Formaldehyde	6 × 10 ⁻¹⁶	39 days
Acetaldehyde	3 × 10 ⁻¹⁵	7.7 days
Higher aldehydes	0.7-3 × 10 ⁻¹⁴	18 h-3.3 days
Alcohols	1-20 × 10 ⁻¹⁶	11-230 days
Ketones	< 6 × 10 ⁻¹⁶	> 38 days
Phenol, cresols	2-13 × 10 ⁻¹²	3-17 min
<i>Biogenic hydrocarbons and sulphur</i>		
Isoprene	7 × 10 ⁻¹³	0.8 h
Monoterpenes	2.5-12 × 10 ⁻¹²	3-15 min
Sesquiterpenes	7-1400 × 10 ⁻¹³	14 s-0.8 h
DMS	1 × 10 ⁻¹²	0.6 h

NO₃· radicals are formed by the reaction between O₃ and NO₂ (R.1.20).



Yet, within urban areas NO₃· is found to be enhanced at higher altitudes when NO₂-rich air near the ground surface combines with O₃-rich urban air aloft (Carslaw et al., 1997; Stutz et al., 2004). This is also attributed to the fact that NO concentrations are higher near the ground, where emissions take place. Consequently, NO reacts with NO₃·, reducing its levels near the surface. As altitude increases, NO concentrations decrease rapidly due to its fast reaction with O₃, resulting in less destruction of NO₃.

NO₃· associates with NO₂ to form dinitrogen pentoxide (N₂O₅) which acts as a reservoir of NO₃· (R.1.21).



This association reaction is reversible and highly temperature dependent, potentially resulting in release of NO₃· far from the initial source. N₂O₅ can also serve as a major route of NO_x conversion to nitric acid HNO₃ and particulate nitrate formation through heterogeneous reactions such as hydrolysis on wet surfaces and aerosol particles (Dentener and Crutzen, 1993).

The reactions between $\text{NO}_3\cdot$ and saturated VOCs are slow while $\text{NO}_3\cdot$ is highly reactive toward unsaturated HCs in particular toward biogenic HCs, such as isoprene and monoterpenes (Atkinson and Arey, 2003b; Brown and Stutz, 2012). Table 1.6 provides some examples of $\text{NO}_3\cdot$ reaction rate coefficients with various types and classes of VOCs.

For alkenes (including isoprene and monoterpenes), the reaction is initiated by $\text{NO}_3\cdot$ addition to the carbon-carbon double bond, generating a nitrooxyalkyl radical, followed by addition of O_2 to form a nitrate- $\text{RO}_2\cdot$ radical. These could further react with other products ($\text{HO}_2\cdot$, NO , NO_2 or $\text{NO}_3\cdot$) to form multifunctional organic nitrates and other species, and possibly contributing to the growth of SOA (Wayne et al., 1991; Fry et al., 2013; Ng et al., 2017).

1.2.3. Oxidation processes

The chemical oxidation of VOCs is usually initiated by one of the above discussed oxidants, $\text{OH}\cdot$, O_3 or NO_3 . The oxidation products depend on the structure of the individual VOC each of which reacts differently as well as the presence of other key air pollutants, most notably NO_x , which can impact the oxidation pathways. VOCs reactivity towards the various oxidants defines their lifetime in the atmosphere.

Overall, there are three key steps in the branching ratio of the reaction products:

- 1) The initial attack of a VOC by one of the oxidants,
- 2) The evolution of $\text{RO}_2\cdot$ and $\text{HO}_2\cdot$ radicals,
- 3) The evolution of $\text{RO}\cdot$ radicals.

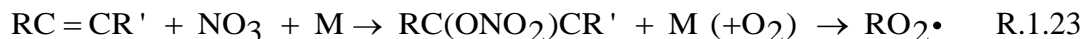
1.2.3.1. The initial attack on VOC by one of the oxidants

As mentioned above, $\text{OH}\cdot$ radicals, which dominate during daytime oxidation, initiate reaction with most VOCs (R.1.10 and R.1.11) with the exception being the fully halogenated compounds (Atkinson, 2000). $\text{NO}_3\cdot$ radicals react slowly with alkanes but more rapidly with aldehydes via H-atom abstraction, followed by reaction with O_2 to yield an $\text{RO}_2\cdot$ radical and HNO_3 (R.1.22) (Wayne et al., 1991; Zhang and Morris, 2015).

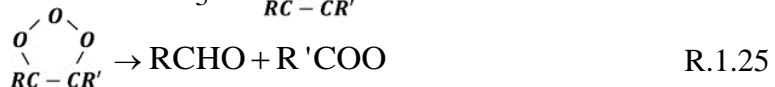
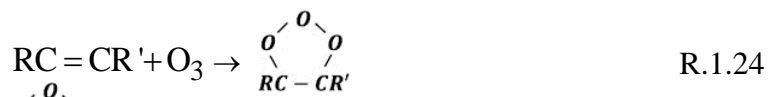


Reaction of $\text{NO}_3\cdot$ with unsaturated BVOCs and AVOCs, especially reactive alkenes and terpenes, are much faster than reactions with the alkanes and can lead largely to nitroxy organic radical formation as well as $\text{HO}_2\cdot$ radicals, NO_2 and relatively stable organic nitrate products (Roberts, 1990; Jenkin and Clemitshaw, 2000; Geyer et al., 2003). These reactions proceed by $\text{NO}_3\cdot$ addition to the carbon-carbon double bond, yielding an organonitrate radical (R.1.23), with H-atom abstraction being insignificant (Atkinson, 1997). In addition, reaction with alkenes has been shown

to dominate the nocturnal loss of $\text{NO}_3\cdot$, consisting of 70% of total loss (Stutz et al., 2010). $\text{NO}_3\cdot$ reaction with alkenes and terpenes has been shown to contribute to SOA formation in high yields (Hoyle et al., 2011; Brown and Stutz, 2012).



O_3 , which is present during daytime and nighttime, has been shown to be reactive with unsaturated organic compounds, especially alkenes (Atkinson and Arey, 2003a). This chemical reaction is known as ozonolysis. Acyclic alkenes proceed by O_3 addition to the carbon-carbon double bond, forming a primary ozonide (POZ), which degrades and produce intermediate compounds, known as Criegee intermediates (CIs), as well as a carbonyl compound (R.1.24 and R.1.25) (Criegee, 1975). The CIs are unstable products containing excess energy that may lead to their further decomposition to form $\text{OH}\cdot$ radicals and other organic fragments (Carslaw and Carslaw, 2001), or may be stabilized through collision with air molecules and can then undergo bimolecular reactions (Johnson and Marston, 2008). Nevertheless, the CIs formed from cycloalkenes preserve both carbonyl and carbonyl oxide moieties within the same product, thus they are more functionalized and have lower volatility than the products of the ozonolysis of acyclic alkenes. Therefore, cycloalkene-derived CIs would be expected to be highly efficient precursors of SOA. Subsequently, the CIs undergo isomerization to form vinyl hydroperoxides ($\text{C}=\text{COOH}$ moiety) which dissociate to $\text{OH}\cdot$ and a conjugated radical that will subsequently react with O_2 to form $\text{RO}_2\cdot$ (Chuong et al., 2004; Kuwata et al., 2011).



As such, once the VOC oxidation reaction has been initiated by one of the oxidants discussed above, it is commonly followed by subsequent reaction with O_2 to produce an $\text{RO}_2\cdot$ radical. It also leads to the formation of non-radical oxidized products.

1.2.3.2. The evolution of $\text{RO}_2\cdot$ radicals

The evolution of $\text{RO}_2\cdot$ radicals depends largely on the environment. This is depicted in Figure 1.6 which illustrates an example of a simplified VOC oxidation mechanism that is initiated by the $\text{OH}\cdot$ radical. One should mention, however, that similar evolution of $\text{RO}_2\cdot$ radicals occurs after the initial attack of a VOC by O_3 and $\text{NO}_3\cdot$ radicals. At high NO_x levels, $\text{RO}_2\cdot$ radicals rapidly react with NO , leading to the formation of an alkoxy radical ($\text{RO}\cdot$) and NO_2 , or may take an alternative pathway that yields an organic nitrate RONO_2 (Spicer et al., 1973; Darnall et al., 1976; Goldman

et al., 2021). In addition, $\text{RO}_2\cdot$ may react with NO_2 , resulting in the generation of a peroxyxynitrate RO_2NO_2 . However, the majority of RO_2NO_2 type compounds thermally decompose under tropospheric conditions (Finlayson-Pitts and Pitts, 2000; Edwards et al., 2003). During nighttime, $\text{RO}_2\cdot$ also reacts with $\text{NO}_3\cdot$ generating an alkoxy $\text{RO}\cdot$ radical and NO_2 .

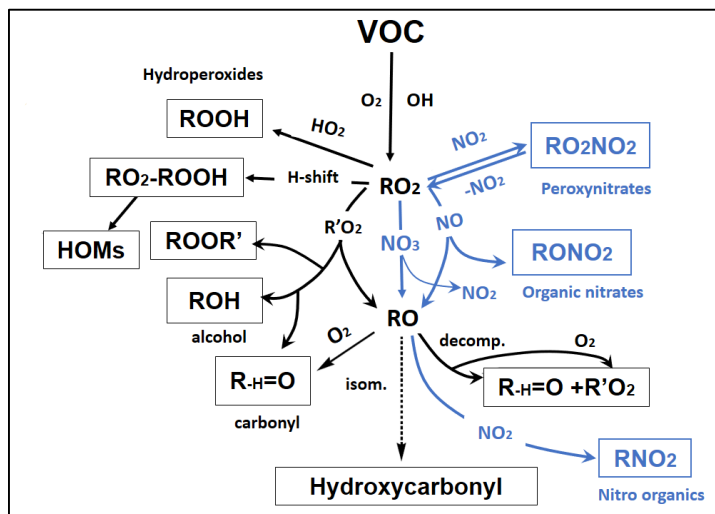


Figure 1.6. General schematic diagram of VOC degradation initiated by OH to form first generation products under atmospheric conditions. The colors blue and black represent the dominant chemical pathways under high and low NO_x conditions, respectively (adapted from Kroll and Seinfeld. (2008)).

At low NO_x concentrations, $\text{RO}_2\cdot$ reacts predominately with $\text{HO}_2\cdot$ and other $\text{RO}_2\cdot$ radicals. The reaction of $\text{RO}_2\cdot$ radicals with $\text{HO}_2\cdot$ is a termination reaction that leads to hydroperoxides (ROOH). The reaction between two $\text{RO}_2\cdot$ radicals can generate $\text{RO}\cdot$ radicals, may form alcohol and carbonyl products, or could lead to a covalently bound peroxy-bridged accretion product (Hallquist et al., 2009). In some cases, the $\text{RO}_2/\text{R}'\text{O}_2$ peroxide channel leads to an ROOR' product containing the sum of carbon atoms of the peroxy radical reactants ($n_{\text{CR}} + n_{\text{CR}'}$) (Mentel et al., 2015). Recently, it has been shown that autoxidation of $\text{RO}_2\cdot$ can occur under atmospheric conditions to form highly oxygenated organic molecules, referred as HOMs (Crouse et al., 2013). These low volatility compounds are a central focus of this thesis work and will be further discussed in section 1.3. Briefly, autoxidation involves a gas-phase process by which $\text{RO}_2\cdot$ undergoes an intra-molecular H-atom shift yielding a new hydroperoxide functionality along with a carbon radical site to which O_2 can rapidly add to form a new, more oxygenated $\text{RO}_2\cdot$. This process can repeat to form a more oxidized and therefore less volatile $\text{RO}_2\cdot$ (Bianchi et al., 2019). This sequence can be interrupted at each stage by one of the previously described bimolecular reactions of $\text{RO}_2\cdot$ resulting in the formation of the so-called HOMs.

1.2.3.3. The evolution of RO· radicals

Like RO₂· radicals, RO· radicals further evolve through three main chemical pathways depending on their structures (Finlayson-Pitts and Pitts, 2000; Aumont et al., 2005; Atkinson et al., 2006; Hallquist et al., 2009) as depicted in Figure 1.6 and described as follows:

- 1) Reaction with O₂ yielding a stable carbonyl product and HO₂·
- 2) Decomposition through a C-C bond scission to form another RO₂· radical and a stable secondary product
- 3) Isomerization through H-atom shift (for RO· with 4 carbon atoms and more) with subsequent addition of O₂ to form more oxidized RO₂· (Vereecken and Francisco, 2012).

The oxidation cycle can take place repeatedly leading to the formation of more oxidized organics with more functional groups that facilitates intramolecular bonding resulting in reduced volatility (Kroll and Seinfeld, 2008). The oxidation products may have the same number of carbon atoms as the parent VOC, or fewer if decomposition took place. Varying functionalities as well as the carbon chain length will indeed affect the vapor pressures of the reaction products. This is depicted in Table 1.7 where the incremental change in vapor pressures are given for a variety of functional groups. This is an approximate relationship that can be used to estimate vapor pressures for compound that have not been measured. For example, addition of a nitrate group (-ONO₂) results in a vapor pressure that is 6.8×10^{-3} times that of the original compound.

Table 1.7. Vapor pressure changes of an organic compound upon addition of a functional group (Kroll and Seinfeld, 2008). The factors are ^a**multiplicative** which implies that the addition of a functional group reduces the vapor pressure by the factor given (i.e. the factor is multiplied by the original vapor pressure of the compound).

Functional group	Structure	Change in vapor pressure (298 K) ^a
Ketone	-C(O)-	0.10
Aldehyde	-C(O)H	0.085
Hydroxyl	-OH	5.7×10^{-3}
Hydroperoxyl	-OOH	2.5×10^{-3}
Nitrate	-ONO ₂	6.8×10^{-3}
Carboxylic acid	-C(O)OH	3.1×10^{-4}
Peroxyacid	-C(O)OOH	3.2×10^{-3}
Acyl peroxy nitrate	-C(O)OONO ₂	2.7×10^{-3}
Carbon	-CH ₂	0.35

1.2.4. Urban tropospheric chemistry

Tropospheric chemistry is a key factor in numerous air pollution problems. Air pollution is a serious concern affecting human health and the environment in a broad sense, especially in urban areas where most people live and work. Today, about 57% of the world's population lives in urban areas (UNCTAD, 2022). Hence, it comes as no surprise to find that anthropogenic activities explain most of the ambient concentrations of VOC emissions in these regions. NO_x is also another major

urban air pollutant that is mainly emitted through combustion processes. Within urban areas, NO is the dominant component of traffic NO_x emissions, but since it reacts with O₃, NO₂ quickly becomes the major reactive nitrogen compound in urban air for most conditions (Seinfeld and Pandis, 2016). Furthermore, releases coming from other areas (rural or other cities, even distant ones) may also account for a sizable fraction of urban air pollution (Huszar et al., 2016).

The presence of these types of pollutants leads to chemistry in urban environments that follows different pathways than in non-urban places such as forests.

OH· radicals are the most important daytime oxidant in the atmosphere for most conditions. In an urban atmosphere, the typical midday peak OH· concentration is approximately 5×10^6 molecules.cm⁻³ (Seinfeld and Pandis, 2016). This radical controls the lifetimes of most AVOCs, including alkanes, alkenes, aromatics and OVOCs. The oxidation of most aromatics is initiated by the addition of OH· to the aromatic ring. In addition, OH· radical may react rapidly with aldehydes, alkanes and ketones predominantly through H-abstraction, as previously discussed in section 1.2.2.1. Both during the daytime and at night, O₃ reaction with alkenes is also quite competitive. At nighttime, oxidation of alkenes by NO₃· competes with that by O₃ (Geyer et al., 2001; Reimann and Lewis, 2007). Nocturnal mixing ratios of NO₃· in urban plumes have been reported to reach up to a few hundred pptv (Wayne et al., 1991), but typically values are 0-10 pptv. N₂O₅ mixing ratios can reach up to 3 ppbv as seen in Boulder, Colorado (Brown et al., 2003), but typical values are 0.01-1 ppbv.

The presence of high NO_x emissions in urban areas is a major determinant of the mechanistic evolution of an RO₂· radical. RO₂· reacts quite rapidly with NO, NO₂ as well as NO₃· during nighttime, and yields products such as organic nitrates, RO· radicals and organic peroxy nitrates. The chemical pathways involving reactive nitrogen compounds are depicted by the blue color in Figure 1.6.

Peroxyacyl nitrates (PANs) are members of another important class of chemical compounds in urban areas, with the general formula RC(O)OONO₂, and whose formation depends significantly on NO_x levels (Seinfeld and Pandis, 2016). As depicted in Figure 1.7, they are also formed in the OH-initiated oxidation of aldehydes (H-atom abstraction) producing an acyl radical RCO·, which subsequently reacts with O₂ to form an acyl peroxy radical RC(O)OO·. This can further react with NO or NO₂, yielding RC(O)O· or a PAN compound (RC(O)OONO₂), respectively. PAN compounds are in thermal equilibrium with the corresponding RC(O)OO· radical and NO₂, meaning that PAN concentrations depend on ambient temperature. PAN acts as a temporary

reservoir for NO_x species, enabling transport from the free troposphere (where temperatures are generally reduced compared to the surface) to the remote troposphere, where NO_x and $\text{RO}_2\cdot$ can be released from PAN decomposition (Fischer et al., 2014).

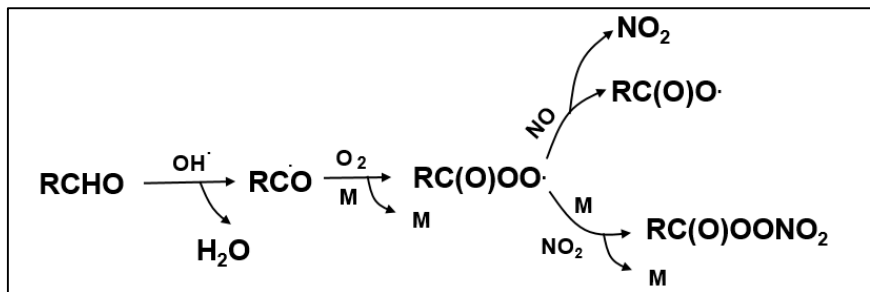


Figure 1.7. PAN simplified formation mechanism.

1.2.5. Rural/forested tropospheric chemistry

Forests release significant levels of BVOCs, which can be significant precursors for SOA formation. They are estimated to account for about 70% of the VOCs from vegetation (Guenther et al., 1995). In addition, forests are often marked by low levels of NO_x , which thus affects oxidation pathways and the rates of sink reactions of reactive products.

The oxidation of BVOCs is initiated either by the addition of O_3 , $\text{NO}_3\cdot$ or $\text{OH}\cdot$ to the carbon-carbon double bond or by H-atom abstraction from a C-H bond by $\text{OH}\cdot$ or $\text{NO}_3\cdot$. The majority of unsaturated BVOCs undergo the addition mechanism except for aldehydes (e.g. methacrolein) which are more likely to undergo H-abstraction (Atkinson and Arey, 2003a). Like other VOCs, during daytime the $\text{OH}\cdot$ radical reacts with almost all unsaturated BVOCs yielding hydroxy-substituted radicals. O_3 can initiate oxidation of unsaturated BVOCs, including isoprene and terpenes. At nighttime, $\text{NO}_3\cdot$ radicals and O_3 can initiate the oxidation chemistry of BVOCs, which is followed by addition of O_2 leading to $\text{RO}_2\cdot$ radicals.

In a forested environment (with relatively low NO_x mixing ratios), $\text{RO}_2\cdot$ oxidation pathways preferentially react with $\text{HO}_2\cdot$, yielding hydroperoxides (ROOH) that may be removed by wet and dry deposition processes, photolyze, or undergo reaction with $\text{OH}\cdot$ (Fehsenfeld et al., 1992; Steiner and Goldstein, 2007; Laothawornkitkul et al., 2009). Organic peroxy radicals also can react with other $\text{RO}_2\cdot$ radicals yielding stable products such as alcohols, ketones, aldehydes and accretion products (ROOR'). For instance, methylvinylketone (MVK), methacrolein (MACR) and formaldehyde are first-generation oxidation products of isoprene (Carlton et al., 2009; Wolfe et al., 2016). Pinonaldehyde and nopinone are the main first-generation products of α -pinene and β -pinene oxidation, respectively (Michoud et al., 2017). A variety of organic acids may also be

generated through the oxidation of BVOCs. For example, pinonic, limonic and caryophyllinic acids are oxidation products of α - and β -pinene, limonene and β -caryophyllene, respectively (Vestenius et al., 2014). Overall, BVOCs oxidation intermediates contain one or more functional groups which make them less volatile and more water soluble than the parent compounds. Thus, they are subject to partitioning between the gas and the particle phases. The oxidation of monoterpenes has been shown to efficiently generate gas phase HOMs which can lead to the formation and growth of particles (Ehn et al., 2014; Mutzel et al., 2015; Bianchi et al., 2019).

BVOCs and their oxidation products are the most important precursors to the global SOA formation (e.g. $\sim 74\%$, 97.5 Tg yr^{-1} , Hodzic et al., 2016). Sesquiterpenes, on the other hand, have the highest SOA yields (Lee et al., 2006; Fry et al., 2014).

The BVOCs, which are present in these forested environments, can also compete with each other for oxidants as shown by recent laboratory experiments. Indeed, McFiggans et al. (2019) recently found that isoprene suppresses SOA mass yields in mixtures with monoterpenes due to the interactions between oxidation products from the different VOCs. The study found that isoprene can scavenge $\text{OH}\cdot$ radicals preventing reactions with monoterpenes, and also reported that the products from isoprene such as peroxy radicals can inhibit the formation of HOMs from α -pinene which significantly decreases the SOA yields of α -pinene in this mixed system. Voliotis et al. (2022) found a clear suppression of the SOA mass yield from α -pinene when mixed with isoprene, but no change in the SOA yield from *o*-cresol when mixed with isoprene. Other studies performed during field campaigns also illustrate that isoprene can suppress NPF from the oxidation of other BVOCs (Kiendler-Scharr et al., 2009; Kanawade et al., 2011; Lee et al., 2016).

1.2.6. Effects of biogenic-anthropogenic interactions on atmospheric organic chemistry

The pathways of VOC oxidation and the formation of SOA may be affected by interactions between BVOCs and anthropogenic emissions such as NO_x , SO_2 , and AVOCs, resulting from the transport of a BVOC-enriched air mass over an area with significant anthropogenic emissions or vice versa. Urban air transported to rural areas can enhance oxidant levels. For example, higher NO_x levels within these NO_x -limited regions decrease the VOC/NO_x ratio, and increase the rate of O_3 production. Also, the concentration of O_3 comprises both in-situ generated O_3 and the levels carried within the urban plume, resulting in higher BVOC reaction rates. Higher NO_2 levels in such urban plume also lead to increase in the rate of NO_3 production. This enhancement of oxidant levels further oxidizing BVOCs thereby contribute to higher levels of more oxidized products, and increase the formation of biogenic SOA (Carlton et al., 2010). Indeed, $\text{NO}_3\cdot$ radicals dominate

oxidation of BVOCs during the night especially in areas where both anthropogenic and biogenic emissions mix (Geyer et al., 2001; Brown et al., 2009). It is also expected that when AVOCs and BVOCs are both present, they compete for oxidants, resulting in SOA formation with different yields and properties (Ahlberg et al., 2017; Li et al., 2022). In these mixed atmospheres, anthropogenic NO_x competes with the $\text{HO}_2 + \text{RO}_2$ and $\text{RO}_2 + \text{R}'\text{O}_2$ channels for $\text{RO}_2\cdot$ radicals derived from BVOCs oxidation, affecting the fate of $\text{RO}_2\cdot$, and thus leading to changes in the distributions of oxidation products (Kroll et al., 2006). Organic nitrates, peroxy nitrates, PANs and carbonyls are thus produced among the major oxidation products (rather than products without nitrogen). Oxidation under higher NO_x amounts could shift the product distribution towards more volatile products and result in lower SOA yields (Presto et al., 2005). Organic nitrates were shown to increase in both the gas and particle phases as input NO increased in simulation chamber experiments (D'Ambro et al., 2016). The effect of NO_x on the chemistry of BVOCs as well as the impact of mixing different organic precursors on particle properties have been investigated through literature studies conducted in both laboratory and ambient air as described in the following sections.

1.2.6.1. Laboratory studies

Chamber experiments revealed the fact that, according to the organic precursor employed and the experimental oxidation conditions, NO_x may either enhance or suppress the generation of SOA. The yield of isoprene-derived SOA shows a non-linear dependence on NO_x levels as the yields increase and then decrease with NO_x concentration (Kroll et al., 2006; Ng et al., 2007; Xu et al., 2014; D'Ambro et al., 2016). Liu et al. (2016) found that the addition of NO_x caused a slight effect on SOA yield of isoprene up to a threshold level, beyond which the yield of SOA decreased. It is likely that such patterns in SOA yield as a function of NO_x , derived from the same precursor may be a function of the various operating conditions of the chamber, the absolute NO concentrations, and the aging time. Kroll et al. (2006) suggested that the reduction in the SOA yield with elevated NO_x is driven by the fragmentation of C-C bonds as a result of $\text{RO}_2 + \text{NO}$ reactions that result in more volatile products. Different pathways, under low and high NO_x conditions, have been observed for the OH-oxidation or ozonolysis of terpenes (Presto et al., 2005; Kroll et al., 2006; Ng et al., 2007; Xu et al., 2014; Han et al., 2016). Presto et al. (2005) observed that the presence of NO_x completely inhibited SOA formation from the ozonolysis of α -pinene for $[\text{VOC}]_0/[\text{NO}_x]_0 \leq 4.5$, suggesting that the compounds produced in the presence of NO (likely greater proportions of organic nitrates) are too volatile to condense. Ng et al. (2007) investigated the NO_x dependence of

SOA yields in the photooxidation of α -pinene and two sesquiterpenes. In the α -pinene experiments, significantly higher SOA yields were obtained under low-NO_x conditions ≤ 2 ppb (39.7%-45.8% for 13.8-47.5 ppb α -pinene) than under high-NO_x conditions ~ 1 ppm (6.6%-21.2% for 12.6-46.6 ppb α -pinene). For sesquiterpenes, a linear increase in SOA yields was observed with increasing NO_x concentrations, most likely due to the lower volatility of sesquiterpene nitrates and suggesting that larger alkoxy radicals tend to isomerize leading to less volatile multifunctional products. The same findings as those for sesquiterpenes were found for alkanes with C>10 (Lim and Ziemann, 2009). The effect of NO_x on SOA formation from the photooxidation of β -pinene has been also investigated. It was reported that SOA yields increased with increasing NO_x (from [VOC]₀/[NO_x]₀>10 up to [VOC]₀/[NO_x]₀<10), caused by the NO_x-induced increase of OH· concentrations, and then decreased at higher NO_x concentrations (Sarrafzadeh et al., 2016).

Pullinen et al. (2020) reported a suppression of HOM accretion products in the gas phase as NO_x concentration increased, which can, in some cases, provide an indication for the observed reductions in the mass concentrations of SOA formed in these experiments.

The yields of SOA in mixtures such as toluene and α -pinene have been demonstrated to depend on the addition sequence of the precursors to the chamber. Loza et al. (2013) observed that first injecting α -pinene into the chamber and then adding toluene led to an increase in the SOA yield while reversing the sequence of injection led to its decrease. This phenomenon was elucidated by induced SOA evaporation experiments, which revealed that α -pinene-derived SOA has greater volatility compared to toluene-derived SOA. The evaporation behavior of the resulting SOA was found to closely resemble that of the SOA from the second precursor, implying a particle structure resembling a core of SOA from the initial precursor enveloped by a layer of SOA from the second precursor.

Zhao et al. (2018) showed a suppressive effect of NO_x on NPF and on the SOA yield derived from the photooxidation of α -pinene and limonene. Organic nitrate from α -pinene photo-oxidation experiments with <1 to 24 ppb NO_x, showed an increase in both the gas and particle phases amounts with largest yields at the highest NO_x concentration studied (Aruffo et al., 2022).

1.2.6.2. Field campaigns

Comprehensive knowledge of the composition, impacts and fate of emissions to the atmosphere from both urban and rural environments is required to develop ways to cope with the threats facing air quality and global climate change, which are interrelated challenges. Moreover, mixtures of

urban and biogenic air masses has been shown to greatly influence many atmospheric chemical processes, thereby altering the yields and properties of the resulting products, notably SOA (McFiggans et al., 2019; Nascimento et al., 2021).

Field campaigns are crucial for the observation and experimental investigation of complex physicochemical processes in the atmosphere. According to the objectives of the specific campaign, measurement strategies are defined along with the choice of instruments to be deployed and selection of the measurement sites and platforms.

Many field research campaigns have focused on urban atmospheres, for example ESQUIF 1998-2000 (Menuet et al., 2000), TexAQS 2000 and TexAQS II 2005-2006 in Texas (Ryerson et al., 2003; Parrish et al., 2009), MILAGRO 2006 in Mexico (Molina et al., 2010), CAREBeijing 2006-2008 in China (Wang et al., 2010), CalNex 2010 in the US (Ryerson et al., 2013), MEGAPOLI 2009-2010 in France (Baklanov et al., 2010), ClearfLo in London, UK 2011-2013 (Bohnenstengel et al., 2015), DISCOVER-AQ 2013 in Texas (Crawford and Pickering, 2014), CAREBeijing-NCP 2013-2014 megacity Beijing and North China Plain (Zhao, 2016), MAPS-Seoul 2015 in Seoul Korea (Cho et al., 2018), and DACCIWA in West African Cities (Abidjan, Côte d'Ivoire and Cotonou, Benin) 2015-2017 (Evans et al., 2018).

Other campaigns have also been conducted in rural / forest areas, for example CELTIC 2003 in North Carolina, US (Stroud et al., 2005), BEACHON 2010 at Manitou Experimental Forest northwest of Colorado Springs, US (Zhou et al., 2015), BEARPEX 2007 in a California Sierra Nevada forest, US (Wolfe et al., 2011), HUMPPA-COPEC-2010 in a southern forest in Finland (Williams et al., 2011), FARCE 2015 on the tropical island of La Réunion of France (Dufлот et al., 2019), CABINEX 2009 and PROPHET-AMOS 2016 in Michigan, US (Steiner et al., 2011; Millet et al., 2018), LANDEX 2017 (Mermet et al., 2021) and CERVOLAND 2018 in the southwest of France (Dusanter et al., 2018).

However, only a few campaigns were carried out in areas where biogenic and anthropogenic emissions are mixed, for example SOS 1990, SEAVS 1995 and SOAS 2013 in the southeast US (Carlton et al., 2018; Nagori et al., 2019), CARES 2010 in Sacramento, California (Zaveri et al., 2012), NPFS 2013 and HI-SCALE 2016 at the ARM Southern Great Plains (SGP) site, Oklahoma, US (Smith and McMurry, 2015; Fast et al., 2019), GO-AMAZON 2014-2015 in the central Amazon Basin, Brazil (Martin et al., 2017) and BAECC 2013 in Hyytiälä, Finland (Petäjä et al., 2016). Some selected campaigns are discussed in the following paragraphs.

The GoAmazon 2014/5 field campaign showed that NO_x emissions from the city enhanced the yield of SOA from biogenic precursors in the Amazon Forest impacted by an urban plume from the city of Manaus. This observation was explained by a substantial increase in OH· and O₃ oxidants due to elevated NO_x levels within the urban plume (Shrivastava et al., 2019; Nascimento et al., 2021). The CARES campaign showed a significant influence of elevated NO_x levels on the enhancement of SOA formation from isoprene. The organic aerosol (OA) concentrations rose from an average of 2.2 μg·m⁻³ under predominantly biogenic emission influence, to an average of 11.4 μg·m⁻³ when anthropogenic emissions from Sacramento mixed with isoprene-rich air from the foothills (Shilling et al., 2013). During the SOAS field campaign, measurements in rural Alabama showed that increased NO_x amounts were shown to enhance nighttime SOA formation via NO₃-oxidation of monoterpenes, which resulted in the formation of condensable organic nitrates (Xu et al., 2015).

Outside of field campaigns, valuable insights can also be obtained from ambient air measurements. For example, observations in an anthropogenic-influenced region in the southeastern US suggest that SOA correlates spatially and strongly with anthropogenic emissions such as CO and AVOCs according to measured water-soluble organic compounds, implying that biogenic SOA formation may be enhanced in polluted plumes (Weber et al., 2007).

Due to discrepancies between laboratory and field measurements, it is apparent that significant uncertainties remain on the impacts of mixing of anthropogenic and biogenic air masses on the production of secondary pollutants and their physicochemical properties. Many urban areas are surrounded by forests where such mixing can occur when the weather conditions are favorable. Therefore, in order to acquire better understanding of the chemical processes involved in the atmospheric transformations of VOCs under different chemical oxidation regimes, it is valuable to study the impacts of chemical processes in mixtures of biogenic and anthropogenic air masses. This is the key objective of the ACROSS project which is directly related to this dissertation.

1.3. Highly Oxygenated Organic Molecules (HOMs): VOC autoxidation products

1.3.1. Definition and formation pathways

It has been found that HOMs, a class of highly oxidized compounds with low volatility, can be rapidly formed in the gas phase from the oxidation of certain VOCs, including monoterpenes and can significantly promote the formation and growth of SOA. HOMs were first observed in the atmosphere in the boreal forest in Finland. Their formation pathways were quantified later in

laboratory studies of the oxidation of monoterpenes by O_3 (Ehn et al., 2010, 2012, 2014). Following their initial observation in the atmosphere as ambient ion clusters with the nitrate ion (NO_3^-), nitrate chemical ionization mass spectrometry has been employed to detect neutral HOMs in the atmosphere and laboratory systems (Ehn et al., 2014). Other ionization methods for detecting HOMs, such as acetate and iodide methods, have also been used (e.g. Bertram et al., 2011; Lee et al., 2014; Berndt et al., 2016; Riva et al., 2019).

In some of the early papers, the term HOMs was not yet coined and such highly oxidized compounds were referred to as ELVOCs in order to emphasize their key role in particle formation and growth (Ehn et al., 2014; Rissanen et al., 2014; Jokinen et al., 2015). Later, it was suggested that such compounds cover larger range of volatility classes, including ULVOCs, ELVOCs, LVOCs and SVOCs, recognizing their ability to contribute to gas-to-particle partitioning with a range of efficiencies (Kirkby et al., 2016; Tröstl et al., 2016; Bianchi et al., 2019; Guo et al., 2022b). Bianchi et al. (2019) defined HOMs as products formed via atmospheric autoxidation of VOCs involving peroxy radicals ($RO_2\cdot$) under atmospherically relevant conditions containing 6 oxygen atoms or more. This last criterion always remains somewhat artificial and under certain circumstances, it is possible to include species with 5 oxygen atoms in the HOM classification. Other researchers define HOMs differently, often making use of oxygen-to-carbon (O:C) ratios.

The process of autoxidation was not recognized as important in atmospheric chemistry until the last decade (Crouse et al., 2013; Ehn et al., 2014; Rissanen et al., 2014). Such reactions were well-known in high-temperature combustion (Taatjes, 2006; Crouse et al., 2013). Overall, it is characterized by an intramolecular H-atom shift within $RO_2\cdot$ radicals yielding a hydroperoxide functionality ($HOO-$) within an alkyl radical. This is followed by rapid addition of O_2 to form a new, more oxygenated $RO_2\cdot$ (an example is depicted in Figure 1.8). This process may occur several times until all abstractable H-atoms are transferred to hydroperoxides (Crouse et al., 2013; Ehn et al., 2017; Møller et al., 2019; Vereecken and Nozière, 2020). It may also be interrupted at each step by one of the classical termination reactions (unimolecular or bimolecular reactions), converting $HOM-RO_2\cdot$ into closed-shell molecules. In some instances, this interruption can result in the formation of $RO\cdot$ radicals, which subsequently contribute to the production of closed-shell molecules. This preserves the number of carbon atoms and produces molecules that can include hydroperoxides ($ROOH$), alcohols (ROH), carbonyls ($R=O$), peroxy acids ($RC(O)OOH$), carboxylic acids ($RC(O)OH$), and ONs.

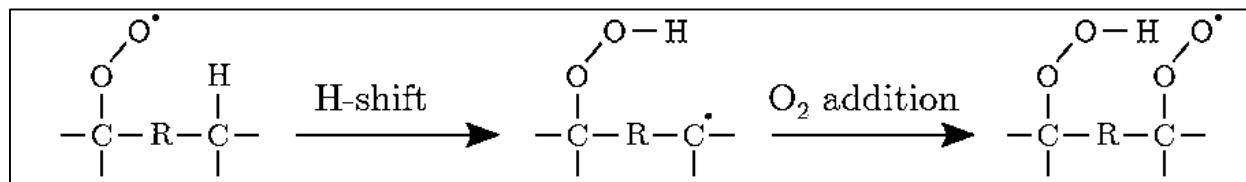


Figure 1.8. General schematic diagram illustrating the key process of autoxidation, where a molecule undergoes intramolecular H-atom shift and subsequent O₂ addition to the carbon-centered radical (Ehn et al., 2014). This can be repeated several times leading to HOMs.

The formation of a carbonyl with OH· loss may be one example of a unimolecular termination, which can occur in the case of a hydroperoxide group in a HOM-RO₂· (Rissanen et al., 2014; Ehn et al., 2017). The rate constant for autoxidation depends primarily on the chemical structure of the compound and for it to be of any real importance in the atmosphere, it is necessary for the intramolecular H-shift to occur at about the same timescales as the lifetime of the RO₂· (Ehn et al., 2017).

HOM accretion products can be other termination products formed via self-reactions of the HOM-RO₂·, which are known as accretion reactions and may play a major role in the initial steps of atmospheric NPF and aerosol growth (Mohr et al., 2017; Berndt et al., 2018b). Functionalization has been shown to significantly weaken C-H bonds. For example, aldehyde groups favor the shift of an H-atom from a C-H bond to a peroxy radical group after a ring opening in the ozonolysis of endocyclic alkenes (Rissanen et al., 2014; Mentel et al., 2015; Jokinen et al., 2015). According to Wang et al. (2017), alkyl-substitution of the aromatic ring might promote intramolecular H-migration. In addition, a few studies have shown that HOM formation is temperature-dependent, whose rate decreases with decreasing temperature (Frege et al., 2018; Stolzenburg et al., 2018; Quééléver et al., 2019).

Many investigations of HOM formation were conducted in simulation chambers, flow tubes and in ambient atmosphere, focusing on biogenic precursors, particularly monoterpenes, which are known to be important contributors to biogenic SOA. Fewer studies have examined HOM formed from AVOCs. Those studies will be summarized in Sections 1.3.2, 1.3.3 and 1.3.4.

1.3.2. Laboratory studies of formation of HOMs from BVOC oxidation

Contributing to nearly 33% of global monoterpene emissions (Sindelarova et al., 2022), the ozonolysis of α-pinene has been one of the most investigated biogenic VOC oxidation systems for HOMs production (e.g. Tröstl et al., 2016; Zhao et al., 2018; Molteni et al., 2019). Limonene is another important HOMs precursor, accounting for 20% of the global monoterpene emissions (Guenther et al., 2012). The presence of an endocyclic double bond as well as an exocyclic double bond, makes limonene an important precursor for SOA with high yields (Ehn et al., 2014; Jokinen

et al., 2015). Generally, research findings indicate that species with an endocyclic double bond exhibit significant production of gas-phase HOMs through ozonolysis compared to organic compounds without endocyclic double bonds. Studies have also revealed that ozonolysis of acyclic and exocyclic monoterpenes, such as myrcene and β -pinene respectively, do not produce HOMs efficiently compared to the endocyclic monoterpenes (Ehn et al., 2014; Jokinen et al., 2015).

Cyclohexene, which is an unsaturated and endocyclic alkene, was also extensively studied in laboratory experiments as a monoterpene surrogate because of their structural similarities, and ability to produce HOMs during ozonolysis. Other cycloalkenes have also been investigated such as cyclopentene, cycloheptene, cyclooctene (Ehn et al., 2014; Hyttinen et al., 2015; Berndt et al., 2015).

The oxidation of BVOCs by $\text{OH}\cdot$ radicals produces more HOMs in some cases (isoprene, β -pinene) and less in other cases (α -pinene, limonene) compared to ozonolysis. This is inferred to be due to different reaction pathways leading to products with different structures and properties (Berndt et al., 2016b, 2016a; Kirkby et al., 2016; Shen et al., 2022; Luo et al., 2023).

The formation of HOMs from NO_3 -radical-initiated oxidation has been studied including reactions of isoprene and various terpenes such as α -pinene, β -pinene, Δ^3 -carene, limonene and α -thujene (Draper et al., 2019; Shen et al., 2021; Zhao et al., 2021; Dam et al., 2022; Mayorga et al., 2022). In the case of isoprene, Zhao et al. (2021) showed the significance of monomers containing 2 nitrogen atoms indicating the importance of second-generation oxidation in HOM formation in this system with the most abundant HOM being $\text{C}_5\text{H}_{10}\text{N}_2\text{O}_8$. The latter has been consistently observed in field studies (Massoli et al., 2018; Xu et al., 2021). Shen et al. (2021) also demonstrated that a distinct unimolecular H-shift termination reaction plays a role in the formation of HOMs organic nitrates, given that a significant portion of the latter comprised carbonylnitrates.

Reported yields of HOMs in the literature from the oxidation of BVOCs by the important atmospheric oxidants at low NO_x conditions and measured using NO_3^- ToFCIMS are summarized in Table 1.8.

The variation in yields of HOMs formed from the same chemical oxidation system (VOC, oxidant) between the various studies may be due to different experimental configurations or to uncertainties in calibration factors used for quantification of the concentrations. For instance, yields of HOMs from isoprene oxidation are generally lower than those from monoterpenes, except for NO_3 -initiated oxidation (Table 1.8).

A scavenger was used in a number of experiments to reduce or eliminate the contribution to oxidation by OH· radicals to obtain HOM yields by ozonolysis alone.

Table 1.8. Molar HOM Yields (\pm uncertainty) from BVOC oxidation, collected from literature studies for various oxidants and using NO_3^- Chemical Ionization Mass Spectroscopy detection.

Reference	BVOC	HOM molar Yields (%)
NO_3		
Dam et al., 2022	Δ^3 -Carene	2.5×10^{-4}
Dam et al., 2022	α -thujene	1×10^{-4}
Dam et al., 2022	β -pinene	5×10^{-5}
Dam et al., 2022	α -pinene	9.8×10^{-6}
Zhao et al., 2021	Isoprene	1.2 (+1.3, -0.7)
Guo et al., 2022	Limonene	1.5 (+1.7, -0.7)
O_3 with OH scavenger		
Jokinen et al., 2015	Isoprene	0.01 (+0.01, -0.005)
Berndt et al., 2015	Cyclopentene	4.8 (\pm 0.2)
Rissanen et al., 2014	Cyclohexene	4.5 (\pm 3.8)
Berndt et al., 2015		6.0 (\pm 0.1)
Berndt et al., 2015	Cycloheptene	5.9 (\pm 0.1)
Berndt et al., 2015	Cyclooctene	5.9 (\pm 0.1)
Jokinen et al., 2015	α -pinene	3.4 (+3.4, -1.7)
Kirkby et al., 2016		2.9 (+2.9, -1.74)
Berndt et al., 2016		2.1 (\pm 0.1)
Jokinen et al., 2015	β -pinene	0.12 (+0.12, -0.06)
Jokinen et al., 2015	Limonene	5.3 (+5.3, -2.65)
Pagonis et al., 2019		11
Jokinen et al., 2015	Myrcene	0.47 (+0.47, -0.24)
Richters et al., 2016	β -caryophyllene	0.5 (+0.5, -0.3)
Richters et al., 2016	α -cedrene	0.6 (+0.6, -0.6)
Richters et al., 2016	α -humulene	1.4 (+1.4, -0.7)
O_3 without OH scavenger		
Ehn et al., 2014	Cyclohexene	4 (\pm 2)
Ehn et al., 2014	α -pinene	7 (\pm 3.5)
Kirkby et al., 2016	α -pinene	3.2 (+3.2, -1.92)
Ehn et al., 2014	β -pinene	< 0.1
Ehn et al., 2014	Limonene	17 (\pm 8.5)
Jokinen et al., 2016	β -caryophyllene	1.7 (\pm 1.28)
OH		
Ehn et al., 2014	α -pinene	< 1
Jokinen et al., 2015		0.44 (+0.44, -0.22)
Kirkby et al., 2016		1.2 (+1.2, -0.7)
Berndt et al., 2016		0.052 (+0.05, -0.03)
Shen et al., 2022		0.8 (+1.2, -0.4); 1.1 (+1.6, -0.6)
Jokinen et al., 2015	β -pinene	0.58 (+0.58, -0.29)
Berndt et al., 2016		0.022 \pm 0.001
Jokinen et al., 2015	Limonene	0.93 (+0.93, -0.047)
Luo et al., 2023		1.97 (+2.52, -1.06)
Jokinen et al., 2015	Myrcene	1 (+1, -0.5)
Jokinen et al., 2015	Isoprene	0.03 (+0.03, -0.015)

A number of studies have been designed to investigate the impact of mixtures of BVOCs on HOMs formation (Lehtipalo et al., 2018; McFiggans et al., 2019; Pullinen et al., 2020; Heinritzi et al., 2020). McFiggans et al. (2019) showed that HOM accretion products may contribute significantly to the yield of SOA. However, several studies found that increasing NO_x concentrations suppressed the formation of HOM accretion products, and also increased the yield of HOM-ONs, hence resulting in the formation of molecules with greater volatilities (Lehtipalo et al., 2018; Rissanen, 2018; McFiggans et al., 2019; Pullinen et al., 2020; Luo et al., 2023).

There are also studies that showed that isoprene suppresses the formation of HOM monoterpene-derived accretion products and thereby reduces particle nucleation and growth of small size SOA (Berndt et al., 2018a; McFiggans et al., 2019; Heinritzi et al., 2020).

1.3.3. Laboratory studies of formation of HOMs from AVOC oxidation

Compared to studies of the oxidation of BVOCs, fewer reports of HOMs formed from the oxidation of AVOCs in laboratory studies have been published (e.g. Rissanen, 2021). The few studies available have shown that the oxidation of aromatics can proceed via autoxidation and may form HOMs.

Wang et al., (2017) investigated the formation of HOMs from the OH-initiated oxidation of alkylbenzenes and showed that an increase in the size of the alkyl group leads to greater HOM yields.

Molteni et al. (2018) studied the formation of HOMs from OH-initiated oxidation of aromatic compounds (benzene, toluene, ethylbenzene, o/m/p-xylene, and 1,3,5-trimethylbenzene (mesitylene)) as well as two polycyclic aromatics (naphthalene and biphenyl), giving HOM yields comparable with those reported from OH· and O_3 oxidation of monoterpenes (in the range of 0.1-2.5%).

Garmash et al. (2020) investigated the potential of several aromatic compounds (benzene, toluene, and naphthalene) to form HOMs from OH-initiated oxidation. They reported a strong dependence of HOM yields on OH concentration, suggesting that the HOMs observed were formed by multiple OH oxidation steps, which was supported by the nature of HOMs that were identified during this study. Similar results have been shown for six aromatic precursors (benzene, toluene, m-xylene, 1,3,5 trimethylbenzene, naphthalene, 1-methylnaphtalene) under low NO_x conditions by (Cheng et al., 2023). Garmash et al. (2020) also investigated the effect of NO_x and the presence of seed aerosol on HOMs amounts. The addition of NO_x to the system changed the HOMs average composition to

favor more ONs. Employing seed aerosols increased the loss rate of HOMs to both chamber walls and aerosols. Based on these results, one should expect an increase of HOM yields by multi-generation OH oxidation and a shift towards the aerosol phase of the partitioning of HOMs in presence of a significant mass of particles. The HOM molar yield from benzene oxidation varied from 4.1% to 14.0% which strongly depended on the OH· concentration.

Wang et al. (2020) studied the formation of HOMs from the photo-oxidation of toluene and naphthalene and found them to efficiently form low-volatility products, with much greater volatility decreases per added oxygen atom than did the corresponding α -pinene systems. The presence of NO_x also suppressed HOM-RO₂· autoxidation with lower HOM concentrations observed. Other studies also showed suppression of the production of HOMs accretion products from the oxidation of aromatic compounds with increasing NO_x concentrations and an increase in the formation of HOM-ONs (Tsiligiannis et al., 2019; Priestley et al., 2021; X. Cheng et al., 2021).

Wang et al. (2021) performed the first study on HOMs formation from oxidation of an alkane, expected to be relatively minor. In this study, it was found, however, that long-chain alkanes (>C₆) undergo autoxidation very efficiently both under atmospheric and combustion conditions. On the contrary, cycloalkanes oxidation showed a significant increase in HOMs yields with increasing oxidation rate. High HOM yields, especially for aldehydes, were achieved from the oxidation of oxygenated VOCs even at low oxidation rates, since the aldehyde functionality was shown to favor autoxidation (Mentel et al., 2015).

Molar HOM yields previously reported in the study from Molteni et al. (2018) and Cheng et al. (2021) which employed the NO₃⁻ ToFCIMS technique, are summarized in Table 1.9.

Table 1.9. Molar HOM Yields from AVOC oxidation by OH, and using NO₃⁻ Chemical Ionization reported in the literature.

Studies	VOC	HOM molar Yields (%)
Molteni, 2018 Cheng et al., 2021	Benzene	0.2 0.22 ± 0.1
Molteni, 2018 Cheng et al., 2021	Toluene	0.1 0.46 ± 0.2
Molteni, 2018	Ethylbenzene	0.2
Molteni, 2018	o/m/p-xylene	1-1.7
Molteni, 2018	Mesitylene	0.6
Molteni, 2018	Naphthalene	1.8
Molteni, 2018	biphenyl	2.5

1.3.4. Observations of HOMs in ambient air

HOMs were first observed in ambient air at the SMEAR II boreal forest station in Finland (Ehn et al., 2010, 2012). Since then, several other studies have reported these compounds in boreal forest air (Jokinen et al., 2016; Berndt et al., 2016b; Yan et al., 2016; Bianchi et al., 2017; Mohr et al., 2017; Zha et al., 2018; Huang et al., 2021). For instance, in the study conducted by Yan et al. (2016), factor analysis revealed the predominant presence of HOMs resulting from the reaction of monoterpenes with OH· or O₃ during daytime. Two types of HOMs were identified: non-nitrogen HOMs and HOMs organic nitrates, both primarily composed of C_{9,10} compounds. Conversely, during nighttime, HOMs arising from the reaction of monoterpenes with O₃ and NO₃· were dominant. Accretion products (C₁₆₋₂₀) with or without nitrogen in their structure were exclusively observed during nighttime. Zha et al. (2018) observed HOMs on two heights, above the canopy of the boreal forest and at the ground level. The findings indicated that nighttime conditions were characterized by temperature inversions and the concentrations of ground-level HOMs were lower than those observed above the canopy. However, under well-mixed boundary layer conditions (characteristic of daytime), the mixing ratios of HOMs were similar in both levels.

Besides the boreal forest, studies have also been conducted in other geographic locations. HOMs were detected at rural sites in central Germany (Jokinen et al., 2014; Mutzel et al., 2015; Kürten et al., 2016; Brüggemann et al., 2017) and in the southeastern US (Brophy and Farmer, 2015; Krechmer et al., 2015; Lee et al., 2016; Massoli et al., 2018). For instance, in the study conducted by Massoli et al. (2018) during the SOAS 2013 campaign, factor analysis was performed on HOM measurements, revealing three factors related to isoprene and three factors related to monoterpenes. HOMs organic nitrates were found to be significant components during both daytime and nighttime. Numerous HOMs were identified, with molecular formulas ranging from C₃ to C₂₀. Isoprene organic nitrates were found to exceed monoterpenes organic nitrates, as well as non-nitrate C₅-HOMs. Notably, C₅H₁₀N₂O₈ dominated the nighttime factor associated with isoprene.

HOMs also have been detected at urban and suburban sites in China (Brean et al., 2019; Mehra et al., 2021; Xu et al., 2021; Wang et al., 2022; Zhang et al., 2022), and at high altitudes and in the free troposphere (Bianchi et al., 2016; Frege et al., 2017). The study of Wang et al. (2022) in Beijing, China, indicates a robust correlation between HOMs and the oxidized organic aerosol (OOA) factor, measured by a ToF-ACSM. This suggests that HOMs significantly contribute to the formation of SOA.

Thesis objectives

Previous evidence in the literature indicates that HOMs are key species that play important roles in the atmospheric chemistry, especially in the formation and evolution of SOA. Information on the composition of HOMs and their formation mechanisms in different environments and chemical oxidation regimes is therefore crucial to answer many unanswered scientific questions.

The measurement of gas-phase HOMs in ambient air can help addressing several key points:

1. Quantify the link between VOCs and their contribution to aerosol formation and growth; assess connections between HOMs composition and SOA properties
2. Understand HOMs contribution to NPF, and estimate their global importance for Cloud Condensation Nuclei (CCN) concentrations and properties
3. Improve model representations of SOA formation

The main focus of this thesis research, therefore, is the investigation of HOMs formation processes for a variety of VOC precursors and atmospheric conditions. This is accomplished by employing a nitrate Chemical Ionization Inlet (NO_3^- CI) that is coupled to an Atmospheric Pressure interface Time of Flight Mass Spectrometry (APi-ToF) to selectively measure HOMs and other molecules. For simplicity, the instrument used in this study is designated as a NO_3^- ToFCIMS throughout this manuscript.

Therefore, the objectives of this thesis are to:

- Perform the characterization and optimization of the NO_3^- ToFCIMS in the laboratory.
- Develop the protocol and perform the calibration of the NO_3^- ToFCIMS.
- Study the composition and concentrations of HOMs in a forested environment at the ACROSS Rambouillet site and examine how these parameters evolve in different conditions, especially during the mixing of urban plume and forested air masses.

To answer these objectives, a series of controlled laboratory experiments in different conditions have been carried out (see chapter 2), as well as a set of simulation chamber experiments involving the oxidation of BVOCs and AVOCs (see chapter 3). The chamber studies were also used to identify a list of potential HOMs products that could be encountered in the field in forested and mixed environments. A series of organic compounds have been tested to identify good candidates to be used as potential organic calibrants and to develop methodology for the calibrations (see chapter 2). Finally, the NO_3^- ToFCIMS was deployed at the top of a 40 m tower (above the forest canopy) in the Rambouillet forest in France, in June-July 2022 during the ACROSS summer field campaign (see chapter 4).

Chapter 2 Instrumentation: A Chemical Ionization Atmospheric Pressure interface Time-of-Flight mass spectrometer (ToFCIMS)

Mass spectrometric methods have revolutionized our understanding of the chemical composition of the atmosphere due to their ability to provide comprehensive information on various trace gases present in a mixture. Molecules are ionized to enable their detection according to their mass-to-charge ratios (m/z). A mass spectrometer is based on three primary components: an ionization source, a mass analyzer and a detector.

The nitrate-ion based chemical ionization atmospheric pressure interface time-of-flight mass spectrometer (NO_3^- ToFCIMS) is the key online MS instrument used in this research and forms the core of the work presented in this dissertation. This instrument can selectively measure important contributors to NPF and growth such as gas-phase non-radical HOMs, highly oxidized peroxy radicals ($\text{HOM-RO}_2\cdot$), some OVOCs (e.g. small diacids), and sulfuric acid (H_2SO_4) (Ehn et al., 2017; Bianchi et al., 2019; Rissanen, 2021).

The working principle, advantages and limitations of this instrument will be described in this chapter. This instrument was characterized in the laboratory using a variety of experiments that will also be described.

2.1. Instrumental Configuration

The NO_3^- ToFCIMS (Aerodyne Research Inc., and ToFwerk AG) consists of two main body parts, namely the chemical ionization (CI) inlet (Eisele and Tanner, 1993; Jokinen et al., 2012) and the atmospheric pressure interface time-of-flight mass spectrometer (APi-ToF) (Junninen et al., 2010). The APi-ToF integrates both the mass analyzer and the detector. This combination of a CI with an APi-ToF has revolutionized the ability to selectively detect specific classes of trace species with high sensitivity.

2.1.1. Chemical Ionization inlet: Nitrate Reagent Ion Production and Reaction

Neutral molecules present in the gas phase first undergo ionization prior to being guided through the APi and detected by the Time-of-Flight Mass Spectrometer (ToFMS). Several ionization techniques exist, each of which has its own advantages and drawbacks. Chemical ionization (CI) is commonly used and is based on chemical reaction in the gas phase between a target molecule and an ionized reagent gas. Ideally, it is a gentle charging technique that preserves the chemical identity of the analyte molecule. This selectivity toward specific classes of gas species is achieved by the choice of the reagent ion used that reduces interferences with other airborne components

and thus minimizes the complexity of the mass spectrum (Huey, 2007). The instrument described herein is operated in the negative ion mode with nitrate as the reagent ion, which has been discovered to selectively ionize HOMs in air samples (Ehn et al., 2014).

The sample gas is fed into the center axis of the CI inlet through a 3/4" stainless steel tube that is surrounded by a coaxial sheath gas flow that carries the nitrate primary ions $(\text{HNO}_3)_{n=0-2} \cdot \text{NO}_3^-$ parallel to the sample flow. This design is ideal for the measurement of low volatility molecules (such as HOMs), because it limits the turbulent interaction between the sample and the inlet surfaces, therefore reducing wall losses. This approach was based on work by Eisele and coworkers for the measurement of tropospheric H_2SO_4 and hydroxyl radicals ($\text{OH}\cdot$) (Eisele and Tanner, 1993).

2.1.2. Nitrate Reagent Ion Production

Primary ions are produced by passing a 30 sccm stream of dry air through a small amount (2-20 mL) of liquid nitric acid (HNO_3) placed in a glass vial, which is mixed with the sheath flow and then subject to soft X-ray radiation, resulting in efficient high density ion production (see Figure 2.1 and Figure 2.2). In this work, this is controlled by a Hamamatsu Photoionizer Model C12646 power supply that drives a Model L9491 source head (9.5 keV). This is an alternative method that is consistent with the conventionally used ^{241}Am radioactive source, which produces ions via the interaction of alpha particles with the sheath gas.

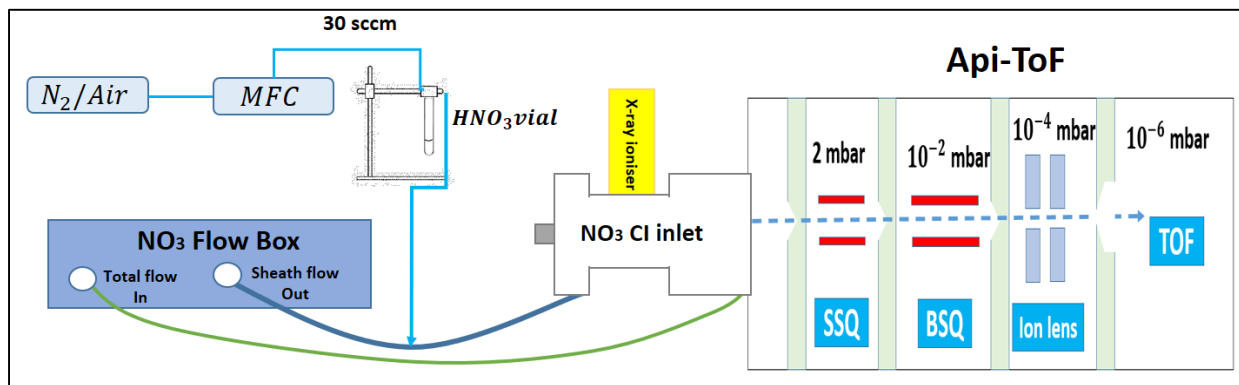
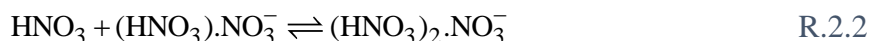
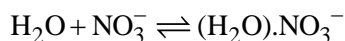


Figure 2.1. Instrumental configuration of the NO_3^- ToFCIMS.

NO_3^- is produced in the sheath flow followed by collisions with the neutral nitric acid molecules and H_2O vapor, resulting in the formation of nitrate ion – nitric acid dimers $(\text{HNO}_3) \cdot \text{NO}_3^-$ (R.2.1), nitrate ion – nitric acid trimers $(\text{HNO}_3)_2 \cdot \text{NO}_3^-$ (R.2.2) and to some extent nitrate ion – water $(\text{H}_2\text{O}) \cdot \text{NO}_3^-$ clusters (R.2.3) (Davidson et al., 1977).





R.2.3

Thereafter, reagent ions are pushed towards the center axis of the inlet by applying electrostatic voltages to the drift tube, which results in interaction with neutral molecules in the sample gas flow with a reaction time of about 200 ms. The product and reagent ions then enter the mass spectrometer and are separated and detected in the APi-ToF system (Section 2.1.4) (Jokinen et al., 2015). The electric field within the inlet is generated by applying negative voltages to the ion source (-125 V) and the ion drift tube (-107 V), as shown in Figure 2.2.

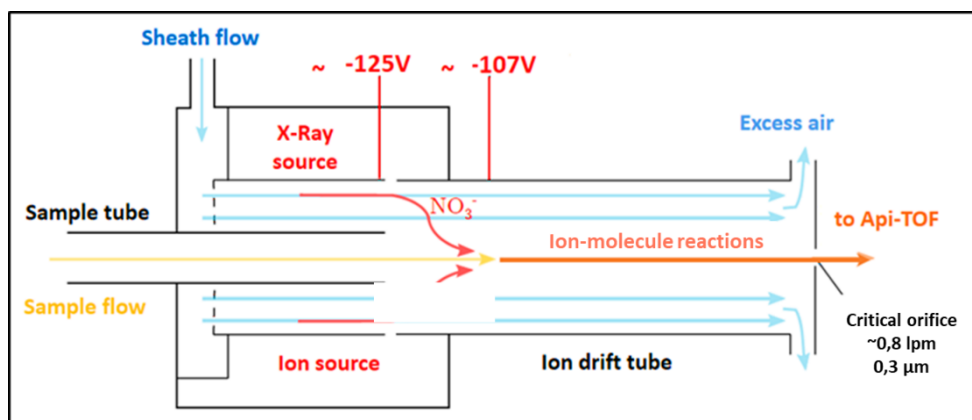
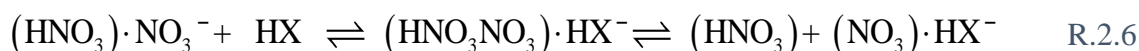
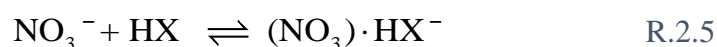
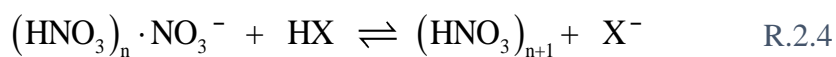


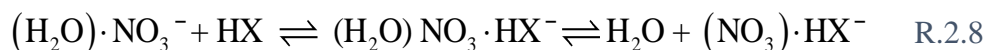
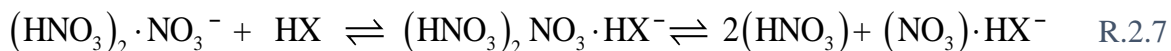
Figure 2.2. Schematic illustration of the chemical ionization inlet used in this work (diagram adapted from Jokinen, 2015 and Garmash, 2020).

2.1.3. Ion-Molecule Reaction

The distinguishing hallmark of CI of gaseous species is the use of ion-molecule reactions to selectively ionize the compounds of interest in the air. This relatively weak ionization method contrasts with strong approaches such as electron impact that result in ionization with significant fragmentation of the analytes.

Within the NO_3^- CI inlet, ion-molecule reaction can proceed by either proton abstraction or by clustering (Field, 1968; Jokinen et al., 2012). The first type is proton (H^+) abstraction from the sample molecule HX by the nitrate ion, forming a negative ion X^- and nitric acid (R.2.4). This chemistry occurs when HX has a gas-phase acidity larger than the reagent ion (e.g. the gas-phase acidity of HNO_3 is $-317.8 \pm 0.2 \text{ kcal}\cdot\text{mol}^{-1}$ (Davidson et al., 1977; Ehn et al., 2010), while the gas-phase acidity of H_2SO_4 is $-299 \pm 3.1 \text{ kcal}\cdot\text{mol}^{-1}$ (Ehn et al., 2010; Wang et al., 2000)) (Topol et al., 2000).





The mechanism of the clustering reaction involves a sample molecule, primarily strong acids and polar species (e.g. OVOCs, HOMs), that generates a stable ion-molecule cluster $(\text{NO}_3) \cdot \text{HX}^-$ by means of collisions with either nitrate ions NO_3^- (R.2.5), nitric acid-nitrate-dimers $(\text{HNO}_3) \cdot \text{NO}_3^-$ (R.2.6) or nitric acid-nitrate-trimers $(\text{HNO}_3)_2 \cdot \text{NO}_3^-$ (R.2.7) (Davidson et al., 1977; Hyttinen et al., 2015, 2018). Along with forming $(\text{HNO}_3)_{n=0-2} \cdot \text{NO}_3^-$ clusters, NO_3^- ions were found to bind with H_2O , which forms $(\text{H}_2\text{O}) \cdot \text{NO}_3^-$ clusters (0.1-2% of total reagent ion signal). They were present in the mass spectra obtained in this work. $(\text{NO}_3) \cdot \text{HX}^-$ can thus be formed via HX and $(\text{H}_2\text{O}) \cdot \text{NO}_3^-$ collisions (R.2.8), hence, the $(\text{H}_2\text{O}) \cdot \text{NO}_3^-$ signals were also included in the normalization procedure in the calculations that will be discussed in the following sections. In the case of collisions with $(\text{HNO}_3) \cdot \text{NO}_3^-$, $(\text{HNO}_3)_2 \cdot \text{NO}_3^-$ and $(\text{H}_2\text{O}) \cdot \text{NO}_3^-$, the intermediate products of R.2.6, R.2.7 and R.2.8 may be formed before being dissociated through collisions, primarily induced by the strength of voltages applied to the various components of the APi, resulting thus in the detection of $(\text{NO}_3) \cdot \text{HX}^-$ (Bertram et al., 2011; Hyttinen et al., 2015).

As $(\text{NO}_3) \cdot \text{HX}^-$ is shown to be formed from different reactions, one should conclude that the ions observed in the time-of-flight mass spectra do not necessarily represent the ions that are generated in the ion source because of the potential effects of collisional dissociation within the inlet (Bertram et al., 2011) and mass-dependent transmission effects (Heinritzi et al., 2016). However, the impact of such processes on the level of signal of detected ions is taken into account while performing the calibration of the instrument and determining calibration coefficients.

Hyttinen et al. (2015) performed quantum chemical computational studies showing how HOMs and NO_3^- are likely to form stable clusters by means of multiple hydrogen bonds, since HOMs are expected to contain multiple hydroperoxide groups ($-\text{OOH}$) in addition to alcohol (OH), and/or carbonyl ($\text{C}=\text{O}$) groups. Additionally, some oxygenated molecules, especially those containing carboxylic acid groups ($\text{C}(\text{O})\text{OH}$), can be found in mass spectra in both the deprotonation and clustering forms. For instance, malonic acid ($\text{C}_3\text{H}_4\text{O}_4$) and tartaric acid ($\text{C}_4\text{H}_6\text{O}_6$) are observed both in the cluster form, $(\text{C}_3\text{H}_4\text{O}_4) \cdot \text{NO}_3^-$ and $(\text{C}_4\text{H}_6\text{O}_6) \cdot \text{NO}_3^-$ respectively, and in the bare ion form (from deprotonation) $\text{C}_3\text{H}_3\text{O}_4^-$ and $\text{C}_4\text{H}_5\text{O}_6^-$. H_2SO_4 is also found to react by deprotonation (HSO_4^-) and by clustering with NO_3^- ($(\text{H}_2\text{SO}_4) \cdot \text{NO}_3^-$).

In this work, the NO_3^- CI inlet was used to investigate HOMs formation in both laboratory systems and field studies. A detailed description of the instrument's component is discussed in the following sections.

2.1.4. Ion Quantification

After ionization, ions are guided through the APi-ToF which was initially developed to measure naturally charged ambient ions (Junninen et al., 2010; Ehn et al., 2010). This means that a CI unit, regardless of the choice of the reagent ion, was not included in the default configuration. The ToFwerk APi-ToF was first deployed at the SMEAR II station in Hyytiälä for atmospheric measurements (Ehn et al., 2010) and in chamber studies (Ehn et al., 2012, 2014).

The resulting product ions enter the vacuum system through a critical orifice (diameter 0.3 mm), at a flow of approximately 0.8 L/min at ambient pressure. Sampling at atmospheric pressure conditions helps to minimize any possible changes in the sample prior to detection, particularly for E(LVOCs) that are more easily lost to walls (Ehn et al., 2012). Subsequently, the ions are focused and pass through a series of elements as they move towards the time-of-flight region of the instrument while excess air is removed in differentially pumped chambers by means of a scroll pump and a three-stage turbo pump (Pfeiffer Vacuum technology AG). The sample pressure must be progressively reduced as the time-of-flight region runs under high vacuum conditions ($\sim 10^{-6}$ mbar). The complete setup of the instrument is shown in Figure 2.1. The NO_3 flow box, shown in Figure 2.1, serves to regulate the inlet sampling flow, by fixing the total flow and the sheath flow. These will be further discussed in sub-section 2.2.1.

The first two APi-ToF chambers consist of a small segmented quadrupole (SSQ) and a large segmented quadrupole (BSQ), controlling transmission of ions through the instrument while ensuring a linear voltage drop during the process. It is worth noting that collisional dissociation with water can occur in the SSQ region whereas declustering is controlled in the BSQ that operates such that only weak bonds can break. The third chamber consists of electrical lenses that focuses ions into a parallel beam for the orthogonal ion extraction region of the time-of-flight chamber. A pressure of 2 mbar is reached in the SSQ region using the scroll pump, while the pressure in the BSQ, ion lens, and time-of-flight region is reduced to 10^{-3} , 10^{-4} , and 10^{-6} mbar, respectively, by means of the turbo pump.

In the time-of-flight region, ions are all given equal kinetic energy, are extracted by a pulser, and then are detected according to their time of flight between the pulse and the signals received by a

multi-channel plate (MCP) detector. The response is then processed (discussed in section 2.1.5) and converted to the mass-to-charge ratio of the ion in question.

The time-of-flight is equipped with a reflectron unit to increase the flight time of ions, which increases the mass resolution. The latter is generally presented as $\frac{m}{\Delta m}$ where m is the m/z of the charged specie and Δm is defined as the full width of a peak at its half-maximum (FWHM) height. In other words, it is described as the ability to separate ions which overlap. Moreover, ToFMS can operate via two possible modes “V-mode” and “W-mode”, where the letters reflect the flight shape using one or three-reflections, respectively, as shown in Figure 2.3 (Jordan et al., 2009). The W-mode increases the flight path leading to higher mass resolution compared to the V-mode, resulting in a better separation of nominally isobaric ions. The longer flight path reduces the number of ions reaching the detector thus leading to lower sensitivities. In this work, the ToFMS operated in the V-mode, reaching a moderate resolution 3500–4000 Th/Th with good sensitivity. The ToFMS is operated at 16.7 kHz frequency with a 60 μ s ToF extraction period. The mass spectrum range is 7–1126 Th. A TofDaq (Tofwerk AG, ToFDaq Version 1.99) recorder has been used to setup the ToF acquisition configuration, to record the mass spectra and to store data in HDF5 file format.

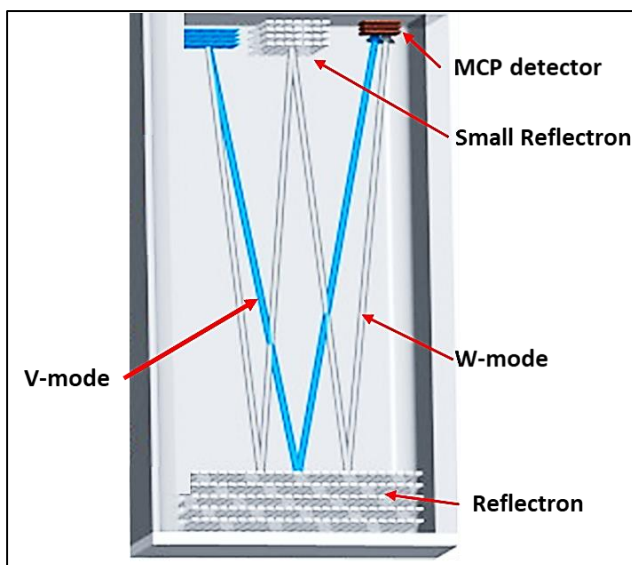


Figure 2.3. The two operation modes of the ToFMS, the V-mode and the W-mode (Jordan et al., 2009).

As ions are driven along their path into the ToF region by electrostatic voltages, the choice of the voltage settings is crucial to efficiently guide the ions while minimizing the occurrence of significant fragmentation. This will be discussed in more detail in the section 2.2.

2.1.5. Data Analysis: Tofware

Data processing plays an important role in treating the raw data obtained from the instrument. The Tofware (Tofware AG, version 3.2.5) software is used to process the HDF5 data files from the

instrument (Stark et al., 2015). Raw data were averaged, prior to data processing, to one-minute values for laboratory experiments and to ten-minute values for field measurements. Data processing encompasses several steps. For this purpose, Tofware includes a specific workflow with a path to be taken by NO_3^- ToFCIMS users, starting with m/z mass calibration, followed by baseline subtraction, and refining the peak shape and width. A comprehensive overview of the data processing and analysis steps that are typically followed is described in the supplement of this manuscript (Supplement S.2.3). Here, particular emphasis is placed on the mass calibration step, which was specifically optimized to enhance the accuracy of peak identification in both laboratory experiments and field campaign measurements.

Mass calibration is usually performed with respect to calibrant peaks with known m/z ratios. Typically, the 3 reagent ion peaks, NO_3^- , $(\text{HNO}_3)\cdot\text{NO}_3^-$ and $(\text{HNO}_3)_2\cdot\text{NO}_3^-$ ($m/z=61.99$; 124.98 ; 187.98 respectively) are used. It is important to have several calibration peaks well distributed along the full m/z range employed, serving as reference points for fitting the relationship between the time of flight and m/z , as described by the empirical Equation 2.1, to achieve accurate peak assignments (example shown in Figure 2.4).

$$\text{ToF} = p1 \times \sqrt{\frac{m}{z}} + p2 \quad \text{Equation 2.1}$$

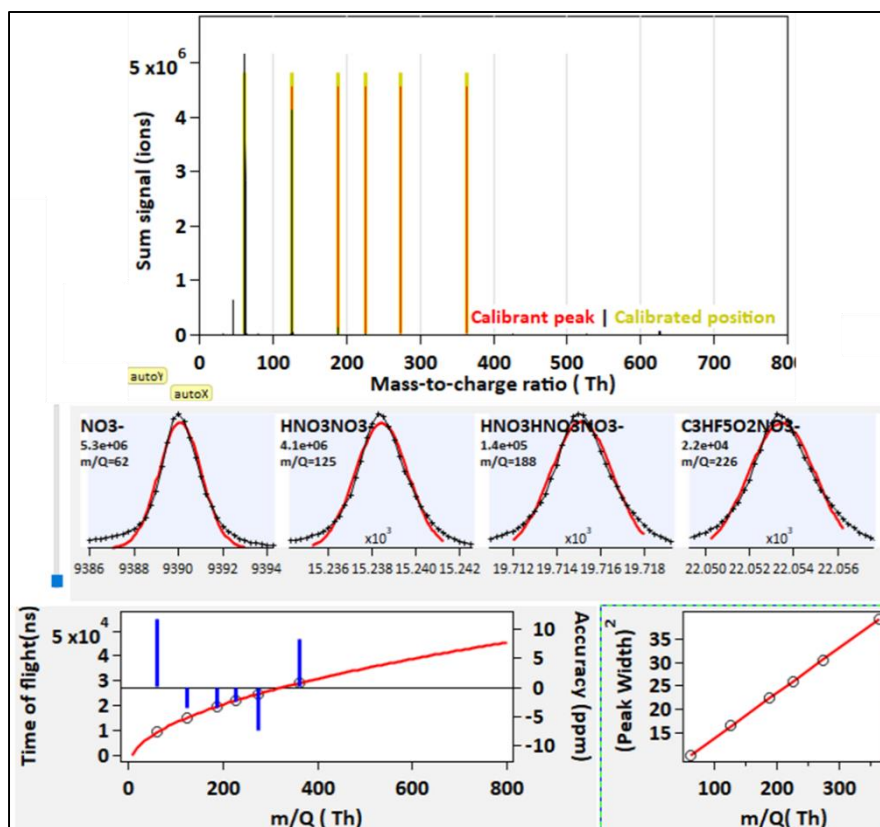


Figure 2.4. An illustrative example of a mass calibration carried out using three reagent ions and several fluorinated organics.

This equation enables the determination of m/z values based on the ions time of flight. Fluorinated organic compounds appeared clearly as contaminants that originated from Teflon® sampling lines used in early experiments and therefore appeared in the mass spectra. This phenomenon is well-known in the use of NO_3^- CIMS (Ehn et al., 2012). To make use of this, several perfluorinated organic acids that covered the upper m/z range were added continuously to the sheath flow, primarily during the field measurements, so that the mass calibration could cover a wider mass range (Table 2.1). These compounds were found to produce two masses: one associated with deprotonation and the other one with a cluster. Furthermore, for the experiments described in section 2.3, the ion peaks related to the organic compounds that were studied were also included in the list of mass registration calibrants. Overall, the peaks selected for this step must be well isolated and relatively abundant.

Table 2.1. List of perfluorinated organic compounds chosen for mass calibration covering a wide range of m/z .

Compound	MW ($\text{g}\cdot\text{mol}^{-1}$)	Chemical Formula	Form of detection
Perfluoropropionic acid	164.03	$\text{C}_2\text{F}_5\text{COOH}$	$\text{C}_3\text{HF}_5\text{O}_2\cdot(\text{NO}_3)^-$ (225.978) > $\text{C}_3\text{F}_5\text{O}_2^-$ (162.982)
2,3,4,5,6-pentafluorobenzoic acid	212.07	$\text{C}_6\text{F}_5\text{COOH}$	$\text{C}_7\text{HF}_5\text{O}_2\cdot(\text{NO}_3)^-$ (274.058) >>> $\text{C}_7\text{F}_5\text{O}_2^-$ (211.07)
Perfluoroheptanoic acid	364.06	$\text{C}_6\text{F}_{13}\text{COOH}$	$\text{C}_7\text{HF}_{13}\text{O}_2\cdot(\text{NO}_3)^-$ (426.048) > $\text{C}_7\text{F}_{13}\text{O}_2^-$ (363.06)
Perfluorononanoic acid	464.08	$\text{C}_8\text{F}_{17}\text{COOH}$	$\text{C}_9\text{HF}_{17}\text{O}_2\cdot(\text{NO}_3)^-$ (526.068) > $\text{C}_9\text{F}_{17}\text{O}_2^-$ (463.08)
Perfluoroundecanoic acid	564.09	$\text{C}_{10}\text{F}_{21}\text{COOH}$	$\text{C}_{11}\text{HF}_{21}\text{O}_2\cdot(\text{NO}_3)^-$ (626,068) >>> $\text{C}_{11}\text{F}_{21}\text{O}_2^-$ (563.09)

> Slightly higher than

>> Significantly higher than

Once the ion calibrants are selected, a preliminary peak fitting is done by using the Gaussian fit type and the typical polynomial fit (Equation 2.1), which is used to relate the m/z to the ToF of the ion. Figure 2.4 illustrates one example of a mass calibration in Tofware.

2.2. Tuning ToFCIMS parameters in the laboratory

2.2.1. Inlet flows

As shown in Figure 2.1, a NO_3^- flow box (containing mass flow controllers) was used to control the sample flow rate by adjusting the sheath and the total flows. The flow rate of the sampling line is determined from the difference of these two and adding the APi sampling flow of 0.8 lpm, discussed in section 2.1.4 (Equation 2.2). The selection of a specific sample flow was based on optimization of the instrument by investigating a range of total and sheath flows. This means that for experiments in a simulation chamber, the sample flow rate was reduced to approximately 6 lpm (Total flow 35 lpm and Sheath flow 30 lpm) due to the sampling capacity from the chamber

as other instruments were sampling at different flow rates. For ambient measurements, sample flow was increased to about 8 lpm (Total 37 lpm and Sheath 30 lpm).

$$\text{Sample flow} = \text{Total flow} - \text{Sheath flow} + 0.8 \text{ lpm} \quad \text{Equation 2.2}$$

Different sets of flows (Figure 2.5) were studied in the laboratory under room temperature conditions (approximately 20°C) and whichever provided the most stable signal were selected. The relative standard deviation (RSD) expressed in % is a measure of the variability of a set of data and was calculated for each data set using Equation 2.3. As shown in Table 2.2, the RSD was lowest for Set 5 and 6 (~1.8% for (HNO₃)·NO₃⁻ and 1.9% for NO₃⁻), allowing us to choose one of them according to the sample flow required. The lower this value is the less scattered is the data.

Table 2.2. Summary of the RSD% values for the 8 data sets.

Set	Total flow (lpm)	Sheath flow (lpm)	RSD% (NO ₃ ⁻)	RSD% (HNO ₃ ·NO ₃ ⁻)
1	40	34	3.6	3.4
2	39	34	3.4	3.5
3	41	34	3.1	3.1
4	42	36	2.9	2.7
5	37	30	2.0	2.0
6	35	30	1.9	1.8
7	44	36	5.9	6.1
8	44	38	3.9	4.1

Figure 2.5 shows the stability of signals as a function of the flows. For instance, it clearly shows the reduced stability of the signals for Set 7, supported by the corresponding RSD% calculations (6.1% for (HNO₃)·NO₃⁻ and 5.9% for NO₃⁻). This may be due to turbulence that develops in the inlet at the higher flows.

$$\text{RSD\%} = \frac{\text{stdv}}{\text{avg}} \times 100 \quad \text{Equation 2.3}$$

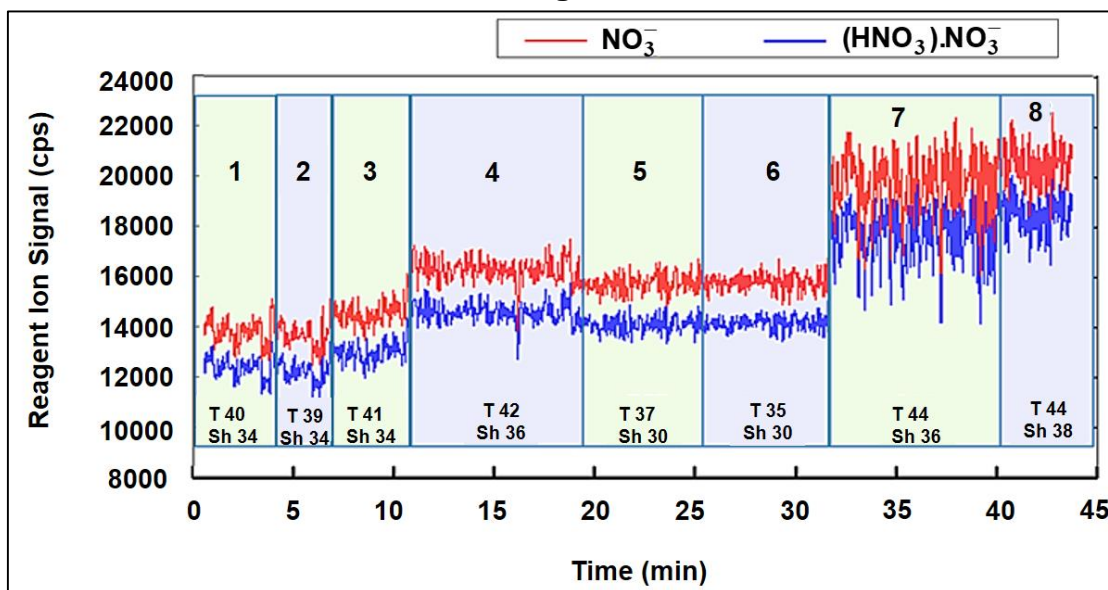


Figure 2.5. The two main reagent ions signal stability with different sets of total (T) and Sheath (Sh) flows.

This study allows us to conclude the importance of testing and choosing the right set of flow parameters, which depends on the instrument configuration and the sampling environment.

2.2.2. Effect of ion trajectory guiding voltages

The various components of the Tofwerk APi, previously discussed in Section 2.1, operate to efficiently transmit molecular ions and nitrate ion clusters that are formed in the CI inlet through the instrument to the detector. The distribution of the product ions between bare ions and ion clusters is influenced significantly by the operating voltages. By changing the electric potentials controlling the various elements, this ion distribution can be altered. The most critical regions of the APi are the first two chambers, the SSQ and BSQ, where collisional dissociation CD (declustering) can occur (Bertram et al., 2011). Collisional dissociation is responsible for breaking down clusters with low binding energy. This ensures that only stable clusters proceed to the ToFMS region for detection. Depending on the strength of CD, one may obtain a more or less complex mass spectrum. It is therefore crucial to control the extent of CD. A factor that affects stability of clusters is the nitrate ion cluster binding energy.

The two SSQ and BSQ chambers contain multiple components (as shown in Figure 2.6). This is why the voltages applied to such components must be adjusted in order to maximize the ion transmission and thus the instrument sensitivity, as well as controlling the peak shape and mass resolving power. Thuner (Tofwerk AG, Version 1.11.0.0) is an automatic optimization software program used to tune the voltages applied. It allows the user to establish relationships between the different components of the APi, which could be difficult by manual means. Table S.2.1 shows the Thuner derived set of voltages initially obtained by Aerodyne.

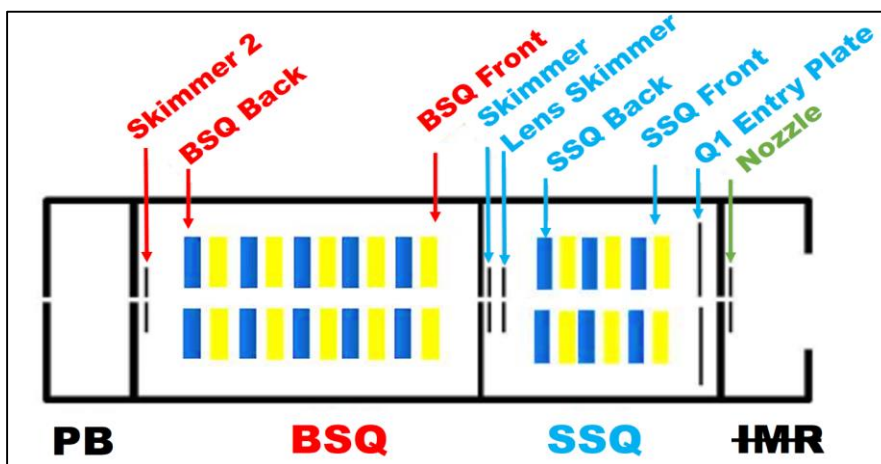


Figure 2.6. The Tofwerk APi schematic showing the SSQ, BSQ, and PB regions and their various components. A chemical nitrate ionization inlet replaces the IMR region within the scope of our work.

Using these values as a starting point, the voltages of the BSQ components were explored in various combinations with the goals of achieving both a proper mass resolution and a good sensitivity of the instrument. Hence, for the initial investigations, the voltages for the components in the other regions (SSQ, PB, and ToF) were held constant while varying the BSQ Back (BSQB) and the BSQ Front (BSQF) voltages. Experiments were conducted with different organic compounds, including pyruvic, succinic, tartaric, and oxalic acids. These tests were conducted under dry air conditions, with temperatures ranging from 25 to 70°C, depending on the specific organic compound being tested. However, only tests using oxalic and succinic acids will be presented here. The results obtained from the other two compounds, tartaric acid and pyruvic acid as well as another test involving oxalic acid, are presented in the supplementary information section of the manuscript (Supplementary material S.2.1).

2.2.2.a. Oxalic acid signals with different sets of voltages

These tuning tests were performed sampling a flow of oxalic acid $C_2H_2O_4$ leading to a mixing ratio of about 8.8 ppbv.

Figure 2.7.a. and Figure 2.8.a. show the behavior of the reagent ion signals with the change between 2 sets of voltages (Set 1: BSQF 6.2 and BSQB 5.7; Set 2 BSQF 7 and BSQB 7).

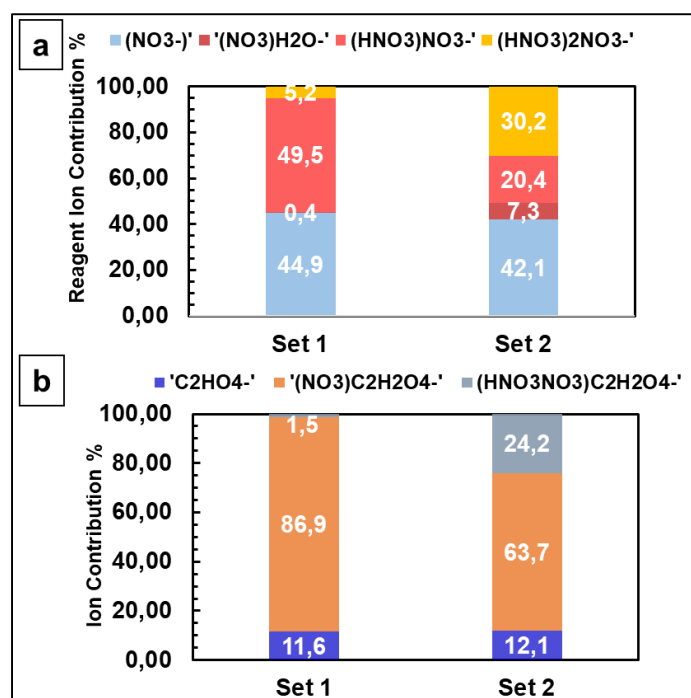


Figure 2.7.a. Percentage contributions of the reagent ions $(HNO_3)_{n=0-2} \cdot NO_3^-$ and $(NO_3) \cdot H_2O^-$. b. Percentage ion contributions of the deprotonated form $C_2HO_4^-$ and the two clusters $(NO_3) \cdot C_2H_2O_4^-$ and $(HNO_3NO_3) \cdot C_2H_2O_4^-$ for oxalic acid ion products. Numbers represent the ion contribution (%) for the various ions.

One can conclude that increasing the voltages of the two BSQ components has shifted the instrument to more efficiently transmit clusters. The contribution of two cluster ions, $(\text{HNO}_3)_2\cdot\text{NO}_3^-$ and $(\text{NO}_3)\cdot\text{H}_2\text{O}^-$, increased from 5% and 0.4% to approximately 30% and 7%, respectively, whereas $\text{HNO}_3\cdot\text{NO}_3^-$ contribution decreased from about 49% to 20%, while the signals of NO_3^- remained almost unchanged. This implies that reagent ions tend to form large clusters for the inlet conditions employed.

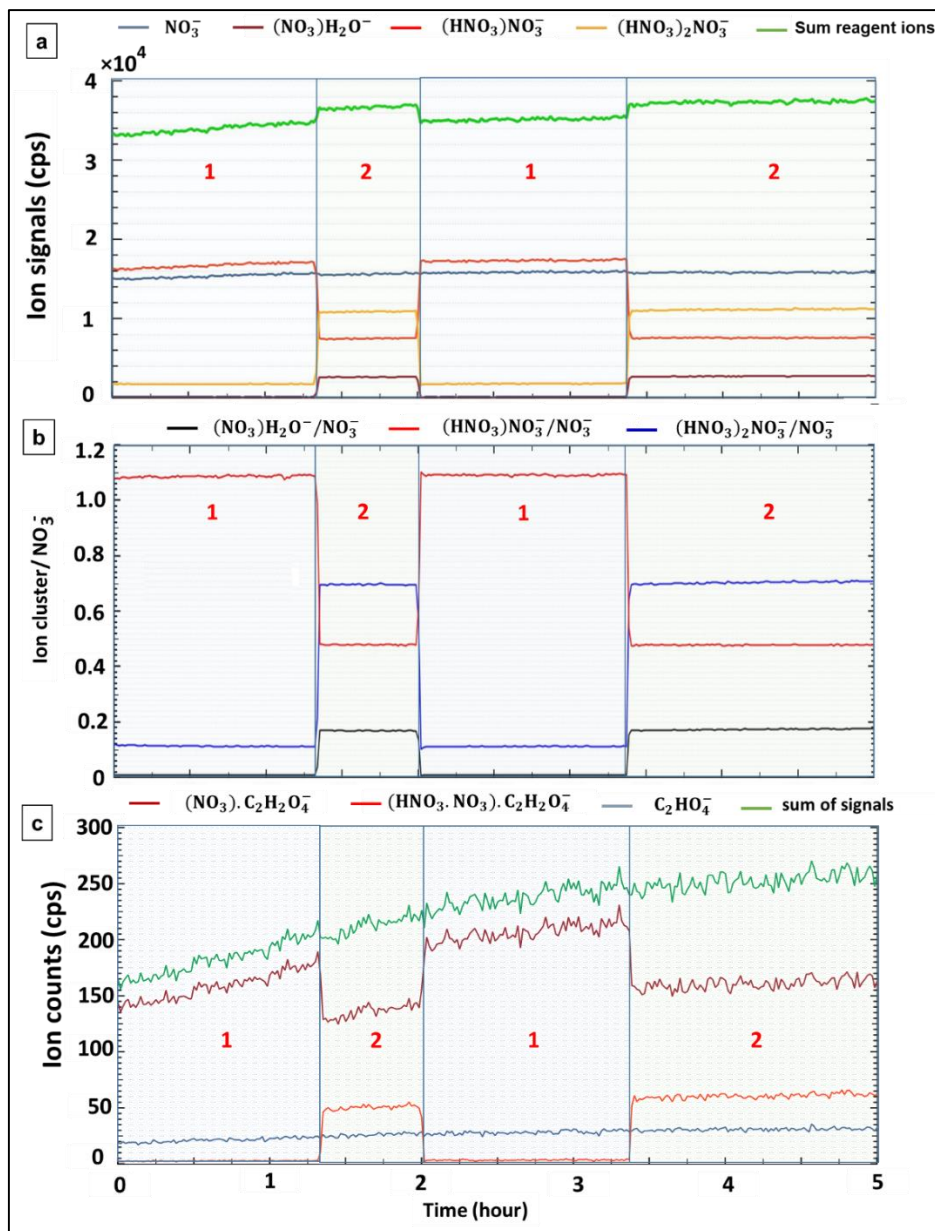


Figure 2.8.a. Signals of nitrate reagent ions according to the set of voltages tested on the instrument. b. Ratios of various nitrate reagent ion signals to NO_3^- as a function of the sets of voltages tested on the instrument. c. Signals of oxalic ions (both the deprotonated and the cluster forms) for the sets of voltages tested on the instrument.

Figure 2.8.b displays the ratio of reagent cluster ion signals to the signals of NO_3^- , indicating the constant values observed for a given species throughout a given applied set. In set 1, the ratio for

$\text{HNO}_3\cdot\text{NO}_3^-/\text{NO}_3^-$ was 1.1, indicating that its signals exceeded those of NO_3^- . The ratio $(\text{HNO}_3)_2\cdot\text{NO}_3^-/\text{NO}_3^-$ was approximately 0.1, indicating its lower importance compared to the two dominant ions, $\text{HNO}_3\cdot\text{NO}_3^-$ and NO_3^- . $(\text{NO}_3)\cdot\text{H}_2\text{O}^-/\text{NO}_3^-$ showed a negligible ratio value. However, when set 2 was applied, the $(\text{HNO}_3)_2\cdot\text{NO}_3^-/\text{NO}_3^-$ ratio became the highest, exceeding 0.7. On the other hand, the $\text{HNO}_3\cdot\text{NO}_3^-/\text{NO}_3^-$ ratio decreased significantly to 0.5, and the importance of $(\text{NO}_3)\cdot\text{H}_2\text{O}^-$ in the system increased, with a $(\text{NO}_3)\cdot\text{H}_2\text{O}^-/\text{NO}_3^-$ ratio of approximately 0.2. These observations indicate that the relative importance and contributions of various reagent ions within the system vary when different sets are applied, and emphasizing the value of utilizing the sum of the various reagent ions when normalizing the analyte signals.

As shown in Figure 2.7.b and Figure 2.8.c, changing the voltages affected the oxalic acid signals including the $(\text{HNO}_3\cdot\text{NO}_3)\cdot\text{C}_2\text{H}_2\text{O}_4^-$ cluster (m/z 214.97) with a contribution of 24% of total $\text{C}_2\text{H}_2\text{O}_4$ signals compared to 1% at lower voltages. C_2HO_4^- (m/z 88.98) bare ion signals remained unchanged with about 12% of total $\text{C}_2\text{H}_2\text{O}_4$ signals from both sets 1 and 2 whereas $(\text{NO}_3)\cdot\text{C}_2\text{H}_2\text{O}_4^-$ (m/z 151.98) decreased slightly to 64% compared to 87% of total contribution. Note that within the first 2 hours of the experiments (set 1 and set 2), the oxalic ion signals were still stabilizing but still gave almost the same information as the repeated tests. Hence, the ratios of $(\text{HNO}_3\cdot\text{NO}_3)\cdot\text{C}_2\text{H}_2\text{O}_4^-/(\text{NO}_3)\cdot\text{C}_2\text{H}_2\text{O}_4^-$ were observed to increase upon change from Set 1 to Set 2 (0.02 to 0.37) as did the ratios of $\text{C}_2\text{HO}_4^-/(\text{NO}_3)\cdot\text{C}_2\text{H}_2\text{O}_4^-$ (0.14 to 0.20).

Furthermore, the sum of all oxalic ion signals from these tests were very similar, differing by only 0.5%. This means that regardless the distribution of the various oxalic acid-containing ions, one should obtain the same sensitivity factor. From these first experiments (repeated later to ensure reproducibility), it may be concluded that increasing the voltage applied to the components of this chamber may ensure more collisions between the different reactive ions and also between these and the molecule of interest, which favors the formation of larger ion clusters. However, it should be noted that when the voltages reach sufficiently bigger difference, collisions between ions can lead to fragmentation (declustering). This may consequently make the interpretation of the mass spectrum a more difficult task. As a preliminary conclusion, since both sets of experiments showed unchanged sensitivity to total oxalic ions, one could state that choosing Set 1 is the most suitable option to achieve a less complex mass spectrum, because in the real atmosphere, the instrument will probably detect a large number of chemical compounds.

2.2.2.b. Succinic acid signals with different sets of voltages

Tests were conducted with addition of $C_4H_6O_4$ (succinic acid) to a mixing ratio of 7.42 ppbv into the instrument. Before proceeding, we waited for the signals to stabilize. Afterwards, four different sets of voltages (Table 2.3 below) were applied to the system.

Table 2.3. Set of Voltage configuration.

Components	Set 1 (V)	Set 2 (V)	Set 3 (V)	Set 4 (V)
Skimmer	2.1	2.1	4	4
BSQ front	6.2	7	6.2	5.7
BSQ back	5.7	7	5.7	6.2

As depicted in Figure 2.9.a and Figure 2.10.a, the transition from Set 1 to Set 2 has shifted the instrument to a more cluster transmission regime but to a somewhat lesser extent, where both cluster $(HNO_3)_2 \cdot NO_3^-$ and $(NO_3) \cdot H_2O^-$ contribution showed an increase from approximately 5% and 0.3% to 21% and 4.5%, respectively, whereas the contribution $HNO_3 \cdot NO_3^-$ ions decreased from about 48% to 25% (Figure 2.10.a). However, the signals of NO_3^- slightly increased by a factor of 1.1 (from about 46% to 49%). This suggests that indeed at higher voltages, the reagent ions tend to form larger clusters, but also that if the voltages are high enough, collisions between ions can cause fragmentation inside the chamber, as was also seen in the tests with oxalic acid, discussed above. Set 2 enabled the appearance of the $(HNO_3 \cdot NO_3) \cdot C_4H_6O_4^-$ cluster (m/z 243.011) with a contribution of 21% of the total $C_4H_6O_4$ signal compared to 2% at Set 1. $C_4H_5O_4^-$ (m/z 117.019) bare ion signals varied slightly with about 11% of total $C_4H_6O_4$ signals from both sets 1 and 2 whereas $(NO_3) \cdot C_4H_6O_4^-$ (m/z 180.015) decreased slightly to 68% compared to 88% of total contribution (Figure 2.10.b.).

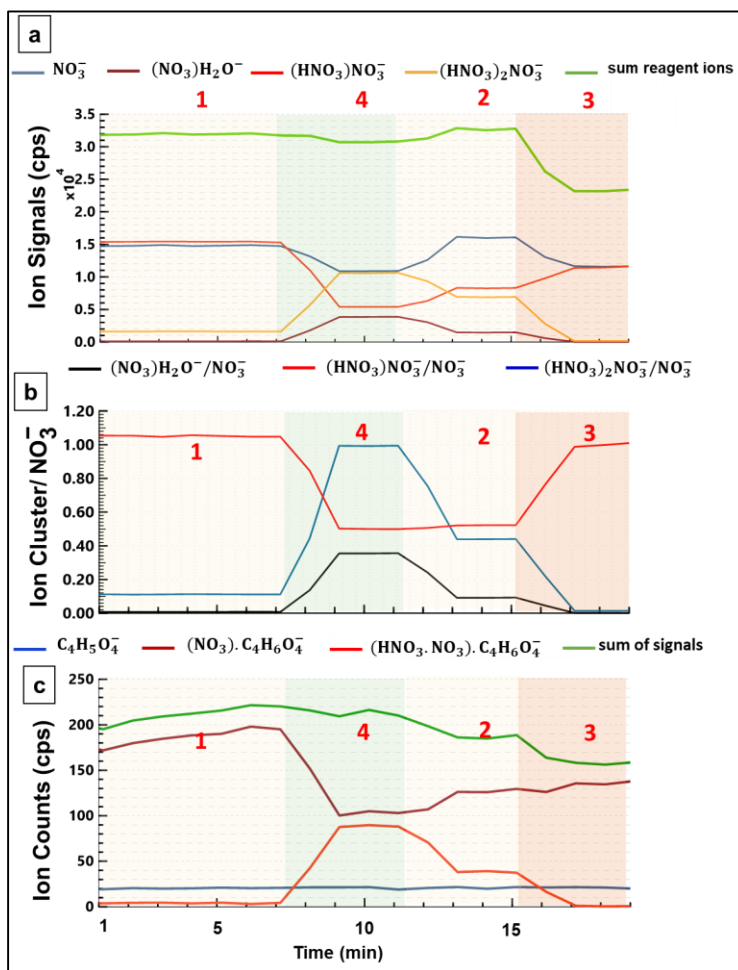


Figure 2.9.a. Signals of nitrate reagent ions according to the set of voltages tested on the instrument (Table 2.3). b. Ratios of various nitrate reagent ion signals to NO_3^- as a function of the sets of voltages tested on the instrument. c. Signals of succinic ions (both the deprotonated and the cluster forms) for the sets of voltages tested on the instrument.

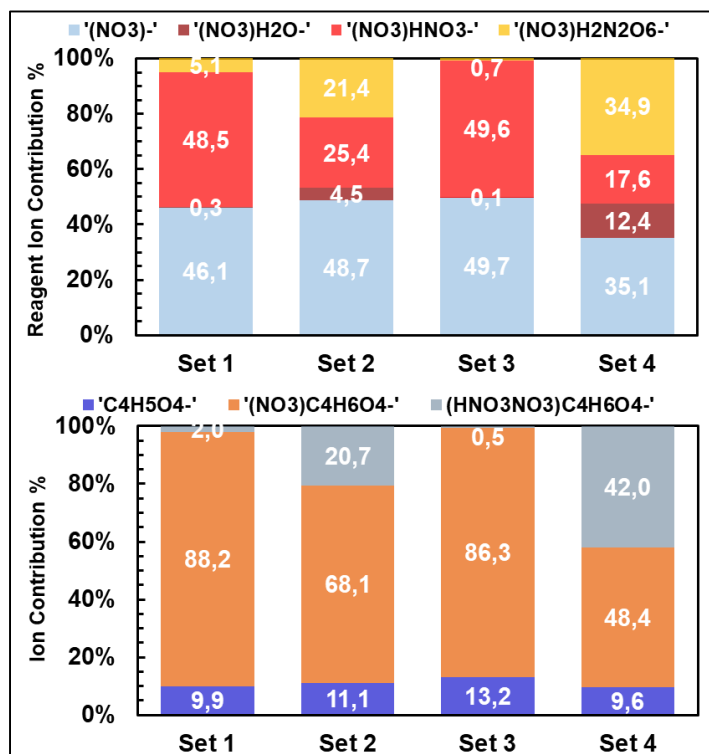


Figure 2.10.a. Percentage contributions of the reagent ions $(\text{HNO}_3)_{n-0.2}\text{NO}_3^-$ and $(\text{NO}_3)\cdot\text{H}_2\text{O}^-$. b. Percentage ion contributions of the deprotonated form $\text{C}_4\text{H}_5\text{O}_4^-$ and the two clusters $(\text{NO}_3)\cdot\text{C}_4\text{H}_6\text{O}_4^-$ and $(\text{HNO}_3\text{NO}_3)\cdot\text{C}_4\text{H}_6\text{O}_4^-$ for succinic acid ion products. Numbers represent the ion contribution (%) for the various ions.

Two additional sets 3 and 4 were tested, employing the same skimmer voltage (4 V) but with a reversal of the BSQF and BSQB voltages at 6.2 and 5.7 V to 5.7 and 6.2 V (Table 2.3). The modification from set 3 to set 4 can shift the instrument to a larger cluster formation regime evidenced by the significant increase in both cluster $(\text{HNO}_3)_2\cdot\text{NO}_3^-$ and $(\text{NO}_3)\cdot\text{H}_2\text{O}^-$ signals, from 0.7% and 0.1% to 35% and 12%, respectively, whereas $\text{HNO}_3\cdot\text{NO}_3^-$ signals decreased by almost a factor of 3 (Figure 2.10.a.). However, the NO_3^- signal decreased from about 50% to 35%. One can conclude a similar contribution of both $(\text{HNO}_3)_2\cdot\text{NO}_3^-$ and NO_3^- which is further shown in Figure 2.9.b with a ratio value of $(\text{HNO}_3)_2\cdot\text{NO}_3^-/\text{NO}_3^-$ equal to about 1. The same reagent ion contribution was also observed in the tests of the 4 set of voltages including oxalic acid (supplement S.2.1.2).

Set 4 increased the abundance of the $(\text{HNO}_3\text{NO}_3)\cdot\text{C}_4\text{H}_6\text{O}_4^-$ cluster with a contribution of 42% of total $\text{C}_4\text{H}_6\text{O}_4$ signals compared to 0.5% at Set 3. This is consistent with the significant increase of $(\text{HNO}_3)_2\cdot\text{NO}_3^-$ clusters. $\text{C}_4\text{H}_5\text{O}_4^-$ bare ion signals slightly decreased to 9% compared to 13% of total $\text{C}_4\text{H}_6\text{O}_4$ signals using Set 3. $(\text{NO}_3)\cdot\text{C}_4\text{H}_6\text{O}_4^-$ also decreased to 48% compared to 87% of total contribution (Figure 2.10.b.).

In order to simplify the mass spectra, the focus is thus either on set 1 or set 3 both yielding negligible second ion cluster $(\text{HNO}_3\text{NO}_3)\cdot\text{C}_4\text{H}_6\text{O}_4^-$. The only voltage difference being the electric

field applied to the skimmer, leading to different ΔV between the BSQF and the skimmer ($\Delta V_1=4.1$ and $\Delta V_3=2.2$). To determine whether set 1 or 3 would be more suitable, the sensitivity towards total $C_4H_6O_4$ ion signals were compared and are summarized for the 4 sets in Table 2.4. The relative difference between the two calibration factors for $C_4H_6O_4$ is not very significant (about 10%). Therefore, set 1 is selected for the operating voltage conditions. It is important to notice that lower calibration factor means higher sensitivity to justify this choice.

Table 2.4. Calibration factors obtained for succinic acid for the various sets of applied voltages.

Set of voltages	Calibration factor (molecules.cm ⁻³)
1	1.68×10^{13}
2	2.22×10^{13}
3	1.87×10^{13}
4	1.69×10^{13}

2.2.3. Single-ion-signal setup

Initially, the ion signals (count.s⁻¹, cps) are derived by normalizing ion peak areas using the value of the so-called single ion signal (SIS), representing the MCP detector's response to single ion (SI) detection events, representing the signal generated from a SI striking the detector in a given time window, with units of mV.ns (Bertram et al., 2011; Khattatov, 2019). To measure this value, data are recorded with the pulsers disabled (held at 0V). Under these conditions, the MCP detector detects scattered background ions. Ion events are distinguished from electronic noise based on a user-adjustable threshold. The voltage of the MCP detector is adjusted to obtain a specific value of the SIS for optimal performance. An increase in the voltage of the MCP detector will be required occasionally as it ages, in order to maintain the SIS and thus prevent mass discrimination as a result of its aging (Müller et al., 2014; Yuan et al., 2016). Mass discrimination is the relative difference in the detection efficiency of ions with different m/z values, arising from several factors including the variation of the MCP operational parameters (Müller et al., 2014). It is recommended maintaining a SIS of about 2.75 mV.ns for the optimal use. This adjustment is automatically achieved every 6 months, using the instrument operation software (Acquility) (Tofwerk, 2016).

2.2.4. Discussion

According to the specific sampling location, the sample flow rate was set (discussed above). The latter is determined by the choice of the total and the sheath flow rates. In addition, the reagent ion signals obtained by varying the flow settings were explored and were found to exhibit more stable signals at lower total flows. This may be explained by the fact that high air flows could cause turbulence and possibly other environmental interferences. The effects of BSQ voltages on the ion

distribution were also investigated and showed that increasing these voltages can shift the instrument to the clustering mode which, depending on the molecule, may lead to a lower sensitivity and a more complex mass spectrum. Set 1 (BSQF 6.2V; BSQB 5.7V and Skimmer 2.1V) was thus selected for further laboratory and field studies. Under these conditions, the majority of the compounds that were tested were found to strongly bond with NO_3^- leading to the formation of stable clusters. Also, the increase in the presence of the $(\text{HNO}_3)_2 \cdot \text{NO}_3^-$ cluster is correlated with the greater formation of $(\text{HNO}_3 \cdot \text{NO}_3) \cdot \text{HX}^-$ cluster. The results also show the contribution of deprotonation as these acids may have relatively large gas-phase acidities (compared to that of nitric acid). For our instrumental conditions, the deprotonated forms of $\text{C}_2\text{H}_4\text{O}_2$, $\text{C}_3\text{H}_4\text{O}_3$ and $\text{C}_4\text{H}_6\text{O}_4$ had relatively small contributions of 12 %, 17% and 10%, respectively. Signals from $\text{C}_4\text{H}_6\text{O}_6$ were about half from deprotonation, which may indicate a lower gas phase acidity. The available literature does not provide quantitative values for the gas phase acidity of $\text{C}_4\text{H}_6\text{O}_6$, making it challenging to explain the observed results in terms of specific gas phase acidity values. Overall, the results may help explain the reason that HOMs, that contain multiple hydroperoxy functional groups, form stable clusters with NO_3^- and are mostly detected as $\text{HOM} \cdot \text{NO}_3^-$ clusters.

2.3. Instrument Sensitivity and calibration

The approach to quantify HOMs under normal sampling conditions is generalized by Equation 2.4.

$$[\mathbf{X}] = \mathbf{C}_X \times \frac{\mathbf{i}_X^- + \sum_{n=0-2} \mathbf{i}_{\text{HX}(\text{HNO}_3)_n \text{NO}_3^-}}{\mathbf{i}_{\text{NO}_3^-} + \mathbf{i}_{(\text{HNO}_3)\text{NO}_3^-} + \mathbf{i}_{(\text{HNO}_3)_2 \text{NO}_3^-} + \mathbf{i}_{(\text{H}_2\text{O})\text{NO}_3^-}} \quad \text{Equation 2.4}$$

Where, $[\mathbf{X}]$ is the concentration of the measured compound X, \mathbf{C}_X is the calibration coefficient (molecules-cm⁻³/ion ratio) reflecting the sensitivity of the instrument to X, \mathbf{i}_X^- is the ion signal of the bare product ion, $\sum_{n=0-2} \mathbf{i}_{\text{HX}(\text{HNO}_3)_n \text{NO}_3^-}$ is the sum of the product ion cluster signals, and $\mathbf{i}_{\text{NO}_3^-} + \mathbf{i}_{(\text{HNO}_3)\text{NO}_3^-} + \mathbf{i}_{(\text{HNO}_3)_2 \text{NO}_3^-} + \mathbf{i}_{(\text{H}_2\text{O})\text{NO}_3^-}$ is the sum of reagent ion signals for NO_3^- , $(\text{HNO}_3) \cdot \text{NO}_3^-$, $(\text{HNO}_3)_2 \cdot \text{NO}_3^-$ and $\text{H}_2\text{O} \cdot \text{NO}_3^-$.

Normalization by the signal of reagent ions, is essential to correct for variations in ionization efficiency and other instrument performance related changes.

In the mass spectra, HOM species are predominately detected as clusters with NO_3^- . However, as mentioned above, this does not explain the entire ion chemistry that occurs within the inlet and the mass spectrometer instrument. Therefore, all forms of the reagent ion (nitrate plus clusters with nitric acid) were considered.

It was discussed above that studies conducted in the laboratory have shown that the degree of clustering depends on the target molecule and on the voltage settings within the instrument. This

also explains the inclusion of the sum of $(\text{HNO}_3)_{n=0-2}\text{NO}_3\cdot\text{HX}^-$ signals in the general equation. The results of these studies will be further discussed in a later section.

In addition, because the $\text{H}_2\text{O}\cdot\text{NO}_3^-$ clusters were identified in the mass spectra and showed a change with sampling humidity conditions, their signals were included in the calculations, although the effects are small compared to the primary reagent ions.

As small organic compounds were found to exist in both deprotonated and clustered forms, the equation contains their corresponding ion signals.

A calibration of the NO_3^- ToFCIMS is thus required to determine its sensitivity to an organic molecule, denoted X, thereby determine the C_X factor necessary in the calculation of the molecule's concentration [X]. To date, there is no direct calibration method capable of evaluating all possible organic compounds.

In this section, the conventional methods used to estimate C_X will briefly be presented. This is followed by a discussion of an experimental protocol applied to organic calibrants and sulfuric acid together with the results obtained.

2.3.1. Conventional methods and challenges

Since the NO_3^- ToFCIMS can detect a wide range of low volatility multifunctional organic species, it is rather difficult to find suitable oxygenated organic standards to determine the appropriate calibration coefficients, particularly since the synthesis of these molecules can be difficult and the precise structures of many HOMs remain unknown at present. Proper C_X values are essential to quantify HOMs concentrations following Equation 2.4. To determine appropriate C_X values, a known concentration of a compound must be sampled. The C_X value is then obtained as the slope of the plot depicting the known concentration as a function of the normalized ion product signals. The most common method used in literature relies on the use of H_2SO_4 as calibrant, whose use assumes it has the same ionization efficiency as HOMs (Ehn et al., 2014; Kirkby et al., 2016). This assumption is based on quantum chemical calculations performed by Ehn et al., 2014, who found that the collision frequencies of $(\text{HNO}_3)_{n=0-2}\cdot\text{NO}_3^-$ with HOMs (designated as ELVOCs in the reference), are equal to that of nitrate clusters with H_2SO_4 , providing a lower limit to the reported concentration of ELVOCs ($k_{i\text{onHOM}}=(1.5-2.8)\times 10^{-9} \text{ cm}^3\text{s}^{-1} \approx k_{i\text{onH}_2\text{SO}_4}=(1.5-2.5)\times 10^{-9} \text{ cm}^3\text{s}^{-1}$). In addition, the ion transmission efficiencies (ITE), reflecting the percentage of the ions sampled that reach the detector, most likely differ with mass and type of molecule (Heinritzi et al., 2016). Using a C_X value determined for H_2SO_4 adds uncertainty to the values obtained. It is also worth

mentioning that in the current definition, some HOMs are classified as ELVOCs, but not all ELVOCs are HOMs (Bianchi et al., 2019).

In brief, calibrations using sulfuric acid are commonly achieved by generating a known amount of OH· in an excess of SO₂ (Berndt et al., 2014). Most studies are based on a dedicated set-up developed to calibrate a NO₃⁻ CI quadrupole MS (CI-QMS) with H₂SO₄. This system was estimated to give an overall uncertainty of around 33% (Eisele and Tanner, 1993; Kürten et al., 2012). Furthermore, Jokinen et al., 2012 presented the first C_X values (Table 2.5) obtained by comparing H₂SO₄ measured in ambient air by a ToFCIMS to concentrations measured by a calibrated CIMS.

Other direct calibrations have been reported in the literature, using other organic compounds such as perfluorinated heptanoic acid C₇HF₁₃O₂ (Ehn et al., 2014), malonic acid C₃H₄O₄ (Krechmer et al., 2015; Isaacman-VanWertz et al., 2018; Massoli et al., 2018), and 4-nitrophenol C₆H₅NO₃ (Cheng et al., 2021). Values of C_X are also corrected by a transmission factor of the sampling apparatus and the calculated concentrations are prone to large overall uncertainties (typically ±50%) from the measurement and calculations (Ehn et al., 2014).

Table 2.5. Reported calibration factors in the literature using a NO₃⁻ ToFCIMS.

Reference	Calibration coefficient (molecule/cm ³)	Calibrant
Jokinen et al., 2012	5 × 10 ⁹ 1.89 × 10 ¹⁰	H ₂ SO ₄
Ehn et al., 2014	1.6 × 10 ¹⁰	C ₇ HF ₁₃ O ₂
Rissanen et al., 2014	1.94 × 10 ¹⁰	H ₂ SO ₄
Berndt et al., 2015, 2016; Jokinen et al., 2014, 2015	1.85 × 10 ⁹	H ₂ SO ₄
Krechmer et al., 2015 Massoli et al., 2018	7.9 × 10 ¹⁰	C ₃ H ₄ O ₄
Mutzel et al., 2015	8.4 × 10 ⁹	H ₂ SO ₄
Kirkby et al., 2016	6.5 × 10 ⁹	H ₂ SO ₄
Kürten et al., 2016	6 × 10 ⁹	H ₂ SO ₄
Riva, 2019	2 × 10 ¹⁰	H ₂ SO ₄
Quéléver et al., 2019	1.65 × 10 ⁹	H ₂ SO ₄
Pullinen et al., 2020	3.7 × 10 ¹⁰	H ₂ SO ₄
Shen et al., 2021 Zhao et al., 2021 Guo et al., 2022 Luo et al., 2023	2.5 × 10 ¹⁰	H ₂ SO ₄
Cheng et al., 2021	1.66 × 10 ¹⁰ 1.62 × 10 ¹⁰	4-nitrophenol H ₂ SO ₄
Xu et al., 2021	1.57 × 10 ¹⁰ 2 × 10 ¹⁰	H ₂ SO ₄
Dam et al., 2022	6 × 10 ¹⁰	H ₂ SO ₄
Wang et al., 2022	1.1 × 10 ¹⁰	H ₂ SO ₄

In addition, many studies use a C_X value from the literature, which implies larger uncertainties (Zha et al., 2018; Wang et al., 2020; Garmash et al., 2020; Meder et al., 2022; Zhang et al., 2022). Heinritzi et al. (2016) showed the importance of estimating the mass-dependent transmission efficiency of a NO_3^- ToFCIMS and the need to apply a correction factor to C_X values. In this publication, they demonstrated a consistent rise in the ITE for the m/z range up to 500, with substantial discrepancy of approximately 25%. Calibration coefficients also proved to be specific to the APi-ToF internal component voltage settings as well as the inlet conditions, such as sampling tube lengths and flow rates (Heinritzi et al., 2016; Kirkby et al., 2016).

Although the reported calibration factors were obtained under different experimental conditions, they generally exhibit a reasonably good level of agreement.

2.3.2. Experimental protocol and results

2.3.2.1. Experimental protocol

In an effort to find a more direct calibration method for the NO_3^- ToFCIMS, potential organic calibrants, consisting mainly of di-carboxylic acids, were selected to evaluate the sensitivity and response of the instrument and are summarized in Table 2.6. These are selected based on their ability to handle safely, their low-to-moderate cost, and readily availability. Table S.2.4 in Supplement S.2.2 includes the chemical structures of the compounds cited in Table 2.6.

Most of these compounds exist as solids at room temperature, exhibiting lower volatility in comparison to many liquid or gas compounds. Consequently, it becomes challenging to identify suitable techniques that primarily involve higher temperatures to encourage their evaporation into the gas phase. Determining the appropriate heating temperature becomes critical in such cases, as organic compounds are often more susceptible to thermal degradation or decomposition than inorganic compounds. This makes direct calibration a more challenging task. Two different calibration approaches were implemented and are discussed in sub-sections 2.3.2.1.A and 2.3.2.1.B. Another approach has been developed to determine the experimental value of the vapor pressure (P_{vap}) for certain solid organic compounds (e.g. malonic acid), which is discussed in sub-section 2.3.2.1.C.

Table 2.6. Candidate organic compounds used to evaluate the sensitivity of the instrument. The yielding response (+ = detected, - = not detected) is based on the appropriate heating temperature. *Upon heating, this compound exhibits color changes, indicating decomposition.

Compound	MW (g.mol ⁻¹)	Chemical structure	Yielding response
Propanoic Acid	74.08	C ₃ H ₆ O ₂	+
Pyruvic Acid	88.06	C ₃ H ₄ O ₃	+
Oxalic Acid	90.03	C ₂ H ₂ O ₄	+
Lactic acid	90.08	C ₃ H ₆ O ₃	+
Malonic Acid	104.06	C ₃ H ₄ O ₄	+
Succinic Acid	118.09	C ₄ H ₆ O ₄	+
2-acetoxypropionic Acid	132.11	C ₅ H ₈ O ₄	-
Glutaric Acid	132.12	C ₅ H ₈ O ₄	-
Salicylic Acid	138.12	C ₇ H ₆ O ₃	-
Adipic Acid	146.14	C ₆ H ₁₀ O ₄	-
Tartaric Acid	150.08	C ₄ H ₆ O ₆	+
2,5-dihydroxy Benzoic Acid	154.12	C ₇ H ₆ O ₄	-
4-nitrocatechol	155.11	C ₆ H ₄ NO ₄	+
Cis-cyclopentane-1,2-dicarboxylic Acid	158.15	C ₇ H ₁₀ O ₄	-
Benzenesulfonic Acid	158.17	C ₆ H ₆ O ₃ S	+*
Piperonylic Acid	166.13	C ₈ H ₆ O ₄	-
Phtalic Acid	166.14	C ₈ H ₆ O ₄	-
Dehydroacetic Acid	168.14	C ₈ H ₈ O ₄	-
t-aconitic Acid	174.11	C ₆ H ₆ O ₆	-
Suberic Acid	174.2	C ₈ H ₁₄ O ₄	-
Citric Acid	192.12	C ₆ H ₈ O ₇	-
Sebacic Acid	202.25	C ₁₀ H ₁₈ O ₄	-
1,2,4-benzenetricarboxylic Acid	210.14	C ₉ H ₆ O ₆	-
1,2,3,4-butanetetracarboxylic Acid	234.16	C ₈ H ₁₀ O ₈	-
1,1,2 Ethane Triethylcarboxylate	246.26	C ₁₁ H ₁₈ O ₆	-
Mellitic Acid	342.17	C ₁₂ H ₆ O ₁₂	-
Agaric Acid	416.55	C ₂₂ H ₄₀ O ₇	-

2.3.2.1.A. Compound screening - Approach 1

The selected organic compounds, in the form of solid powder, are placed in ¼ inch outside diameter stainless steel tubes. The compounds are confined by filters, composed of stainless steel grids or glass wool, on each end that serve to keep solid materials from entering the instrument (see Figure 2.11.b). This tube, designated as the source tube (ST), is heated using a temperature controller to a fixed temperature whose value depends on the compound and falls within the range of 20 to 90°C. Heating serves to increase the gas phase vapor pressure of the compound. The choice of temperature varies with the compound being studied and is determined through experimental testing. These tests involve gradually increasing the temperature while measuring with the instrument, and ensuring that the compound does not decompose. Additionally, it was observed

that the signals from the reagent ions began to diminish beyond a certain temperature. Therefore, selecting an appropriate heating temperature is of utmost importance.

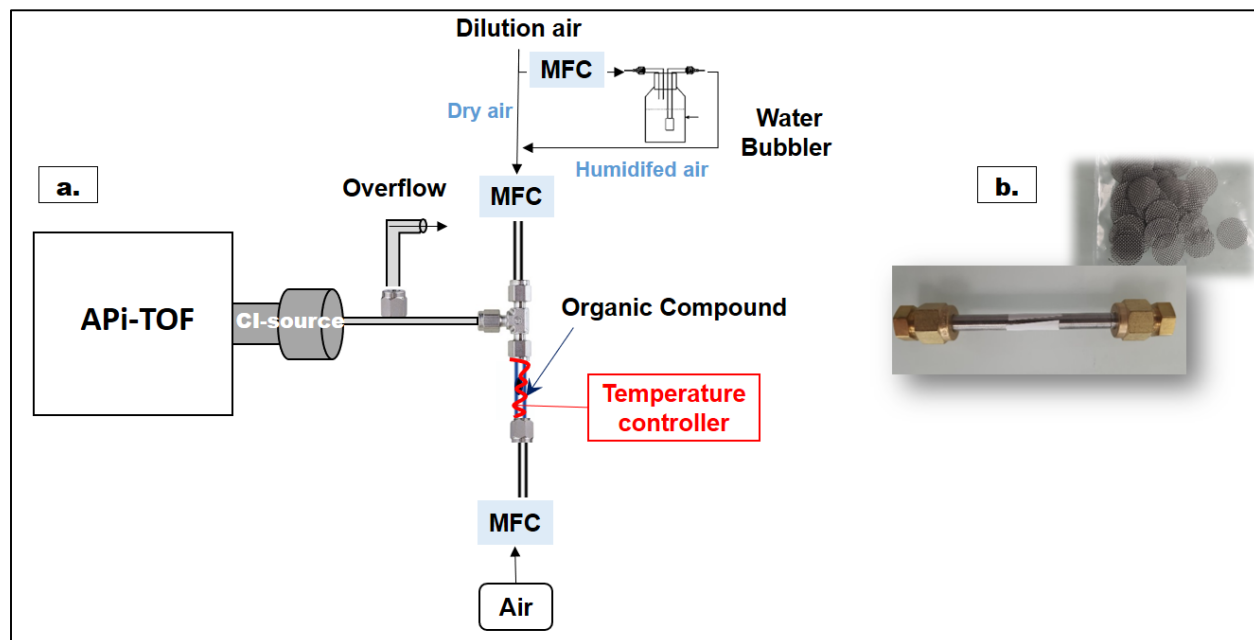


Figure 2.11. Experimental set-up used for NO_3^- ToFCIMS calibration with organic compounds. b. Stainless steel grids and tube containing the organic compound.

Subsequently, the vaporized compounds are transferred out of the ST by a regulated flow of synthetic air (100 to 500 sccm) controlled by a calibrated mass flow controller (MFC). The flow is diluted by additional dry zero air that controls the final concentration and provides excess flow to the inlet (see Figure 2.11.a). For experiments investigating the effects of relative humidity (RH) on the instrument performance, humidification of zero air was accomplished using a water bubbler filled with purified water. The humidified air flow rate is controlled using a separate MFC, allowing a range of RH levels to be produced by varying the ratio of wet to dry air flow rates.

Not all the compounds listed in Table 2.6 were detectable by the instrument regardless of the ST temperature or flow. The instrument was found to respond to the following organic compounds: propionic, pyruvic, lactic, oxalic, succinic, tartaric, malonic acids, as well as 4-nitrocatechol (the only tested nitrophenol). Consequently, additional research was performed on these compounds. Other compounds of Table 2.6 were not detectable by the NO_3^- ToFCIMS.

Using the approach 1 described above, concentrations produced and injected into the ToFCIMS were calculated based on Equation 2.5.

$$[\text{OC}](\text{ppbv}) = \frac{F_{\text{OC}}(\text{sccm}) \times P_{\text{vap}}(\text{Pa})}{(F_{\text{OC}}(\text{sccm}) + F_{\text{diluent}}(\text{sccm})) \times P_{\text{atm}}(\text{Pa})} \times 10^9 \quad \text{Equation 2.5}$$

Where, [OC] is the concentration of the organic compound, in ppbv, F_{OC} is the flow through the ST, in standard $\text{cm}^3 \cdot \text{min}^{-1}$ (sccm), P_{vap} is the vapor pressure of the organic compound, in Pa, at the ST temperature employed, F_{diluent} is the dilution flow, in sccm, and P_{atm} is the ambient pressure, in Pa.

The overall formula is multiplied by 10^9 to convert the concentration to ppbv. For these experiments, vapor pressures are obtained either experimentally (see section 2.3.2.1.c) or extracted from literature.

The P_{vap} of a compound at a specific temperature T_2 was calculated using the Clausius–Clapeyron Equation (Equation 2.6) by using a known value of the P_{vap} at a reference T_1 and either the enthalpy of vaporization for a liquid or the enthalpy of sublimation for a solid compound, as appropriate.

$$\ln\left(\frac{P_2}{P_1}\right) = \frac{\Delta H_{\text{vap/sub}}}{R} \times \left(\frac{1}{T_1} - \frac{1}{T_2}\right) \quad \text{Equation 2.6}$$

Where, P_1 and P_2 are the vapor pressures at temperatures T_1 and T_2 , respectively, and $\Delta H_{\text{vap/sub}}$ is the enthalpy of vaporization or sublimation; R is the gas constant ($8.314 \text{ J mol}^{-1} \text{ K}^{-1}$).

2.3.2.1.B. Compound screening - Approach 2

The experimental methodology of Approach 2 consists of the two main elements:

- An atmospheric simulation chamber, the CSA chamber (at LISA), which is a cylindrical Pyrex reactor (volume: 977 L, length: 6 m, diameter: 45 cm) designed for the study of atmospheric gas processes under controlled conditions. It is also equipped with instrumentation for analysis using ultraviolet/visible and infrared spectroscopy (Doussin et al., 1997; Picquet-Varrault et al., 2005).

For our experimental studies, a FTIR spectrometer (Bruker Vertex 80) instrument was used, that is capable a maximum spectral resolution of 0.5 cm^{-1} and an optical path length of 214 m (the method will be discussed in detail in Chapter 3).

- A vacuum line coupled to a bulb of known volume (0.3 L) was used to prepare gaseous OCs from liquid standards to inject into the chamber (Figure 2.12). The basic principle relies on placing the compound in a glass finger connected to the vacuum line which is immersed in a cold trap of liquid nitrogen and is then pumped to remove volatile impurities. Then, after isolating the pump, the finger is brought up to room temperature allowing the evaporation of the compound into the bulb.

The concentration of the compound injected into the chamber is calculated as follows:

$$[\text{OC}] (\text{ppbv}) = \frac{(P_{f,\text{bulb}} - P_{i,\text{bulb}}) \times V_{\text{bulb}}}{P_{\text{CSA}} \times V_{\text{CSA}}} \times 10^9 \quad \text{Equation 2.7}$$

Where, $P_{i,\text{bulb}}$ is the initial bulb pressure (limit vacuum around 10^{-4} mbar), $P_{f,\text{bulb}}$ is the final bulb pressure, P_{CSA} is the CSA chamber pressure, V_{bulb} and V_{CSA} are the bulb and CSA chamber volumes, respectively.

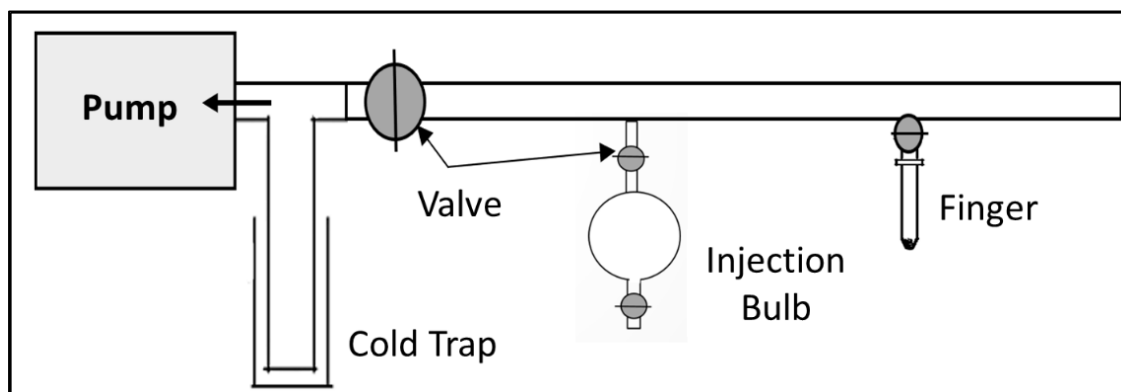


Figure 2.12. Vacuum line for the preparation of the compounds injected into the simulation chamber.

The principle of this approach is based on different steps, summarized in Figure 2.13:

- 1- Fill the CSA with nitrogen gas to reach a pressure slightly higher than ambient pressure; ($\Delta P = P_{\text{CSA}} - P_{\text{atm}} \approx 5$ mbar)
- 2- Injecting one of the liquid organics, (e.g. Pyruvic acid) into the chamber, by passing synthetic air through the bulb;
- 3- Collect FTIR spectra and ensure the stabilization of the corresponding signal;
- 4- The chamber contents are diluted as they are sampled by the NO_3^- ToFCIMS (sampling at around 6 lpm), through a heated stainless steel line ($\sim 40^\circ\text{C}$);
- 5- Additional dilution is applied by introducing N_2 into the chamber at a rate that maintains the chamber pressure by using a pumping system (total dilution flow rate around 23 lpm);
- 6- Collect signals of the compounds by NO_3^- ToFCIMS;
- 7- Compare the normalized ion counts of the OC obtained by the NO_3^- ToFCIMS to the concentration obtained from the FTIR data treatment in order to obtain a calibration factor.

It should also be noted that this approach was not appropriate for the tested solid compounds because of their low vapor pressures and the high detection limits for the FTIR. These tests were carried out in dry conditions.

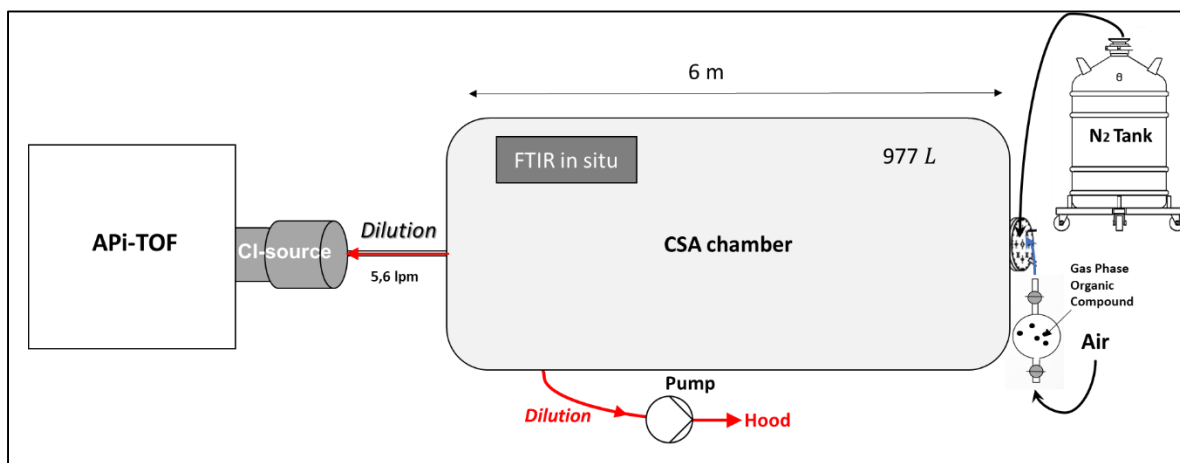


Figure 2.13. The experimental setup to deduce the sensitivity of NO_3^- ToFCIMS to an organic compound from its concentration derived by FTIR spectrometry using the CSA chamber.

The Analysis of Infrared Spectra (ANIR) software was used to process the FTIR spectra. It is based on a classic fitting routine of the spectra. For that, reference spectra of the compound in question must be available with known optical path $L(\text{cm})$, reference concentration of the absorbing species C ($\text{molecule}\cdot\text{cm}^{-3}$), and thus the effective absorption cross sections as a function of wavelength or wavenumber, $\epsilon(\lambda)$.

It is important to note that the total uncertainty (in %) mentioned in the subsequent results encompasses all the uncertainties associated with the components used to calculate C_x (e.g. ion signals, MFC, P_{vap} , $\Delta H_{\text{vap/sub}}$, etc.).

2.3.2.1.C. Experimental Determination of Vapor Pressure for Malonic Acid

A set of experiments was conducted in the laboratory to find an experimental value of the P_{vap} of malonic acid (a solid at room temperature). The experiment is described as follows:

- The first step consists of flowing 300 sccm of air through the ST, which is heated to 50°C and connected to the instrument. It was left running for a week or more so that a measurable loss of mass could be determined using a very sensitive analytical balance (accuracy 0.1 mg).
- The vapor pressure of the compound could then be deduced using Equation 2.8 that is obtained from the ideal gas equation. This experiment was performed 3 times.

$$P_{\text{vap}_{\text{exp}}} = \frac{\Delta m_{\text{meas}}(\text{g}) \times R \times T(\text{K})}{\text{MW}(\text{g}\cdot\text{mol}^{-1}) \times V(\text{L})} \quad \text{Equation 2.8}$$

Where, P_{vapexp} is the vapor pressure obtained experimentally, in atmospheres (atm), Δm_{meas} is the weight loss (g), T is the temperature (K), V is the volume of air (L), found by multiplying the air flow rate over the source tube (lpm) by the time (min), and $R = 0.082057 \text{ L}\cdot\text{atm}\cdot\text{mol}^{-1}\cdot\text{K}^{-1}$.

2.3.2.2. Outcomes from the Approach 1

- **Pyruvic acid under dry conditions**

Two experiments were conducted by putting a piece of glass wool with some drops of pyruvic acid in a ST. The $P_{\text{vap,C}_3\text{H}_4\text{O}_3}$ at a specific T was calculated using Equation 2.6 with a literature value for the standard molar enthalpy of vaporization ($\Delta H_{\text{vap,C}_3\text{H}_4\text{O}_3}$ at 298.15 K) of $53.6 \pm 2.1 \text{ kJ}\cdot\text{mol}^{-1}$ (Emel'yanenko et al., 2018). The calculation used a P_{vap} of $289.9 \pm 7.3 \text{ Pa}$ at a temperature of 308.2 K experimentally obtained (Emel'yanenko et al., 2018). The normalized signals of $\text{C}_3\text{H}_4\text{O}_3$ showed a linear increase with the flow through to the ST ($R^2=0.98$; see Figure 2.14). The $C_{\text{C}_3\text{H}_4\text{O}_3}$ values from both experiments yielded an average of $4.64 \times 10^{15} \text{ molecule}\cdot\text{cm}^{-3}/\text{ion}$ ratio with 5% of total uncertainty. By comparing this result with the values reported in the literature (Table 2.5), one can conclude that NO_3^- ToFCIMS exhibit low sensitivity to $\text{C}_3\text{H}_4\text{O}_3$ despite its high O/C ratio.

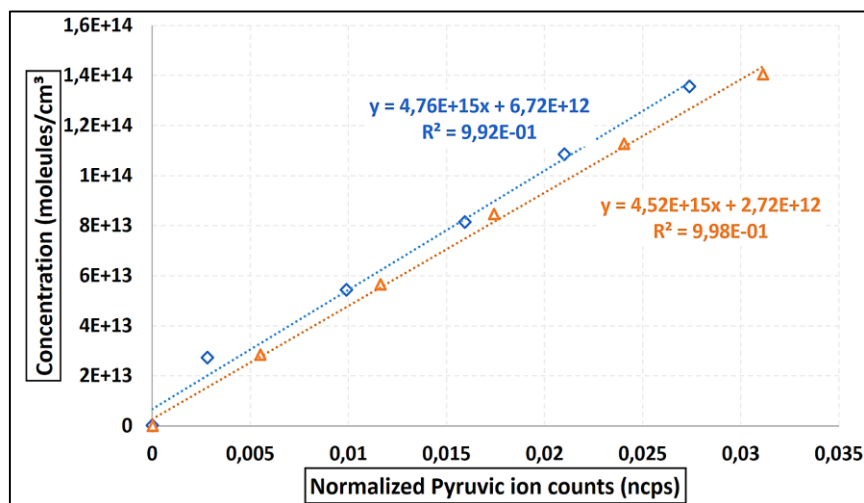


Figure 2.14. NO_3^- ToFCIMS sensitivity (slope) to pyruvic acid derived from the linear curve showing the injected concentration versus the pyruvic ion signals normalized to the total ion count of the reagent ions.

- **Oxalic acid under dry conditions**

Several experiments were performed to evaluate the sensitivity of the instrument towards oxalic acid ($\text{C}_2\text{H}_2\text{O}_4$) using Approach 1. An average of the solid $P_{\text{vap,C}_2\text{H}_2\text{O}_4}$ (298 K) values reported in the literature has been used in Equation 2.6 ($P_{\text{vap,avg}} = 1.89 \pm 0.8 \times 10^{-2} \text{ Pa}$) (Noyes and Wobbe, 1926; Bradley and Cotson, 1953; Wit et al., 1983; Booth et al., 2010). The P_{vap} at the experimental T was calculated according to Equation 2.6 by taking the average of the published sublimation enthalpies $\Delta H_{\text{sub,C}_2\text{H}_2\text{O}_4} = 91 \pm 9 \text{ kJ}\cdot\text{mol}^{-1}$ (Bilde et al., 2015). Figure 2.15 shows the $C_{\text{C}_2\text{H}_2\text{O}_4}$ obtained. The

average value obtained was $C_{C_2H_2O_4} = 1.16 \times 10^{13}$ molecule.cm⁻³ was achieved with 44% of total uncertainty. This value is about 3 orders of magnitude higher than the values reported in the literature for HOMs (meaning less sensitive). Yet, it is more than 2 orders of magnitude lower than the value reported for malonic acid (Table 2.5). Once again, despite its high O/C ratio, the results suggest that the NO₃⁻ ToFCIMS exhibits lower sensitivity towards C₂H₂O₄ but demonstrates better sensitivity than C₃H₄O₃.

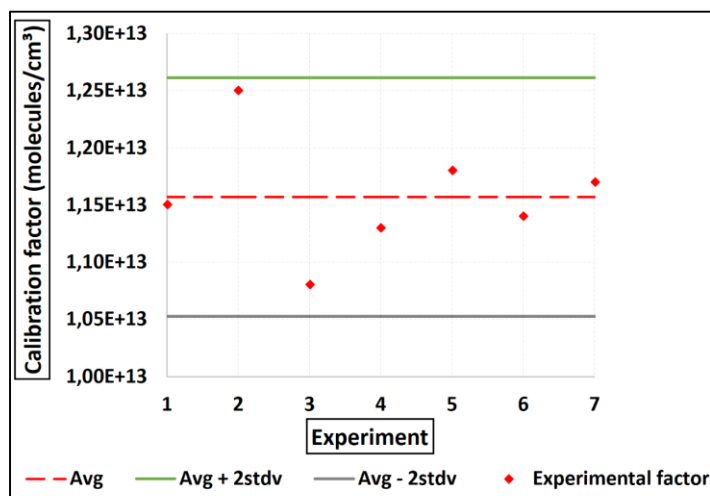


Figure 2.15. Oxalic calibration coefficients obtained showing the mean (red line) and 95% confidence intervals (green and grey lines). The red symbols depict the factors obtained from each experiment.

- **Succinic acid under dry conditions**

Several experiments were conducted to evaluate the response of the instrument to succinic acid (C₄H₆O₄). The solid $P_{\text{vap},C_4H_6O_4}(298\text{ K})$ is equal to $(7.7^{+5.0}_{-3.0}) \times 10^{-5}$ Pa from Bilde et al. (2015) who fitted all values reported in literature to obtain this result. $P_{\text{vap}}(T)$ has also been calculated according to Equation 2.6 by taking the average of the published sublimation enthalpies $\Delta H_{\text{sub,succinic}} = (115 \pm 15)$ KJ.mol⁻¹. An average value of $C_{C_4H_6O_4} = 1.65 \times 10^{13}$ molecule.cm⁻³ was achieved with about 66% of total uncertainty. Figure 2.16 shows the $C_{C_4H_6O_4}$ obtained from four successful tests. They are within a factor of 2 from the one obtained for C₂H₂O₄, but they are still quite different (differ by 42%). However, it is still approximately 3 orders of magnitude higher (meaning less sensitive) than the values reported in the literature (Table 2.5). This observation further suggests that the NO₃⁻ ToFCIMS exhibits low sensitivity towards C₄H₆O₄.

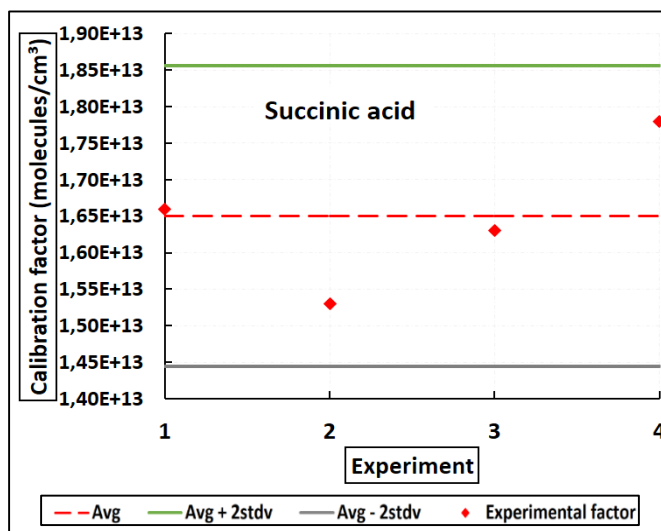


Figure 2.16. Succinic acid calibration coefficients obtained. The red symbols depict the factors obtained from each experiment performed.

- **Malonic acid under dry conditions**

Following the procedure described in section 2.3.2.1.C, a mean value of $P_{\text{vap,C}_3\text{H}_4\text{O}_4}(323 \text{ K}) = (1.48 \pm 0.15) \times 10^{-2} \text{ Pa}$ was obtained. $P_{\text{vap,C}_3\text{H}_4\text{O}_4}(298 \text{ K}) = 4.50 \times 10^{-4} \text{ Pa}$ was determined using Equation 2.6 employing the average of three published sublimation enthalpies $\Delta H_{\text{sub,C}_3\text{H}_4\text{O}_4} = (111.8 \pm 14) \text{ kJ.mol}^{-1}$ (Ribeiro da Silva et al., 1999; Booth et al., 2010; Cappa et al., 2008). This experimental value for the vapor pressure of malonic acid is comparable to the average of $P_{\text{vap,C}_3\text{H}_4\text{O}_4}(298 \text{ K}) = 4.88 \times 10^{-4} \text{ Pa}$ obtained in these studies with a relative difference (RD) of 7.7%. Our experimental value was used to estimate the calibration factor for $\text{C}_3\text{H}_4\text{O}_4$.

Following Approach 1 (section 2.3.2.1.A.), an average value of $C_{\text{C}_3\text{H}_4\text{O}_4} = 4.27 \times 10^{12} \text{ molecule.cm}^{-3}$ was achieved with about 30% of total uncertainty (Figure 2.17). This value is about one and a half orders of magnitude greater than that found in the literature (Table 2.5) but lower than the calibration factor values obtained for $\text{C}_2\text{H}_2\text{O}_4$, $\text{C}_3\text{H}_4\text{O}_3$ and $\text{C}_4\text{H}_6\text{O}_4$. This indicates that the NO_3^- ToFCIMS exhibits higher sensitivity towards $\text{C}_3\text{H}_4\text{O}_4$ compared to the other compounds that were tested.

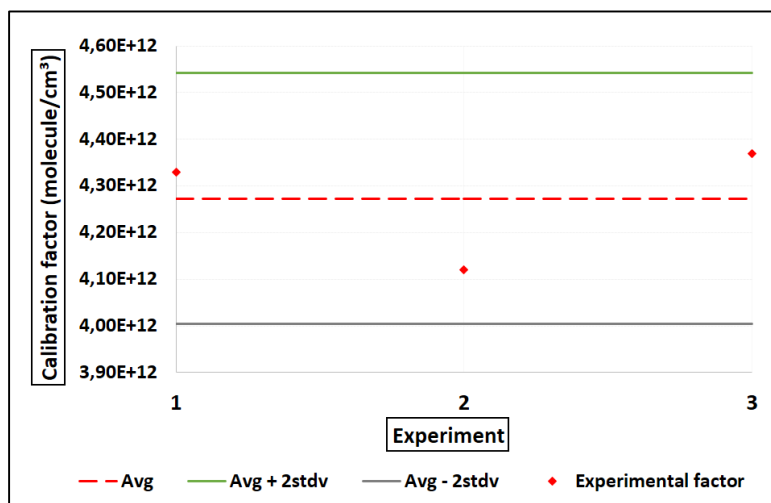


Figure 2.17. Malonic calibration coefficients obtained within a 95% confidence interval. The red symbols depict the factors obtained from each experiment performed.

- **Tartaric acid under dry conditions**

For calibration of the instrument to tartaric acid ($C_4H_6O_6$), the $P_{vap,C_4H_6O_6}(298\text{ K})=(1.79\pm 0.72)\times 10^{-4}$ Pa was taken from Booth et al. (2010) who reported the only experimentally obtained values of $P_{vap,C_4H_6O_6}$ and $\Delta H_{sub,tartaric}$. As with the other molecules studied, $P_{vap,C_4H_6O_6}(T)$ was calculated using Equation 2.6 with $\Delta H_{sub,tartaric} = (68\pm 10)$ kJ.mol⁻¹. The average value obtained in this study for $C_{C_4H_6O_6}$ is 5.84×10^{12} molecule.cm⁻³ with an estimated 43% total uncertainty. Figure 2.8 shows the $C_{C_4H_6O_6}$ values obtained. This value is similar to that obtained for $C_3H_4O_4$ in this study. However, it is still approximately two orders of magnitude higher than the values reported in the literature for HOMs.

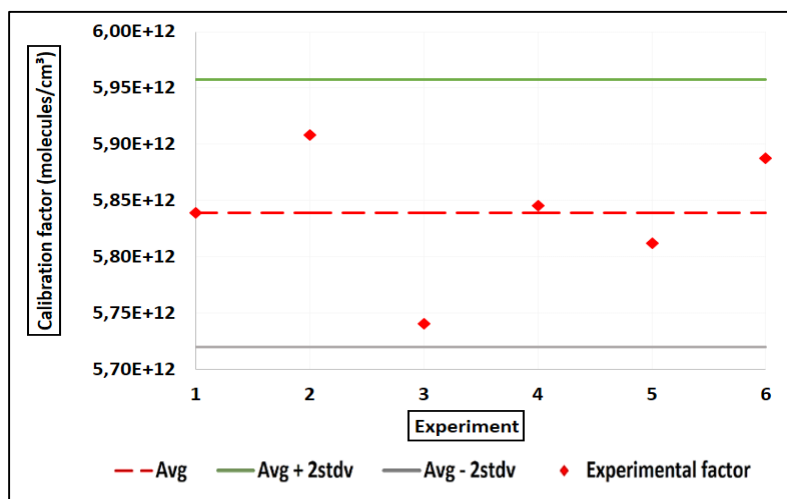


Figure 2.18. Tartaric calibration coefficients obtained within a 95% confidence interval. The red symbols depict the factors obtained from each experiment performed.

- **4-Nitrocatechol under dry conditions**

The $P_{\text{vap, C}_6\text{H}_5\text{NO}_4}$ (313 K) equals $(1.49 \pm 0.055) \times 10^{-3}$ Pa which was determined experimentally in the laboratory following the approach used for $P_{\text{vap, C}_3\text{H}_4\text{O}_4}$ (323 K), described in section 2.3.2.1.C. Using $\Delta H_{\text{sub, C}_6\text{H}_5\text{NO}_4} = (121.1 \pm 1.4)$ kJ.mol⁻¹ (Silva et al., 1986), $P_{\text{vap, C}_6\text{H}_5\text{NO}_4}$ (298 K) can be determined using Equation 2.6. An average value of $C_{\text{C}_6\text{H}_5\text{NO}_4} = 1.49 \times 10^{11}$ molecule.cm⁻³ was obtained with estimated 16% total uncertainty (Figure 2.19). Among all the tested compounds, 4-nitrocatechol demonstrates the lowest C_x , indicating that, of the compounds studied, the instrument is more sensitive towards this molecule. However, even with this better sensitivity, $\text{C}_6\text{H}_5\text{NO}_4$ still exhibits values approximately one order of magnitude higher than those reported in the literature for HOMs.

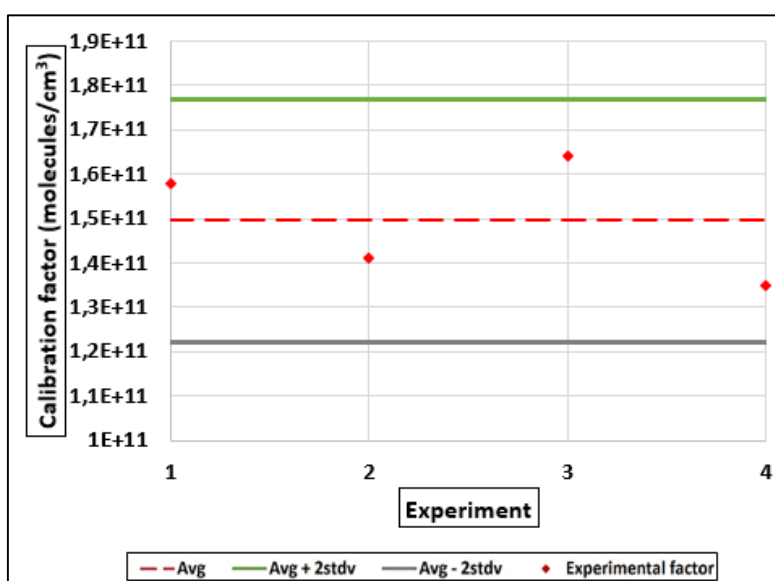


Figure 2.19. 4-Nitro-catechol calibration coefficients obtained within a 95% confidence interval. The red symbols depict the factors obtained from each experiment performed.

2.3.2.3. Outcomes from Approach 2

Two experiments were conducted by adding pyruvic acid to the CSA chamber. Figure 2.20 shows the time series of pyruvic acid concentrations obtained by FTIR and the corresponding normalized ion signals from the NO_3^- ToFCIMS for the two experiments, Experiment 1 and Experiment 2. The yellow shaded regions depict the periods when dilution was applied to the chamber.

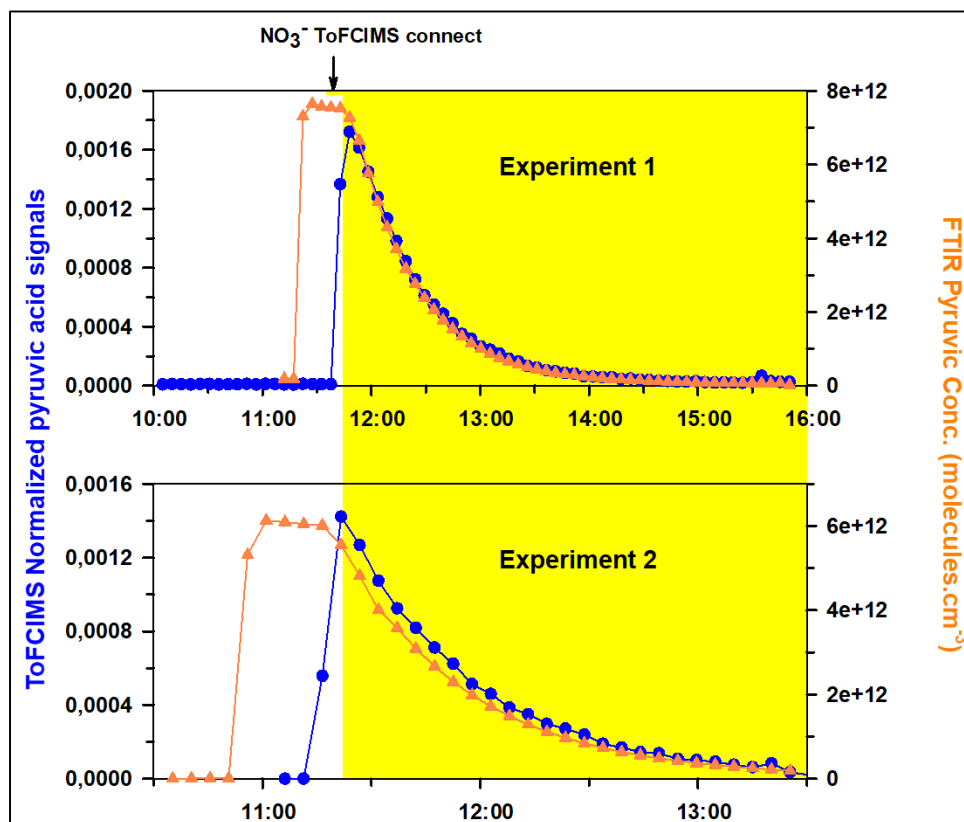


Figure 2.20. Time series of pyruvic acid concentrations obtained by FTIR and the corresponding normalized ion signals from the NO_3^- ToFCIMS.

In addition, fitting the pyruvic concentrations measured using FTIR versus the normalized pyruvic acid ion signals obtained from ToFCIMS yields a slope that equals the pyruvic acid calibration factor, $C_{\text{C}_3\text{H}_4\text{O}_3}$ (Figure 2.21). Individual values can be calculated using Equation 2.9.

$$C_{\text{C}_3\text{H}_4\text{O}_3} = \frac{[\text{C}_3\text{H}_4\text{O}_3]_{\text{FTIR}} \text{ (molecules.cm}^{-3}\text{)}}{\text{Ionratio}_{\text{C}_3\text{H}_4\text{O}_3}} \quad \text{Equation 2.9}$$

Where, $C_{\text{C}_3\text{H}_4\text{O}_3}$ is the calibration factor, in molecules.cm⁻³/ion ratio, $[\text{C}_3\text{H}_4\text{O}_3]_{\text{FTIR}}$ is the concentration obtained from the FTIR analysis, in molecules.cm⁻³, and $\text{Ion ratio}_{\text{C}_3\text{H}_4\text{O}_3}$ is the normalized ion signal for pyruvic acid obtained with the ToFCIMS.

The average of $C_{\text{C}_3\text{H}_4\text{O}_3}$ values calculated from both experiments yields a value of $(3.81 \pm 0.03) \times 10^{15}$ molecule.cm⁻³. The relative difference between this value and the one obtained by Approach 1 is 18%. This discrepancy may be explained, for instance, by uncertainty in the $P_{\text{vap,C}_3\text{H}_4\text{O}_3}$ and $\Delta H_{\text{sub,C}_3\text{H}_4\text{O}_3}$ values used in the calculation through the first approach or the uncertainties in the reference spectrum included by Approach 2. However, in both cases, the $C_{\text{C}_3\text{H}_4\text{O}_3}$ value obtained here is about 5 orders of magnitude greater than the factors found in the literature using H_2SO_4 as calibrant (Table 2.5) and it can therefore be confirmed that our NO_3^- ToFCIMS exhibits low sensitivity towards $\text{C}_3\text{H}_4\text{O}_3$.

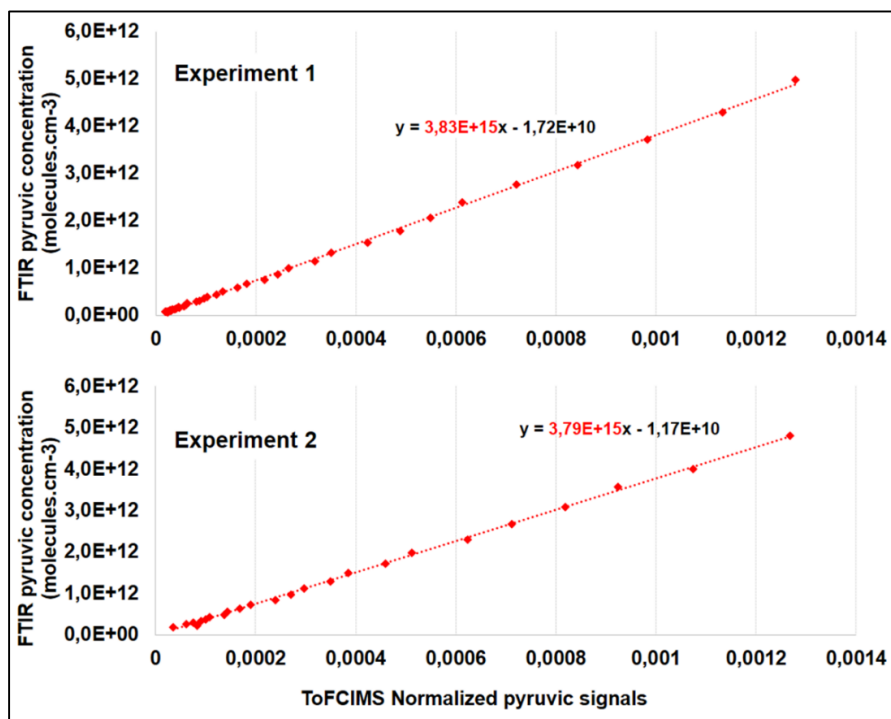
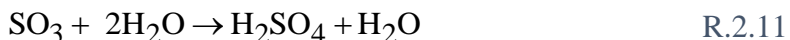
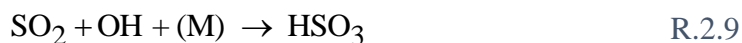


Figure 2.21. FTIR pyruvic acid concentration vs normalized pyruvic acid signals of ToFCIMS. The red dashed lines are the fitted trend lines. The slopes equal the calibration factor for each experiment.

2.3.3. Conventional calibration protocol and results

To make accurate comparisons between our laboratory studies, field results, and reports in the literature, we also calibrated the NO_3^- ToFCIMS instrument using H_2SO_4 as the calibrant, a procedure followed in several studies (e.g. Rissanen et al., 2014; Mutzel et al., 2015; Pullinen et al., 2020). This calibration procedure includes generating a specific amount of $\text{OH}\cdot$ to which is added SO_2 that reacts to form H_2SO_4 , following reactions R.2.9, R.2.10 and R.2.11. A calibration unit was used that was developed based on the work of Kürten et al. (2012). It consists of a mercury lamp providing 184.9 nm UV radiation and a quartz glass tube to which is added a flow of humidified air. $\text{OH}\cdot$ radicals are generated from the photolysis of water vapor by the ultraviolet radiation.



Three calibration setups were performed for the NO_3^- ToFCIMS instrument (Table 2.7). In the first setup, the calibration source was connected to the instrument using a Swagelok tee. The second setup involved connecting the calibration unit to the ToFCIMS through a 1-meter $\frac{3}{4}$ -inch stainless steel tube. This configuration was used to sample ambient air during the ACROSS field campaign (refer to Chapter 4). Finally, the third setup replicated the calibration approach described in section

2.3.2.1.A. and Figure 2.11, which was used to apply the calibration approach 1. The first two setups were designed to assess the wall loss of sulfuric acid in the 1-meter tube. The third setup was conducted to collect data to compare the calibration factors obtained from the H₂SO₄ source and the organic compounds tested in section 2.3.2.

Table 2.7. The calibration factor deriving from three experimental setups, described briefly in the comments column.

Setup N°	Inlet sampling flow (slpm)	CH ₂ SO ₄ (molecules/cm ³)	Comments
1	8	2.82×10 ⁹	source connected to the inlet using a Swagelok tee
2	8	4.22×10 ⁹	source connected to a 1 m length tube (ACROSS campaign setup)
3	6	8.07×10 ⁹	source connected to apparatus used in calibration approach 1

To conduct a calibration experiment, different H₂SO₄ concentrations were generated. The SO₂ concentration was kept constant while varying the OH concentrations. SO₂ was delivered from a ALPHAGAZ™ Mix cylinder (9.04 ppm) to create mixing ratios of about 772 ppbv in the source. To prevent absorption of UV light by ambient O₂ and H₂O vapor in the space between the mercury lamp and the quartz tube, the unit was purged with dry N₂ (ALPHAGAZ 2). The mass flow controllers were calibrated in order to allow accurate measurement of the flows. The H₂O vapor mixture was generated by passing an air flow through a bubbler. Photolysis of water vapor occurs when the air/water vapor mixture is exposed to UV light, which produces OH· (R.2.12).



The H₂O vapor mixing ratio and OH concentration are determined using Equations 2.10 and 2.11, respectively.

$$[\text{H}_2\text{O}] = \frac{Q_{\text{H}_2\text{O}}}{Q_{\text{H}_2\text{O}} + Q_{\text{SO}_2} + Q_{\text{air}}} \times \frac{P_{\text{sat}}(T) \times N_A}{R \times T} \quad \text{Equation 2.10}$$

Where, Q_{H₂O}, Q_{SO₂} and Q_{air} are the humidified air, the SO₂ and the dry air flow rates, respectively, p_{sat}(T) is the saturation vapor pressure of water, at temperature T, calculated using the Antoine Equation (Bridgeman and Aldrich, 1964), N_A is Avogadro's Number, defined as the number of atoms, molecules or ions in one mole of a substance, and R is ideal gas constant .

$$[\text{OH}] = I \times t_r \times \sigma_{\text{H}_2\text{O}} \times \Phi_{\text{H}_2\text{O}} \times [\text{H}_2\text{O}] \quad \text{Equation 2.11}$$

Where, I is the photon flux (photons- cm⁻²- s⁻¹), t_r is the illumination time (s). The quantity I × t_r is determined from actinometry experiments based on the photolysis of N₂O producing NO_x (Kürten et al., 2012). Other parameters in Equation 2.11 include σ_{H₂O}, which is the absorption cross

section of water vapor at 184.9 nm (Creasey et al., 2000), $\Phi_{\text{H}_2\text{O}}$ which is the photolysis quantum yield and is assumed equal to 1, and $[\text{H}_2\text{O}]$, which is the concentration of water calculated from Equation 2.10. The various parameters and the values used in this study are listed in Table 2.8.

Table 2.8. Parameters employed in the H_2SO_4 source used during calibration experiments of the NO_3^- ToFCIMS.

Parameter	Value	Units
$Q_{\text{H}_2\text{O}}$	10-300	slcm
Q_{N_2}	0.098	slpm
Q_{SO_2}	1.08	slpm
Q_{air}	11.4	slpm
$p_{\text{sat}}(\text{T})$	0.02771	atm
N_{A}	6.022×10^{23}	molec- cm^{-3} -mol $^{-1}$
T	23	$^{\circ}\text{C}$
R	0.08206	L.atm.mol $^{-1}$ K $^{-1}$
$\text{I} \times t_{\text{r}}$	2.1×10^{11}	photons- cm^{-2}
$\sigma_{\text{H}_2\text{O}}$	7.22×10^{-20}	cm^2
$\Phi_{\text{H}_2\text{O}}$	1	-

The concentrations of H_2SO_4 were determined by assuming that only the reaction between OH and SO_2 took place, and no changes in relative humidity (RH) occurred during the calibration process. Consequently, the H_2SO_4 calibration factors, denoted $C_{\text{H}_2\text{SO}_4}$ were calculated using Equation 2.4. Table 2.7 summarizes the calibration factors with the corresponding inlet sampling conditions.

The $C_{\text{H}_2\text{SO}_4}$ values obtained from the three setups are within the range reported in the literature $(0.165\text{-}6) \times 10^{10}$ molecules- cm^{-3} /ion ratio (see Table 2.5). Comparing setups 1 and 2 revealed a loss of approximately 33% in H_2SO_4 levels along the 1-meter sampling line. The $C_{\text{H}_2\text{SO}_4}$ obtained from setup 3 largely differs from those obtained for organic acids through our calibration approach 1. Additionally, we conducted a comparison between our daytime H_2SO_4 data obtained during the field campaign at the tower's summit and using $C_{\text{H}_2\text{SO}_4}$ determined with setup 2 (see table 2.7) and data acquired from another NO_3^- CIMS instrument (SAMU, LPC2E laboratory, University of Orleans; Kukui et al., 2021). This comparison exhibited good agreement, resulting in a calibration factor of 5.74×10^9 molecules- cm^{-3} , corresponding to a discrepancy of approximately 27% with $C_{\text{H}_2\text{SO}_4}$ achieved by setup 2.

Finally, the limits of detection (LOD, calculated as 3 times the standard deviation of the blank), the limits of quantification (LOQ, determined as 10 times the standard deviation of the blank), and the precision (evaluated by the relative standard deviation, RSD, of the average) were assessed in the various calibration experiments. Calibrations using OVOCs resulted in LOD ranging from 1.5 to 26 ppt and LOQ ranging from 5 to 87 ppt. For calibrations using H_2SO_4 , LOD ranged from 7 to 18 ppq and LOQ ranged from 20 to 60 ppq. Overall precision was within the range of 0.6% to 7%.

2.3.4. Discussion

Calibration exercises are essential for determining the accuracy of analytical instruments. Therefore, we performed calibrations on the NO_3^- ToFCIMS instrument to determine its sensitivity and linearity for detecting a series of organic compounds.

The first calibration method is highly sensitive to variations in the temperature of the sample. This parameter must be well controlled to obtain an accurate estimation compound concentration within the instrument. Due to the lack of suitable flow controllers for part of the experimental tests, one may explain in part the variations in calibration values obtained.

All the compounds listed in Table 2.6 were not detected by the instrument, possibly due to either the instrument's lack of sensitivity towards them or the requirement of a more rigorous method to generate those low-volatile compounds. It is also possible that higher heating temperatures could be required to enhance detection, but the maximum temperatures that could be used without changing the instrument's performance was such that some compounds were not produced in detectable amounts.

Table 2.9. Summary of the calibration factors resulted for the organic compounds measured with the NO_3^- ToFCIMS. *Following Approach 1; **Following Approach 2

Compound	C_x (molecules-cm ⁻³)
Pyruvic Acid	$4.64 \times 10^{15*}$
	$3.81 \times 10^{15**}$
Succinic Acid	$1.65 \times 10^{13*}$
Oxalic Acid	$1.16 \times 10^{13*}$
Tartaric Acid	$5.84 \times 10^{12*}$
Malonic Acid	$4.27 \times 10^{12*}$
4-nitrocatechol	$1.49 \times 10^{11*}$

The findings reveal significant variability in the calibration factors (Table 2.9) of the compounds that were studied with 4-nitrocatechol exhibiting the greatest sensitivity, followed by malonic acid, tartaric acid, oxalic acid, succinic acid, and the least sensitive, pyruvic acid. This indicates the dependence of the sensitivity of the NO_3^- ToFCIMS on the type of organic compound resulting in calibration factors that vary greatly in magnitude. The results suggest that it is not appropriate to rely on a single calibration factor obtained from H_2SO_4 for the quantification of the species detected at the lower mass range (small OVOCs) by this technique. The $C(\text{pyruvic})$ shows good agreement between our first approach and using the simulation chamber, with a relative difference of 18%. Furthermore, the $C(\text{malonic})$ is found to be of about 2 orders of magnitude higher than the one reported by Krechmer et al. (2015) and Massoli et al. (2018). Considering all the C_x values in Table 2.5, an average value of about 2×10^{10} molecules.cm⁻³ is obtained ($\sigma = 1.97 \times 10^{10}$ molecules-cm⁻³),

which is about one order of magnitude lower than the one obtained for 4-nitrocatechol by our instrument, more than 2 orders of magnitude lower than malonic and tartaric acid, 3 orders of magnitude lower than oxalic and succinic acid and more than 5 orders of magnitude lower than pyruvic acid. It should be recognized, however, that each instrument has a unique set of operational parameters that dictate its performance, sensitivity, and detection capabilities. The location and design of the sampling line (length, diameter, type, etc.) and sampling environment can also have a significant impact on the accuracy and representativeness of the sample being analyzed, as factors such as temperature and humidity which vary depending on the location and may affect the performance of the analytical instrument being used.

The tested compounds are probably not suitable to account for HOMs calibration factors because of their oxidation state or chemical structure.

Finally, the conventional calibration method for the NO_3^- ToFCIMS using H_2SO_4 was applied following an approach similar to that described by Kürten et al. (2012). This calibration was implemented utilizing three setups: the first involved linking the calibration unit to the ToFCIMS using a 1-meter $\frac{3}{4}$ -inch stainless steel tube (employed during ambient air sampling in the ACROSS field campaign), the second directly connected the calibration source to the instrument using a Swagelok tee and the third replicated the calibration approach 1 outlined in section 2.3.2.1. The $\text{C}(\text{sulfuric})$ obtained from the three setups ($2.83\text{-}8.08 \times 10^9$ molecules- cm^{-3}) is within the reported literature range for H_2SO_4 calibration ($0.165\text{-}6 \times 10^{10}$ molecules- cm^{-3}). A comparison between setups 1 and 2 indicated a loss of approximately 33% in H_2SO_4 levels along the 1-meter sampling line. Comparatively, the $\text{C}(\text{sulfuric})$ values derived from setup 3 substantially differs from those obtained for organic acids using our calibration approaches 1 and 2, demonstrating a relative difference of 100%. Additionally, one final comparison was used by comparing our daytime H_2SO_4 data collected during the Rambouillet field campaign with data from a SAMU instrument, resulting in a calibration factor of 5.74×10^9 molecules- cm^{-3} . This corresponds to a difference of 27% with setup 2.

The $\text{C}(\text{sulfuric})$ of 4.22×10^9 molecules- cm^{-3} is employed to quantify HOMs in the Rambouillet forest. This choice is made because it aligns with the instrumental configuration utilized during the field campaign (setup 2). This choice also allows for accurate comparisons between other field findings previously reported in the literature that quantified HOMs using a calibration factor derived from sulfuric acid as the calibrant.

Chapter 3 Formation of HOMs from simulation chamber studies of VOC oxidation

One of the many steps taken to address the objectives of this thesis work consisted of performing a series of experiments in the CESAM simulation chamber studying the oxidation of a selected set of VOCs. As a result of these studies, potential HOMs products of these reactions that may be encountered in the field in forest and mixed environments were identified. Comparisons with experiments reported in the literature were also conducted to investigate the performance of the instrument.

3.1. CESAM Chamber: General description

The CESAM chamber (Chambre Expérimentale de Simulation Atmosphérique Multiphasique) is located in the LISA laboratory. It is a 4.2 m³ cylindrical shaped reactor (2 m diameter, 2.3 m height) made of stainless steel (Figure 3.1). It enables studies of multiphase atmospheric chemistry and physics involving gas and/or condensed phase processes. The full description of the chamber is given in Wang et al. (2011).

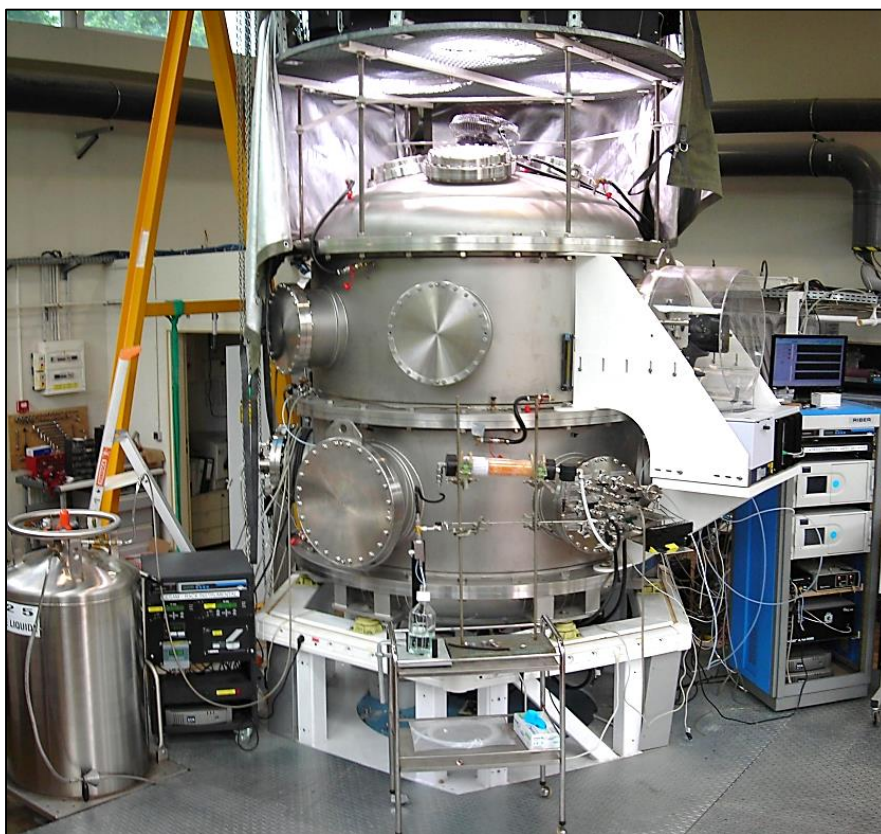


Figure 3.1. A photograph of the CESAM atmospheric simulation chamber located in the LISA laboratory at the Université Paris-Est Créteil (Maurin, 2013).

Prior to each experiment, the chamber is efficiently evacuated by means of two pumping systems described below:

- A primary pumping system (Bush® Cobra™ N0100–0300B) enhanced by a roots pump (Leybold® RUVACTM WAU 501), to reach a final pressure of around 10^{-1} mbar;
- A secondary pumping system consists of a turbo pump (Leybold® Turbovac 361®) that reaches a final pressure of about 10^{-4} mbar, depending on the wall cleanliness.

This is a crucial step to remove volatile impurities and residual substances adsorbed on the chamber walls from previous experiments. If contamination persists, high levels of ozone are added to achieve cleaner conditions.

Once the chamber is clean, it is filled with synthetic air created from liquid N₂ boil-off to a pressure of about 800 mbar and O₂ from a gas cylinder (Airliquide Alphagaz 1) to a final pressure near ambient. The pressure is measured by two Baratron® sensors (MKS, 622A and MKS, 626A), that can measure over the range from 10^{-4} to 1500 mbar. During experiments, compensation flows add N₂ and O₂ to automatically maintain a constant pressure as gas is removed by the analytical instruments sampling the chamber. This is accomplished using two flow controllers (MKS 1179C with maximum flow rates of 5000 sccm and 20000 sccm) that are programmed to maintain the desired pressure of 5 mbar above ambient pressure.

Air is stirred within the chamber using a fan in order to increase the homogeneity of the reaction mixture. Furthermore, the chamber temperature (T) and relative humidity (RH) are continuously measured by means of a Vaisala sensor HMP234 with a precision of $\pm 0.1^\circ\text{C}$ at 20°C and $\pm 1\%$ for $\text{RH} < 90\%$ and $\pm 2\%$ for $\text{RH} > 90\%$. These readings are used to control the chamber T and RH. The experiments discussed in this chapter were all conducted at dark and dry conditions.

3.2. Experimental Configuration Employed in Chamber Studies

A series of experiments were conducted to study the oxidation reactions of individual VOCs (BVOCs and AVOCs) and BVOC mixtures. The chamber contained no added NO_x nor aerosol seed particles (except for the AVOCs oxidation experiments). SOA can thus be formed from nucleation of pure organic vapors. In general, the daily schedule includes either one oxidation study (such as for AVOCs), or up to two studies (for BVOCs ozonolysis experiments). Consequently, for days with two studies, the duration of each experiment was reduced by approximately an hour. To accommodate this adjustment, the initial O₃ concentrations were increased to speed up the oxidation rate, taking into consideration the reactivity of the BVOCs involved (Table 3.1). Upon completion of the first experiment of the day, the contents of the chamber were removed though

pumping for one to two hours. This was found to sufficiently clean the chamber in most cases. The experiments were performed under dry conditions at temperatures of 290±4 K.

Table 3.1. The rate coefficients of selected BVOCs for reaction with O₃ and OH· radicals at 298 K (<https://iupac-aeris.ipsl.fr/>; ^aHantschke et al. (2021)).

BVOC	k _{O₃+BVOC} (cm ³ .molecule ⁻¹ .s ⁻¹)	k _{OH+BVOC} (cm ³ .molecule ⁻¹ .s ⁻¹)
α-pinene	9.6 × 10 ⁻¹⁷	5.4 × 10 ⁻¹¹
limonene	2.2 × 10 ⁻¹⁶	1.7 × 10 ⁻¹⁰
Δ³-carene	4.9 × 10 ⁻¹⁷	8.2 × 10 ^{-11a}

After filling the chamber, a ventilation system and the compensation flow control system are activated. As discussed in section 3.3, several analytical instruments that measure the gas and particle phase compositions are connected to the chamber approximately 30 min before the addition of the VOC in order to collect background signals and characterize the initial state.

The BVOCs selected for these studies are listed in Table 3.1.

These compounds were chosen for two reasons:

- 1) There are many studies of the formation of HOMs from the ozonolysis of α-pinene reported in the literature. This provides baseline information on the performance of the NO₃⁻ ToFCIMS and allows us to compare the results of α-pinene to less well-studied BVOCs (e.g. limonene and Δ³-carene).
- 2) The field measurements took place in the Rambouillet forested area (see chapter 4 section 4.1). The average emission potentials of terpenes centered on the Rambouillet supersite were extracted from the MEGAN emissions inventory (Figure S.3.1) and showed that these type of BVOCs are emitted in non-negligible quantities there.

The vacuum line, similar to the one shown in Figure 2.12, was coupled to a 2.1 L glass bulb and used to sample a known pressure of the BVOC of interest. The bulb is then connected to the chamber and the content is transferred by passing a N₂ flow through the bulb. Another 30 min period with only air and VOC in the chamber was collected to measure its level and stability.

O₃ is then produced by corona discharge generator of O₂ (BMT, Messtechnik, 802N) and added directly to the chamber. It is known that OH· radicals arise as secondary products of ozonolysis. To eliminate reactions of OH· radicals, cyclohexane was added to the chamber to act as an OH· scavenger.

3.3. Analytical Instruments and Quantities Measured

The NO₃⁻ ToFCIMS was connected to the chamber using a 1.2 m length of ¼ inch diameter stainless steel tubing (ID = 4.57 mm) that was heated to 40°C to reduce wall losses. The sample

flow into the instrument was 6 lpm and spectra were acquired at 1 s time intervals. The residence time within this sampling line was about 200 ms.

Additional ancillary measurements were also connected to the chamber to follow the evolution of key components. The basic principles of this instrumentation is described in sections 3.3.1 and 3.3.2. Figure 3.2 illustrates an overview of the experimental setup for the chamber experiments conducted.

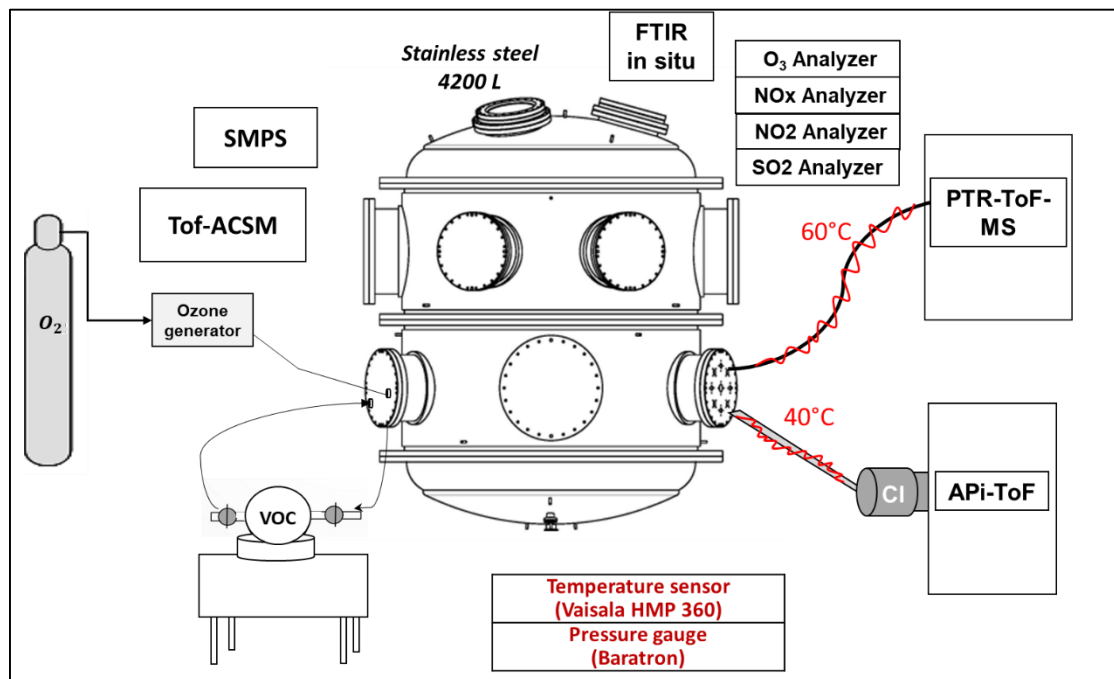


Figure 3.2. Overview of the experimental setup of CESAM.

3.3.1. Additional Gas-phase instruments

3.3.1.1. Fourier Transform Infrared spectrometer (FTIR)

The CESAM chamber is characterized by the presence of an in situ FTIR (Bruker™ Tensor 37® Bruker Optics GmbH). This instrument employs an MCT (mercury-cadmium-telluride) detector that is cooled with liquid N₂ (77 K) (Yi et al., 2021). The multiple-pass optical path is 182 m. The spectra were obtained at a resolution of 0.5 cm⁻¹. One hundred interferograms were collected to generate five minute averages, and then converted to spectra. These provide information in the 500 to 4000 cm⁻¹ IR spectral region. It was only operated for the first set of experiments and it was used to track the amount of the VOC studied to verify the values retrieved by the PTR-MS (section 3.3.1.2) instrument. However, the high level of cyclohexane (5-15 ppmv) in the chamber prevented the FTIR from tracking the evolution of the VOC. The possible reason is that the cyclohexane solution may have contained components that absorb in the region where the VOCs do, thereby masking the bands.

3.3.1.2. Proton Transfer Reaction Time of Flight Mass Spectrometer (PTR-MS)

The evolution of VOC concentrations in the chamber was quantified by a PTR-MS instrument (Kore Technology, UK). It provides detection and quantification of gas-phase organic compounds with detection limits as low as tens of pptv using hydronium ions as the reagent ions. This method is not capable of distinguishing between the various monoterpenes, and thus provides the total amount of these compounds (Jordan et al., 2009).

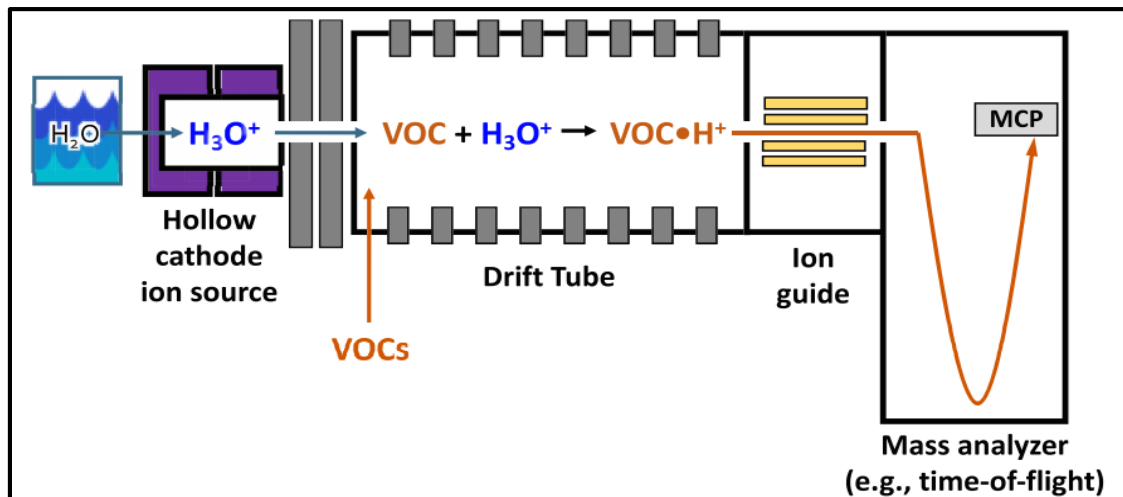


Figure 3.3. The operating principle of a PTR-ToF-MS (Blake et al., 2009).

As shown in Figure 3.3, the instrument consists of a hollow cathode discharge where hydronium H₃O⁺ ions are produced from water vapor. These ions then enter the reactor where a proton transfer reaction (PTR) occurs between the H₃O⁺ ions and the VOC (referred to as R) according to reaction R.3.1, for those situations where the VOC proton affinity (PA) is greater than that of water (691 kJ/mol at 298K, Hunter and Lias, 1998).



The reagent and product ions then enter the ToF-MS where they are separated according to their time of flight and detected. Air was sampled from the chamber through a 60°C heated ¼ inch PFA (perfluoroalkoxy alkanes) line at a flow rate of 250 mL.min⁻¹. Data were collected at a 1 min time resolution.

The VOC mixing ratio (ppbv) is calculated following Equation 3.1.

$$C_{\text{VOC}} = \frac{i_{(\text{VOC}_{\text{net}})}}{(i_{(\text{H}_3\text{O}^+)} + X_r \cdot i_{(\text{H}_3\text{O} \cdot \text{H}_2\text{O}^+)})} \times \frac{150000}{R_{(f, \text{VOC})}} \quad \text{Equation 3.1}$$

Where, $i_{(\text{VOC}_{\text{net}})}$ is net VOC signal, defined as the difference of signals between the ambient (or chamber) sample and zero air, $i_{(\text{H}_3\text{O}^+)}$ are the signals of H₃O⁺ ions at m/z 21 Th multiplied by 500,

$i_{(\text{H}_3\text{O}\cdot\text{H}_2\text{O}^+)}$ is the signals of the first water cluster ions $\text{H}_3\text{O}^+(\text{H}_2\text{O})$ at m/z 39 Th multiplied by 250, X_r is a correction factor which accounts for the effect of humidity on the sensitivity of the VOC being measured, $R_{f,\text{VOC}}$ is the sensitivity of the method as determined by calibration, in $\text{cps}\cdot\text{ppb}^{-1}$, 150 000 is the number of primary H_3O^+ ions in counts per second (Michoud et al., 2017).

3.3.1.3. Ozone, NO_x , NO_2 and SO_2 analyzers

The time-dependent concentrations of O_3 were continuously monitored using an O_3 analyzer (Horiba® APOA 370®), which is based on the principle of absorption of 253.7 nm light by O_3 . Data from the analyzer are averaged for 1-minute at a sample flow rate of $0.7 \text{ L}\cdot\text{min}^{-1}$ (lpm). The detection limit is about 1 ppbv. Interferences in this method could occur, particularly for some VOCs that absorb in this wavelength range.

Measurements of NO_x , NO_2 and SO_2 were made in order to verify the cleanliness of the chamber (Horiba APNA-370 (based on ozone chemiluminescence for direct measurements of NO and a molybdenum converter for indirect measurements of NO_x and hence NO_2 by difference), Teledyne T500U (based on CAPS technology for direct NO_2 measurement) and Horiba APSA-370 (based on ultraviolet fluorescence at 215 nm for direct SO_2 measurements), respectively).

3.3.2. Particulate phase analysis

3.3.2.1. Scanning Mobility Particle Sizer (SMPS)

An SMPS instrument sampled from the chamber measure the size distributions and the number concentrations of particles. As depicted in Figure 3.4, the SMPS consists of three main elements:

- 1) a radioactive source (^{85}Kr) that imparts a charge onto the sampled particles,
- 2) a differential mobility analyzer (DMA, TSI, model 3080) where particles are separated within an electric field based on their electrical mobility,
- 3) a butanol condensation particle counter (CPC, TSI model 3010), which quantifies the number of particles exiting the DMA.

Data are recorded from the instrument every 3 min. It is operated with a sample flow rate of 1 lpm.

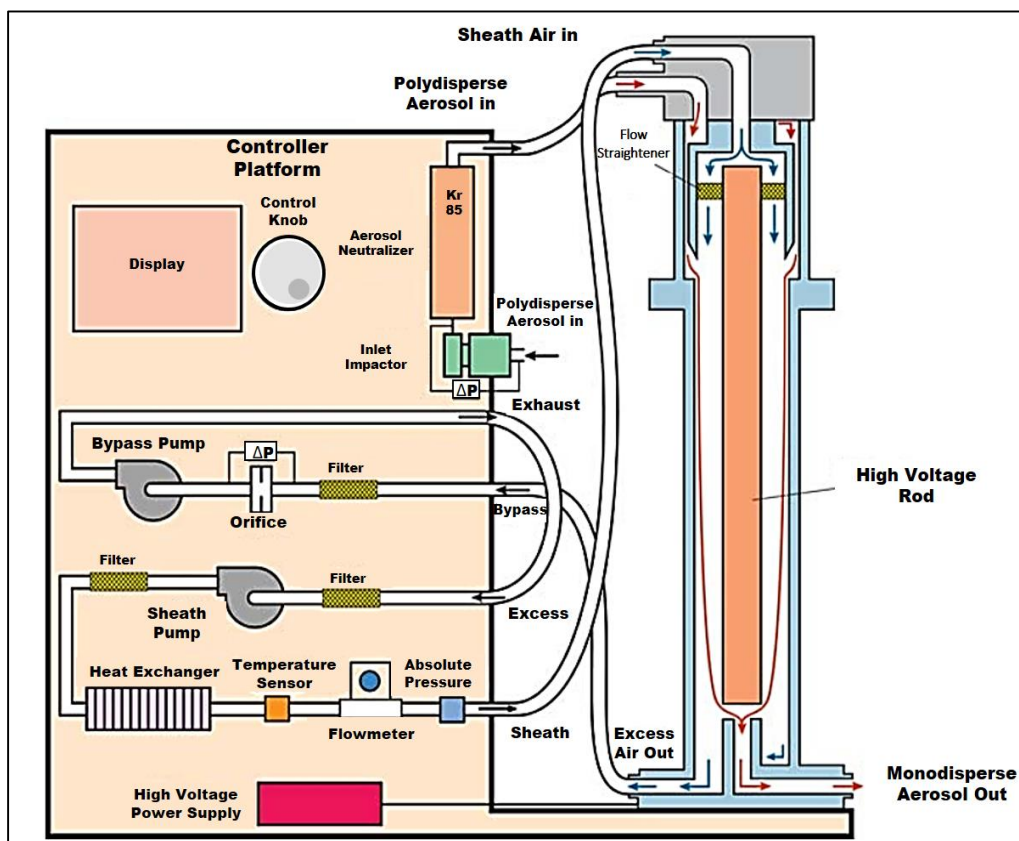


Figure 3.4. Schematic of the SMPC-CPC TSI Series 3080 (Series 3080 Operation and Service Manual, 2009).

The particle size distributions are divided into 64 size classes within the size range from 19.5 to 881.7 nm. The particle mass concentration ($\mu\text{g}\cdot\text{m}^{-3}$) was obtained by assuming a spherical particle shape and a density of $1.4\text{ g}\cdot\text{cm}^{-3}$ (Fry et al., 2014).

3.4. Chamber Experiments

The following monoterpenes, α -pinene, limonene, and 3-carene, were acquired from Sigma-Aldrich with stated purities of 97.5%, >95.0%, and >90.0% respectively. The initial chamber concentrations of individual BVOCs were about 50 ppbv. Mixtures of monoterpenes were also studied, consisting of two different BVOCs at about 25 ppbv each. The experimental conditions used for each experiment are shown in Table 3.2. The cyclohexane OH scavenger was added to the chamber in an excess amount estimated based on the product of the ratio of the reaction rate coefficient of $\text{C}_6\text{H}_{12}+\text{OH}$ to that of $\text{VOC}+\text{OH}$ times the amount of VOC used (Equation 3.2). The actual concentration added to the chamber is then determined and the percentage of OH· radicals that react with the scavenger is calculated using Equation 3.2.

$$\% \text{OH}_{\text{reacted with C}_6\text{H}_{12}} = \frac{[\text{C}_6\text{H}_{12}] \times k(\text{C}_6\text{H}_{12} + \text{OH})}{([\text{C}_6\text{H}_{12}] \times k(\text{C}_6\text{H}_{12} + \text{OH}) + [\text{VOC}]_1 \times k(\text{VOC}_1 + \text{OH}) + [\text{VOC}]_2 \times k(\text{VOC}_2 + \text{OH}))} \times 100 \quad \text{Equation 3.2}$$

Table 3.2. Experimental conditions for the CESAM chamber studies (ppbv±1 stdv of signal uncertainty). Experiment numbers starting with the letter ‘O’ refer to VOC reaction with ozone. [VOC]₀, [Cyclohexane]₀ and [O₃]₀ are the initial levels of VOC, cyclohexane and ozone, in ppbv.

Exp. Number	VOC	[VOC] ₀ (ppbv)	[Cyclohexane] ₀ (ppbv)	[O ₃] ₀ (ppbv)	% OH reacting with C ₆ H ₁₂
Individual					
O1	α-pinene	49.4 ± 4.6	4988	265	92
O2	α-pinene	53.2 ± 3.9	4975	300	92
O3	limonene	50.4 ± 5.3	14587	194	91
O4	limonene	50.6 ± 5.7	14973	266	92
O5	3-carene	52.4 ± 2.0	7961	317	92
O6	3-carene	47.8 ± 3.3	8043	468	93
Mixtures					
O7	3-carene, limonene	27.1 ± 1.7, 34.2 ± 2.7	14968	172	94
O8	limonene, α-pinene	25.4 ± 3.2, 28.1 ± 3.9	9990	172	92

In addition to the previous studies discussed, we contributed to chamber experiments that were mechanistic studies to explore, understand and quantify the reaction oxidation products from the reaction of two BVOCs, α-phellandrene and β-phellandrene with NO₃· radicals. Some studies involved the addition of trans-2-butene (C₄H₈) to the reaction system to investigate its impact on the chemical pathways, and thus the nature and yields of the oxidation products, particularly focusing on organic nitrates and SOA yields. The experimental conditions used in these studies are presented in Table 3.3, with the number of experiments preceded by the letter 'N' to indicate initiation by NO₃· radicals. In these experiments, the ToFCIMS sample was diluted by combining a 1 lpm flow rate from the chamber with synthetic air flow at a rate of 5 lpm.

Table 3.3. Experimental conditions of the BVOC + NO₃ chamber experiments. [VOC]₀ and [t-C₄H₈]₀ are the initial levels of α,β-phellandrene and trans-2-butene, in ppbv and ppmv, respectively. The reaction time is defined as the period starting from the initial injection of the oxidant and extending until the end of the experiment. Experiment numbers starting with the letter ‘N’ and ‘N’ refer to α-phellandrene and β-phellandrene reaction with NO₃, respectively.

Exp. Number	VOC	[VOC] ₀ (ppbv)	[t-C ₄ H ₈] ₀ (ppmv)	Reaction time (min)
N1	α-phellandrene	290	0	60
N2		280	0	80
N3		75	0	40
N4		50	0	18
N5		70	0	65
N6		250	0	30
N7		480	0	60
N8		165	10	75
N9		205	10	60
N10		280	10	35
N11		80	10	55
N12		80	0	60
N'1	β-phellandrene	295	0	100
N'2		270	0	95
N'3		205	0	70
N'4		65	0	65
N'5		67	0	70
N'6		205	0	25
N'7		31	1	50
N'8		180	1	85
N'9		72	1	75
N'10		62	1	85

The ToFCIMS instrument was also employed in chamber experiments involving photooxidation of AVOCs. These chamber experiments focused on the study of the oxidation of toluene and m-xylene by OH· radicals produced by the photolysis of H₂O₂.

Table 3.4. Experimental conditions for the CESAM chamber studies from AVOC + OH reactions. Experiment numbers starts with the letter ‘H’ referring for reaction with hydroxyl radicals. [VOC]₀, [NO]₀, [seed] and the flow of H₂O₂ are the variables initially injected into the chamber. *Ammonium sulfate

Exp. Number	AVOC	[VOC] ₀ ppbv	[NO] ₀ (ppbv)	[Seed] [*] (µg·m ⁻³)	Flow H ₂ O ₂ (lpm)	RH (%)
H1	toluene	510	11.36	30.05	5	32
H2	toluene	510	None	30.91	5.3	25
H3	m-xylene	512	None	29.05	5.2	25
H4	m-xylene	514.5	6.64	31.08	5	31

Table 3.4 provides the initial conditions for conducting these experiments. Figure S.3.2 displays the temporal variations in the AVOCs concentrations and aerosol mass concentrations for experiments H1 to H4. There were no HOMs observed with the ToFCIMS instrument in these experiments. Our hypothesis is that the introduction of inorganic particle seeds in these experiments resulted in rapid partitioning of HOMs into the particulate phase. Another possibility is that the chemical systems studied here leads to low HOMs formation preventing detection in quantifiable amounts. The formation of gas-phase HOMs from aromatic compounds (including cases of toluene and m-xylene) reacting with OH· radicals has been investigated in a number of studies reported in the literature (Wang et al., 2017; Molteni et al., 2018; Garmash et al., 2020; Wang et al., 2020; Cheng et al., 2021). They successfully identified a variety of HOMs, with HOM yields ranging from 0.1% to 0.46% for toluene and 1% to 1.7% for m-xylene (Table 1.9). However, seeds were only included in the study of Garmash et al. (2020), who extensively demonstrated the significant impact of adding seeds to experiments involving benzene and toluene. This led to a significant reduction in gas-phase HOMs, thereby supporting our hypothesis.

3.5. Data Corrections in Chamber Studies

3.5.1. Correction from dilution

Since N₂ was continuously added to the chamber to compensate for the removal of samples from the chamber by instruments, this resulted in dilution of the gas and particle concentrations on an ongoing basis. A correction for this dilution is required to obtain the proper yields of the various products formed. The method to calculate the corrections has been employed in this study, and was developed and described in the dissertation of Maurin, (2013). The relevant formula is presented in Equation 3.3.

$$\mathbf{m}(t)_{\text{corrected}} = \mathbf{m}(t-1)_{\text{corrected}} + \Delta\mathbf{m}_{\text{measured}} + \frac{Q_p}{V} \bar{\mathbf{m}}_{\text{measured}} e^{-\frac{Q_p}{V}\Delta t} \Delta t \quad \text{Equation 3.3}$$

Where, $\mathbf{m}(t)_{\text{corrected}}$ is the corrected amount of material at time t , $\mathbf{m}(t-1)_{\text{corrected}}$ is the corrected amount of material at time $t-1$, $\Delta\mathbf{m}_{\text{measured}}$ is the difference in measured amount of material between time t and $t-1$, Q_p is the dilution flow rate (lpm), V is the chamber volume (L), $\bar{\mathbf{m}}_{\text{measured}}$ is the measured amount of material averaged for t and $t-1$, Δt is the time interval between time t and $t-1$.

3.5.2. Correction due to particle wall losses

It is well-known that interactions with walls in simulation chambers can significantly affect the fate of particulate and gas-phase components (Doussin et al., 2023). To quantify the impact of particle deposition on chamber walls, one must estimate the rate constants for particle deposition (k_w) as a function of particle diameter (D_p). To accomplish this, the research methodology developed by Lamkaddam, (2017) was employed, which specifically investigated aerosol deposition characteristics in CESAM. The determination of k_w was based on experimental control tests conducted with ammonium sulfate particles having a density of 1.77 g/cm³. The data obtained from these experiments were utilized to apply a model initially developed by Lai and Nazaroff, (2000), which incorporates various parameters such as reactor shape and dimensions, as well as particle density, to determine the deposition rate constants. The corrected particle number concentration is determined using Equation 3.4 (Lamkaddam, 2017).

$$\mathbf{N}_{\text{corrected}}(t) = \mathbf{N}_{\text{measured}}(t) + k_w \int_0^t \mathbf{N}_{\text{measured}} dt \quad \text{Equation 3.4}$$

Where, k_w is the particle deposition rate constants, in s, $\mathbf{N}_{\text{corrected}}(t)$ is the corrected number concentration at time t , and $\mathbf{N}_{\text{measured}}(t)$ is the measured number concentration at time t .

3.6. HOMs formation from monoterpene ozonolysis

3.6.1. Ozone-initiated reactions of α -pinene, limonene and 3-carene

α -pinene oxidation. The compound α -pinene has a bicyclic structure and is characterized by a single endocyclic double bond. During the ozonolysis of α -pinene, similar to all alkenes, a significant process is the formation of Criegee Intermediates (CIs) (section 1.2.3). These may undergo 1,4 H-atom shift resulting in the formation of a vinylhydroperoxide (VHP), followed by loss of an OH· radical and the formation of a vinoxy radical. This is followed by the addition of O₂ to form the first α -pinene RO₂·, C₁₀H₁₅O₄· (Iyer et al., 2021). Figure 3.5 illustrates part of the

mentioned pathway, which focuses on an example of one of the CIs obtained from the primary ozonide (POZ) decomposition.

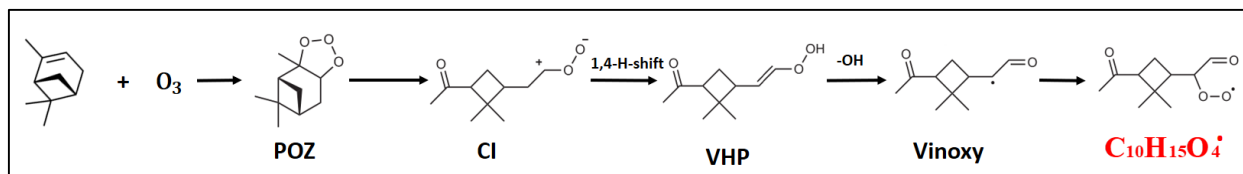


Figure 3.5. α -pinene Ozonolysis initiation reaction (Iyer et al., 2021).

limonene oxidation. Limonene is a compound with a single ring structure and featuring an endocyclic and an exocyclic double bond. As limonene may undergo two initiation reactions with O_3 , laboratory studies have shown that it produces HOMs at nearly twice the rate of α -pinene in chamber studies (Table 1.8). The ozonolysis of limonene is initiated by the addition of O_3 to one of the two double bonds with the reaction occurring more rapidly on the endocyclic bond (Maksymiuk et al., 2009; Wang et al., 2023). It generally follows a mechanism similar to that of α -pinene (Figure 3.6). Tomaz et al. (2021) proposed an overview of a possible autoxidation mechanism for limonene ozonolysis that may explain at least some of the chemical formulas for HOMs that were seen mass spectra collected during this study.

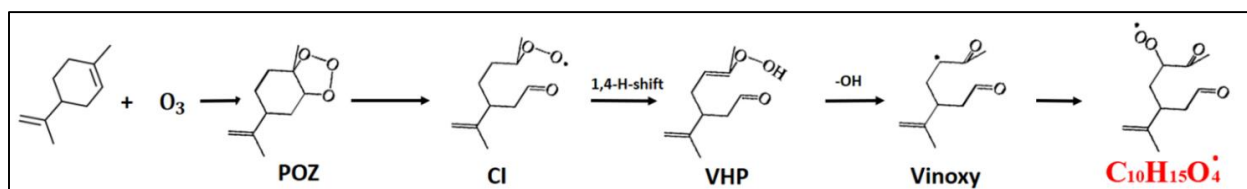


Figure 3.6. Limonene ozonolysis initiation reaction following the reaction sequence of one of the major CIs (Wang et al., 2023).

3-carene oxidation. 3-carene is a monoterpene with a structure similar to α -pinene, with the primary difference being the location and size of the small ring structure. It is thus expected that it would exhibit similar kinetics and product distributions because of the likely similar oxidation mechanism. However, recent research has revealed that even such subtle differences can significantly influence the oxidation mechanism of these compounds (Draper et al., 2019; Hantschke et al., 2021). The initiation reaction of 3-carene oxidation by O_3 is illustrated in Figure 3.7.

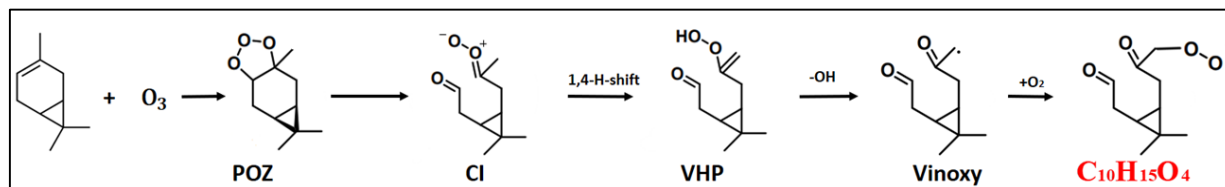


Figure 3.7. Example of 3-carene ozonolysis initiation reaction following the reaction sequence of one of the major CIs (Wang et al., 2019).

3.6.2. General scheme for HOM Formation from monoterpene ozonolysis

Figure 3.8 illustrates the generalized scheme for monoterpene ozonolysis in the absence of NO_x . This scenario aligns with results of our experimental studies. As previously depicted in Figure 3.5, 3.6 and 3.7, the ozonolysis of monoterpenes is expected to initiate in a similar manner, leading to the creation of initial $\text{RO}_2\cdot$ radicals, specifically with the molecular formula $\text{C}_{10}\text{H}_{15}\text{O}_4\cdot$. Notably, all the radical species, highlighted in red for $\text{RO}_2\cdot$ and purple for $\text{RO}\cdot$, contain an odd number of 15 hydrogen atoms. The number of hydrogens offers insights into terminal functional groups and bimolecular reactions leading to the formation of HOMs.

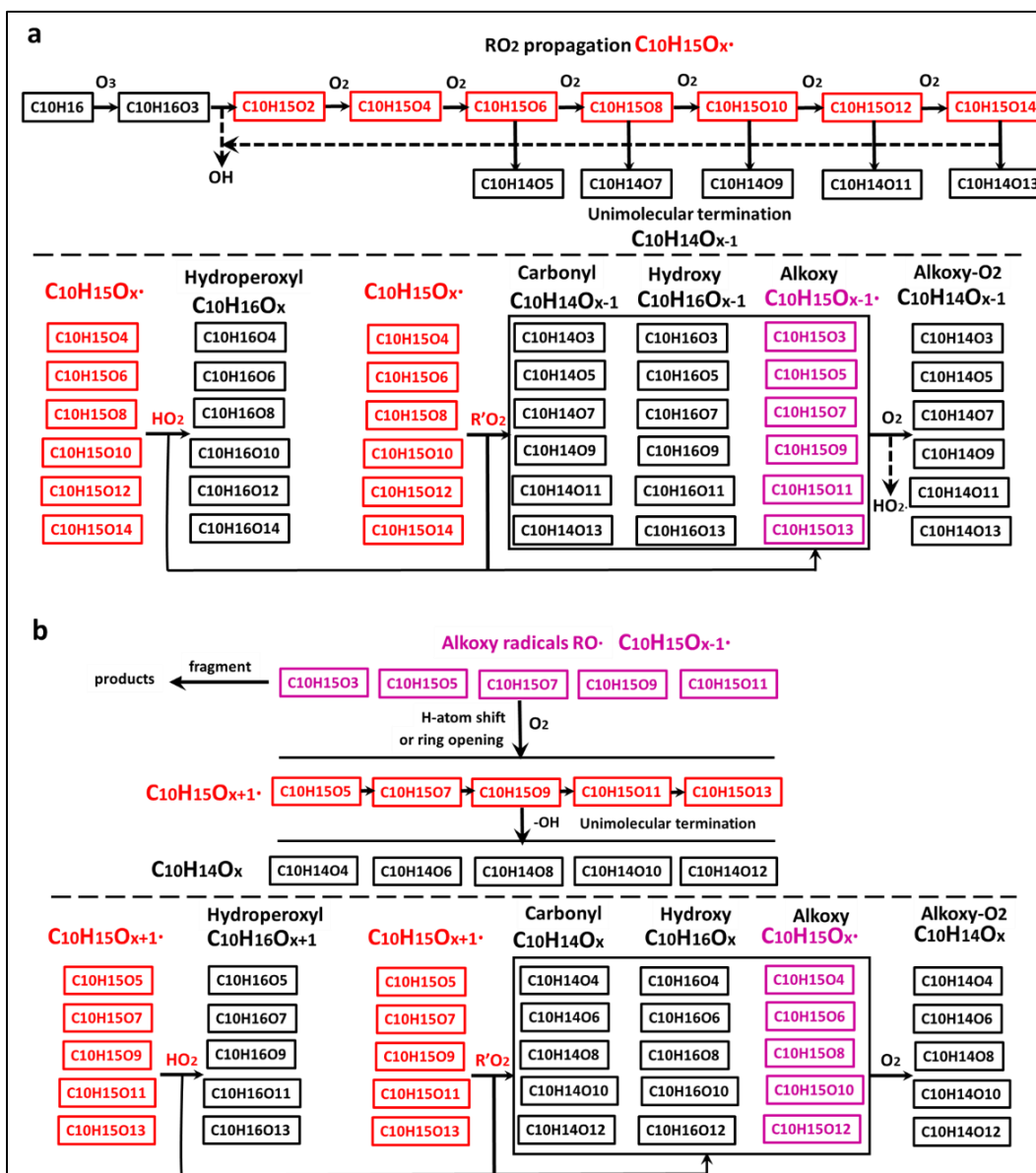


Figure 3.8. Scheme showing the generalized formation mechanism of HOMs from monoterpene $\text{C}_{10}\text{H}_{16}$ ozonolysis in the absence of NO_x . Formulas highlighted in red and purple are peroxy and alkoxy radicals, respectively, both possessing an odd number of hydrogen atoms ($n=15$), and in black closed-shell products with an even number of hydrogen atoms ($n=14,16$). x is the oxygen number with even values initially coming from autoxidation pathway, denoted the RO_2 propagation channel (adapted from Molteni et al., 2019).

In Figure 3.8.a, the depicted pathways illustrate the progression of the reaction by HOM-RO₂· and their associated products. In Figure 3.8.b, potential routes are presented, which the resulting RO· radicals could also potentially traverse. The C₁₀H₁₅O₄· radical acts as the initiator of the autoxidation mechanism, denoted as the RO₂· propagation pathway. This involves H-atom shifts and successive O₂ additions in repeating cycles. Consequently, the resulting HOM-RO₂· radicals, characterized by the general formula C₁₀H₁₅O_x·, should possess an even number of oxygen atoms, denoted as x. This number could for instance reach up to 14 oxygen atoms. These radicals are anticipated to be detectable at a m/z difference of 32 Th.

As detailed in Figure 1.6, the RO₂· propagation pathway competes with classic termination reactions. The rates of these reactions are influenced by the structure of organic compounds and experimental conditions. In general, RO₂· may experience unimolecular termination reactions through H-atom shifts, leading to the elimination of an OH· radical. This process results in closed-shell molecules, denoted as C₁₀H₁₄O_{x-1}, terminated with a carbonyl functional group (x-1 = odd number). It's worth noting that this step requires the presence of at least one hydroperoxide group in the molecule. The first suitable radical for this process is thus C₁₀H₁₅O₆·.

C₁₀H₁₅O_x· radicals may also react with HO₂·, resulting in closed-shell molecules described by the general formula C₁₀H₁₆O_x, marked by a hydroperoxide functional group. Another outcome could be the formation of a HOM-RO· radical with the general formula C₁₀H₁₅O_{x-1}·. In addition, C₁₀H₁₅O_x· radicals can also react with other peroxy radicals, R'O₂, yielding a carbonyl functional group with the formula C₁₀H₁₄O_{x-1}, a hydroxyl functional group with the formula C₁₀H₁₆O_{x-1} or HOM-RO· radicals with the formula C₁₀H₁₅O_{x-1}. In addition, it is expected that the RO₂+R'O₂ channel may lead to accretions products (ROOR'), as discussed in section 1.3.1.

HOM-RO· radicals formed from RO₂ + HO₂ and RO₂ + R'O₂ pathways, can in turn undergo further reaction. They can react with O₂ yielding C₁₀H₁₄O_{x-1} molecules (and HO₂). As demonstrated in Figure 3.8.b, they can undergo intramolecular rearrangements, including H-atom shift or ring openings. Subsequently, they can react with O₂, resulting in a distinct category of HOM-RO₂· radicals with an odd number of oxygen atoms. These radicals have the molecular formula C₁₀H₁₅O_{x+1}· (x+1 = odd number), and may further undergo termination reactions in a manner similar to those previously discussed. An alternative scenario involves the unimolecular decomposition of HOM-RO· radicals; leading to the generation of two fragments.

3.7. Results from chamber experiments

3.7.1. Ozonolysis reaction of α -pinene

Figure 3.9 shows the time dependencies of the gas-phase precursors, namely α -pinene and O_3 , along with the total HOMs mixing ratios, in units of part per trillion by volume (pptv), and aerosol amounts (mass and number concentrations) for α -pinene oxidation experiment, O1 that was carried out at a temperature of 16.5°C with an initial α -pinene mixing ratio of 50 ± 4.6 ppbv. The HOMs signals were converted to pptv using the same calibration factor as employed for the ACROSS field study. The start of the oxidation reaction, which was initiated by the first injection of O_3 into the chamber, is considered as time 0 (yellow shaded region). Upon the injections of O_3 into the chamber, there was a marked increase in the total HOMs levels, and they reach their maximum after about 10 minutes. Thereafter, their levels decrease gradually, coinciding with an increase in the mass and the number concentrations of particles, with the number concentration remaining nearly constant after about 20 minutes of reaction whereas the mass continues to increase during the balance of the experiment.

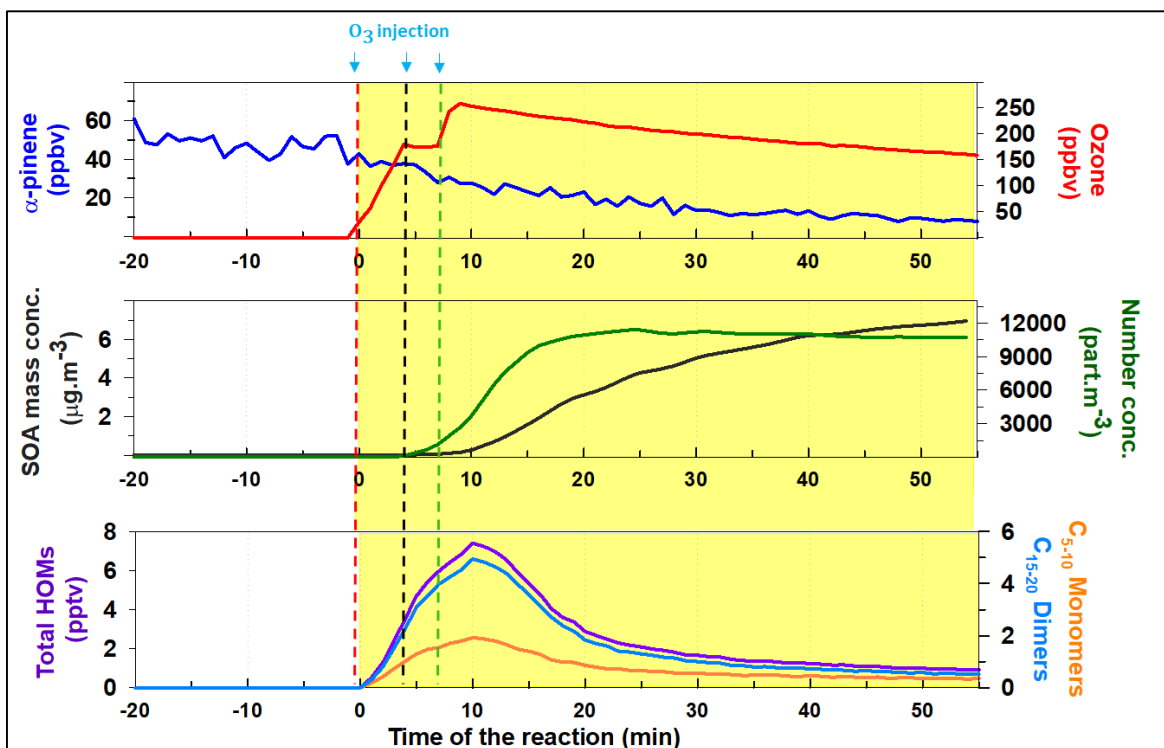


Figure 3.9. Experiment O1-time series of gas phase precursors, α -pinene (in blue) and O_3 (in red), along with the SOA mass and number concentrations (in black and green, respectively), the gas phase products (in pptv), total HOMs (in purple), the sum of C_{5-10} monomers (in orange) and C_{15-20} dimers (in light blue).

The max-min normalization method was employed to divide the monomer and dimer data by their respective peak values (Figure 3.10). This technique, expressed by Equation 3.5 below, ensures that the values are scaled between 0 and 1 (Panda and Jana, 2015). Notably, the minimum value in

the datasets remains at 0, resulting in no alteration to its corresponding value. By applying this method, both the monomer and dimer data were brought to a comparable range, facilitating a clearer comparison of their decay characteristics. Our observations suggest that the decay rate of HOM monomers is slower than that of dimers, with their levels remaining at non-zero levels. This particular trend may be explained by the establishment of an equilibrium between the gas and particle phases. These findings are consistent with the results obtained from a report in the literature that indicates the dominance of particle phase HOM dimers over the monomers in the aerosol phase during α -pinene ozonolysis experiments (Zhao et al., 2023). Nevertheless, other reasons may explain the dominance of dimers in the particle phase, for instance the formation of dimers in the gas phase.

$$X_{\text{norm}} = \frac{X - X_{\text{min}}}{X_{\text{max}} - X_{\text{min}}} \approx \frac{X}{X_{\text{max}}} \quad \text{Equation 3.5}$$

Where, X_{norm} is the min-max normalized data, X is the original data, X_{min} is the minimum value of the data (0 in the present case), and X_{max} is the maximum value of the data.

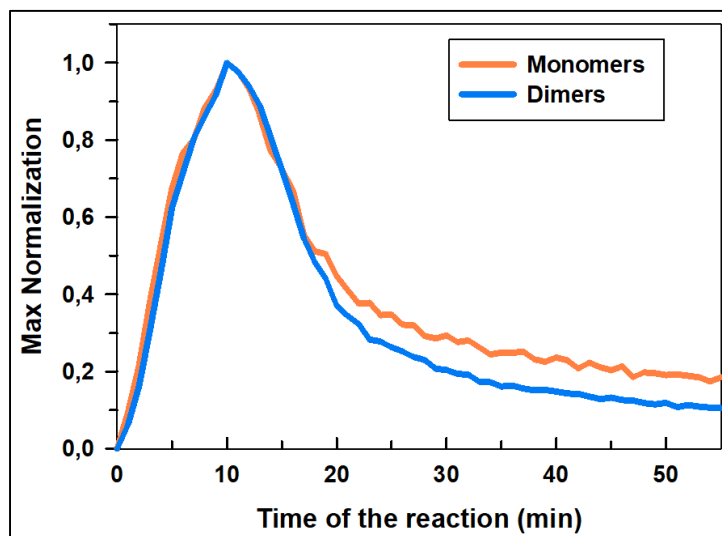


Figure 3.10. Visualization of monomer (orange plot) and dimers (blue plot) data sets using Min-Max Normalization.

One notices that the dominance of dimers over monomers provides evidence of the importance of the monomer- $\text{RO}_2\cdot$ association reactions.

Figure 3.11 shows the mass spectrum (in two m/z ranges) averaged from the start of reaction time to the maximum HOMs level (at about 10 minutes). The y-axis depicts the average of the normalized signals. The mass spectrum analysis reveals that all 158 detected HOMs were observed in a clustered form with NO_3^- . Additionally, due to the absence of NO_x in the chemical environment, both closed-shell and radical products with even and odd m/z hydrogen numbers (refer to section 3.6.2) were observed, and consisted solely of the elements C, H, and O. The

effectiveness of the OH· scavenger is evident, as there are a significantly fewer products with reduced amounts resulting from the reaction between OH· and α -pinene, for example C₁₀H_{14,16}O₈ and C₁₀H₁₆O₆ are three of the prominent peaks from the latter reaction (Poulain et al., 2022), but are not present in our studies (maximum ion ratio of 10⁻⁵). C₁₀H₁₆O₈ may be formed from the reaction of C₁₀H₁₅O₈· with HO₂.

C₁₀H_{14,16}O_{7,9,11}, are the dominant C₁₀ HOMs in these experiments (Figure 3.11.a), along with mainly C₅H₆O₇ and C₈H₁₂O₇. Other C_{5,7,8,9} carbon skeleton products were also detected but to a lesser extent. Two peroxy radicals, namely C₁₀H₁₅O₈· and C₁₀H₁₅O₁₀·, were also identified but in significantly reduced amounts compared to closed-shell molecules. The presence of even oxygen numbers in the HOM-RO₂· radicals strengthens the hypothesis that the initial RO₂ in α -pinene ozonolysis is C₁₀H₁₅O₄· (Figure 3.5).

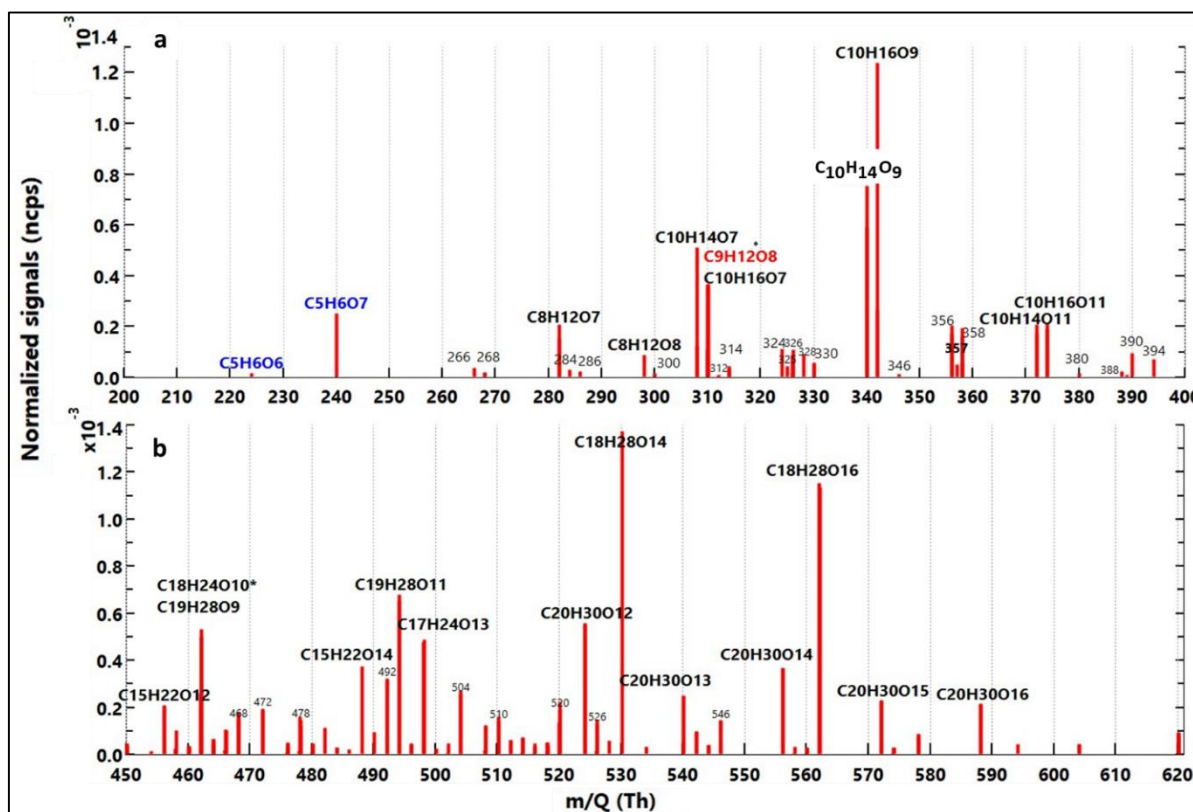


Figure 3.11.a. Averaged mass spectrum of α -pinene ozonolysis experiment-O1 in the monomers mass range (200-400 Th). b. Averaged mass spectrum of α -pinene ozonolysis in the dimers mass range (450-620 Th). The x-axis displays mass to charge ratio (m/z Th) while the y-axis exhibits the normalized signal, as discussed in section 2.3. The m/z values include the mass of the nitrate ion (NO₃⁻), but not shown in the chemical formulas. The compounds the highest signals are presented.

The predominant monomeric molecules (containing 10 or less carbon atoms), which are anticipated to arise from reactions involving C₁₀H₁₅O₁₀· with an R'O₂, are C₁₀H₁₆O₉ and constitute an alcohol product. In addition, C₁₀H₁₄O₉ may be produced from the same reaction or through unimolecular decomposition with the loss of OH· both leading to C₁₀H₁₄O₉· which is presumed to contain a

carbonyl functional group. $C_{10}H_{16}O_9$ has larger signals than $C_{10}H_{14}O_9$ ($C_{10}H_{16}O_9 / C_{10}H_{14}O_9 \approx 1.8$) which can be attributed to the specific reactivity of the involved radicals. It is important to consider an additional possible pathway in which HOM-RO \cdot radicals are involved. This pathway could contribute, at least partially, to the formation of products with similar or different molecular formulas. For instance, this pathway may also explain the higher signal of $C_{10}H_{16}O_9$.

$C_{10}H_{14}O_7$ and $C_{10}H_{16}O_7$ emerge as the second most prevalent termination products identified within the mass spectrum. These compounds are anticipated to originate from the reaction involving $C_{10}H_{15}O_8\cdot$ with $R'O_2$. Although other radicals were not directly observed in the spectrum, their termination products were detected. For instance, $C_{10}H_{14}O_{11}$ and $C_{10}H_{16}O_{11}$ were observed and are most likely the termination products derived from the peroxy radical $C_{10}H_{15}O_{12}\cdot$. It is possible that other radicals also exist at concentrations below the detection limit, have undergone rapid reactions, or have been lost due to loss on the chamber walls or aerosols.

Fragmentation of reaction products also occurred during the reaction studied. The identification of products at $C_{5,7,8,9}$ is a clear indication of fragmentation of the C_{10} carbon skeleton. This process is believed to have entailed the production of RO \cdot radicals via $RO_2 + R'O_2 / HO_2$ reaction, which can result in the cleavage of a C-C bond adjacent to the alkoxy group. The formulas for two predominant fragmentation C_5 -molecules, namely $C_5H_6O_6$ and $C_5H_6O_7$, are highlighted in blue color in Figure 3.11. We can conclude that these C_5 fragments originate from α -pinene rather than cyclohexane, as these species were not identified in the other chemical systems involving limonene and 3-carene, despite the presence of cyclohexane at elevated concentrations. Similar molecules were observed in chamber experiments reported in the literature (Ehn et al., 2012; Zhao et al., 2023).

The accretion products observed (Figure 3.11.b) are composed primarily of two products: $C_{18}H_{28}O_{14,16}$. These may be formed from the reaction between $C_{10}H_{15}O_x\cdot$ and $C_8H_{13}O_y\cdot$ with the number of oxygen atoms in the dimer equal to $x+y-2$. The fragmentation of $C_{10}H_{15}O_x\cdot$ could potentially account for the detected $C_8H_{13}O_y\cdot$, as demonstrated by Molteni et al. (2019), resulting in loss of CH_2O_2 from the radical. One possible combination resulting in the formation of $C_{18}H_{28}O_{14}$ may be reaction between $C_{10}H_{15}O_8\cdot$ and $C_8H_{13}O_8\cdot$. The latter may also explain the importance of $C_8H_{12}O_7$ as one main fragmentation product. $C_8H_{13}O_8\cdot$ radicals may also undergo unimolecular reaction or reaction with $R'O_2$ yielding $C_8H_{12}O_7$. Two possible combinations resulting in the formation of $C_{18}H_{28}O_{16}$ include $C_{10}H_{15}O_{10}\cdot$ reaction with $C_8H_{13}O_8\cdot$ and $C_{10}H_{15}O_8\cdot$ reaction with $C_8H_{13}O_{10}\cdot$. Significant signals that were observed are attributed to families of

$C_{20}H_{30}O_{12-16}$ (with overlapping peaks of $C_{19}H_{26}O_{10-17}$) and $C_{19}H_{28}O_{9-16}$ which can be formed from combination of $C_{10}H_{15}O_{x+y}$ or $C_{10}H_{15}O_x$ with $C_9H_{13}O_y$.

It is worth mentioning that when no fragmentation occurs, dimers typically consist of twice as many carbon atoms as the corresponding monomer species. Ideally, for a compound with 10 carbon atoms (C_{10}), the dimer contains 20 carbon atoms. However, in cases where fragmentation processes occur, which appear to be active in the α -pinene ozonolysis, the dimers can have fewer carbon atoms compared to twice that in the original monomer species.

Overall, the most prominent C_{10} -monomers and C_{19-20} dimers as reported in the literature are similar to those obtained from this experiment, but with different distributions that may be caused by the precursors mixing ratios (Jokinen et al., 2015; Kirkby et al., 2016; Quéléver et al., 2019; Zhao et al., 2023). Earlier studies have indicated that the generation of gas-phase intermediates, particularly those with low volatility, can vary with the initial precursor concentrations (Chen et al., 2019, 2022). Changing the initial amounts of the precursors may thus shift the prevalence of specific reaction pathways, resulting in variations in the distributions and amounts of the resulting products. Overall, yields of products are higher at lower initial precursor amounts.

The consistency of the α -pinene ozonolysis results was verified in another experiment (Experiment O-2). Shown in Figure 3.12.a are two different mass spectra as evidence. The initial conditions of Experiments O-1 and O-2 were similar (see Figure S.3.3). The normalized signals showed that the overall product distribution and pattern was quite similar in experiments O-1 and O-2. Figure 3.12.b, illustrates the peak ratios from Experiment O2/Experiment O1 and it shows that the majority of the molecules were detected with a ratio of about 1 except for a few products.

For a comprehensive listing of the full range of HOMs identified within the 2 experiments, Table S.3.1 present the peaks observed with exact masses and elemental composition (O/C and H/C ratios).

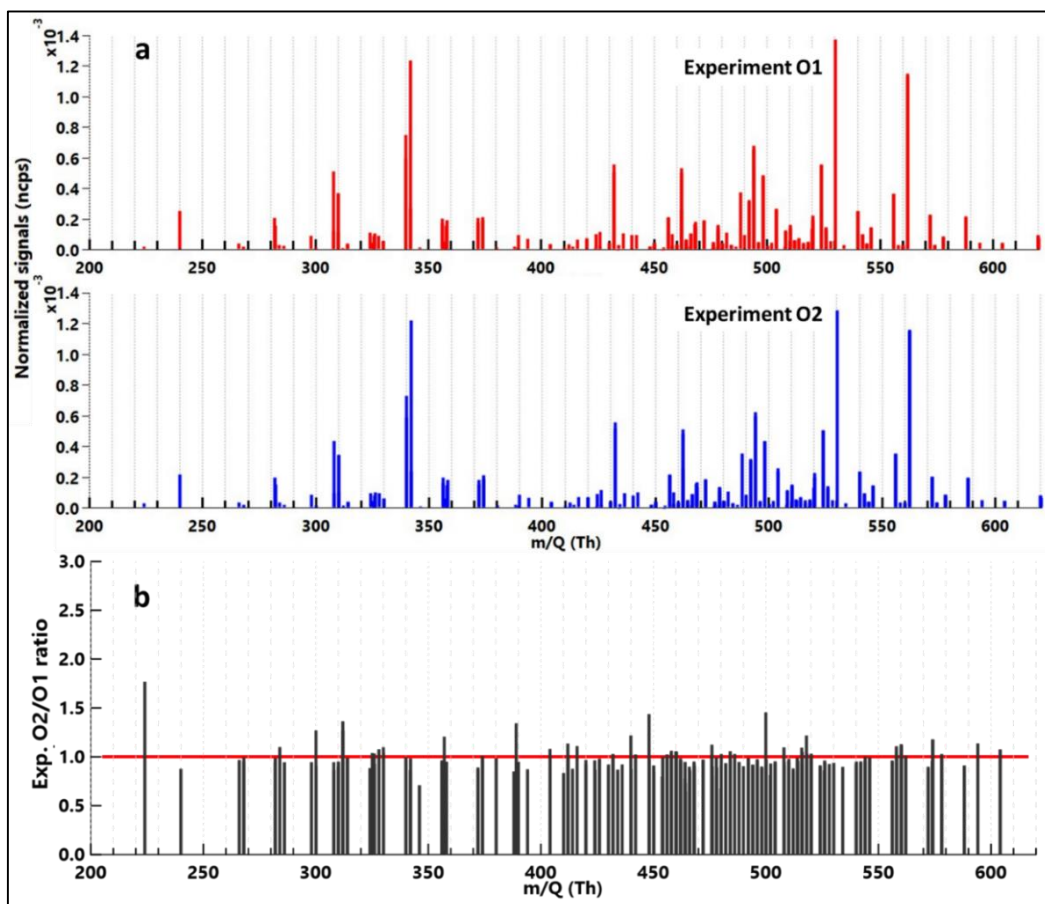


Figure 3.12.a. Comparison of average mass spectra obtained from Experiment O1 (red bars) and O2 (blue bars). b. Ratio of peaks detected from Experiment O2 to Experiment O1. The red bar shows the ratio of 1.

3.7.2. Limonene Ozonolysis experiments

In Figure 3.13, time series data from the limonene oxidation Experiment O-3 is presented, as presented for Experiment O-1 in Figure 3.9. The experiment was conducted at temperatures in the range of 17-17.1°C with an initial limonene concentration of 50.4 ± 5.3 ppbv.

As in the α -pinene ozonolysis experiments (O-1 and O-2), after the injection of O_3 into the chamber there was a rapid and significant increase in the level of total HOMs. This level peaked after approximately 5 minutes of reaction time followed by a gradual decrease as products transfer to the aerosol phase. There was a gradual increase in the mass of aerosols and a significant rise in the particle number concentration, after about 10 minutes.

We observed significantly greater aerosol amounts (mass and number) in the ozonolysis of limonene compared to α -pinene (Figure 3.9 and Figure 3.13). This outcome is anticipated due to the presence of two double bonds in limonene, in accordance with previous studies in the literature (Koch et al., 2000; Jonsson et al., 2006; Youssefi and Waring, 2014; Cain et al., 2021). The levels

of HOM dimers in the limonene experiment surpassed those of monomers, as in the α -pinene experiments.

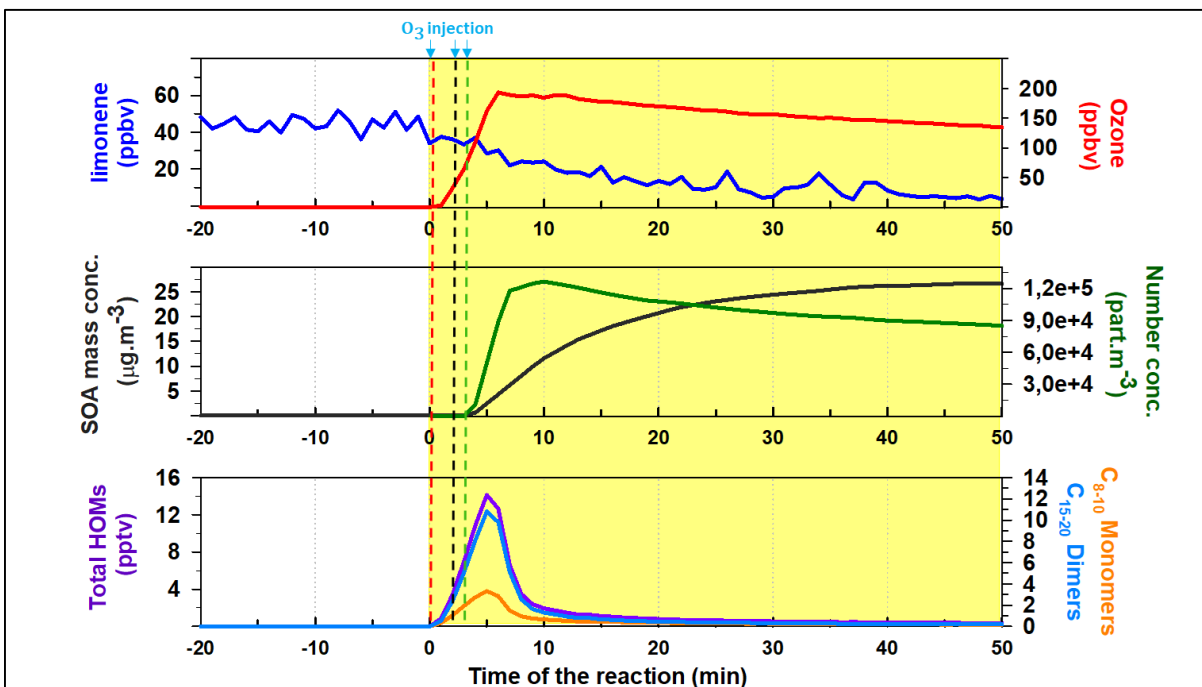


Figure 3.13. Experiment O3-time series of the gas phase precursors limonene (in blue) and O₃ (in red), along with the SOA mass and number concentrations (in black and green, respectively), the gas phase products (in pptv), total HOMs product (in purple), the sum of C₈₋₁₀ monomer (in orange) and C₁₆₋₂₀ dimer (in light blue).

The mass spectrum from Experiment O-3 is depicted in Figure 3.14. Only 41 peaks were observed and identified (Table S.3.2). Similar to the α -pinene ozonolysis mass spectra, the most abundant closed-shell monomers identified exhibited the general formulas C₁₀H_{14,16}O_{7,9,11}. Two RO₂· radicals, C₁₀H₁₅O_{8,10}·, were also observed with somewhat lower intensities. Among the detected monomer fragments within the mass range, C₈H₁₂O₇ was the sole fragment identified and with a much lower intensity than C₁₀ monomers. However, a portion of the fragmentation process was observed in the dimer product range, with the predominant presence of C₁₈ and C₁₉ carbon skeleton products (Table S.3.2).

Another notable difference between oxidation of α -pinene and limonene is the relative abundance of products generated. For limonene, the C₁₀H₁₄O₉ species exhibits higher signal intensity compared to the C₁₀H₁₆O₉ species (C₁₀H₁₆O₉ / C₁₀H₁₄O₉ \approx 0.6 compared to 1.8 for α -pinene). This could be attributed to the reduced formation of RO· radicals, as evidenced by the occurrence of fewer products of fragmentation.

The most abundant dimers observed during this experiment are $C_{19}H_{30}O_{12,14}$, $C_{19}H_{28}O_{11,14}$ and $C_{20}H_{30}O_{12,14,16}$. Although $C_{10}H_{15}O_6$ molecules were not observed in the mass spectrum, their reaction with $C_{10}H_{15}O_8$ may explain the formation of $C_{20}H_{30}O_{12}$ (Tomaz et al., 2021).

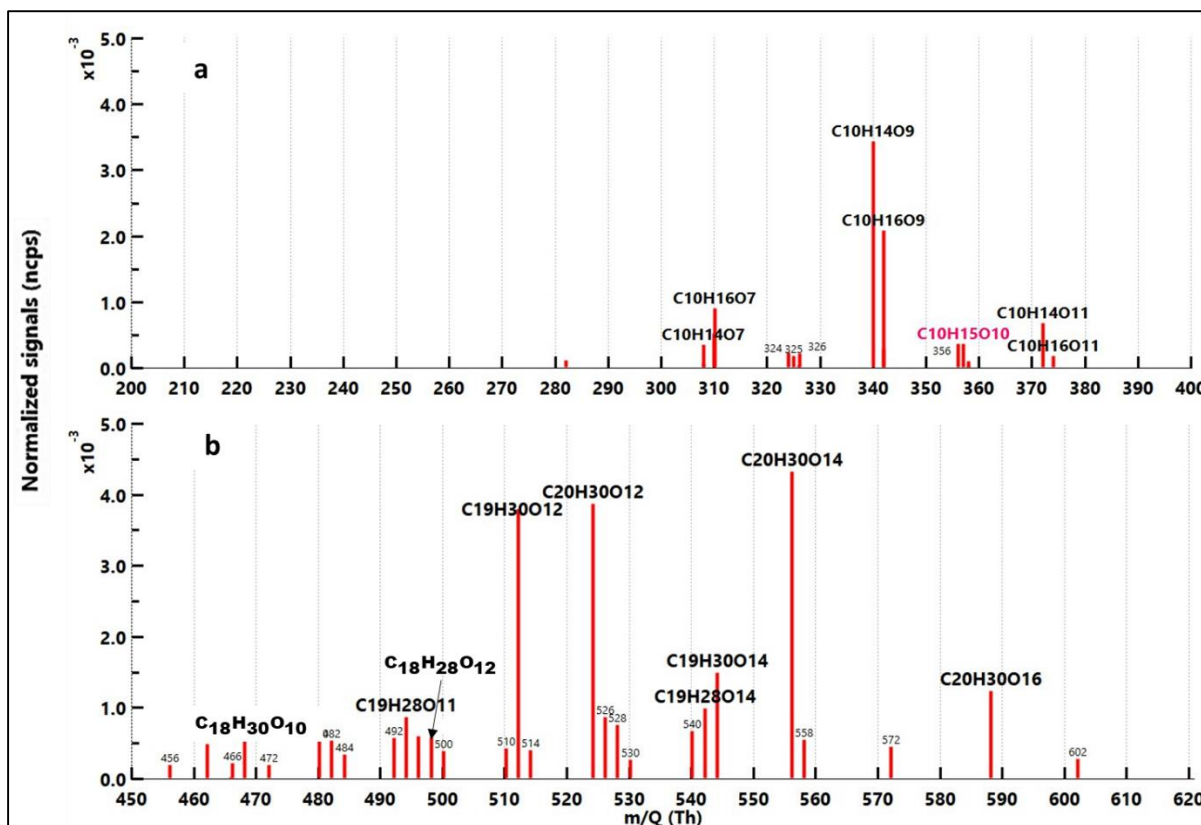


Figure 3.14. Average mass spectrum of limonene ozonolysis experiment-O3 in the monomer mass range (200-400 Th). b. Average mass spectrum of limonene ozonolysis in the dimer mass range (450-620 Th). The x-axis displays mass to charge ratio (m/z Th) while the y-axis exhibits the normalized signal, as explained in section 2.3. The m/z value include the mass of the nitrate ion (NO_3^-). The compounds with the highest signals are presented.

To validate the reproducibility of limonene ozonolysis experiments, a second experiment (Experiment-O4) was conducted, involving an initial amount of 51.3 ± 5.7 ppbv of limonene at 17.5 - $17.6^\circ C$. The O_3 concentrations were slightly different from the previous limonene experiment (Figure S.3.4), but the normalized signals of the overall product distributions remained consistent between the two experiments (O-3 and O-4). Figure 3.15.a presents the two corresponding mass spectra. Figure 3.15.b illustrates the peak ratios between Experiment O4 and Experiment O3, revealing that most molecules were detected with a ratio of approximately 1.

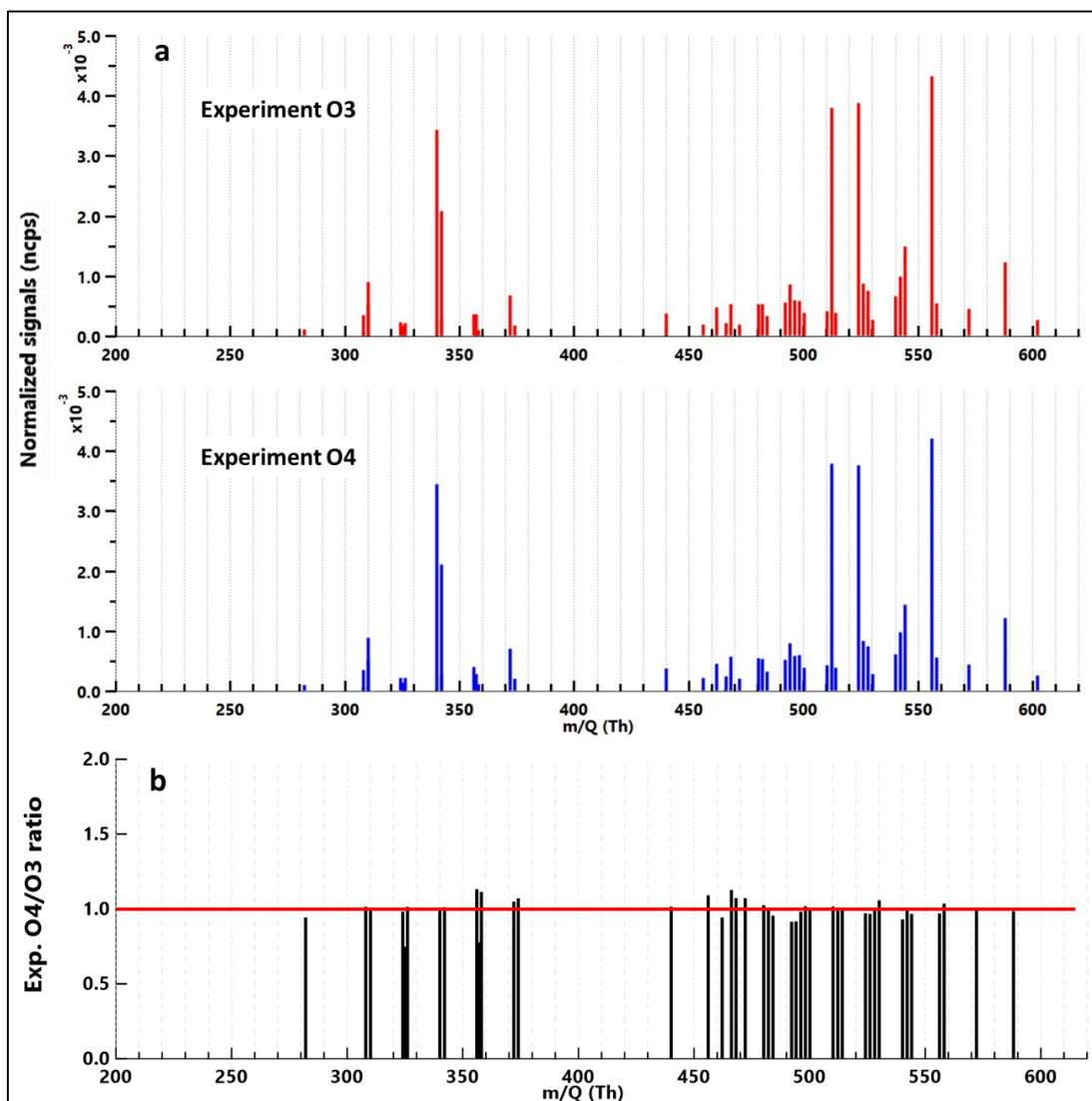


Figure 3.15. a. Comparison of average mass spectrum obtained from Experiments O3 (top) and O4 (bottom). b. Ratio of peaks detected from Experiment O4 to Experiment O3. The red bar points to the ratio equal to 1.

3.7.3. 3-carene Ozonolysis experiments

Two studies of 3-carene oxidation were conducted. The first one (Experiment-O5) was carried out at a temperature of 19.9-20°C and 52.4 ± 2.02 ppb initial terpene mixing ratio (Figure 3.16). The levels of HOMs peaked at 5 minutes. Subsequently, the decrease in HOMs levels, coincided with an increase in aerosol mass and number, as in the other studies of monoterpenes.

Like the experiments with α -pinene, it is evident that the decay rate of HOM monomers is slower than that of dimers. For both α -pinene and limonene, the gas phase concentration of dimers was about 30% greater than that of monomers. The average mass spectrum (Figure 3.17) depicts the peaks identified through the NO_3^- ToFCIMS analysis. Overall, 79 compounds were detected.

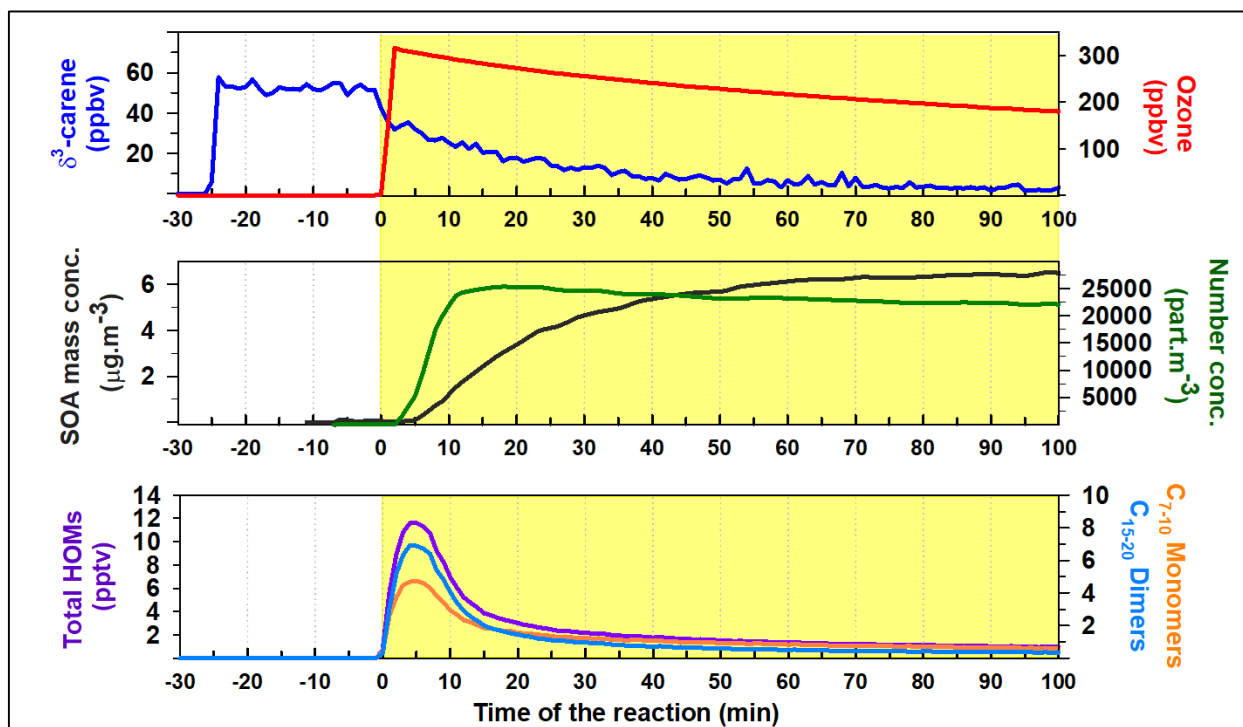


Figure 3.16. Experiment O5-time series of gas phase precursors, 3-carene (in blue) and O₃ (in red), along with the SOA mass and number concentrations (in black and green, respectively), the gas phase normalized total HOMs products (in purple), the sum of C₇₋₁₀ monomers (in orange) and C₁₅₋₂₀ dimers (in light blue).

The primary HOMs products from the 3-carene experiments were similar to α -pinene and limonene. We can notice similar distributions of C₁₀ monomers those of α -pinene ozonolysis, with the most abundant closed-shell monomers identified in the 3-carene experiments exhibiting a general formula of C₁₀H_{14,16}O_{7,9,11}. Limited fragmentation occurred in this reaction system with some C₇₋₉ monomers observed with one noteworthy distinction which is the presence of a peak identified as C₉H₁₂O₉ exhibiting the highest signals among the entire mass spectrum. An alternative explanation could be that the observed peak corresponds to C₁₀H₁₆O₈ rather than C₉H₁₂O₉. However, the peak identification protocol (as described in S.2.3.4) resulted in a significant deviation (112 ppm) between the exact mass of C₁₀H₁₆O₈ and the observed peak. Evidence of the fragmentation process was observed in the dimer product mass range (Table S.3.3). About 5% of the dimer signals is due to C₁₈H₂₈O_{11,13}, 18% is due to C₁₉H₂₈O_{9,11,13}, and 19% is due to C₂₀H₃₀O_{10,12,14,16}.

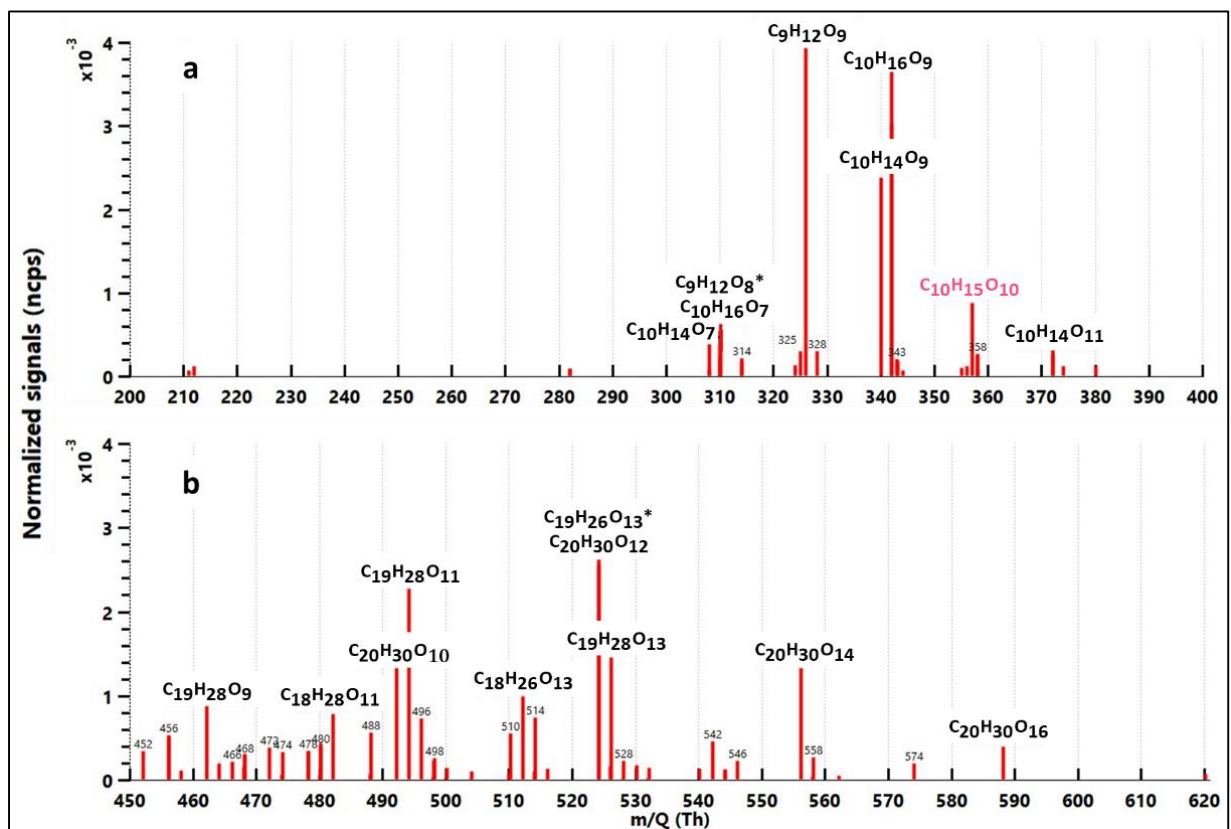


Figure 3.17. Average mass spectrum of 3-carene ozonolysis experiment-O5 in the monomers mass range (200-400 Th). b. Average mass spectrum of 3-carene ozonolysis in the dimers mass range (450-620 Th). The x-axis displays mass to charge ratio (m/z Th) while the y-axis exhibits the normalized signal, as explained in section 2.3. The m/z value demonstrated is aligned with the nitrate ion (NO_3^-). The compounds with relatively higher signals are presented, although some peaks may have overlapping signals, but the dominant one is displayed (*for example).

To confirm the results from Experiment-O5, an additional experiment (Experiment-O6) was conducted with an initial 3-carene mixing ratio of 47.8 ± 3.3 ppbv and a temperature range of 20.3-20.4 °C. However, the levels of O_3 were significantly greater in O6 compared to O5 (Figure S.3.5). As a result, in O6 the HOMs products exhibited different temporal behavior and lower levels, approximately one order of magnitude lower. The mass spectra from Experiment-O5 and Experiment-O6 are shown in Figure S.3.6. One hypothesis that can be proposed is that the larger amount of O_3 in Experiment-O6 might have influenced the reaction kinetics and led to the formation of more volatile compounds with different chemical properties that were not detected by the NO_3^- ToF-CIMS. It is evident that Experiment-O6 proceeded at a faster rate, indicated by a reduction in reaction time compared to Experiment-O5 (Table 3.5).

Table 3.5. Summary of the experimental conditions, the BVOC and the reaction time in min. The reaction time is defined as the period starting from the initial injection of the oxidant and extending until the end of the experiment.

Experiment	BVOC	Reaction time (min)
O1	α -pinene	47.00
O2	α -pinene	50.00
O3	limonene	28.00
O4	limonene	24.00
O5	3-carene	59.00
O6	3-carene	41.00
O7	3-carene+limonene	40.00
O8	α -pinene+limonene	46.00

3.7.4. Ozonolysis experiments of BVOC mixtures

Two additional experiments were performed using mixtures of BVOCs: limonene + 3-carene (Experiment-O7, that had 81 identified peaks shown in Table S.3.4) and limonene + α -pinene (Experiment-O8, with 105 identified peaks shown in Table S.3.5). The purpose of these experiments was to examine whether the types of HOMs changes when different BVOCs are present in a mixed system. For each system, the two BVOCs are injected at similar mixing ratios. Due to limonene's faster reaction rate with O₃, it is expected that limonene dominates the production of HOMs. This expectation is confirmed in the mass spectra of these two experiments (Figure 3.18). The distribution of products, particularly in the monomer mass range and specifically the ratios C₁₀H₁₆O₇/C₁₀H₁₄O₇ and C₁₀H₁₆O₉/C₁₀H₁₄O₉, were very similar to those found in the ozonolysis experiments (O3 and O4) with limonene only. Experiment O7 exhibited a greater formation of dimers compared to ozonolysis of the individual compounds, with many of the same peaks as found in the limonene-only experiments as well as the largest peaks from the 3-carene-only experiments. This resulted in a higher signal of HOMs for the terpene mixture. However, these effects were not observed in the limonene + α -pinene experiment.

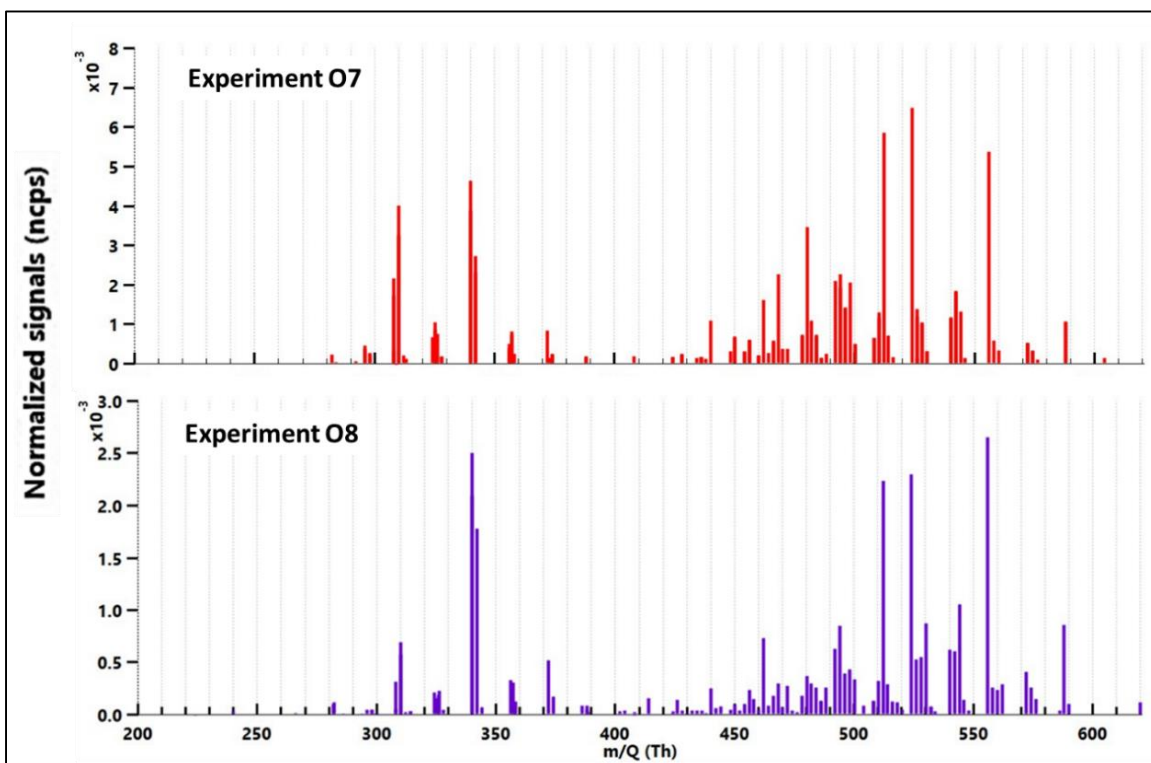


Figure 3.18. Comparison of the average mass spectrum obtained from Experiments O7 (red bars) and O8 (purple bars).

3.7.5. α,β -phellandrene + $\text{NO}_3\cdot$ reactions

The NO_3^- ToFCIMS was employed in the experiments involving α,β -phellandrene + $\text{NO}_3\cdot$ experiments to help characterize our instrument but also to assess the significance of nitrates formed within the context of oxidation chemistry. The outcomes of the α,β -phellandrene + $\text{NO}_3\cdot$ reaction systems are comprehensively discussed in two separate studies authored by my colleague, Sergio Harb, where I also contributed as a co-author (Harb et al., 2023a, 2023b). These studies discuss the mechanism and possible products of the chemistry, including those related to HOMs formation.

In this section, the reaction pathways leading to HOMs formation from α -phellandrene and β -phellandrene oxidation are briefly presented.

In general, $\text{NO}_3\cdot$ reacts with alkenes (including α - and β -phellandrene) through addition to one of the two C=C bonds, with H-abstraction negligible, resulting in the creation of nitrooxy-alkyl radicals ($\text{C}_{10}\text{H}_{16}\text{NO}_3\cdot$) with an even hydrogen atom number. $\text{C}_{10}\text{H}_{16}\text{NO}_3\cdot$ subsequently reacts with O_2 yielding the first $\text{RO}_2\cdot$ radical ($\text{C}_{10}\text{H}_{16}\text{O}_2\text{NO}_3\cdot$). $\text{C}_{10}\text{H}_{16}\text{O}_2\text{NO}_3\cdot$ can further evolve through subsequent H-atom shift and O_2 addition yielding $\text{C}_{10}\text{H}_{16}\text{NO}_y\cdot$ (where y is an odd number) with additional $-\text{OOH}$ functional groups. $\text{C}_{10}\text{H}_{16}\text{NO}_y\cdot$ undergoes unimolecular or bimolecular termination reactions following $\text{RO}_2 + \text{RO}_2$, $\text{RO}_2 + \text{NO}_3$ and $\text{RO}_2 + \text{HO}_2$ reactions. Monomers with

a closed-shell structure containing a single nitrogen atom exhibit an odd hydrogen count (15 or 17 H). Nitrooxy-alkoxy radicals ($\text{NO}_3\text{-RO}\cdot$) can be formed from $\text{RO}_2 + \text{RO}_2$ and $\text{RO}_2 + \text{NO}_3$ reactions. In these studies, N_2O_5 was introduced continuously in small amounts, generating continuously maintained low NO_3 concentrations. RO_2 self-reactions are thus expected to contribute the most to the loss of RO_2 . This was confirmed by performing numerical simulations using the Master Chemical Mechanism, MCM (Saunders et al., 2003). The results of these simulations are included in the supplement material of the Harb et al. papers. The ToFCIMS measurements allowed identification of numerous HOM organic nitrates. The products observed and the experimental conditions for these studies have been compiled and are included in the supplementary material of this dissertation (Table S.3.6-10).

For the α -phellandrene + NO_3 chemical system, HOMs were quickly formed after initiation of the reaction. Figure 3.19 present an example of the mass spectra obtained from α -phellandrene Experiment-N6. The spectra are divided into two distinct mass regions 330 to 390 m/z and 500 to 660 m/z. Overall, 22 HOM compounds, which all included a N atom, were detected including 8 C_9 ($\text{C}_9\text{H}_{14}\text{N}_2\text{O}_{9,10}$) and C_{10} monomers ($\text{C}_{10}\text{H}_{15}\text{NO}_{8,9,11}$, and $\text{C}_{10}\text{H}_{17}\text{NO}_{8-10}$), as well as C_{17} ($\text{C}_{17}\text{H}_{26}\text{N}_2\text{O}_{12-16}$) and C_{20} dimers ($\text{C}_{20}\text{H}_{32}\text{N}_2\text{O}_{10-18}$). The number of nitrogen atoms can provide indications of secondary double bond oxidation or the chemistry involving $\text{RO}_2 + \text{NO}_2$, which arises from the presence of NO_2 produced in the decomposition of N_2O_5 . No $\text{HOM-RO}_2\cdot$ radicals were detected.

$\text{C}_{10}\text{H}_{15}\text{NO}_8$ and $\text{C}_{10}\text{H}_{17}\text{NO}_8$ were the two most prominent monomers detected. This is consistent with the results obtained from studies involving reactions of β -pinene with $\text{NO}_3\cdot$ (Shen et al., 2021; Dam et al., 2022) and limonene with $\text{NO}_3\cdot$ (Guo et al., 2022a). The higher signals for $\text{C}_{10}\text{H}_{15}\text{NO}_8$ (carbonyl product) compared $\text{C}_{10}\text{H}_{17}\text{NO}_8$ (hydroxyl product), suggesting that $\text{C}_{10}\text{H}_{15}\text{NO}_8$ is formed through an additional reaction pathway other than $\text{RO}_2 + \text{RO}_2$, i.e. $\text{RO}\cdot + \text{O}_2$.

Regarding the accretion products, $\text{C}_{20}\text{H}_{32}\text{N}_2\text{O}_{16}$ is the highest peak among all detected HOMs, which could result from accretion reactions such as $\text{C}_{10}\text{H}_{16}\text{NO}_9\cdot + \text{C}_{10}\text{H}_{16}\text{NO}_9\cdot$, $\text{C}_{10}\text{H}_{16}\text{NO}_{10}\cdot + \text{C}_{10}\text{H}_{16}\text{NO}_8\cdot$, or $\text{C}_{10}\text{H}_{16}\text{NO}_{11}\cdot + \text{C}_{10}\text{H}_{16}\text{NO}_7\cdot$. $\text{C}_{17}\text{H}_{26}\text{N}_2\text{O}_{12-16}$ dimers may involve the reaction between a $\text{C}_7\text{-RO}_2\cdot$ radical and a $\text{C}_{10}\text{-RO}_2\cdot$ radical. This supports the formation of a $\text{C}_7\text{-RO}_2\cdot$ radical through the alkoxy fragmentation of a C_{10} monomer. This was confirmed by the detection of acetone in this system using PTR-MS.

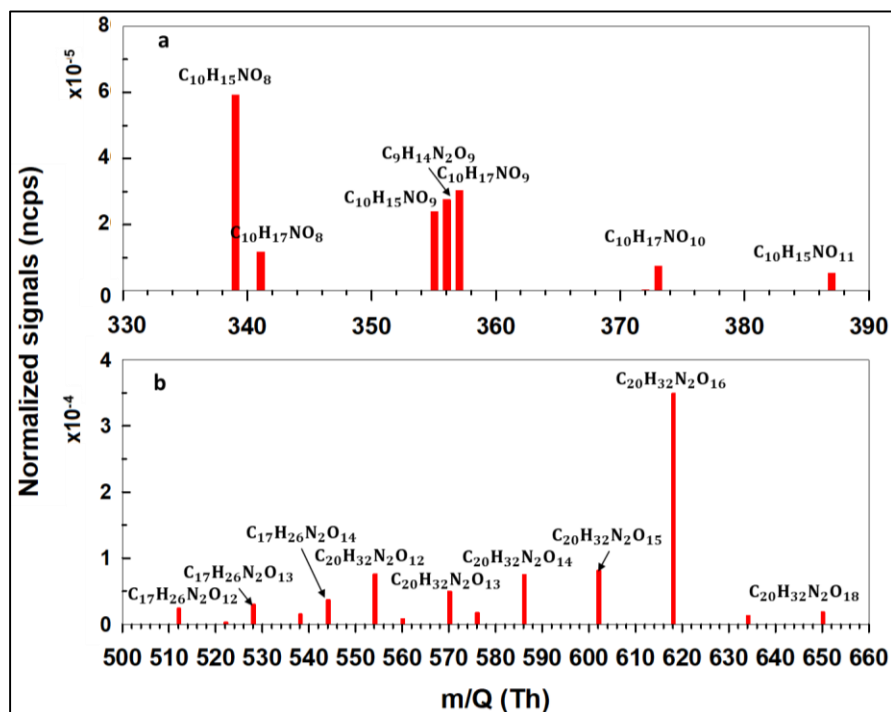


Figure 3.19. Averaged Mass Spectrum of Exp. N6 for α -phellandrene + NO₃ in the monomers mass range (330-390 Th). b. Averaged Mass Spectrum of Exp. N6 for α -phellandrene + NO₃ in the dimers mass range (500-660 Th). The x-axis displays mass to charge ratio (m/z Th) while the y-axis exhibits the normalized signal. The m/z value include the mass of the nitrate ion (NO₃⁻). The compounds with the highest signals are presented. The averaging is performed for spectra collected during the first 10 min after the addition of N₂O₅.

Additional experiments involving VOC mixtures were conducted with the addition of C₄H₈ (trans-2-butene) into the α -phellandrene + NO₃ system (refer to Table 3.3) to explore the influence of such combinations on the chemistry, including HOM and SOA formation. Experiment N11 (with C₄H₈) and N12 (without C₄H₈) are compared to study this influence, since they are both performed in similar conditions (with initial BVOC mixing ratios of about 80 ppb and oxidation times of about 1 hour). The primary distinctions in product composition and quantities are depicted in Figure 3.20. In brief, a notable reduction in the signals of the primary HOM dimer C₂₀H₃₂N₂O₁₆ was observed in N11. The C₁₀H_{15,17}NO₉ and C₉H₁₄N₂O₉ signals were also reduced. Conversely, new products like C₁₀H₁₅NO₁₀ and C₁₀H₁₄N₂O₁₃₋₁₅ emerged. However, as anticipated from accretion reactions involving C₁₀-RO₂[·] and C₄-RO₂[·], no C₁₄ dimers were detected. One hypothesis is that these dimers could have formed at a later stage of the reaction and potentially partitioned directly into the particulate phase. One plausible explanation is that the α -phellandrene + NO₃ reaction is the primary and dominant pathway during the initial phase of the experiment. However, as the BVOC is depleted, the significance of the C₄H₈ + NO₃ reaction increases, leading to formation of C₄ HOM-RO₂[·]. This could potentially result in the presence of low levels of C₄ HOMs that may not be detectable by the ToFCIMS or may rapidly partition into the particle phase.

Furthermore, the introduction of C₄H₈ results in a reduction (up to 50%) in both aerosol number and mass. It is clear that additional investigations are required to fully understand this influence. A detailed discussion and interpretation of the results are presented in the studies in preparation.

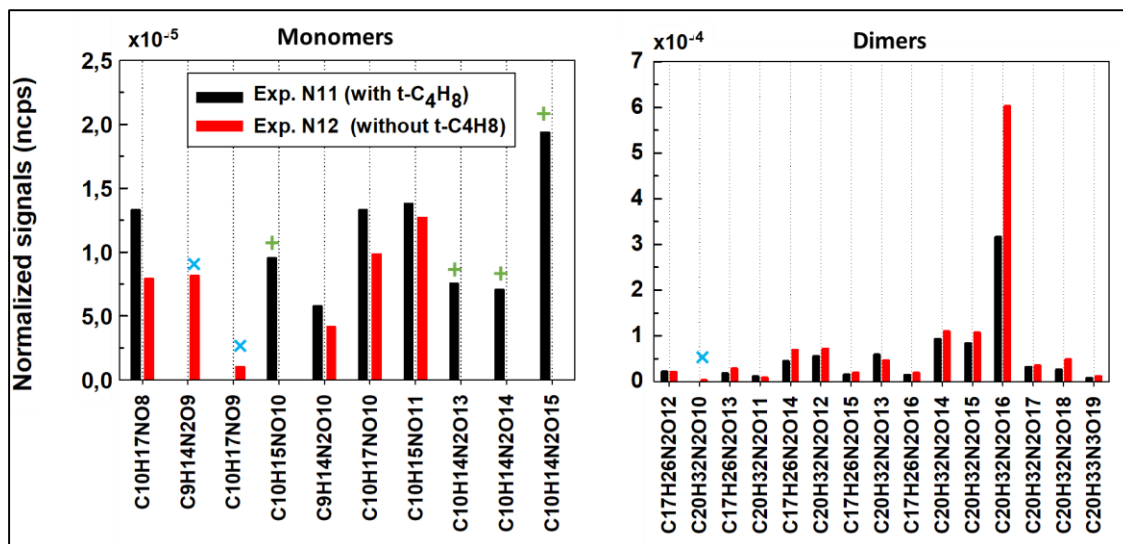


Figure 3.20. Comparison of monomers and dimers detected from α -phellandrene + NO₃ in Exp. N11 (with t-butene) vs Exp. N12 (without t-butene). The values of the normalized signals for the first 10 min reaction after the addition of N₂O₅. Symbol '+' refer to the presence of new products in Experiment N11 that are not found in Experiment N12. Symbol 'x' refer to the absence of products within the Experiment N11 that were found in Experiment N12.

3.8. Discussion

In order to prepare the ACROSS field campaign, a series of experiments were carried out in the simulation chamber of CESAM (sections 3.4 to 3.7). The main objectives of these experiments were to identify potential products that would possibly be encountered in the atmosphere to help in the interpretation of the results obtained in the field and to investigate the performance of the instrument by comparing these results to the one from the literature. Thus, the nitrate ToFCIMS was included in three main chamber campaigns, relying on three different types of reaction systems.

The first group of experiments investigate the reaction of three biogenic VOC precursors: α -pinene, limonene and 3-carene, with ozone in the presence of an OH· radical scavenger. These experiments are conducted without the addition of NO_x or particulate seeds, indicating that the SOA formation is expected from the pure organic nucleation of low volatility species. The primary gas phase HOMs observed from the oxidation of the three monoterpenes shared significant similarities, with the most prominent monomers being C₁₀H_{14,16}O_{7,9,11}. However, their relative abundance showed notable variations, indicating differences in the branching ratios for key processes in each mechanism (Liu et al., 2022). In the case of α -pinene, significant fragmentation occurred in the reaction system resulting in the formation of monomer fragments, particularly C₅H₆O₇ and

$C_8H_{12}O_7$, $C_{10}H_{14,16}O_{7,9,11}$ were the dominant C_{10} monomers, which aligns with similar elemental formulas identified in many literature studies (Ehn et al., 2014; Quéléver et al., 2019; Zhao et al., 2023). Additionally, the dimer region was dominated by $C_{18}H_{28}O_{14,16}$ along with $C_{19}H_{28}O_{9,11}$ and $C_{20}H_{30}O_{12-16}$. For 3-carene and limonene experiments, $C_{10}H_{14,16}O_{7,9,11}$ were also the dominant C_{10} monomers in their respective mass spectra, with minimal fragmentation products. This chemical composition is consistent with reports in the literature (Jokinen et al., 2015; Draper et al., 2019). In the dimer region, limonene experiments primarily featured $C_{20}H_{30}O_{12,14,16}$ and $C_{19}H_{30}O_{12,14}$, which aligns with findings reported by Jokinen et al. (2015). In the experiments involving 3-carene, the highest levels of detected dimers were $C_{19}H_{28}O_{11,13}$ and $C_{20}H_{30}O_{10,12,14,16}$. Similar compounds were also detected by Draper et al. (2019). Notably, a significant difference emerged during our experiments compared to the literature findings. Unlike previous reports, we detected higher levels of dimers compared to monomers. This discrepancy may be attributed to variations in experimental conditions (e.g. differing levels of precursors) thus the chemical kinetics occurring within our experiments. This statement is supported by the findings reported in Molteni et al. (2019), indicating that an increase in the levels of reacted α -pinene lead to an increased dominance of dimers over monomers within the chemical system.

Two additional mixture experiments were conducted. Pairs of monoterpenes (limonene with 3-carene and limonene with α -pinene) were studied and these experiments demonstrated the dominance of the limonene oxidation products with distribution and abundances similar to limonene-only experiments. The mixture of limonene and 3-carene exhibited a greater formation of dimers (compared to the single monoterpene experiments) which was not observed in the limonene+ α -pinene study. The second group of experiments focused on the reaction of two other monoterpene precursors, α -phellandrene and β -phellandrene with $NO_3\cdot$ radicals. The mass spectra showed the presence of a few monomers, but the most significant contribution came from C_{17} and C_{20} organic nitrates.

The last group of laboratory experiments involved studies of the reaction of the AVOCs toluene and m-xylene with $OH\cdot$ radicals. No HOMs were detected in these experiments. The addition of seed particles to the chamber in these experiments appears to have scavenged any HOMs produced into the particle phase, preventing their detection in the gas phase.

Finally, these experiments demonstrated the instrument's ability to detect a wide range of compounds, even when they were present at relatively low concentrations, often at levels as low as a few parts per quadrillion by volume (ppqv).

Chapter 4 Characterization of HOMs in a forested region during an atmospheric measurement field campaign: ACROSS

4.1. The ACROSS Project

ACROSS (Atmospheric ChemistRy Of the Suburban foreSt) was an integrative, innovative, large-scale project, awarded under the French research grant “Make Our Planet Great Again” (MOPGA), and funded by the French National Research Agency (ANR). It is a framework for exploration of the atmospheric interactions between urban anthropogenic emissions within the Paris urban area and rural biogenic emissions originating from the forest of Rambouillet. The project seeks to advance our understanding of the influence of mixing these distinct air masses on the oxidation chemistry, composition, and reactivity of the troposphere.

The primary focus of ACROSS involves a comprehensive measurement campaign using multiple platforms that took place in the summer of 2022. The key objectives include:

- Enhancing our comprehension of tropospheric oxidation chemistry, particularly focusing on the chemical mechanisms of VOCs and their resulting product yields.
- Investigating the horizontal and vertical changes in gas and particle properties.
- Evaluating and improving the accuracy of air quality model predictions and their representations.
- Providing advances in knowledge for various scientific disciplines, such as atmospheric chemistry and physics, analytical chemistry, physical chemistry, and organic chemistry.
- Advancing our knowledge of emissions originating from biological systems.
- Contributing to improved air quality and its associated advantages.

There is a significant involvement of graduate students and collaboration with two urban Paris projects: H2C (Heat and Health in Cities) and sTREEt (Impact of Urban Tree Stress on Air Quality). More details on the implementation of the ACROSS campaign will be provided in the following section 4.2.

4.2. Ambient measurement site description

Within the ACROSS project, a summer ground field campaign took place between June 13 and July 23, 2022 at several sites including a super site situated within the Rambouillet forest, specifically near La Boissière-École, France (coordinates: 48.6866N 1.7045E) (see Figure 4.1). Measurements at this site were conducted both at ground level and atop a 40-meter tower.



Figure 4.1. Photos of the measurement site in the Rambouillet Forest (from the top of the tower on the left) and a view of the 40-m tower (on the right) during the ACROSS summer campaign.

The Rambouillet forest consists predominantly of deciduous trees, including sessile and pedunculate oaks, as well as softwoods such as Scots and lario pine. Table 4.1 provides a distribution of the various tree species present across the forest's surface for the Rambouillet Forest, represented in percentages of the forest surface (ONF, 2006).

Table 4.1. The distribution of tree species in the Rambouillet forest (ONF, 2006).

Species	% of the surface
Sessile and pedunculate oaks	68
Beech	2
Chestnut	2
Other deciduous trees	3
Softwoods	19
Public spaces (lawns, heathlands, etc.)	6

The supersite is situated approximately 50 km west-southwest of central Paris, making it susceptible to be influenced by the urban plume during east-northeasterly wind regimes. The Greater Paris area, encompassing both the City of Paris and its surrounding suburban regions, stands as Europe's most highly populated megacity, boasting an estimated population of around 12 million inhabitants (World Population Review, 2023). This region hosts a diverse array of urban activities, which collectively contribute to notable levels of anthropogenic emissions, including AVOCs, NO_x, and PM. Furthermore, Greater Paris occupies a distinctive geographical position, being located some distance from other major European cities (264 km from Brussels and 344 km from London) and countries (370 km from the Netherlands and 500 km from Germany). The region is characterized by a multitude of urban woodlands (such as Bois de Boulogne and Bois de Vincennes) and is surrounded by forested areas (like the Rambouillet massif (with the Haute Vallée de Chevreuse Regional Natural Park), Fontainebleau massif, Villeferney forest, Jouy forest, etc.) (from the ACROSS white paper).

Based on 16 years of surface O₃ and NO_x data at several Paris suburban sites, the Rambouillet supersite was found to be a good candidate and the most probable place to study the interaction between Paris urban plume and its biogenic emissions, under adequate meteorological conditions, and to meet the primary objectives of the ACROSS project (Cantrell and Michoud, 2022). The ACROSS project incorporates additional ground-based measurement stations to monitor the chemical progression of the urban plume. These stations are highlighted in Figure 4.2 and encompass:

- Two urban sites within Paris at the Campus Paris Rive Gauche (PRG), University of Paris Cité and QUALAIR at Sorbonne university.
- Two experimental suburban sites: SIRTA (Site Instrumental de Recherche par Télédétection Atmosphérique), situated at Ecole Polytechnique in Palaiseau, positioned between the Rambouillet supersite and Paris (<https://sirta.ipsl.fr/>).
- A downwind site managed by the Université d'Orléans, CNRS.
- Airparif and Lig'Air air quality network stations.



Figure 4.2. Map of the main site locations involved in the ACROSS campaign.

Airborne observations were carried out from 14 June until July 6 using the ATR-42 aircraft, which is part of the French research aircraft fleet. This aircraft is operated by the French office of aircraft instrumented for environmental research (SAFIRE). Briefly, the ATR-42 was equipped with a range of instruments to measure both the gas-phase (a UV absorption analyzer for O₃, analyzers for NO and NO₂, PICARRO analyzer for CO, CO₂, CH₄ and H₂O, a PTRMS for VOCs) and particle species (a condensation particle counter (CPC), a nephelometer, sampling on filters, a GRIMM optical particle counter, etc.).

4.3. Instrumentation Deployed for Ambient Measurements at the Rambouillet supersite

This part of this thesis research centers on the data gathered at the Rambouillet supersite during the campaign, with particular emphasis on the information obtained through the NO_3^- ToFCIMS instrument situated on top of the tower.

4.3.1. Deployment of NO_3^- ToFCIMS during ACROSS campaign

The NO_3^- ToFCIMS was operated with the same parameters used in the laboratory, with a spectral sampling rate of 16.7 kHz and with spectra covering a wide mass-to-charge range (7-1126 m/z). The average mass resolving power was approximately 3700, with a mass accuracy of more than 10 ppm, achieved through the methodology detailed in Chapter 2 section 2.1.5. Ambient air was directly drawn into the inlet at a flow rate of about 8 lpm through a 1-meter long $\frac{3}{4}$ inch o.d and 0.61 inch i.d. stainless-steel tube. Background zeroing occurred automatically every 3 hours for a duration of 10 min by means of the ‘TPS scripting settings’ feature via Aquility software. Zero air generation relied on an oil-free air compressor (Vevor model 550-9l) that channels ambient air, maintaining a controlled pressure, through a HC trap to attain a nearly pollutant-free air at ambient humidity. The instrument was housed in a room at the top of the tower (Figure 4.3) which was eventually equipped with air-conditioning to prevent pump failure caused by elevated temperatures during heatwaves that were encountered during the campaign. Successful measurements spanned a period of over 21 days, encompassing 14 full-day data coverage (over the entire 24-hour period of a day) and 7 partial day data acquisition (portions of the day). The missing data were a result of instrument malfunctions, such as the previously mentioned pump failure, as well as other unforeseen technical issues. Data points were collected every second and subsequently averaged over 10-minute intervals for post-processing. Raw data underwent background signal subtraction.



Figure 4.3. Photos showing, from left to right, the room atop of the tower, the installation of the NO_3^- ToFCIMS and the instrument in its acquisition mode during the ACROSS summer campaign.

The SSQ pressure ranged from 2.10 to 2.21 mbar, while the BSQ pressure ranged between approximately 2.2 and 2.4 mbar, with variations occurring throughout the day. Significant diurnal variations in the reagent ions were also observed, presumably due to changes in T and RH over the course of the day. This supports the necessity of normalizing data over the sum of the reagent ion signals including the first water cluster.

The majority of ions identified in the mass spectra were observed as clusters with NO_3^- ions, comprising approximately 90% of the detected ion peaks. Only about 10% of the ion peaks corresponded to deprotonated ions, primarily appearing at m/z values below 200. These deprotonated ions exhibited significantly lower signal intensities compared to the dominant cluster peaks.

In the upcoming sections, the molecular formulas will be showcased without the inclusion of the NO_3^- cluster ion, and the signals of the peaks present in both forms are summed. The reported values, in units of pptv, were calculated using Equation 2.4 with the calibration factor $\text{C}_{\text{H}_2\text{SO}_4}$ of $4.22 \times 10^9 \text{ molecules} \cdot \text{cm}^{-3}$ established in Section 2.3.3, using the field setup (setup 2) and determined by generation of known H_2SO_4 amounts.

4.3.2. Additional Instruments Positioned atop of the tower

Numerous other instruments were positioned atop the tower and are summarized in Table 4.2.

The measurements encompassed a diverse array of parameters:

- Gaseous species, including O_3 , NO, NO_2 , NO_x , NO_y , NO_3 , N_2O_5 , HONO, SO_2 , CO, CO_2 , CH_4 , VOCs, HOMs, H_2SO_4 ,
- Aerosol composition,
- Radicals, encompassing $\text{HO}_2 \cdot + \text{RO}_2 \cdot (\text{AOx})$,
- Meteorological factors, including solar radiation (SR), wind speed (WS) and direction (WD), temperature (T), relative humidity (RH) and ambient pressure (P).

Table 4.2. Measurement techniques deployed during the campaign at the top of the tower.

Parameter	Instrument	Sampling type	Team
O ₃	UV absorption	Manifold	LISA
SO ₂	Pulsed Fluorescence	Manifold	LISA
NO _x	O ₃ chemiluminescence & CAPS	Direct + Manifold	LISA
NO _y	O ₃ chemiluminescence + gold converter	Direct	LISA & IMT
HONO	IBBCEAS	Direct	LISA
NO ₃ & N ₂ O ₅	IBBCEAS	Direct	LISA
NH ₃	Passive tubing	Direct	INRAE
HOMs	Nitrate-ToF-CIMS	Direct	LISA
VOCs & OVOCs	PTR-QiTofMS	Manifold & dedicated line	IMT & INRAE
VOCs	GC/FID & GC/FID/MS	Manifold	ICARE & IMT
CO, CO ₂ & CH ₄	PICARRO	Manifold	LSCE
HO ₂ + RO ₂	PERCA	Direct	IMT
OH reactivity	FAGE reactivity	Manifold	PC2A
Eddy covariance fluxes (VOC, CO ₂ , H ₂ O, wind, O ₃ , NO _x , N ₂ O, CH ₄)	PTR-QiTofMS, LICOR7500, Fast O ₃ , MIRO	Dedicated line	INRAE
Aerosol chemical composition	ToF-AMS	Dedicated line	IMT
Wind speed & direction	young	Direct	CNRM
Net radiation	CNR1 (campbell)	Direct	CNRM
Photolysis frequencies	spectroradiometre	Direct	IMT

4.4. Campaign Data Overview

To ensure synchronization with the data acquired by fellow researchers in the field, all timestamps have been consistently converted to Coordinated Universal Time (UTC). Figure 4.4 provides a visual depiction of the temporal evolution of parameters measured at the top of the tower, categorized by the research groups responsible for contributing the data (names enclosed in parentheses). Figure 4.4.a. presents meteorological factors including SR and T. In Figure 4.4.b–f, the mixing ratios of some of the gaseous species, namely NO, NO₂, O₃, SO₂, isoprene, the sum of MVK/MACR/ISOPOOH fragment, monoterpenes and sesquiterpenes are shown. The last plot depicted in Figure 4.4.g visualizes the total HOMs and the H₂SO₄ mixing ratios collected by the NO₃⁻ ToFCIMS.

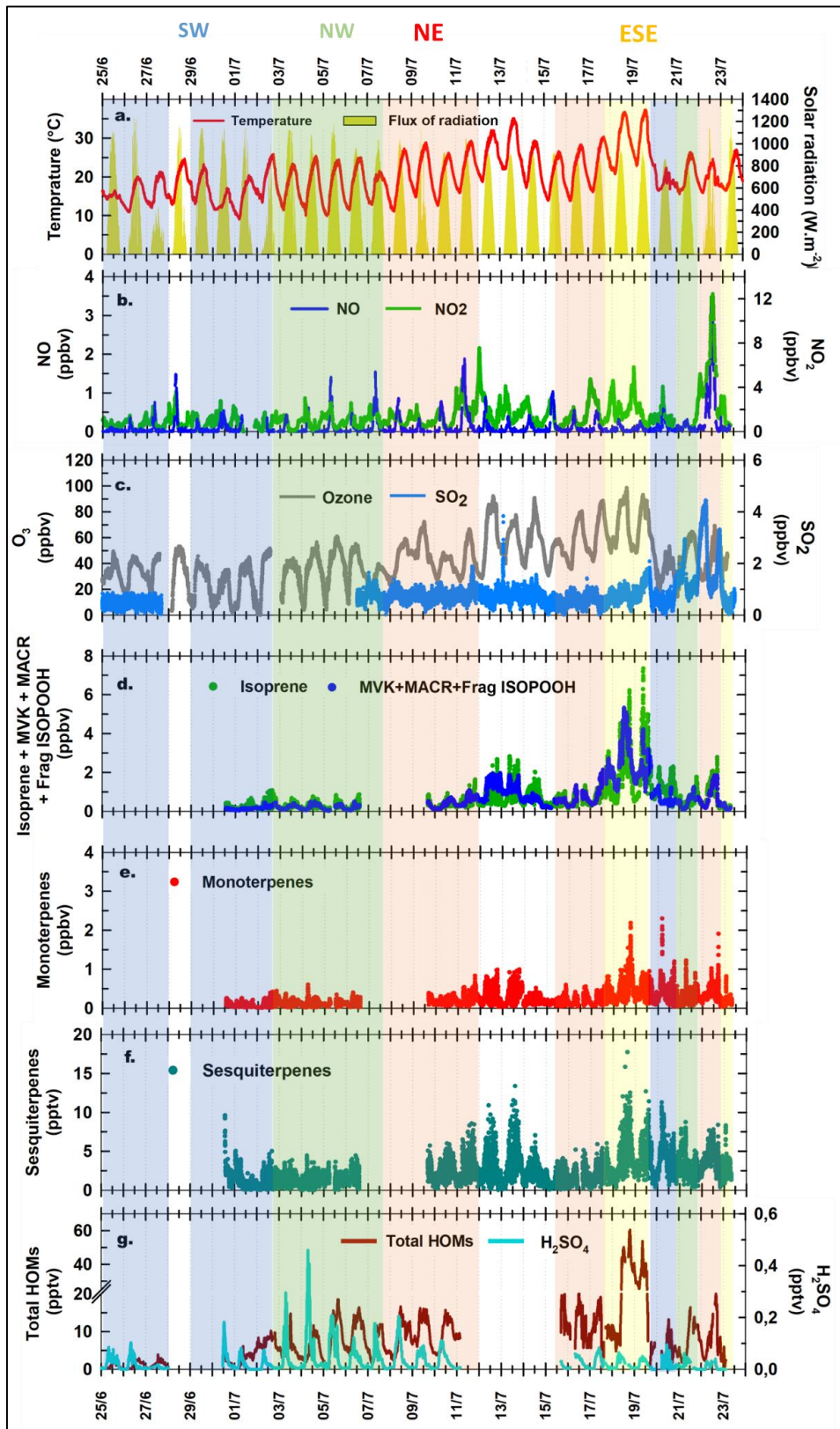


Figure 4.4. Temporal data overview during ToFCIMS operation at the top of the tower. a. T and SR (Météo-France). b. NO and NO₂ (IMT, LISA). c. O₃ and SO₂ (LISA). d. isoprene and sum of MVK/MACR/ISOPOOH (IMT). e. monoterpenes (IMT). f. sesquiterpenes (IMT). g. Total HOMs (break at 20 pptv) and H₂SO₄ (this study, LISA). A color-coded banner at the top of the figure is employed to highlight time intervals corresponding to distinct major wind origins: blue for southwestern winds, green for northwestern winds, light red for northeastern winds and yellow for east-southeastern winds (Figure S.4.1–4.8).

During specific time periods, namely from June 25th to the 27th, from June 30th to July 2nd in the late afternoon, and on July 20th, an analysis of air masses using the Hybrid Single-Particle Lagrangian Integrated Trajectory (Hysplit, Stein et al., 2015) back trajectory calculations reveals that the site experienced prevailing southwesterly winds, highlighted in blue shaded areas in Figure 4.4 (daily back trajectories showed in Figures S.4.1, S.4.2, S.4.3 and S.4.8). This wind direction coincided with cooler temperatures ranging from 10 to 25°C and lower O₃ mixing ratios. The O₃ levels varied from a few ppbv during the night to approximately 55 ppbv during the day. Furthermore, this situation also correlated with lower NO and NO₂ mixing ratios at the site, varying between a few tens to hundreds of pptv and reached up to about 1.5 and 3.7 ppbv on June 28th. As depicted in Figure 4.4.g, the total mixing ratios of HOMs were lower during the specified time periods (0–15 pptv) compared to other periods (few pptv to 60 pptv). Another notable period was characterized by higher levels of HOMs, spanning from the morning of 18 July until the late afternoon of 19th of July. This period was characterized by air masses originating from the east-southeast direction (back trajectories shown in Figure S.4.7) accompanied with anti-cyclonic weather conditions and high temperatures peaking above 36°C during the day, highlighted in the yellow shaded region. This period will undergo dedicated investigation and comparative analysis versus other periods characterized by relatively cleaner conditions observed at the site, as detailed in Section 4.5.3. This comparative examination aims to provide insights into the sources and atmospheric processes during varying meteorological conditions.

Moreover, a significant and consistent observation throughout the campaign is the presence of NO_x at the site probably from local sources possibly photolytic and/or forested soil emissions. This makes difficult to differentiate between anthropogenic and biogenic contributions. The NO_x diurnal cycles, as depicted in Figure 4.5.c, indicate that NO₂ concentrations are characterized on average by a primary peak at 6:00 and a secondary peak at 23:00 both around 2.0 ppbv. Meanwhile, NO reaches its highest concentration around 0.5 ppbv on average at 7:00, while O₃ peaks between 12:00 and 15:00 around 62 ppbv.

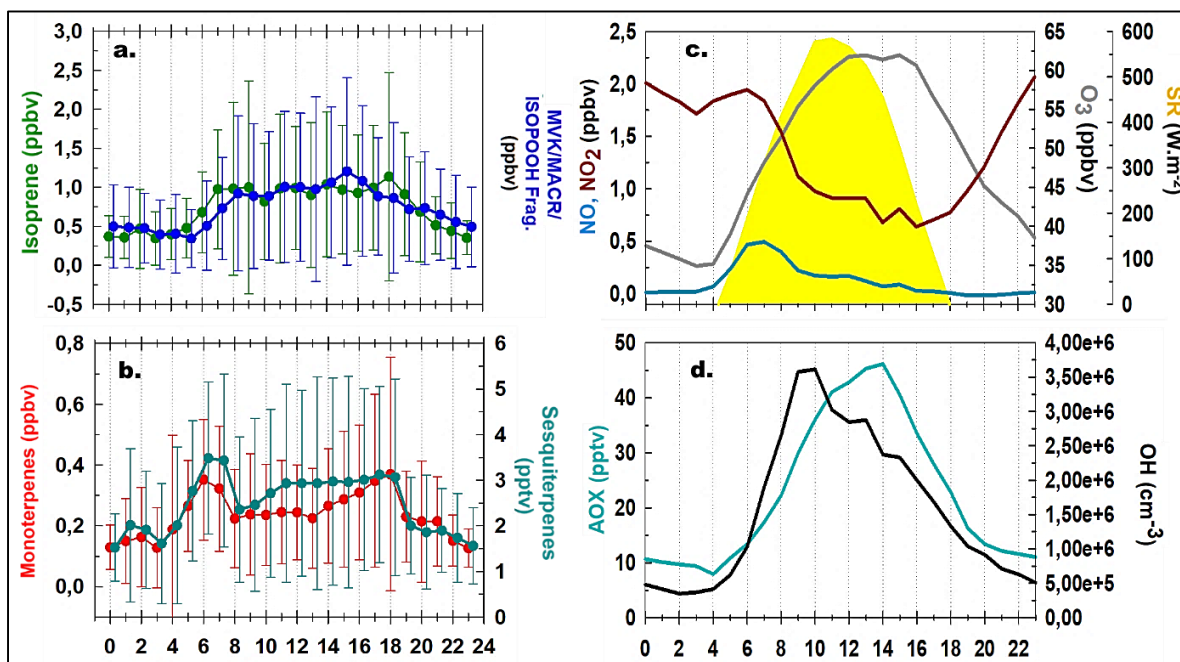


Figure 4.5. The average diurnal cycles of: a. isoprene and the sum of MVK/MACR/ISOPOOH frag. b. Monoterpenes, and sesquiterpenes. c. NO, NO₂, O₃ on the right y-axis starting at 30 ppbv and SR on the right offset y-axis. d. AOx (tower level) and OH concentrations (ground level). The error bars represent one standard deviation.

Over the entire monitoring period, the total HOM mixing ratios follow a distinct diurnal trend, featuring a marked increase during morning daylight hours (Figure 4.6). This pattern suggests enhanced photochemical OH-initiated reactions, primarily involving isoprene and its oxidation products (Figure 4.5.a), which significantly contribute to this observed increase. The average total HOM mixing ratios (± 1 standard deviation) was approximately 8.7 ± 9.0 pptv, corresponding to $2.2 \pm 2.3 \times 10^8$ molecules.cm⁻³.

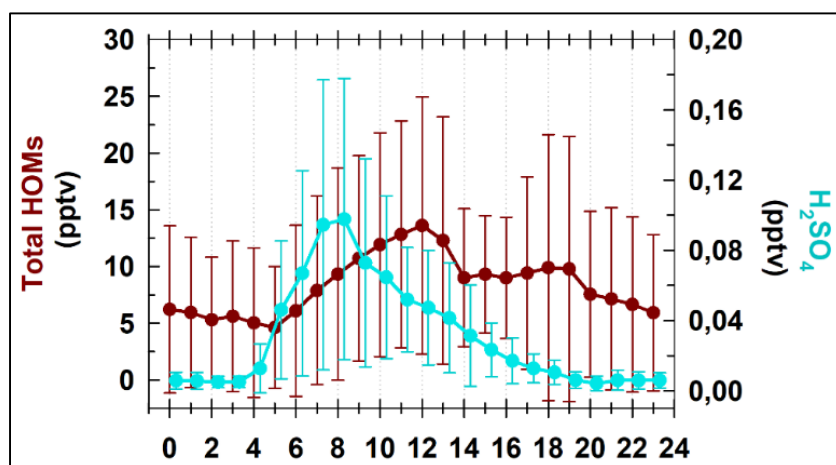


Figure 4.6. Diurnal profiles of total HOMs and H₂SO₄ mixing ratios throughout the study period. The error bars represent one standard deviation.

In addition, the highest levels of H₂SO₄ were observed during the morning hours, specifically around 7:00-8:00. The concentrations in this time window ranged from 4.6×10^5 to 1.2×10^7

molecules.cm⁻³ (corresponding to about 0.02 to 0.5 pptv). These levels are in line with those detected in comparable remote locations, such as a rural site in Germany (Kürten et al., 2016) or the Hyytiälä boreal forest in Finland (Petäjä et al., 2009).

4.5. Results of ACROSS Measurements

4.5.1. Overview of Spectral analysis for HOMs

Overall, 442 peaks were identified in the mass spectra (HOMs, HOM-ONs, OVOCs, H₂SO₄). Figure 4.7 depicts the averaged daytime (positive values, above the zero line) and nighttime mass spectra (negative values, below the zero line) throughout the period when data are available (June 25 - July 23). Labels in Figure 4.7.b, c, and d display elemental formulas for major species, excluding the NO₃⁻ reagent ion cluster from the formula. However, the m/z values (x-axis) include the NO₃⁻ mass (61.9883 m/z). In Figure 4.7.a, the mass range of 140-600 is covered, encompassing the majority of identified HOMs molecules. The lower part of the range includes some OVOCs not attributed to HOMs, like C₃H₄O₄ and C₆H₅NO₃ detected at m/z 165.9994 and 201.0153, respectively. These are two of the most abundant species identified by the NO₃⁻ ToFCIMS at the tower level.

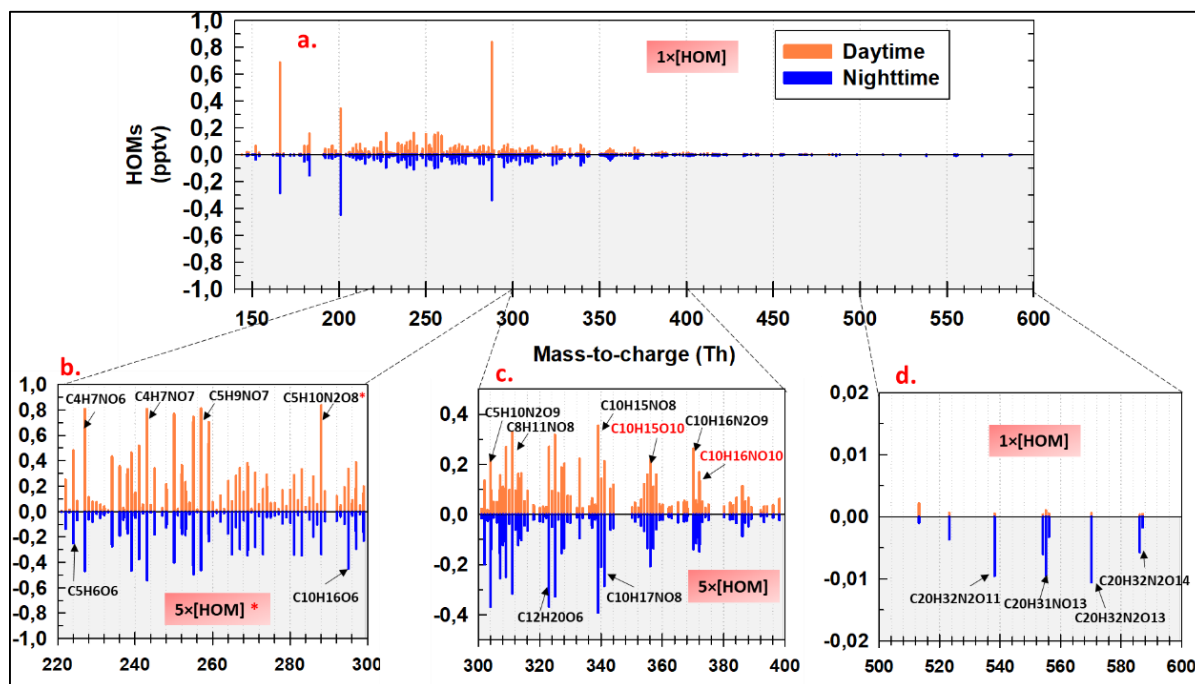


Figure 4.7.a. Average mass spectra for the daytime period (4:00-19:00) and the nighttime (20:00-03:00) across the study period. The gray shaded area represents the nighttime spectrum (below zero line). The red text reflects suggested formulas for HOM-RO₂. The red asterisk on highlights C₅H₁₀N₂O₈ molecules with mixing ratios not scaled (1x[HOM]). a, b. The expanded mass spectra of the mass ranges 220-300 and 300-400 have peak levels scaled by 5 except for the one marked by an asterisk. c. The expanded mass spectra of the dimer mass range 500-600, all peaks levels remained unchanged. For b, c and d, the major peaks are labeled.

The dinitrates $C_5H_{10}N_2O_8$ are the predominant isoprene oxidation products on the site, particularly during daytime. These dinitrates were observed as second-generation products from the oxidation of isoprene by $OH\cdot$ radicals (leading to $RO_2\cdot$ radicals) in the presence of NO (Lambe et al., 2017; Jaoui et al., 2021) which results in nitrate formation in a fraction of the reactions. The increased numbers of hydrogen atom in $C_5H_{10}N_2O_8$ compared to isoprene, which contains only 8 H-atoms, can be attributed to the addition of $OH\cdot$ on the two double bonds of isoprene.

Figure 4.7.b, c, and d provide closer views of the mass regions relevant to our study, likely associated with isoprene products (C_4 and C_5), monoterpenes products and isoprene accretions (C_6 - C_{10}), and monoterpenes accretions (C_{20}). Generally, major peaks consist mainly of organic nitrate monomers in both daytime and nighttime spectra. In the nighttime spectra, the main variation observed is the detection of nitrogen-containing C_{20} dimers.

It is surprising that the levels of accretion products were either negligible during the day or significantly lower during the night compared to monomer products. This observation contradicts our findings from the chamber experiments detailed in Chapter 3, where dimers were the dominant species in the mass spectra. Additionally, the major C_{18-20} dimers that we encountered in the chamber experiments were absent throughout the field campaign. This unexpected difference between the field observations and the chamber experiments strongly suggests that complex atmospheric factors are influencing the composition and abundance of these compounds in real-atmosphere conditions. One possible explanation could be the presence of pre-existing particles in ambient air, which may enhance the partitioning of these extremely low volatile products into the particle phase. Another factor could be the presence of NO_x species, which might suppress the formation of dimers and promote the generation of monomer products, especially organic nitrates.

4.5.2. HOM Classification via PCA Analysis

Principal component analysis (PCA) was used as an initial step to separate and group the large number of species detected by the NO_3^- ToFCIMS, based on similar time profiles. PCA is a commonly employed statistical method used to reduce the dimensionality of multivariate datasets while retaining a significant amount of information (Jolliffe and Cadima, 2016). Scaling the data (normalization) before applying PCA ensures that all variables contribute equally to the analysis. The initial analysis yielded five principal components (PCs) that collectively explained approximately 82% of the data variance. These PCs were characterized by their respective time profiles and the contributions of individual molecules to each component. The eigenvalues, which

represent the amount of variance captured by each PC, generally indicate the first component (labeled PC1) as the highest value followed by PC2 and so on. However, since the time profiles obtained for these five PCs were scaled values, a more detailed manual analysis was conducted to identify the molecules that made the greatest contributions to each component, examine their time profiles and consequently summing their respective mixing ratios. For instance, in the case of PC1, it was observed that the contributing molecules could be further subdivided. Consequently, a secondary PCA was performed on PC1, resulting in the identification of two sub-groups. Furthermore, the temporal evolution of the various molecules within these sub-groups was carefully checked to ensure consistency. This analysis was extended to the other four PCs. As a result, a total of 7 distinct components were obtained, which are shown and discussed in this section.

Figure 4.8 displays the time profiles of the different components throughout the whole campaign period where each component shows a distinct diurnal pattern.

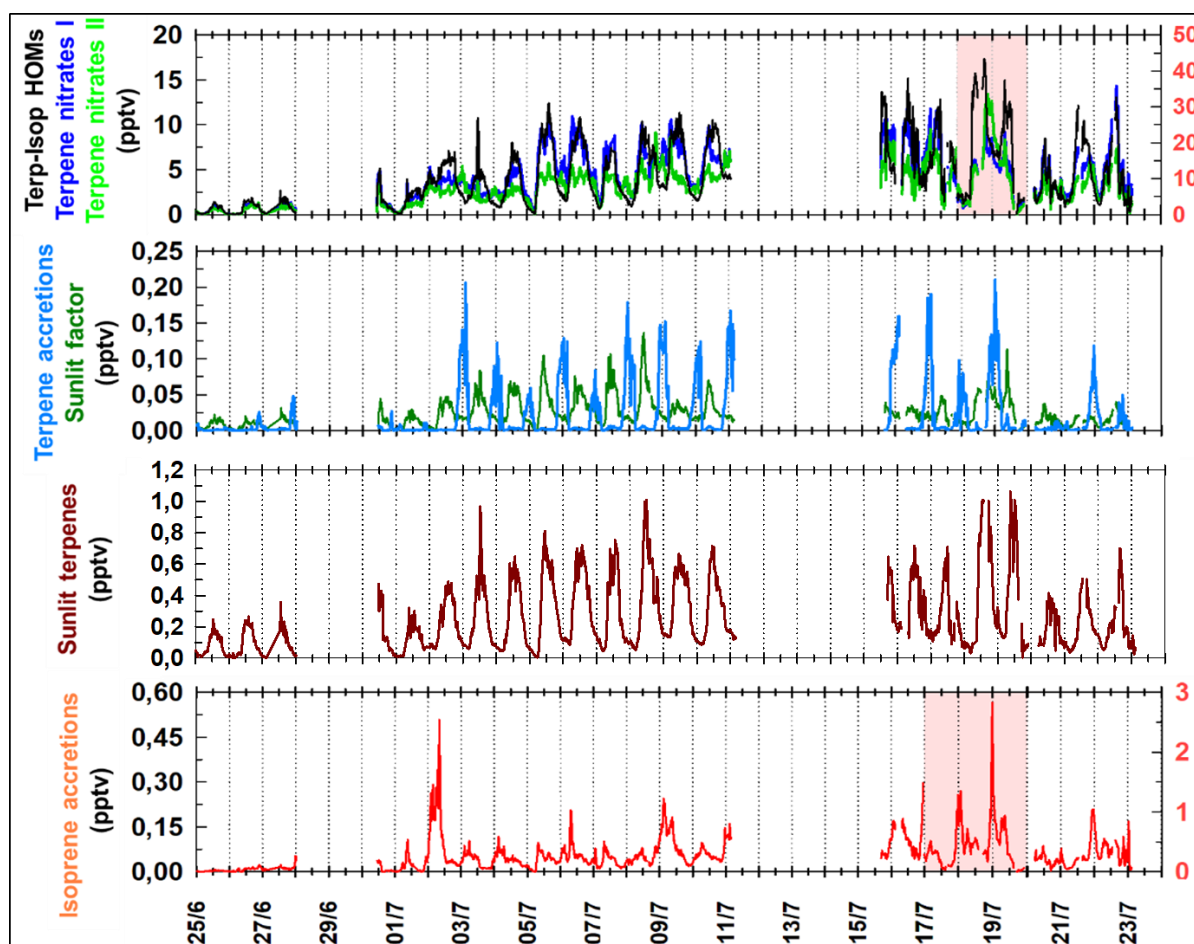


Figure 4.8. Time profiles of PCA-derived components from HOM data collected by the NO_3^- ToFCIMS throughout the campaign. Terpene nitrate I and II levels are multiplied by three to enhance their visibility. The shaded region in red corresponds to a time interval aligned with the red tick labels on the y-axis, positioned to the right to enhance visibility of the lower component levels.

It is evident that the first three components (Terpene-Isoprene HOMs (black), Terpene nitrates I (blue), and Terpene nitrates II (light green)) display significantly higher levels compared to the others (Terpene accretions (light blue), Sunlit factor (dark green), Sunlit terpenes (dark red), or Isoprene accretions (orange)). This observed difference in levels can be attributed to the varying number of molecules contributing to each component and their respective observed levels.

The naming convention for these components is based on the primary precursors most likely responsible for generating the HOMs within each component, taking into account whether the dominant class of molecules consists of nitrates or non-nitrates. However, there are two exceptions where the nomenclature also considers the peak timing, Sunlit Terpenes and the Sunlit factor, with the precursors leading to the latter component are uncertain.

Specifically, Terpene-Isoprene HOMs encompass 190 molecules, Terpene nitrates I consist of 53 molecules, Terpene nitrates II comprise 35 molecules, Terpene accretions involve 10 molecules, Sunlit component entails 7 molecules, Sunlit terpenes encompass 26 molecules, and finally, Isoprene accretions comprise 8 molecules (see Tables 4.3, 4.4, 4.5 and 4.6). Hence, the variations in both the number and concentrations of the molecules contribute to the discrepancies observed in the time profiles of the different components. It is worth noting that this method did not identify a distinct and specific component for the oxidation products of AVOCs. However, this is not meant to imply that such compounds were not measured during the campaign.

Notably, the separation of these components could not be achieved based on the primary precursors of HOMs at the site, namely isoprene, monoterpenes, and to a lesser extent, sesquiterpenes. This is due to the fact that, at the tower level, the diurnal patterns of these precursors exhibited similarities, as illustrated in Figure 4.4.d–f, and more distinctly in the average diurnal cycles presented in Figure 4.5.a and Figure 4.5.b. Overall, the isoprene mixing ratios were on average about 3 to 4 times higher than mixing ratios of monoterpenes at the tower level, while sesquiterpenes were observed to be at significantly lower levels (< 20 pptv).

Table 4.3. The molecules contributing to the Terpene-Isoprene HOMs component with molecules sorted in descending order of their contribution to the component.

Terpene-Isoprene HOMs							
Molecules	Contrib. (%)	Molecules	Contrib. (%)	Molecules	Contrib. (%)	Molecules	Contrib. (%)
C ₅ H ₁₀ N ₂ O ₈	12.5	C ₁₀ H ₁₆ O ₆	0.6	C ₈ H ₈ O ₆	0.3	C ₁₆ H ₁₉ NO ₆	0.1
C ₅ H ₁₁ NO ₆	2.7	C ₁₀ H ₁₈ O ₈	0.6	C ₇ H ₁₄ O ₅	0.3	C ₁₂ H ₂₀ O ₇	0.1
C ₅ H ₉ NO ₇	2.6	C ₉ H ₁₄ O ₄	0.6	C ₈ H ₁₂ O ₇	0.3	C ₉ H ₁₄ O ₁₁	0.1
C ₄ H ₇ NO ₆	2.6	C ₈ H ₁₀ O ₅	0.6	C ₅ H ₉ NO ₅	0.2	C ₄ H ₈ O ₆	0.1
C ₈ H ₁₂ O ₅	2.4	C ₆ H ₁₂ O ₄	0.5	C ₁₀ H ₁₈ O ₆	0.2	C ₅ H ₁₂ O ₅	0.1
C ₅ H ₇ NO ₇	2.3	C ₉ H ₁₄ O ₆	0.5	C ₅ H ₅ NO ₉	0.2	C ₁₄ H ₂₂ O ₉	0.1
C ₄ H ₇ NO ₇	2.0	C ₉ H ₁₂ O ₆	0.5	C ₉ H ₁₂ O ₁₁	0.2	C ₇ H ₁₆ N ₂ O ₈	0.1
C ₅ H ₁₁ NO ₇	1.9	C ₁₀ H ₁₆ O ₅	0.5	C ₁₁ H ₁₇ NO ₇	0.2	C ₆ H ₆ O ₄	0.1
C ₅ H ₉ NO ₆	1.8	C ₉ H ₁₂ O ₇	0.5	C ₈ H ₇ NO ₆	0.2	C ₁₇ H ₂₃ NO ₅	0.1
C ₇ H ₈ O ₆	1.6	C ₇ H ₁₃ NO ₅	0.5	C ₈ H ₁₃ NO ₉	0.2	C ₆ H ₄ O ₅	0.1
C ₆ H ₁₀ O ₅	1.5	C ₄ H ₄ O ₆	0.5	C ₁₅ H ₁₇ NO ₈	0.2	C ₁₃ H ₂₂ O ₆	0.1
C ₅ H ₆ O ₆	1.4	C ₈ H ₁₀ O ₁₀	0.5	C ₉ H ₁₃ O ₁₀	0.2	C ₁₅ H ₂₂ O ₆	0.1
C ₇ H ₈ O ₅	1.4	C ₉ H ₁₇ NO ₇	0.5	C ₉ H ₁₁ NO ₅	0.2	C ₄ H ₆ O ₈	0.1
C ₈ H ₁₂ O ₄	1.4	C ₈ H ₁₄ O ₆	0.5	C ₁₀ H ₁₈ O ₇	0.2	C ₁₄ H ₂₂ O ₈	0.1
C ₄ H ₇ NO ₈	1.4	C ₄ H ₄ O ₅	0.5	C ₉ H ₁₇ NO ₈	0.2	C ₇ H ₁₀ O ₈	0.1
C ₄ H ₅ NO ₇	1.4	C ₅ H ₁₀ O ₄	0.5	C ₄ H ₆ O ₂	0.2	C ₁₅ H ₂₆ O ₇	0.1
C ₅ H ₈ O ₅	1.2	C ₇ H ₆ O ₆	0.5	C ₇ H ₁₂ O ₆	0.2	C ₁₂ H ₁₈ O ₇	0.1
C ₅ H ₁₀ O ₅	1.2	C ₁₀ H ₁₈ O ₅	0.4	C ₁₀ H ₁₅ N ₂ O ₈	0.2	C ₁₂ H ₂₀ O ₆	0.1
C ₇ H ₁₀ O ₅	1.1	C ₇ H ₁₀ O ₇	0.4	C ₁₀ H ₁₃ NO ₈	0.2	C ₈ H ₁₄ O ₇	0.1
C ₉ H ₁₇ NO ₆	1.1	C ₆ H ₁₀ O ₆	0.4	C ₁₂ H ₂₁ NO ₆	0.2	C ₁₃ H ₂₀ O ₇	0.1
C ₇ H ₅ NO ₅	1.1	C ₄ H ₈ O ₅	0.4	C ₈ H ₁₀ O ₈	0.2	C ₁₅ H ₂₄ O ₆	0.1
C ₇ H ₁₂ O ₅	1.0	C ₈ H ₁₀ O ₇	0.4	C ₄ H ₆ N ₂ O ₈	0.2	C ₁₄ H ₂₄ O ₆	0.1
C ₈ H ₁₄ O ₅	1.0	C ₉ H ₁₂ O ₅	0.4	C ₆ H ₈ O ₇	0.2	C ₁₃ H ₂₂ O ₇	0.1
C ₄ H ₆ O ₅	1.0	C ₅ H ₆ O ₇	0.4	C ₁₃ H ₂₃ NO ₇	0.2	C ₁₄ H ₂₆ O ₅	0.1
C ₅ H ₈ N ₂ O ₈	1.0	C ₁₀ H ₁₄ O ₆	0.4	C ₅ H ₁₀ N ₂ O ₇	0.2	C ₁₀ H ₂₀ O ₁₀	0.1
C ₇ H ₁₀ O ₄	0.9	C ₅ H ₄ O ₆	0.4	C ₁₇ H ₂₃ NO ₄	0.2	C ₁₂ H ₁₈ NO ₆	0.1
C ₆ H ₈ O ₆	0.9	C ₁₀ H ₁₆ O ₁₀	0.4	C ₁₀ H ₁₄ NO ₆	0.2	C ₁₂ H ₁₆ O ₈	0.1
C ₄ H ₆ O ₆	0.8	C ₁₀ H ₁₆ N ₂ O ₈	0.4	C ₁₂ H ₁₉ NO ₈	0.2	C ₁₀ H ₁₄ NO ₇	0.1
C ₈ H ₁₂ O ₆	0.8	C ₉ H ₁₄ O ₁₀	0.4	C ₁₆ H ₁₇ NO ₅	0.2	C ₇ H ₁₃ NO ₈	0.1
C ₉ H ₁₄ O ₅	0.8	C ₄ H ₈ NO ₆	0.4	C ₁₈ H ₂₄ NO ₆	0.2	C ₅ H ₇ NO ₄	0.1
C ₁₀ H ₁₆ N ₂ O ₉	0.8	C ₆ H ₉ NO ₈	0.3	C ₇ H ₈ O ₈	0.2	C ₅ H ₇ NO ₃	0.1
C ₈ H ₁₀ O ₆	0.8	C ₇ H ₁₃ NO ₇	0.3	C ₁₁ H ₁₇ N ₂ O ₇	0.1	C ₆ H ₉ NO ₉	0.1
C ₁₀ H ₁₆ NO ₉	0.8	C ₁₁ H ₁₈ O ₅	0.3	C ₅ H ₁₀ NO ₁₀	0.1	C ₁₂ H ₁₆ O ₇	0.1
C ₇ H ₁₀ O ₆	0.8	C ₆ H ₈ O ₄	0.3	C ₇ H ₈ O ₄	0.1	C ₁₅ H ₂₂ O ₈	0.1
C ₁₅ H ₁₈ O ₆	0.8	C ₆ H ₁₀ N ₂ O ₉	0.3	C ₄ H ₆ O ₃	0.1	C ₁₀ H ₁₆ O ₁₁	0.1
C ₈ H ₁₄ O ₄	0.8	C ₉ H ₁₄ O ₈	0.3	C ₁₃ H ₂₃ NO ₆	0.1	C ₉ H ₁₆ O ₁₁	0.1
C ₆ H ₈ O ₅	0.8	C ₁₀ H ₁₆ O ₄	0.3	C ₁₇ H ₂₀ O ₆	0.1	C ₅ H ₄ O ₇	0.1
C ₆ H ₆ O ₅	0.8	C ₅ H ₄ O ₅	0.3	C ₈ H ₁₀ O ₄	0.1	C ₁₅ H ₂₂ O ₉	0.05
C ₆ H ₆ O ₆	0.7	C ₁₀ H ₁₄ O ₈	0.3	C ₅ H ₁₀ O ₇	0.1	C ₈ H ₁₆ O ₆	0.05
C ₅ H ₆ O ₄	0.7	C ₇ H ₁₄ N ₂ O ₈	0.3	C ₁₂ H ₁₉ NO ₁₁	0.1	C ₅ H ₁₀ O ₃	0.04
C ₉ H ₁₄ O ₉	0.7	C ₁₀ H ₁₆ NO ₇	0.3	C ₈ H ₁₂ O ₈	0.1	C ₇ H ₁₂ O ₃	0.04
C ₅ H ₉ N ₃ O ₁₀	0.7	C ₁₀ H ₁₆ O ₇	0.3	C ₉ H ₁₆ O ₇	0.1	C ₁₀ H ₁₈ O ₁₂	0.04
C ₇ H ₁₂ O ₄	0.7	C ₄ H ₅ NO ₆	0.3	C ₁₀ H ₁₇ O ₁₀	0.1	C ₁₈ H ₃₄ O ₅	0.03
C ₅ H ₈ O ₄	0.7	C ₉ H ₁₄ O ₇	0.3	C ₁₀ H ₁₇ O ₁₁	0.1	C ₆ H ₄ O ₆	0.03
C ₆ H ₆ N ₂ O ₆	0.6	C ₆ H ₆ O ₈	0.3	C ₁₁ H ₁₆ O ₈	0.1	C ₈ H ₁₄ O ₃	0.02
C ₆ H ₁₀ O ₄	0.6	C ₈ H ₁₀ O ₁₁	0.3	C ₁₀ H ₁₈ O ₁₀	0.1		
C ₇ H ₈ O ₇	0.6	C ₉ H ₁₆ O ₆	0.3	C ₇ H ₆ O ₅	0.1		
C ₉ H ₁₅ NO ₈	0.6	C ₉ H ₁₂ O ₈	0.3	C ₅ H ₈ N ₂ O ₁₀	0.1		

Table 4.4. The molecules contributing to the Terpene nitrates I component with molecules sorted in descending order of their contribution to the component.

Terpene nitrates I					
Molecules	Contrib. (%)	Molecules	Contrib. (%)	Molecules	Contrib. (%)
C₆H₁₁NO₆	8.0	C₅H₅NO₇	2.0	C₁₇H₂₂O₆	0.7
C₅H₇NO₆	5.4	C₁₀H₁₉NO₇	2.0	C₁₀H₁₄O₄	0.6
C₆H₉NO₇	4.6	C₈H₁₃NO₈	1.8	C₈H₁₅NO₈	0.6
C₈H₁₃NO₇	4.4	C₇H₁₂N₂O₈	1.8	C₉H₁₃NO₆	0.6
C₇H₁₃NO₆	4.3	C₇H₁₄N₂O₇	1.8	C₁₂H₁₈O₁₁	0.5
C₇H₁₁NO₆	4.1	C₅H₆N₂O₉	1.7	C₁₆H₁₈O₆	0.5
C₉H₁₅NO₇	4.1	C₁₅H₁₉NO₅	1.6	C₁₀H₁₄N₂O₉	0.5
C₁₀H₁₅O₈	4.0	C₁₅H₂₀NO₆	1.6	C₈H₉NO₇	0.5
C₁₀H₁₇NO₇	4.0	C₈H₁₆N₂O₇	1.5	C₁₆H₂₄NO₆	0.4
C₁₀H₁₅O₇	3.3	C₁₅H₁₈NO₇	1.3	C₁₅H₂₅NO₇	0.4
C₆H₇NO₇	3.3	C₁₀H₁₆N₂O₁₀	1.3	C₁₀H₁₅N₂O₆	0.4
C₈H₁₁NO₈	3.3	C₇H₈O₁₀	1.3	C₁₀H₁₃NO₇	0.4
C₁₀H₁₇NO₆	3.1	C₁₀H₁₇O₉	1.1	C₄H₄O₄	0.4
C₆H₇NO₈	3.0	C₁₆H₂₂NO₆	1.0	C₁₅H₂₃NO₆	0.3
C₅H₅NO₈	3.0	C₉H₁₀NO₁₂	0.8	C₁₅H₂₃NO₉	0.3
C₆H₁₀N₂O₈	2.1	C₅H₁₀O₈	0.7	C₇H₇NO₆	0.2
C₁₀H₁₆NO₁₀	2.0	C₉H₁₆O₉	0.7	C₇H₁₂O₇	0.2
C₁₆H₂₂NO₅	2.0	C₈H₁₂O₁₀	0.7		

Table 4.5. The molecules contributing to the Terpene nitrate II and Terpene accretions components, respectively, with molecules sorted in descending order of their contribution to the component.

Terpene nitrates II				Terpene accretions	
Molecules	Contrib. (%)	Molecules	Contrib. (%)	Molecules	Contrib. (%)
C₁₀H₁₅NO₈	5.9	C₁₀H₁₅NO₆	3.0	C₂₀H₃₂N₂O₁₃	18.5
C₉H₁₅NO₆	5.7	C₁₀H₁₄O₉	2.5	C₂₀H₃₁NO₁₃	18.3
C₇H₁₁NO₇	5.4	C₆H₇NO₉	2.5	C₂₀H₃₂N₂O₁₁	17.2
C₈H₁₁NO₇	5.1	C₁₀H₁₅NO₉	2.4	C₂₀H₃₂N₂O₁₄	10.0
C₁₀H₁₅NO₇	4.9	C₁₀H₁₅O₁₀	1.9	C₂₀H₃₂N₂O₁₂	9.7
C₈H₁₃NO₆	4.8	C₅H₁₁NO₁₀	1.9	C₂₀H₃₁NO₁₁	7.8
C₇H₉NO₇	4.8	C₁₀H₁₄O₇	1.3	C₂₀H₃₂NO₁₃	6.8
C₈H₁₅NO₆	4.7	C₆H₁₁NO₈	1.2	C₂₀H₃₂N₂O₁₅	4.4
C₅H₇NO₈	4.6	C₅H₇NO₉	1.0	C₂₀H₃₁NO₁₅	3.7
C₆H₁₁NO₇	4.5	C₁₅H₁₉NO₆	1.0	C₂₀H₃₂N₂O₁₆	3.7
C₁₀H₁₉NO₆	4.2	C₇H₁₁NO₉	0.8		
C₁₀H₁₇NO₈	3.8	C₁₀H₁₆N₂O₁₁	0.5		
C₅H₉NO₈	3.7	C₇H₇NO₅	0.5		
C₁₀H₁₅O₉	3.7	C₅H₉NO₄	0.4		
C₇H₁₁NO₈	3.4	C₅H₉N₂O₉	0.3		
C₆H₅NO₈	3.1	C₆H₁₃N₂O₈	0.3		
C₁₂H₂₃NO₆	3.1	C₄H₅NO₅	0.3		
C₈H₁₅NO₇	3.0				

Table 4.6. The molecules contributing to the Sunlit factor, Sunlit terpenes, and Isoprene accretions components, respectively, with molecules sorted in descending order of their contribution to the component.

Sunlit factor		Sunlit terpenes				Isoprene accretions	
Molecules	Contrib. (%)	Molecules	Contrib. (%)	Molecules	Contrib. (%)	Molecules	Contrib. (%)
$C_{15}H_{25}N_2O_{10}$	21.6	$C_{10}H_{18}O_9$	15.0	$C_{18}H_{33}NO_7$	3.1	$C_5H_{10}N_2O_9$	52.2
$C_{17}H_{33}N_2O_8$	19.9	$C_{18}H_{24}O_6$	7.7	$C_{18}H_{32}O_9$	2.9	$C_5H_8N_2O_9$	26.8
$C_{15}H_{25}NO_{10}$	19.2	$C_{10}H_{16}O_8$	6.3	$C_{18}H_{34}O_6$	2.8	$C_{10}H_{17}N_3O_{12}$	7.4
$C_{18}H_{34}N_2O_9$	14.1	$C_5H_9NO_{10}$	5.8	$C_{19}H_{34}O_9$	2.8	$C_{10}H_{17}N_3O_{13}$	4.3
$C_{18}H_{33}N_3O_{10}$	9.5	$C_5H_8O_7$	5.4	$C_{18}H_{36}O_6$	2.3	$C_{10}H_{16}N_2O_{12}$	4.3
$C_{18}H_{32}N_2O_{10}$	8.6	$C_6H_{12}O_6$	5.1	$C_{18}H_{34}O_9$	2.1	$C_{10}H_{18}N_2O_{11}$	2.9
$C_{17}H_{31}N_3O_8$	7.1	$C_{15}H_{24}O_9$	4.6	$C_{18}H_{32}O_7$	1.9	$C_{10}H_{16}N_2O_{13}$	1.3
		$C_{18}H_{34}O_8$	4.5	$C_{18}H_{33}NO_9$	1.9	$C_{10}H_{17}N_3O_{14}$	0.9
		$C_{15}H_{26}O_8$	4.5	$C_{18}H_{33}NO_6$	1.6		
		$C_{10}H_{13}NO_6$	4.2	$C_{18}H_{32}N_2O_8$	1.4		
		$C_{15}H_{24}O_8$	3.7	$C_6H_8O_8$	1.4		
		$C_4H_4O_8$	3.7	$C_{18}H_{32}N_2O_9$	1.1		
		$C_{14}H_{26}O_7$	3.1	$C_{18}H_{31}NO_7$	1.0		

Figure 4.9 shows the average daily patterns (one-hour bins) of the seven identified components observed in the analysis. Additionally, the graph includes one standard deviation error bars for each bin, indicating the variability observed. The error bars effectively capture the fluctuations seen in the average daily cycle, indicating that they offer a thorough representation of the daily variation during the specified period. The plots in Figure 4.9 have been separated into Figures 4.10, 4.13, 4.14, 4.15, 4.16, 4.17 and 4.8 to show each component individually, as they are discussed in the text of the next sub-sections.

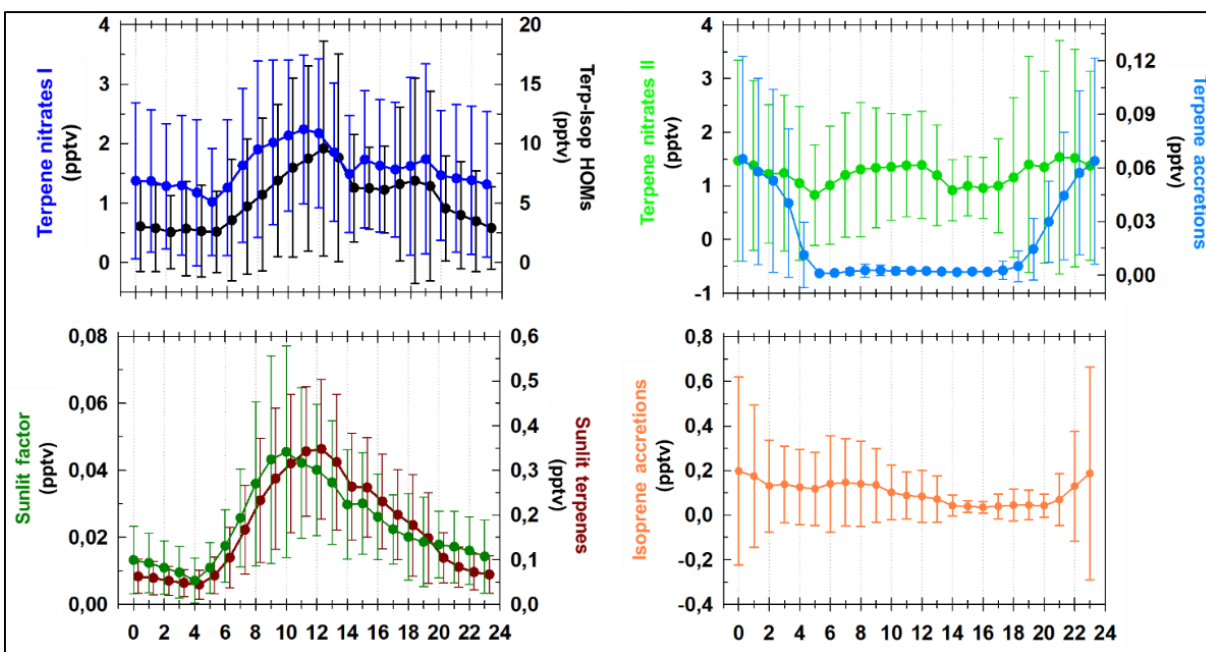


Figure 4.9. The average diurnal cycles of PCA-derived components from HOM data collected by the NO_3^- ToFCIMS throughout the campaign. The error bars represent one standard deviation of the bin for which the average is shown by the symbol.

4.5.2.1. Terpene-Isoprene HOMs

The Terpene-Isoprene HOMs component (Figure 4.10) exhibits distinct characteristics throughout the day. It begins to rise at 5:00, reaching its peak around 12:00, consistent with the peak hours of solar radiation (Figure 4.5.c), followed by a smaller enhancement at 18:00. This component persists during the night, but at significantly lower levels, with levels near constant between 23:00 and 5:00. The prominent molecules are those containing one nitrogen (1-N) C₄ and C₅ organic nitrates, primarily C₅H_{9,11}NO_{6,7}, C₅H₇NO₇, and C₄H₇NO_{6,7}, which are most likely isoprene nitrates, also observed in laboratory experiments reported in the literature involving isoprene with OH· radicals in the presence of NO_x, but also potentially arising from reactions with NO₃· (Lee et al., 2016; Lambe et al., 2017; Zhao et al., 2021; Wu et al., 2021). For example, during nocturnal chemistry, C₅H₁₁NO₆ likely underwent a two-step oxidation process initiated by NO₃· and OH·.

2-N isoprene nitrates, also denoted as dinitrates, are found within this component, with C₅H₁₀N₂O₈ being the most prevalent species, accounting for 12.5% of the compounds listed in this category (Table 4.3). The dinitrate is also the most abundant HOM compound detected among all HOMs, representing about 6.2% of all observed compounds.

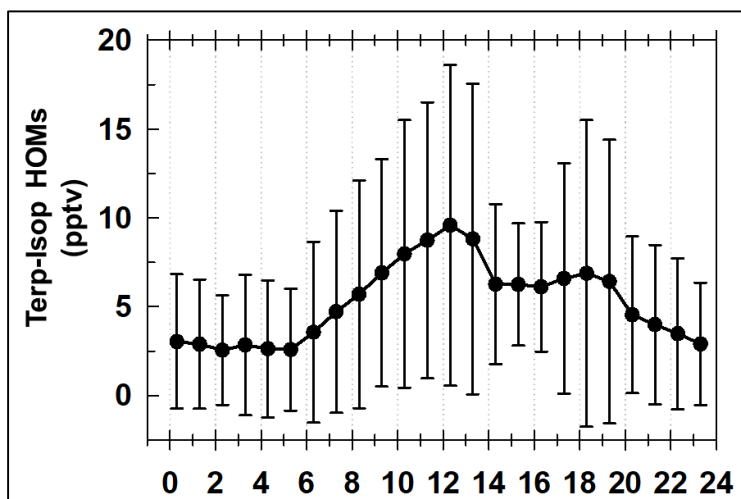


Figure 4.10. The average diurnal cycles of PCA-derived Terpene-Isoprene HOMs component from HOM data collected by the NO₃⁻ ToFCIMS throughout the campaign. The error bars represent one standard deviation of the bin for which the average is shown by the symbol.

Notably, during the Southern Oxidant and Aerosol Study (SOAS) 2013 campaign, where isoprene dominated the BVOC forest emissions, C₅H₁₀N₂O₈ was also found as the most abundant species (Massoli et al., 2018). Other laboratory evidence shows that this compound may also be products from NO₃-initiation reaction of isoprene (Ng et al., 2008; Zhao et al., 2021) and in field observations in urban regions in Shanghai, China where small enhancement occurred during the nighttime (Xu et al., 2021). Additionally, two less abundant isoprene dinitrates C₅H₈N₂O_{8,10} and

one isoprene trinitrate $C_5H_9N_3O_{10}$ are found in this component, which were also detected in the field during the SOAS 2013 campaign and were suggested as products of isoprene under high NO_x conditions (Massoli et al., 2018), and were also found in laboratory investigations involving isoprene oxidation by $NO_3\cdot$ (Wu et al., 2021; Zhao et al., 2021). The Terpene-Isoprene HOMs component also includes non-nitrate C_4 and C_5 compounds, for instance, $C_4H_6O_{5,6}$ and $C_5H_{8,10}O_5$, observed in chamber studies involving the oxidation of isoprene 4-hydroxy-3-hydroperoxy (4,3-ISOPOOH) by $OH\cdot$ radicals and during SOAS 2013 campaign (Krechmer et al., 2015). However, some C_5 products, mainly $C_5H_6O_{6,7}$, have never been observed in isoprene-related chemistry. Instead, they have been detected as fragmentation products in chamber experiments (Chapter 3) involving oxidation of monoterpenes by O_3 and $OH\cdot$ radicals.

This component also includes both nitrates and non-nitrates C_{6-10} products. The most abundant monoterpene-related oxidation products in this component are $C_6H_{10}O_5$, $C_8H_{12}O_{4,5,6}$, $C_7H_8O_{5,6}$, and $C_7H_{10,12}O_{5,6}$. Furthermore, C_{10} series products, including mainly $C_{10}H_{14}O_{6,8}$, $C_{10}H_{16}O_{4-7}$, $C_{10}H_{18}O_{5-8,10,12}$, $C_9H_{12}O_{5-8}$, $C_9H_{14}O_{4-9}$, and $C_9H_{16}O_{5-7,11}$, have been observed from oxidation of monoterpenes by $OH\cdot$ radicals and O_3 in previous studies (Molteni et al., 2019; Praplan et al., 2015; Shen et al., 2022; Tröstl et al., 2016), also some were detected in the chamber experiments conducted in this thesis. Some C_{6-9} products could potentially be oxidation products from AVOCs (e.g. toluene, benzene, C_8 -aromatics, C_9 -aromatics). Plus, the possibility of the accretion reactions of isoprene oxidation products should be considered.

The external parameters correlations with HOMs as expressed by the Pearson correlation coefficient (R) (Figure 4.11.a), shows that Terpene-Isoprene HOMs is best correlated ($R > 0.6$) with isoprene and its oxidation product MVK/MACR/Fragment of ISOPOOH as well as with monoterpenes and some fingerprint terpenes oxidation products especially nopinone. It also shows good correlation with O_3 concentration ($R=0.68$), OH reactivity ($R=0.76$), AOX (sum of RO_2 and HO_2) ($R=0.75$) and temperature ($R=0.78$).

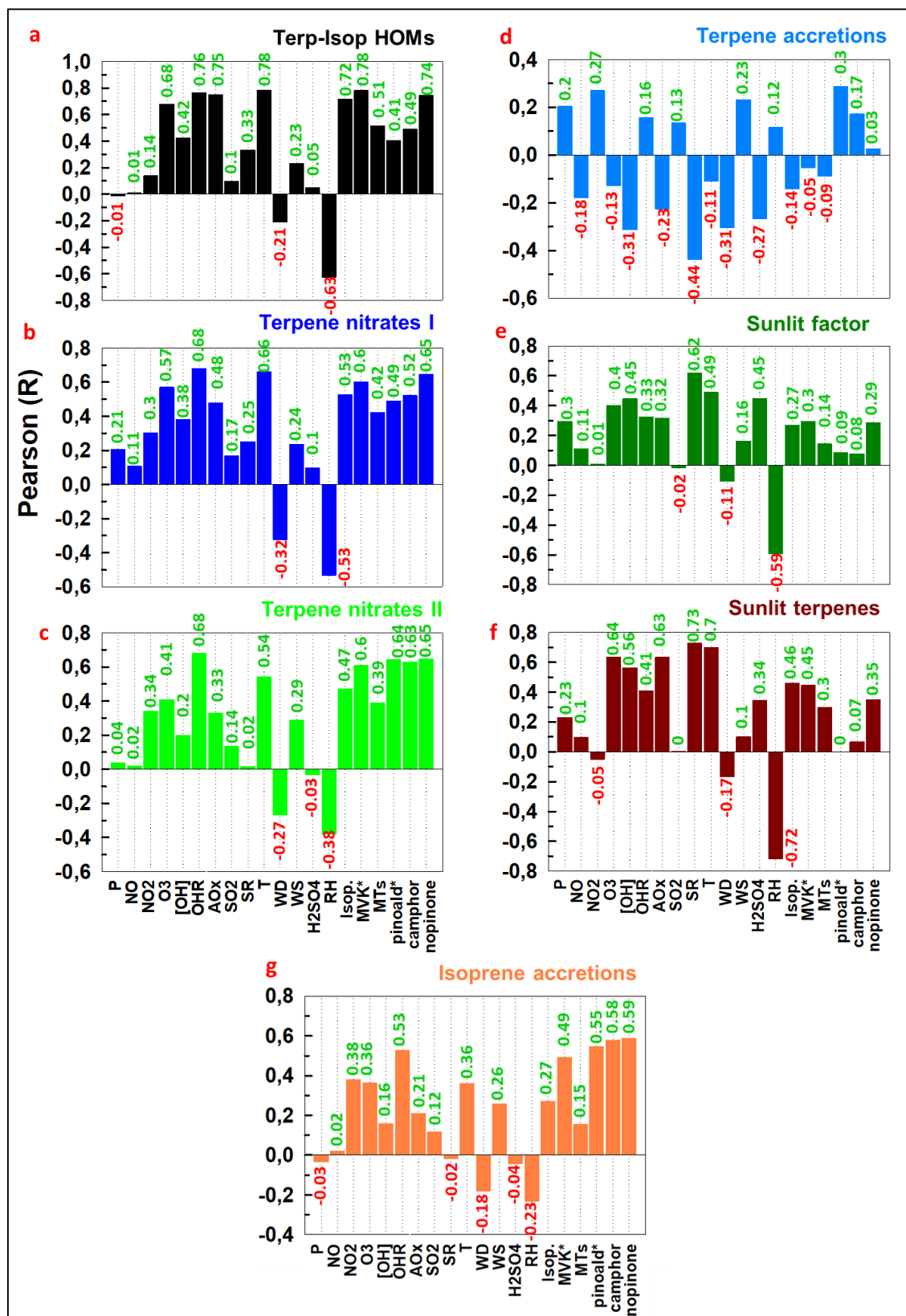


Figure 4.11. Pearson correlation coefficients between the 7 principal components of the PCA analysis (a-f) and gas-phase tracers (NO, NO₂, O₃, OH concentration [OH], OH reactivity (OHR), AOx, SO₂, H₂SO₄, Isop. for isoprene, MVK* for MVK/MACR/ISOPOOH Frag, Monoterpenes (MTs), types of MTs such as pinoaldehyde, camphor, and nopinone), and meteorological factors (P, SR, T, WD, WS, and RH). All measurements were taken at the top of the tower except for [OH]. The green labels represent positive values of Pearson correlation, while the red labels represent negative values.

Figure 4.12 illustrates the diurnal cycles of key HOMs included in this component, which are predominantly attributed to the oxidation products of isoprene and monoterpenes. This presentation serves to demonstrate that their temporal patterns align closely with those of the Isoprene-Monoterpenes HOMs component, thereby confirming the validity of the classification methodology outlined in main section 4.5.2. Moreover, it is evident that isoprene-non-nitrates and isoprene-nitrate HOMs make the largest contribution to this component, with their average levels up to 5 times greater than those of monoterpenes, except for $C_5H_{10}N_2O_8$.

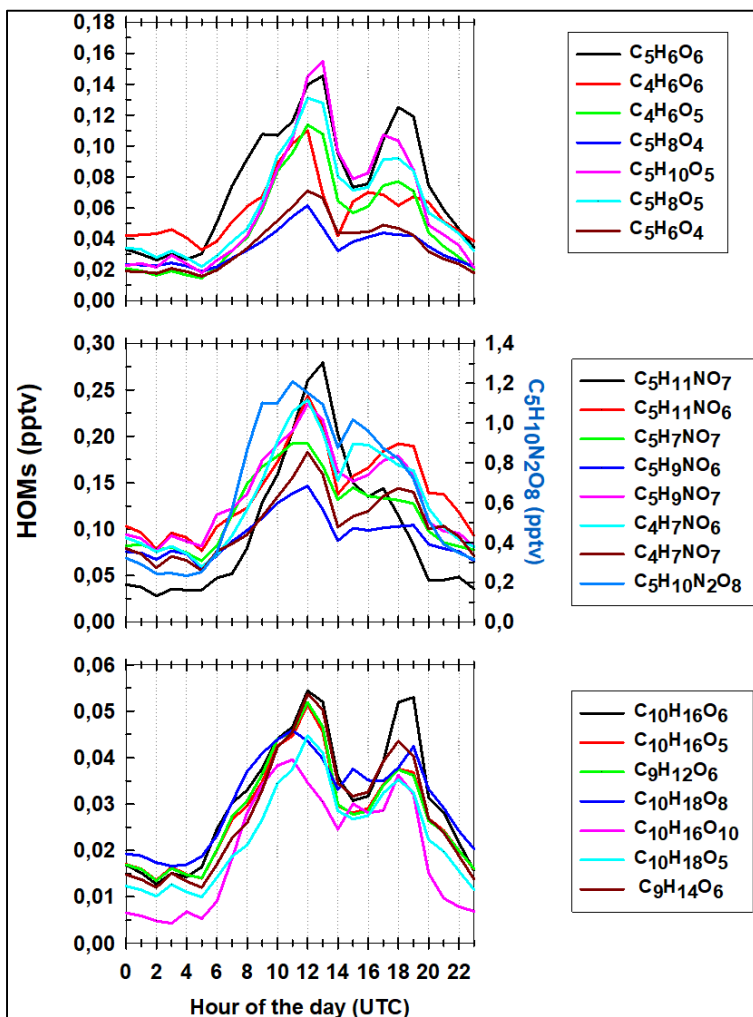


Figure 4.12. Examples of diurnal cycles for the major isoprene and monoterpene nitrate and non-nitrate HOMs in the component Terpene-Isoprene HOMs.

4.5.2.2. Terpene nitrates I

The diurnal profile of terpene nitrates I also begins to rise at 5:00 and peaks at 11:00 around 2.2 pptv (Figure 4.13). Afterward, it gradually decreases and stabilizes between 15:00 and 19:00. It is also present at significant levels (between 1 and 1.5 pptv) during nighttime but lower than during daytime. This component primarily comprises HOM-nitrates, with only a few non-nitrate HOM compounds that are most likely associated with the oxidation of monoterpenes (Table 4.4).

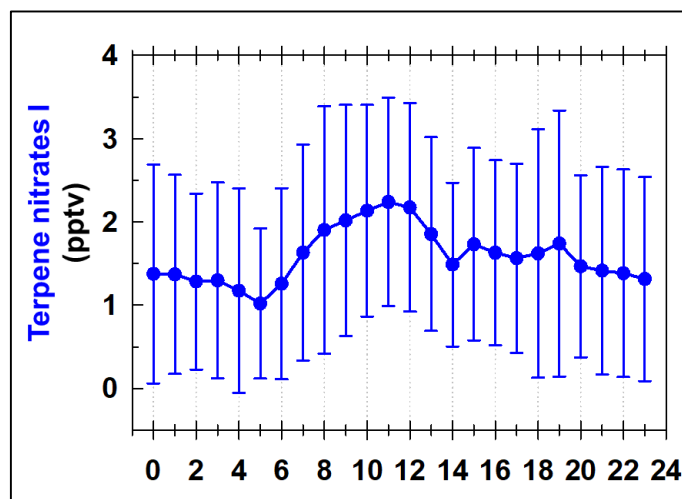


Figure 4.13. The average diurnal cycles of PCA-derived Terpene nitrates I component from HOM data collected by the NO_3^- ToFCIMS throughout the campaign. The error bars represent one standard deviation of the bin for which the average is shown by the symbol.

The prominent non-nitrate HOMs in this component include organic radicals like $\text{C}_{10}\text{H}_{15}\text{O}_{7,8}\cdot$, $\text{C}_{10}\text{H}_{17}\text{O}_9\cdot$, and the closed-shell compounds like $\text{C}_7\text{H}_8\text{O}_{10}$, $\text{C}_5\text{H}_{10}\text{O}_8$, and $\text{C}_9\text{H}_{16}\text{O}_9$. Jokinen et al. (2014) demonstrated from laboratory experiments that $\text{C}_{10}\text{H}_{15}\text{O}_8\cdot$ radicals are involved in the formation of organic nitrates. The characteristic HOM-nitrates in this component correspond to $\text{C}_7\text{H}_{11,13}\text{NO}_6$, $\text{C}_6\text{H}_{11}\text{NO}_6$, $\text{C}_6\text{H}_7\text{NO}_{7,8}$, $\text{C}_6\text{H}_9\text{NO}_7$, $\text{C}_5\text{H}_5\text{NO}_{7,8}$ and the dinitrates $\text{C}_5\text{H}_6\text{N}_2\text{O}_9$, $\text{C}_6\text{H}_{10}\text{N}_2\text{O}_8$ and $\text{C}_{10}\text{H}_{16}\text{N}_2\text{O}_{10}$. Additionally, there are smaller peaks for C_{8-10} and C_{15-16} organic nitrates, with C_{15} possibly being oxidation products of sesquiterpenes, although accretion reactions cannot be neglected. Despite being mostly organic nitrates, these peaks do not display strong correlation with NO concentration (Figure 4.11.b). The small differences between day and night levels of this component indicate that it is presumably linked to initiation reaction by $\text{OH}\cdot$ radicals and O_3 and involves NO_x termination reactions (Luo et al., 2023). The contribution of ozonolysis to Terpene nitrates I during daytime is not negligible as the radical $\text{C}_{10}\text{H}_{15}\text{O}_8\cdot$, with 4% contribution to Terpene nitrates I, is one major HOM- $\text{RO}_2\cdot$ resulting from the ozonolysis of monoterpenes, as shown in chamber experiments conducted in this study (see Chapter 3). $\text{C}_7\text{H}_8\text{O}_{10}$, $\text{C}_8\text{H}_{12}\text{O}_{10}$, $\text{C}_9\text{H}_{16}\text{O}_9$ were also observed from our chamber experiments involving the ozonolysis of α -pinene. Furthermore, the formation of this component during the nighttime hours also indicates the probable involvement of NO_3 -initiated reaction. These results are supported by the correlation plot in Figure 4.11.b which shows similar findings as that of Terpene-Isoprene HOMs with the highest correlations being with OH reactivity, O_3 , $\text{MVK}/\text{MACR}/\text{Fragment of ISOPOOH}$, nopinone and temperature ($R > 0.6$).

4.5.2.3. Terpene nitrates II

The Terpene nitrates II component has a diurnal pattern relatively flat with a broad peak between 8:00 and 12:00 (Figure 4.14). It then decreases before rising again, leading to a more intense broader peak during the nighttime between 19:00 and 00:00. One also notices from the error bars their importance during the night which highlights the high variability of nighttime concentrations of the compounds included in this component.

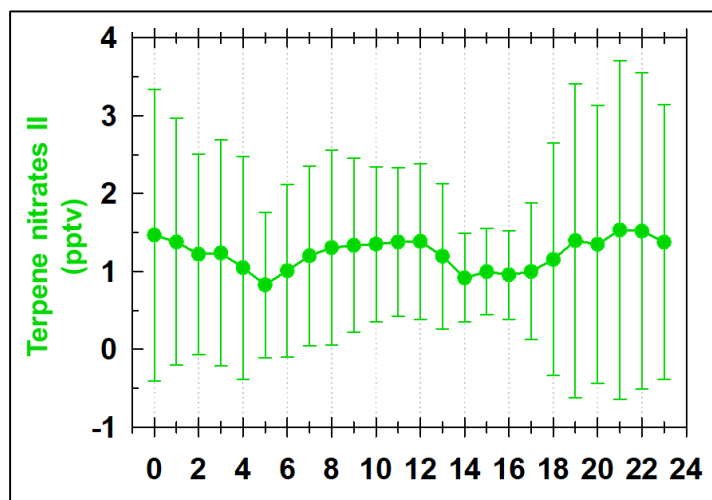


Figure 4.14. The average diurnal cycles of PCA-derived Terpene nitrates II component from HOM data collected by the NO_3^- ToFCIMS throughout the campaign. The error bars represent one standard deviation of the bin for which the average is shown by the symbol.

This category primarily consists of organic nitrate monomers, particularly within the $\text{C}_{10}\text{H}_{15}\text{NO}_{6-9}$ series, with $\text{C}_{10}\text{H}_{15}\text{NO}_8$ being the largest peak, accompanied by $\text{C}_9\text{H}_{15}\text{NO}_6$ (Table 4.5). Four exceptions in this category are non-nitrate HOM-radicals, $\text{C}_{10}\text{H}_{15}\text{O}_{9,10}\cdot$, and closed-shell monomers, $\text{C}_{10}\text{H}_{14}\text{O}_{7,9}$. The diurnal pattern suggests that during daylight hours, reactions with O_3 and $\text{OH}\cdot$ radicals in the presence of NO results in production of species in this component. On the other hand, during nighttime, NO_3 -initiated chemistry plays a significant role in the formation of Terpene nitrates II, with the major C_{10} organic nitrates observed in the α/β -phellandrene + NO_3 chamber experiments of this study (see Chapter 3), and also documented in various laboratory studies reported in the literature (e.g. Faxon et al., 2018; Shen et al., 2021; Guo et al., 2022). These are supported by the plot of correlation for Terpene nitrates II (Figure 4.11.c) which shows the highest correlation ($R > 0.6$) with OH reactivity and monoterpenes oxidation products and good correlations ($R > 0.3$) with O_3 , NO_2 , AOx and temperature. The main difference between Terpene nitrates I and Terpene nitrates II components is the higher levels of the latter during the night. This suggests the increased importance of NO_3 -initiated reactions in the formation of HOMs within the Terpene nitrates II during the nighttime.

4.5.2.4. Terpene accretions

The Terpene accretions component displays a daily profile that increases after sunset and reaching its maximum at 23:00-00:00 around 0.07 pptv (Figure 4.15). It then decreases progressively to negligible levels (<0.01 pptv) after sunrise starting at 5:00. Similar observations were reported by Kürten et al. (2016) at a rural site in central Germany. The presence of NO, which peaks in the morning at 7:00 (Figure 4.5), may partially explain the suppression of accretion formation and the increase of the termination reactions of HOM-RO₂· during daytime, as evidenced in laboratory experiments of Rissanen (2018). The increase of this component coincides well with the increase in NO₂ and the consumption of O₃, which in part presumably result in NO₃· radical formation. Also, this is consistent with the decrease in NO concentration which reduces the termination reaction and enhances the accretion channel.

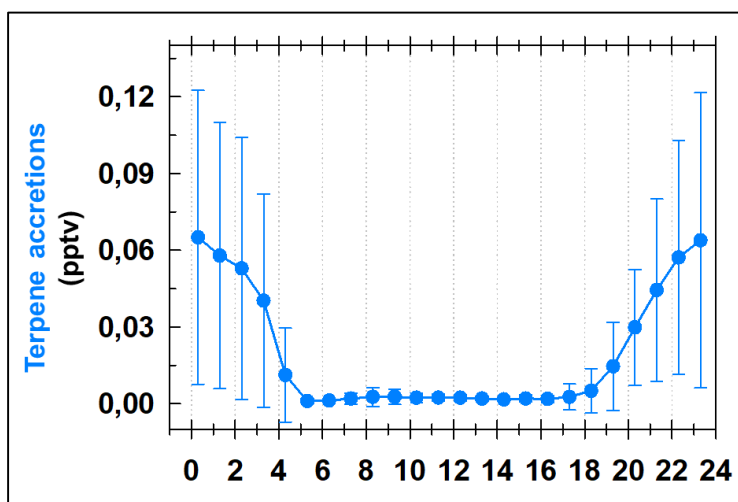


Figure 4.15. The average diurnal cycles of PCA-derived Terpene accretions component from HOM data collected by the NO₃⁻ ToFCIMS throughout the campaign. The error bars represent one standard deviation of the bin for which the average is shown by the symbol.

The composition of the Terpene accretions component consists solely of 1N-C₂₀ and 2N-C₂₀ dimers, as shown in Table 4.5. The presence of one nitrogen atom in the C₂₀H₃₁NO_{11,13,15} family suggests that the nitrogen atom likely originated from one of its parent RO₂ species, which underwent NO₃-initiated oxidation. The other RO₂· species are most likely the result of O₃-initiated reactions. Furthermore, the presence of two nitrogen atoms in the C₂₀H₃₂N₂O₁₁₋₁₆ family was also detected in laboratory experiments involving the oxidation reaction of monoterpenes with NO₃ radicals conducted in this study (see chapter 3). Similar composition findings were suggested by Yan et al. (2016). Overall, approximately 64% of the compounds in Terpene accretions are 2N-C₂₀ dimers, while the remaining 36% are 1N-C₂₀ dimers. Terpene accretions shows negative correlation with solar radiation, as expected based on its diurnal profile, as well as with H₂SO₄ (Figure 4.11.d).

This supports the conclusion that these molecules are specific during nighttime and their formation may be suppressed by the presence of other compounds existing at higher levels during the day, particularly NO, HO₂ and R'O₂, as suggested by Kürten et al. (2016). Another possible explanation could involve the photolysis of these accretion products, although to the best of my knowledge, there is currently no experimental evidence available to support this hypothesis.

4.5.2.5. Sunlit component

Moving on to the Sunlit component, we find that it displays a broad diurnal pattern with a peak at 10:00 am around 0.05 pptv (Figure 4.16).

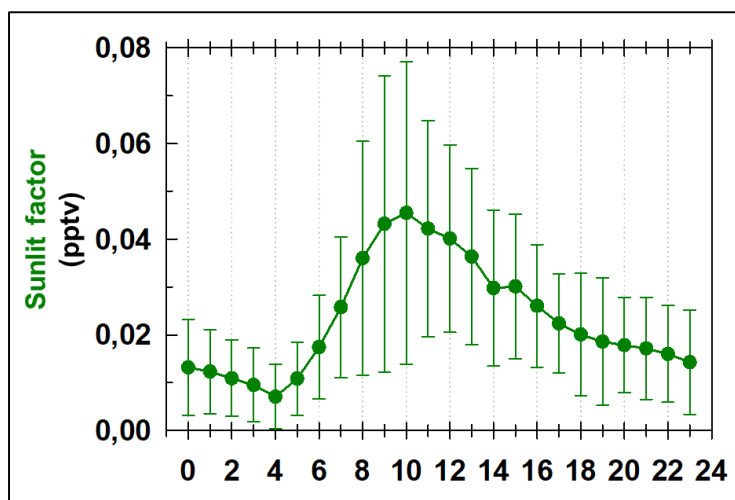


Figure 4.16. The average diurnal cycles of PCA-derived Sunlit component from HOM data collected by the NO₃⁻ToFCIMS throughout the campaign. The error bars represent one standard deviation of the bin for which the average is shown by the symbol.

Notably, the Sunlit component introduces a new category of compounds comprising both nitrates and non-nitrates with C₁₈ molecular structures. Some of these specific compounds have been observed in both the gas and the particulate phases, measured by FIGAERO-CIMS using iodide and acetate reagent ions during ambient measurements in Hyytiälä, Finland (Mohr et al., 2017). Accretion formation pathways from the oxidation reactions of monoterpenes were suggested in the latter study. Insufficient information is currently available in both the literature and our study to assess these formation pathways comprehensively. The Sunlit component also consists of a few C₁₅ and C₁₇ organic nitrates. These may be accretions from monoterpenes oxidation while C₁₅ may also be oxidation products from sesquiterpenes. Figure 4.11.e shows that the Sunlit component has fair correlation with the solar radiation, temperature, OH and H₂SO₄ (R>0.45). The correlation with OH indicates that the chemistry represented by this factor may be influenced mainly by oxidation processes initiated by the OH· radical. The involvement of NO is also likely to be present,

especially considering that all the molecules included in this component are organic nitrates (Yan et al., 2016).

4.5.2.6. Sunlit terpenes

The Sunlit terpenes component shows an increase starting at 5:00 and reaches its maximum levels around 0.35 pptv at 12:00 (Figure 4.17). Interestingly, it is predominantly present during the daylight hours, with significantly lower levels (about five times lower) during the night. This suggests that the compounds in this component are predominantly formed as a result of reactions involving OH· radicals and/or O₃, in the presence of NO. Also, the Sunlit terpenes component shows high correlation with solar radiation and temperature ($R > 0.7$) and a fair correlation with OH reactivity, OH· and O₃ concentrations ($R > 0.4$, Figure 4.11.f). The major peak in this component corresponds to C₁₀H₁₈O₉ molecules, which contribute approximately 15% of the Sunlit terpenes component. This component also includes C₁₈ compounds previously discussed for the sunlit component.

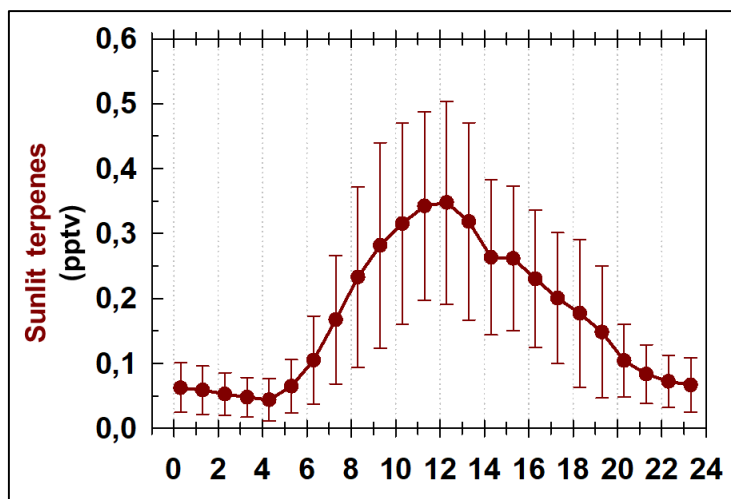


Figure 4.17. The average diurnal cycles of PCA-derived Sunlit component from HOM data collected by the NO₃⁻ ToFCIMS throughout the campaign. The error bars represent one standard deviation of the bin for which the average is shown by the symbol.

4.5.2.7. Isoprene accretions

The Isoprene accretions component displays a distinct diurnal profile, with slightly greater prominence during nighttime (Figure 4.18). It starts to increase from 21:00, peaking at 23:00 around 0.2 pptv, with a small enhancement observed between 6:00 and 8:00 around 0.15 pptv. It then progressively and gradually decreases to a minimum between 15:00 and 20:00 around 0.05 pptv.

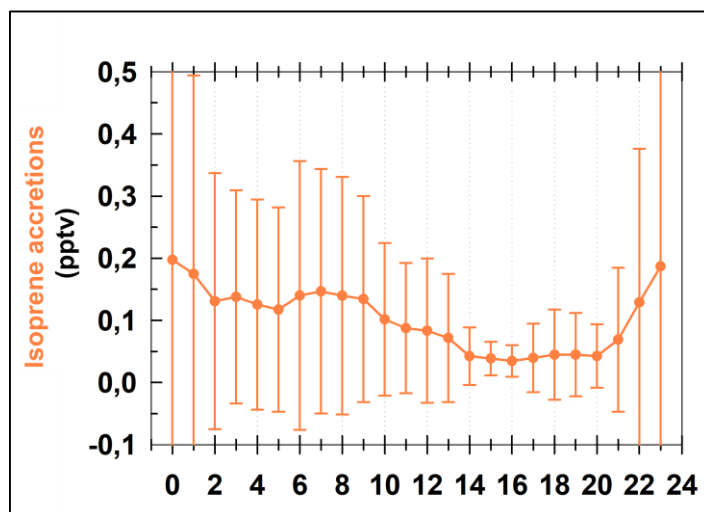


Figure 4.18. The average diurnal cycles of PCA-derived Sunlit component from HOM data collected by the NO_3^- ToFCIMS throughout the campaign. The error bars represent one standard deviation of the bin for which the average is shown by the symbol.

The contributors of this component are C_5 and C_{10} nitrates, probably formed through accretion processes from isoprene oxidation products, with the two major contributors to this component are the two dinitrates, $\text{C}_5\text{H}_8\text{N}_2\text{O}_9$ and $\text{C}_5\text{H}_{10}\text{N}_2\text{O}_9$, accounting for 27% and 52% of the component. These specific molecules have been observed in laboratory studies involving isoprene reactions with $\text{NO}_3\cdot$ (Wu et al., 2021; Zhao et al., 2021), which aligns with their presence mostly during nighttime. These molecules have also been detected in the mass spectrum obtained during measurements of the oxidation of isoprene by $\text{OH}\cdot$ radicals in the presence of NO (Lambe et al., 2017) and in the reaction involving limonene + OH in high NO_x conditions (Luo et al., 2023). This may explain the small increase in the levels of this component observed between 6:00 and 8:00, which is consistent with the higher NO levels at the site. Additionally, compounds such as $\text{C}_{10}\text{H}_{17}\text{N}_3\text{O}_{12-14}$, $\text{C}_{10}\text{H}_{16}\text{N}_2\text{O}_{12,13}$, and $\text{C}_{10}\text{H}_{18}\text{N}_2\text{O}_{11}$ can be formed through accretion processes from $\text{C}_5\text{-RO}_2\cdot$ nitrates, as observed in the studies of Wu et al. (2021) and Zhao et al. (2021). $\text{C}_{10}\text{H}_{17}\text{N}_3\text{O}_{12-14}$ could also be C_{10} -monomers, seen in the study involving limonene + NO_3 (Guo et al., 2022a). The formation of $\text{C}_{10}\text{H}_{18}\text{N}_2\text{O}_{11}$ has been detected from the oxidation of limonene by $\text{OH}\cdot$ radicals in the presence of NO (Luo et al., 2023), while $\text{C}_{10}\text{H}_{16}\text{N}_2\text{O}_{12,13}$ has been observed in the oxidation experiment involving α -pinene + NO_3 (Lambe et al., 2017). Figure 4.11.g shows that the highest correlation of Isoprene accretions are with the three terpene oxidation products ($R > 0.5$), and with MVK, MACR, and the ISOPOOH isoprene oxidation products ($R > 0.4$). It also shows fair positive correlations with NO_2 , O_3 and temperature ($R > 0.3$).

One can notice from the correlations that all components, except for Terpene accretions, show negative correlations with RH and positive correlations with temperature. Similar correlations were

observed during the SOAS 2013 field campaign (Massoli et al., 2018). Brüggemann et al. (2017) also showed the decrease of HOMs signals under higher RH conditions, during a field study in a rural site in Southeastern Germany (F-BEACH 2014). The latter study suggests an increase of RH induces fast phase transition of HOMs. However, Li et al., (2019) reported no effect induced by RH variation on the abundance of gas-phase HOMs in laboratory investigations involving the ozonolysis of α -pinene, limonene and Δ^3 -carene. Finally, Frege et al. (2018) and Quéléver et al. (2019) found that HOMs are more efficiently formed at higher temperature, which is supported by the positive correlations found within this work.

4.5.3. Case studies

This section examines individual cases to investigate the factors influencing the formation of different components of HOMs. By analyzing various parameters within these specific scenarios, our goal is to uncover the factors that impact the production of HOMs. These case studies aim to improve our understanding of the mechanisms guiding HOMs generation and how these processes vary in different situations.

We consider three distinct time periods: Study-1 (30th June to 4th July), Study-2 (18th and 19th July) and Study-3 (7th to 11th July).

Study-2 had clear skies and high temperatures exceeding 36°C during daylight hours, and with average daily temperatures of around 29°C. In contrast, during Study-1, there was cloudy weather and cooler average temperatures of 16.7°C. The diurnal patterns for various species (BVOCs, NO, NO₂, AOx, and OH levels) and parameters (temperature, SR, WS) are illustrated in Figure 4.19, alongside the seven components of HOMs. Table 4.7 provides the average values of several parameters for each case study period.

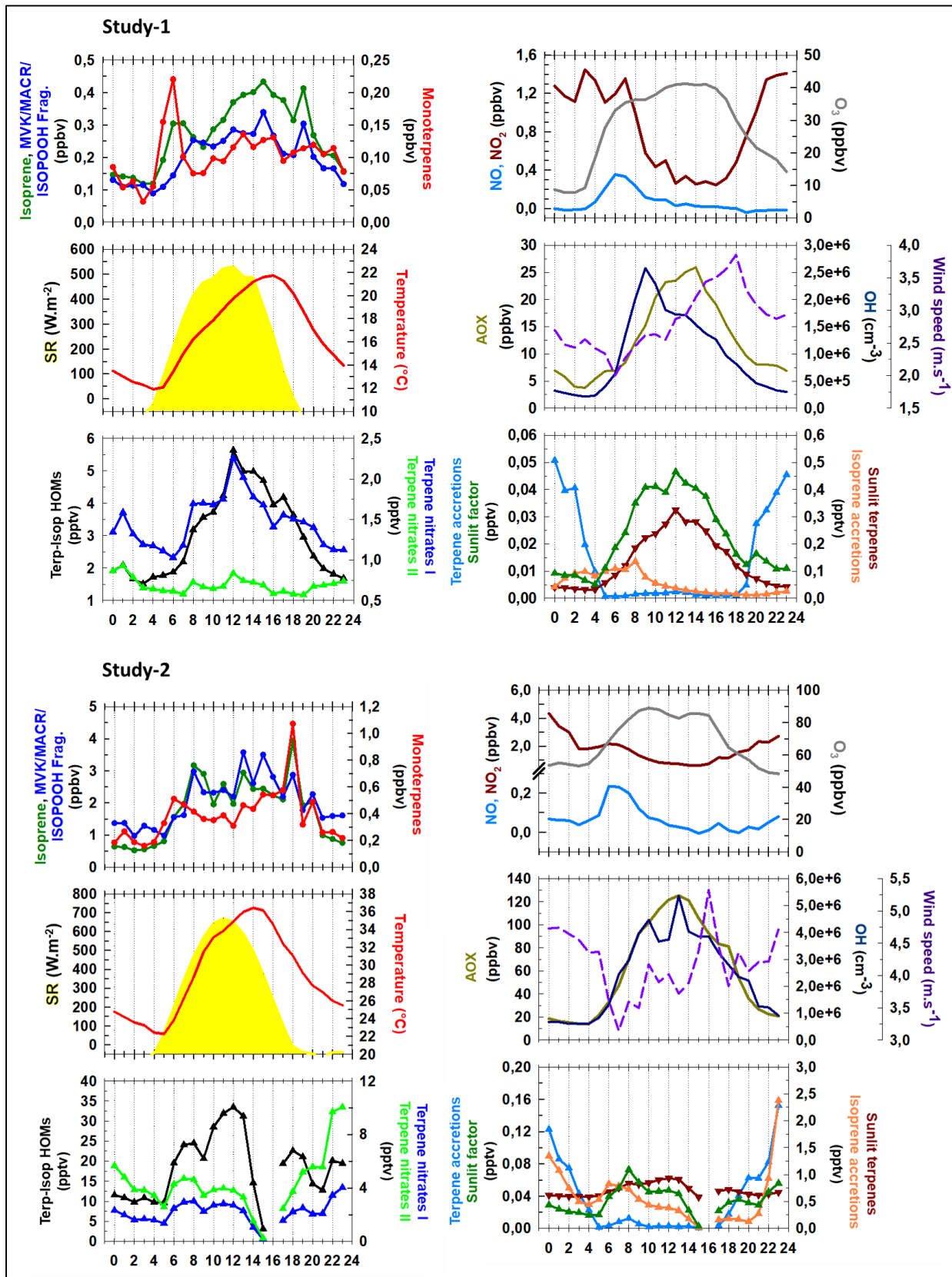


Figure 4.19. Diurnal variations of measured parameters at the top of the tower: Study-1 (upper panel) and Study-2 (lower panel).

Table 4.7. Summary of Statistics for the different case studies.

Case study	NO ₂ (ppbv)	NO* (ppbv)	O ₃ (ppbv)	Isoprene* (ppbv)	MTs* (ppbv)	Total HOMs (pptv)	AOx* (pptv)	OH* (×10 ⁶) cm ⁻³	T (°C)
Study-1	0.86±0.45	0.06±0.11	27.8±12.1	0.27±0.1	0.10±0.04	4.9±1.5	12.6±7.3	0.99±0.74	16.7±3.4
Study-2	1.8±0.95	0.07±0.07	68.8±14.9	1.8±0.97	0.39±0.19	29±8.9	60.4±40.9	2.4±1.5	28.9±4.8
Study-3	1.5±0.65	0.16±0.26	43.2±8.3	×	×	8.8±3.2	17.5±10.4	1.8±1.6	20.5±4.2

*Preliminary results; × Data not available. Mean± 1 standard deviation

It's important to highlight that Study-2 coincided with an air mass originating east of the site and anticyclonic conditions, while Study-1 was influenced by southwesterly winds.

Our observations unveil significant differences in air composition between the two studies. Specifically, O₃ levels were notably elevated in Study-2, reaching up to 100 ppbv, which was more than twice the peak level in Study-1. Furthermore, NO₂ levels in Study-2 were approximately twice the levels of NO₂ in Study-1, indicating variations in air pollution. Alongside the aforementioned distinctions, Study-2 exhibited slightly higher wind speeds than Study-1. Additionally, isoprene, MVK/MACR/ISOPOOH, and monoterpenes levels were on average around 8, 10, and 5 times higher, respectively, with highest values between 8:00 and 18:00.

As indicated in Figure 4.19, AOx levels during Study-2 were over five times higher than those in Study-1 during the same times of day. Analogous fluctuations in the levels of HOMs measured at the site is also observed during the two period with HOMs concentrations being 6 times higher during Study-2 compared to period of Study-1.

Additionally, when comparing OH concentrations during daylight hours, we found that OH levels in Study-2 were more than twice those observed in Study-1. Interestingly, the patterns of OH concentrations differ between the two studies. In Study-1, OH peaked at 10:00 around 2.28×10^6 cm⁻³, coinciding with the peak of solar radiation, while in Study-2, OH peaked at around 13:00 around 5.36×10^6 cm⁻³.

It is important to note that the significant increase in the formation of HOMs in Study-2, by up to a factor of 10, may be attributed to various factors, such as polluted conditions, more rapid chemical reactions at the higher temperatures, elevated levels of oxidants, and increased biogenic emission rates. Furthermore, as polluted air masses containing high levels of NO_x were transported to the site during Study-2, the influence of the NO₃-initiated component (Terpene nitrates II) increased, ultimately assuming a dominant role at night. In the context of Study-1, no distinct nocturnal increase was observed in the levels of the first three components.

Another important finding involves the diurnal profile of Isoprene accretions, as depicted in Figure 4.19, where there were significantly higher levels found during Study-2, peaking at 23:00 at mixing

ratios of around 2.5 pptv. In contrast, this component remains low during Study-1. This observation further supports the influence of NO_3 -initiated chemistry. Notably, this trend closely aligns with the nocturnal variations observed in the Terpene accretions component, providing further support for the previously proposed hypothesis that Isoprene accretions are most likely second generation products (2-N C_5 HOMs) and accretion products (2-N and 3-N C_{10} HOMs) resulting from the reaction of isoprene with NO_3 . This explanation elucidates the rationale behind the nomenclature chosen for this component. A small enhancement was also observed between 6:00 and 8:00 around 0.9 pptv, aligning with the morning peaks in monoterpenes and NO levels. One potential explanation is the involvement of termination reactions by NO during this time window. The significant decline observed in the various HOMs in Study-2 around 14:00-15:00 was initially thought to be linked to operational challenges faced by the instrument pumps in the elevated ambient temperature environment. However, a thorough examination of the operational parameters, including the pressures of the SSQ and BSQ components, as well as the temporal variation in reagent ion counts, revealed that the instrument was functioning normally. This led us to hypothesize that additional factors or parameters may be required to fully explain this phenomenon.

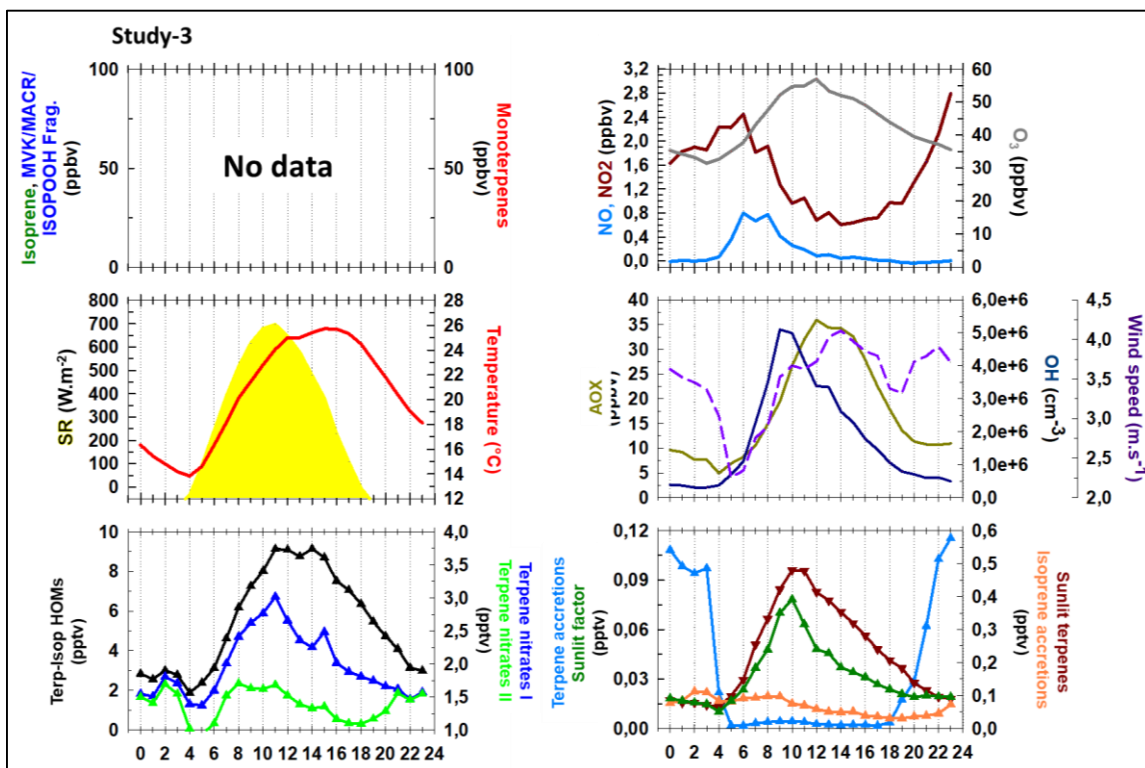


Figure 4.20. Diurnal variations of measured parameters at the top of the tower: Study-3.

Study-3 is characterized by air masses originating from the northeast of the research site, aligning with the initial objectives of the ACROSS project. Study-3's parameter levels fall between those of

Study-1 and Study-2. Throughout Study-3, clear skies and warm temperatures prevailed, with daytime temperatures peaking around 26°C and with daily averages about 20°C. Figure 4.20 visually depicts diurnal patterns for various species and parameters, like previously shown in Figure 4.19.

In terms of O₃ levels, Study-3 showed average concentrations peaking around 60 ppbv at 12:00, between the average peak values of Study-1 (41 ppbv) and Study-2 (90 ppbv). Additionally, Study-3 exhibited a distinct NO₂ concentration trend, with an initial peak at 6:00 around 2.4 ppbv followed by a larger peak at 23:00 around 2.8 ppbv. NO levels during Study-3 were roughly between two and three times higher than Study-1 and Study-2, indicating more elevated air pollution transported to the site. However, VOC data from the PTRMS for this specific time period are unfortunately unavailable.

During Study-3, AOx levels reached a noon maximum of 36 ppbv, around one-third that of Study-2 levels. Similarly, HOM levels were lower in Study-3 compared to Study-2, yet approximately twice as high as those in Study-1. Furthermore, the average daily concentration of OH· radicals in Study-3 was approximately 1.78×10^6 molecules.cm⁻³ approximately 25% lower than Study-2 but higher by approximately 80% compared to Study-1.

Throughout daylight hours, during Study-3 terpene nitrates I dominated over terpene nitrates II, while nighttime levels of these components were nearly equal.

To gain deeper insights into the formation and evolution of various HOM components over time, it is crucial to consider additional factors, especially the physical and chemical properties of aerosols. These properties can offer insights into the intricate ways HOMs are generated and removed from the gas-phase. Additionally, efforts are ongoing to validate VOC data collected using appropriate instruments on the site.

4.5.4. Other measured OVOCs

The ToFCIMS detected various other oxidized molecules, in particular C₂ and C₃ compounds, but also C₄, C₆, and C₇ compounds. Figure 4.21 displays the time series of the prominent OVOCs which are not classified as HOM species (non-HOM compounds). Notably, C₂H₂O₄ (oxalic acid) and C₃H₄O₄ (malonic acid) were prevalent, contributing approximately 0.5% and 5%, respectively to the total of observed compounds. It is worth mentioning that malonic acid is the second most abundant species measured by the ToFCIMS at the site. These two compounds exhibit a strong correlation with each other ($R \approx 0.83$). Another important compound is succinic acid (C₄H₆O₄), which is a C₄ dicarboxylic acid, and which is defined as a non-HOM compound due to its strong

correlations with oxalic ($R \approx 0.79$) and malonic acids ($R \approx 0.7$). Succinic acid was found to contribute about 0.6% of the total of all observed compounds. An additional significant C_3 compound identified at the site is $C_3H_4O_5$, constituting around 0.4% of the total contribution. This compound shows notable correlations with oxalic acid ($R \approx 0.84$) and malonic acid ($R \approx 0.87$), and is likely to be tartronic acid (2-hydroxymalonic acid). These organic acids exhibit notable formation during daylight hours and have minimal levels during the nighttime, underscoring the predominant influence of photochemical oxidation in their formation (Ye et al., 2021).

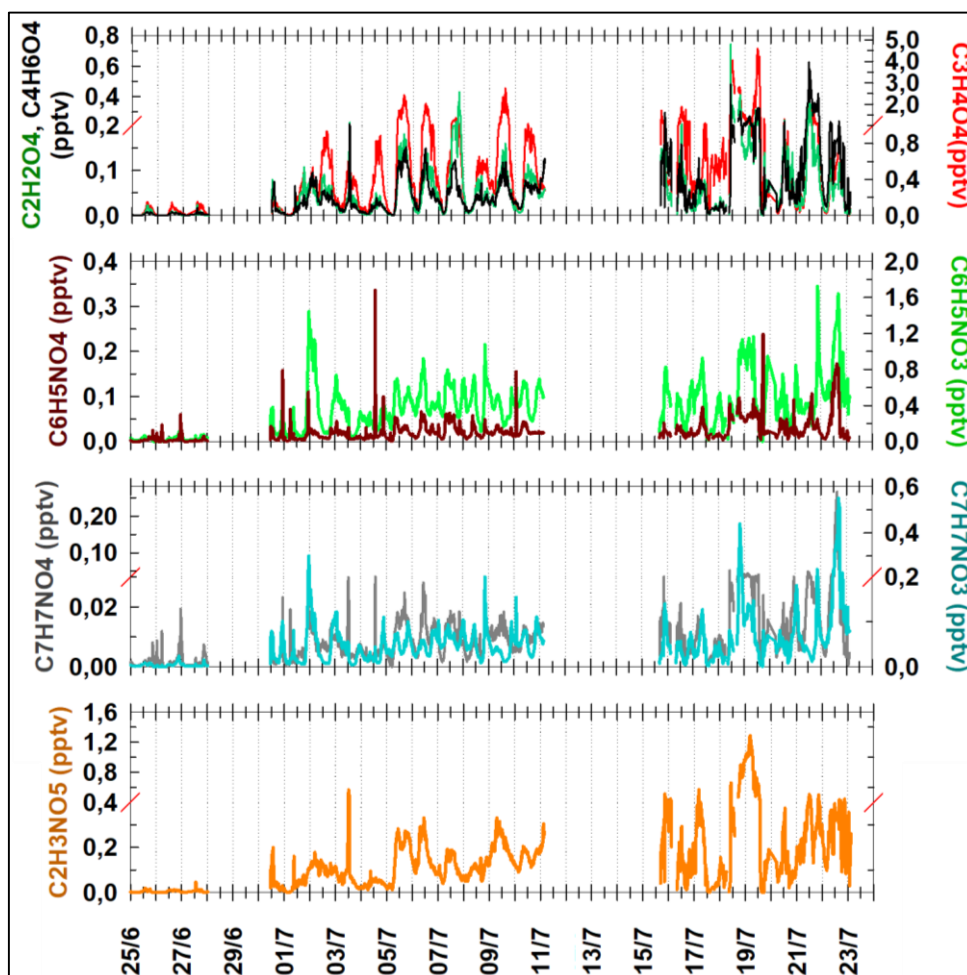


Figure 4.21. Time Series of major Non-HOM species detected by the NO_3^- ToFCIMS on the tower level.

Another noteworthy contributor is $C_2H_3NO_5$, accounting for 1.5% of the total HOM species, which corresponds to the primary PAN (peroxyacetyl nitrate) formed through the reaction of acetylperoxy radicals with NO_2 . The acetyl peroxy radicals are formed from OH reaction with acetaldehyde in the presence of NO_2 (Atkinson, 2000). The mass spectrum obtained from the ToFCIMS measurements does not show any evidence of the presence of other PANs.

Additionally, a prominent nitrophenol observed on-site is $C_6H_5NO_3$, ranking as the third most prevalent compound with an individual contribution of 3.5%. Other nitrophenols that include

C₆H₅NO₄, C₇H₇NO₃ and C₇H₇NO₄ are always observed in the measurements. Although these four molecules were previously associated with biomass burning (Mohr et al., 2013; Yan et al., 2016; Massoli et al., 2018) and vehicle emissions (Harrison et al., 2005; Inomata et al., 2015; Mehra et al., 2021), these observations suggest that other sources may be responsible for their formation. Notably, during a fire event on the afternoon of July 19th, only C₆H₅NO₄ displayed a noticeable spike in its levels, while C₆H₅NO₃, C₇H₇NO₃, and C₇H₇NO₄ levels did not exhibit a distinct increase. Furthermore, no significant increase was observed during periods of polluted air mass conditions for these compounds.

Table 4.8 presents the molecular formulas of the previously discussed non-HOM organics detected by the ToFCIMS at the top of the tower. The molecules are listed in descending order according to their contribution to the overall spectrum.

Table 4.8. C₂-C₃ nitrates and non-nitrates molecules and C₆-C₇ nitrophenols detected by the ToFCIMS at the tower level, listed in descending order based on their contribution to the overall spectrum. *non-nitrate C₄.

Molecules	Contribution (%)
C ₃ H ₄ O ₄	5.0
C ₆ H ₅ NO ₃	3.5
C ₂ H ₃ NO ₅	1.4
C ₄ H ₆ O ₄ *	0.6
C ₂ H ₂ O ₄	0.5
C ₇ H ₇ NO ₃	0.5
C ₃ H ₄ O ₅	0.4
C ₃ H ₆ O ₃	0.3
C ₃ H ₅ NO ₆	0.2
C ₆ H ₅ NO ₄	0.2
C ₃ H ₃ NO ₂	0.1
C ₃ H ₄ O ₆	0.1
C ₂ H ₄ O ₄	0.1
C ₃ H ₃ NO ₆	0.1
C ₃ H ₆ O ₄	0.1
C ₇ H ₇ NO ₄	0.1
C ₂ H ₂ O ₅	0.1
C ₂ H ₂ O ₃	0.1
C ₃ H ₇ NO ₅	0.1
C ₃ H ₅ NO ₃	0.05
C ₃ H ₄ O ₈	0.04
C ₂ H ₆ O ₅	0.04
C ₃ H ₄ O ₇	0.03
C ₃ H ₆ O ₂	0.03
C ₃ H ₄ O ₃	0.02
C ₃ H ₂ O ₄	0.02
C ₃ H ₂ O ₅	0.02
C ₃ H ₂ O ₃	0.02
C ₃ H ₄ O ₂	0.02
C ₂ H ₃ NO ₃	0.02
C ₂ H ₄ O ₃	0.02
C ₃ H ₇ NO ₂	0.01

4.5.5. Gas-phase HOMs relationship to Organic Aerosols detected by a Time-of-Flight Aerosol Mass Spectrometer (ToF-AMS)

In this section, we assess the potential impact of observed HOMs on the particulate phase by analyzing the relationships between total HOMs and PCA-derived factors, as obtained from the NO_3^- ToFCIMS data, and the observations using a Time-of-Flight Aerosol Mass Spectrometer (ToF-AMS) instrument (Ferreira de Brito et al., 2023), at the top of the tower. It's important to emphasize that we should not expect a perfect match between these two datasets. This is because there is an anticipated time delay between the formation of HOMs in the gas-phase and their subsequent partition into the particle phase.

Organic aerosols (OA) derived from the AMS instrument (OA-AMS) are formed from various processes including primary combustion and secondary atmospheric reactions. Positive Matrix Factorization (PMF) analysis is typically employed for source apportionment of the OA datasets, helping to differentiate between various sources (Mohr et al., 2009; Sofowote et al., 2015; Liu et al., 2021). However, at the date of this work, this analysis has not yet been applied. This additional information could enhance our understanding of the sources contributing to HOMs formation and sinks in the atmosphere.

Figure 4.22.a illustrates a time series plot depicting total HOMs (dark red trace) and OA-AMS (light red trace) levels. Their profiles reveal a degree of similarity, with a time lag between them, as anticipated. Figure 4.22.b depicts the diurnal cycles of the three PCA-derived components: Terpene-Isoprene HOMs (black trace), Terpene nitrates I (blue trace), and Terpene nitrates II (light green trace). The diurnal cycle calculations were applied for the same period of time acquisition for HOM components and OA-AMS. Within the same plot, these are compared to the diurnal cycle of OA-AMS (red dashed trace), with data points related to the significant fire event in the afternoon of July 19th excluded.

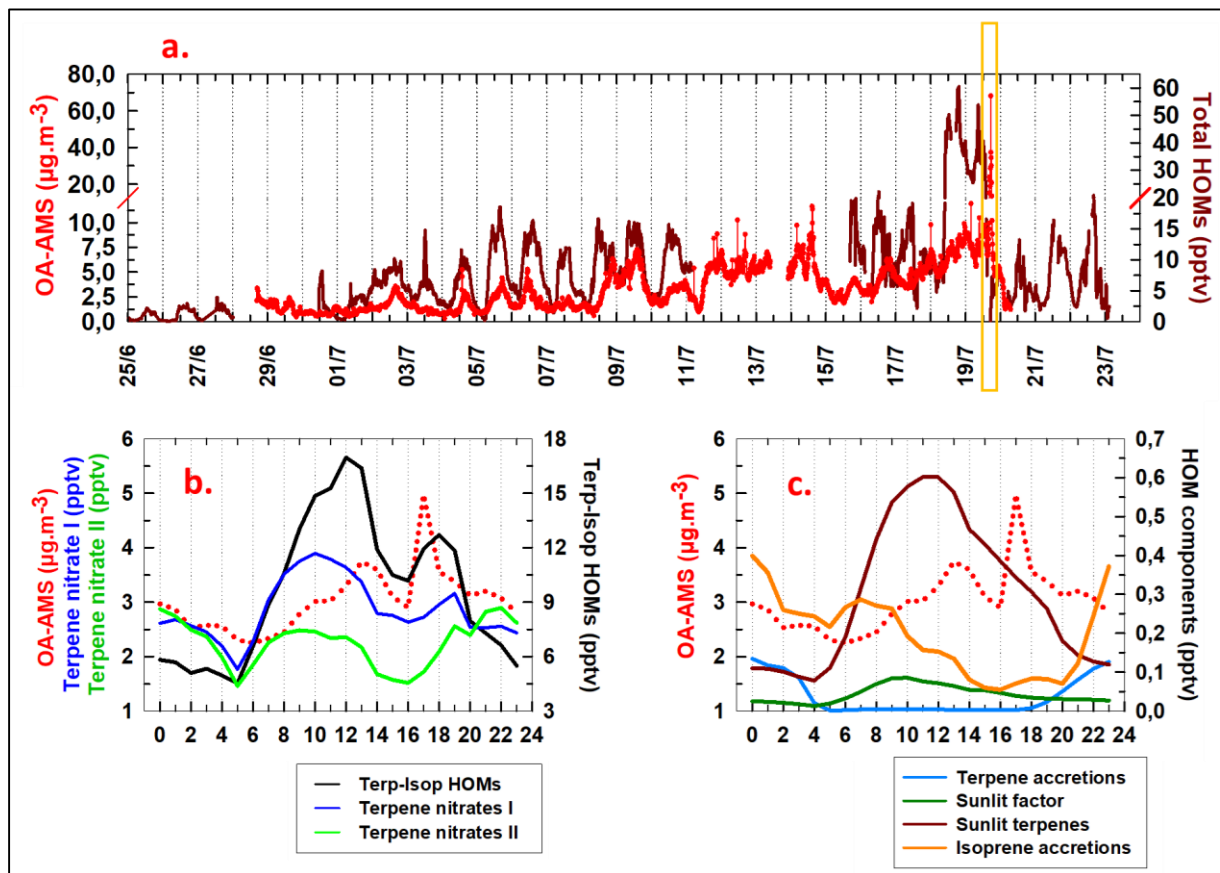


Figure 4.22.a. Temporal data of total HOMs (dark red trace) and OA-AMS (light red dotted trace). The yellow squared area represents a significant biomass burning event that occurred in the afternoon of July 19th. Breaks are introduced at 12.5 for the left y-axis and 20 for the right y-axis. b, c. Diurnal cycles of PCA-derived HOM components and OA-AMS data. Data related to biomass burning have been excluded from the diurnal cycle calculations.

The diurnal pattern of Terpene-Isoprene HOMs closely looks like that of OA-AMS, with the HOMs peaking an hour earlier at noon and again at 18:00. Similarly, Terpene nitrates I exhibit a diurnal profile with peaks at 10:00 and 19:00, consistent with the daytime enhancements observed in OA-AMS. Terpene nitrates II also display a similar pattern to the Terpene nitrates I, particularly during the night (between midnight and 5:00). To further validate these similarities and relationships, Pearson correlation coefficients were calculated using all available data from days where both HOMs and AMS data were collected (Figure 4.23.a). Additionally, separate calculations were performed for daytime and nighttime data (Figure 4.23.b and 4.23.c). These calculations reveal medium to strong correlations for all three HOM monomers components with OA-AMS for the 24-hour period ($R > 0.7$), during daytime ($R > 0.6$), and notably during nighttime ($R > 0.8$).

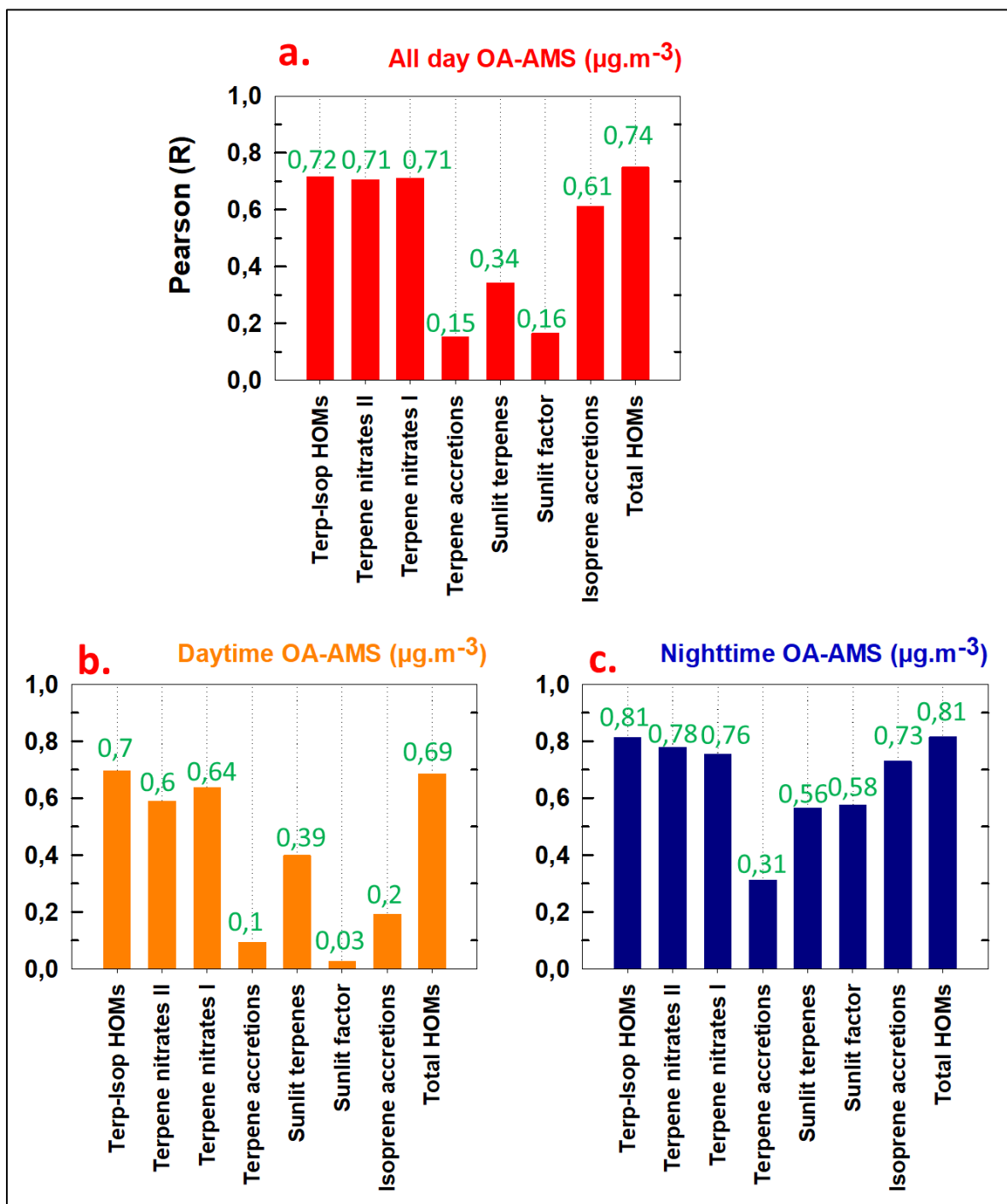


Figure 4.23. Pearson correlation coefficient between the OA-AMS and the 7 principal components of the PCA analysis. a. throughout the day. b. daylight (6:00–19:00). c. nighttime (21:00–4:00).

Similarly, Figure 4.22.c presents the diurnal cycles of the four other PCA-derived components that are also compared with OA-AMS values: Terpene accretions (light blue trace), Sunlit factor (dark green trace), Sunlit terpenes (dark red trace), and Isoprene accretions (orange trace). The diurnal pattern of Isoprene accretions demonstrates a strong correlation with that of OA-AMS, particularly during the nighttime ($R > 0.7$). Overall, the robust relationships observed between Terpene-Isoprene HOMs, Terpene nitrates I, Terpene nitrates II, and Isoprene accretions with OA-AMS provide

support that HOMs tend to condense onto the particle phase, possibly contributing to a significant portion of the organic mass at the site. It is clear that additional quantitative data is required to substantiate these findings.

Conversely, Terpene accretions, Sunlit factor, and Sunlit terpenes display weak-to-moderate correlations with OA-AMS, notably during the daytime, as indicated by the low Pearson correlation coefficient displayed in Figure 4.23.b ($R < 0.4$). These components, suggested to be primarily accretion products, have presumably low volatility and thus are expected to participate in the SOA formation and growth. Consequently, one might expect better correlations between their observed diurnal patterns and OA-AMS. Nevertheless, this was not the case in this study. One possibility is that these molecules are present at significantly lower levels (below 1 pptv) compared to other constituents, especially the monomer components. As a result, they contribute only minimally to the total OA, potentially explaining the lower correlations observed compared with the monomer components.

4.6. Discussion

The NO_3^- ToFCIMS was deployed at the top of the 40-meter in the Rambouillet forest supersite in France during the ACROSS campaign in the summer of 2022. The instrument displayed great sensitivity, detecting levels lower than 0.1 pptv. Successful measurements spanned over 21 days, including 14 full-day data coverage (24 hours) and 7 partial-day data acquisitions. The mass spectra analysis revealed that about 90% of the identified molecules were clusters with NO_3^- ions, while the remaining 10% were deprotonated ions, mainly organic acids with much weaker signal intensities.

On the tower level, isoprene amounts stood out as the dominant BVOCs. On average, they were 3-4 times higher than the total concentration of monoterpene compounds. In contrast, sesquiterpenes were detected at much lower concentrations, typically below 20 pptv. Interestingly, the diurnal patterns of these BVOCs showed similarities in their fluctuations over the course of a day. NO_x was consistently observed throughout the campaign, likely from local sources, including photolytic or forested soil emissions.

Total HOM concentrations varied due to factors such as wind direction, temperature, VOC precursors, ozone, and NO_x levels at the site. The highest HOM levels were observed around 60 pptv in the afternoon of July 18, with daytime levels ranging from 3 pptv to 21 pptv and nighttime levels from 0.2 to 12 pptv. The average total HOM mixing ratio measured throughout the day was

approximately 8.7 ± 9 pptv. In addition, H_2SO_4 levels were also explored, with the highest concentrations occurring in the morning hours, ranging from approximately 0.02 to 0.5 pptv, consistent with levels detected in similar rural locations in Germany and Finland.

A contrast emerged between field observations and chamber experiments regarding the abundance of accretion products compared to monomer products. This suggests complex atmospheric factors at play, possibly involving pre-existing particles or NO_x species influencing HOMs composition.

A total of 442 peaks were identified in the mass spectra, including HOMs, HOM-ONs, OVOCs, and H_2SO_4 . Dinitrates $\text{C}_5\text{H}_{10}\text{N}_2\text{O}_8$ were the predominant isoprene oxidation products, especially during the daytime, accounting for about 6.2% of all observed compounds. Major peaks consisted mainly of organic nitrates in both daytime and nighttime.

PCA statistical revealed seven distinct components, including Terpene-Isoprene HOMs, Terpene nitrates I, Terpene nitrates II, Terpene accretions, Sunlit component, Sunlit terpenes, and Isoprene accretions. Each component exhibited different influences, correlating with meteorological and precursor parameters, as evident from their distinct diurnal patterns.

The Terpene-Isoprene HOMs component was present during the daytime and to a lesser extent during the nighttime. It included numerous types of molecules likely associated with both isoprene and monoterpene oxidation by $\text{OH}\cdot$ and O_3 during the day and O_3 and $\text{NO}_3\cdot$ during the night. The predominant molecules were one, two and to less extent, three nitrogen containing C_4 and C_5 organic nitrates, $\text{C}_5\text{H}_{9,11}\text{NO}_{6,7}$, $\text{C}_5\text{H}_7\text{NO}_7$, and $\text{C}_4\text{H}_7\text{NO}_{6,7}$, $\text{C}_5\text{H}_8\text{N}_2\text{O}_{8,10}$, $\text{C}_5\text{H}_9\text{N}_3\text{O}_{10}$ presumably from the oxidation of isoprene by $\text{OH}\cdot$ radicals in the presence of NO , during the day, and potentially arising from reactions with $\text{NO}_3\cdot$ during night. The Terpene nitrates I component was present during both daytime (maximum on average 2.2 pptv at 11:00) and nighttime (up to on average 1.5 pptv). This component primarily consists of HOM-nitrates, particularly $\text{C}_7\text{H}_{11,13}\text{NO}_6$, $\text{C}_6\text{H}_{11}\text{NO}_6$, $\text{C}_6\text{H}_7\text{NO}_{7,8}$, $\text{C}_6\text{H}_9\text{NO}_7$, $\text{C}_5\text{H}_5\text{NO}_{7,8}$ and the dinitrates $\text{C}_5\text{H}_6\text{N}_2\text{O}_9$, $\text{C}_6\text{H}_{10}\text{N}_2\text{O}_8$ and $\text{C}_{10}\text{H}_{16}\text{N}_2\text{O}_{10}$ with a few non nitrate HOMs, $\text{C}_7\text{H}_8\text{O}_{10}$, $\text{C}_5\text{H}_{10}\text{O}_8$, $\text{C}_9\text{H}_{16}\text{O}_9$ and including $\text{C}_{10}\text{H}_{15}\text{O}_{7,8}\cdot$, $\text{C}_{10}\text{H}_{17}\text{O}_9\cdot$ radicals, most likely associated with the oxidation of monoterpenes. The Terpene nitrates II component was also present during both daytime (maximum on average about 1.4 pptv at 12:00) and nighttime (up to on average 1.5 pptv at 21:00-22:00). For some days, it showed higher formation during the night such as on the night of 2 to 3 July and 8 to 9 July. This category primarily consists of organic nitrate monomers, particularly within the $\text{C}_{10}\text{H}_{15}\text{NO}_{6-9}$ series. NO_3 -initiated chemistry plays a significant role in the formation of Terpene nitrates II. The detection of nitrogen-

containing dimer compounds ($C_{20}H_{31}NO_{11,13,15}$ and $C_{20}H_{32}N_2O_{11-16}$) supports the existence of the nocturnal NO_3 +monoterpene reaction pathway, marking the Terpene accretions component. The latter solely forming after dark (maximum around 23:00-midnight with an average mixing ratio of 0.1 pptv) and disappearing throughout the daylight, possibly suppressed due to the presence of NO. The Sunlit component displayed a broad diurnal pattern, correlated with solar radiation, temperature, and H_2SO_4 , indicating its sensitivity to $OH\cdot$ radicals and the presence of NO. It possibly includes $C_{15,17,18}$ accretions from monoterpenes oxidation, while C_{15} may also be possibly originating from oxidation of sesquiterpenes. The Sunlit terpenes component shows a broad peak during the daytime (maximum at noon on average 0.25 pptv) and about five times lower during the night. The highest contribution is for $C_{10}H_{18}O_9$. This is most likely associated to monoterpene oxidation especially by $OH\cdot$ radicals possibly in the presence of NO. Finally, the Isoprene accretions component displays greater prominence during nighttime and a small enhancement in the morning. These were suggested to be isoprene oxidation product, with major contribution of $C_5H_8N_2O_9$, $C_5H_{10}N_2O_9$, and $C_{10}H_{17}N_3O_{12-14}$, $C_{10}H_{16}N_2O_{12,13}$, and $C_{10}H_{18}N_2O_{11}$.

Additionally, individual case studies were conducted to explore the factors influencing the formation of various HOM components. Three distinct studies were presented: Study-1, which represented relatively clean environmental conditions and cooler temperatures; Study-2, reflecting a heatwave period coinciding with polluted conditions; and Study-3, where parameter levels fell between those of Study-1 and Study-2. It was observed that the formation of HOMs was significantly enhanced, by a factor of up to 10, under conditions of higher temperatures, intense photochemical activity, and transport of pollution, as seen in Study-2 when compared to Study-1 and Study-3. Furthermore, a substantial increase in HOM organic nitrates, whether in the form of monomers or dimers, was particularly noted during nighttime in Study-2 conditions. This can be attributed to the transport of polluted air masses to the site containing elevated levels of NO_x , which exerted a greater influence on NO_3 -initiated reactions, ultimately assuming a dominant role during nighttime hours.

Finally, we explored the relationship between HOMs and the organic aerosol collected by an AMS instrument, which was also deployed at the top of the tower. In summary, the four PCA-derived components, namely Terpene-Isoprene HOMs, Terpene nitrates I, Terpene nitrates II, and Isoprene accretions, exhibited robust correlations with the OA-AMS data, supporting the idea that HOMs tend to condense into the particle phase. However, components primarily composed of accretion products, such as Terpene accretions, Sunlit factor, and Sunlit terpenes, displayed weaker

correlations, possibly due their considerably lower levels and subsequent limited contribution to the overall organic aerosol.

Overall, these comprehensive analyses provide insights into the complex chemistry of organic compounds in the forest environment, with various factors influencing their concentrations and formation pathways.

Conclusions and Perspectives

This thesis work focuses on gas-phase highly oxygenated organic molecules (HOMs), a class of low volatile compounds, detected using a NO_3^- ToFCIMS. Initially, a detailed examination of the NO_3^- ToFCIMS instrument was carried out in the laboratory, along with the implementation of a series of calibration approaches (Chapter 2). This was followed by controlled simulation chamber experiments aimed to mimic various environmental conditions (Chapter 3). Finally, HOMs were identified in the Rambouillet forest during the large-scale ACROSS field campaign, in summer 2022 (Chapter 4). The results of these chapters highlight the complex nature of HOMs and their significant impacts on atmospheric processes.

To meet the first objective of my thesis, the calibration and operational aspects of the NO_3^- ToFCIMS instrument have been extensively explored in the laboratory to ensure its accuracy and reliability for detecting HOMs as well as other oxygenated volatile organic compounds (OVOCs). The first experiments, detailed in Chapter 2, revealed that the choice of sample flow rate should be determined by carefully adjusting total and sheath flow rates to optimize instrument performance. It was observed that lower total flows resulted in more stable reagent ion signals, possibly due to the avoidance of turbulence and other environmental interferences associated with high air flows. Furthermore, we investigated the effects of two instrumental components, BSQ Front (BSQF) and BSQ Back (BSQB), on ion distribution. Specific voltage settings (BSQF 6.2V; BSQB 5.7V; Skimmer 2.1V) were selected for further laboratory and field studies as they facilitated stable cluster formation with NO_3^- for most tested organic compounds.

The second main goal of this thesis was to develop a reliable protocol for calibrating the NO_3^- ToFCIMS instrument. This process is crucial as it helps assess the instrument's ability to accurately detect HOMs, ensuring its sensitivity and linearity. Two calibration methods were used. Approach-1 consisted of introducing detectable compounds into the instrument at a controlled temperature. Approach-2 involved injecting pyruvic acid into a simulation chamber, collecting data using the ToFCIMS, and comparing ToFCIMS signals with pyruvic concentrations determined through FTIR measurements. Calibration factors were established for pyruvic, oxalic, malonic, succinic, and tartaric acids, as well as 4-nitrocatechol, and significant differences were observed. This variability highlighted that the NO_3^- ToFCIMS sensitivity is compound-specific, underscoring the importance of tailoring calibration approaches for different compounds rather than relying on a single factor. The use of H_2SO_4 calibration was also explored to be able to compare our field results

with existing literature studies. The corresponding calibration factors were obtained for different setups ($2.83\text{-}8.08 \times 10^9$ molecules. cm^{-3}) and were found to align with reported literature ranges for H_2SO_4 calibration ($1.65\text{-}60 \times 10^9$ molecules. cm^{-3}).

Chapter 3 outlines a series of experiments conducted in the CESAM simulation chamber, which were part of the preparations for the ACROSS field campaign. These experiments were conducted to fulfill in part the third objective of this thesis. The primary aims of these experiments were to identify potential atmospheric products to help field data interpretation and to assess the instrument's performance by comparing the results with existing literature. The NO_3^- ToF-CIMS was employed in three distinct time periods, each involving different reaction systems.

In the first set of experiments, the reactions of three BVOC precursors, namely α -pinene, limonene, and 3-carene, with ozone were each explored in the presence of cyclohexane as an $\text{OH}\cdot$ radical scavenger. These experiments were conducted without the addition of NO_x or particulate seeds, thus exploring conditions of SOA formation expected to result from the organic nucleation of low volatility species. HOMs were observed during the oxidation of these monoterpenes, primarily featuring $\text{C}_{10}\text{H}_{14,16}\text{O}_{7,9,11}$ monomers. However, there were notable variations in their relative abundances, suggesting differences in the branching ratios for key processes in each reaction mechanism. α -pinene exhibited significant fragmentation, yielding specific monomer fragments such as $\text{C}_5\text{H}_6\text{O}_7$ while limonene and 3-carene experiments had minimal fragmentation. Interestingly, these findings were generally consistent with previous literature reports, though an important discrepancy emerged as higher levels of dimers were detected in these experiments compared to monomers, possibly attributed to variations in experimental conditions and chemical kinetics.

The second group of experiments involved studies of monoterpene mixtures, where pairs of compounds (limonene with 3-carene and limonene with α -pinene) were examined. Limonene's oxidation products dominated in these mixtures, showing distributions and abundances similar to those observed in limonene-only experiments. However, the limonene and 3-carene mixture exhibited a more significant formation of dimers compared to individual monoterpene experiments, in contrast to the limonene and α -pinene mixture.

The third set of experiments focused on the reaction of two other monoterpene precursors, α -phellandrene and β -phellandrene, with $\text{NO}_3\cdot$ radicals. While a few monomers, primarily

$C_{10}H_{15,17}NO_{8,9}$, were detected, the most substantial contribution came from C_{17} and C_{20} organic nitrates.

The final group of laboratory experiments explored the reaction of aromatic AVOCs, namely toluene and m-xylene, with $OH\cdot$ radicals. Surprisingly, no HOMs were detected in these experiments, possibly due to the addition of seed particles to the chamber, which may have quickly scavenged any HOMs produced into the particle phase, thus preventing their detection in the gas-phase.

Chamber experiments demonstrated the versatility of the instrument, showcasing its ability to detect a wide range of compounds, even at very low concentrations, often as low as a few parts per quadrillion (ppqv). These findings contribute to a better understanding of atmospheric chemistry and have significant implications for interpreting data from the ACROSS field campaign.

Finally, Chapter 4 covers the deployment of the NO_3^- ToFCIMS instrument at the top of the 40-meter tower in the Rambouillet forest supersite in France during the ACROSS campaign in the summer of 2022. The instrument demonstrated remarkable sensitivity, detecting compounds at levels lower than 0.1 pptv. Isoprene was the dominant BVOC at the tower level, with amounts 3-4 times higher than monoterpene compounds. NO_x was consistently observed throughout the campaign.

Total HOM concentrations varied due to factors like wind direction, temperature, VOC precursors, ozone, and NO_x levels. The field observations revealed a significant contrast with chamber experiments regarding the abundance of accretion products compared to monomer products. This suggests that complex atmospheric factors, such as pre-existing particles or NO_x species, are influencing the composition of HOMs in real atmospheric conditions.

In total, 442 peaks were identified in the mass spectra, including HOMs, HOM-ONs, OVOCs, and H_2SO_4 . Principal Component Analysis (PCA) identified seven distinct HOM components, each exhibiting different influences correlated with meteorological and precursor parameters. These components are Terpene-Isoprene HOMs, Terpene nitrates I, Terpene nitrates II, Terpene accretions, Sunlit component, Sunlit terpenes, and Isoprene accretions.

The diurnal patterns of these components varied, with Terpene-Isoprene HOMs, Terpene nitrates I and II were detected during the daytime and nighttime. The Terpene accretions component was unique, forming exclusively after sundown. The Sunlit component and Sunlit terpenes exhibited a peak during the daytime. Isoprene accretions were more prominent during nighttime.

Several case studies explored the factors influencing the formation of these HOM components, with Study-2, representing a heatwave period with transport of polluted air masses to the site, showing significantly enhanced HOM levels compared to Study-1 and Study-3. The presence of polluted air masses with elevated NO_x levels played a dominant role in NO_3 -initiated reactions during nighttime hours.

Finally, the relationship between HOMs and organic aerosol collected by AMS instrument at the tower top was investigated. Four PCA-derived components, Terpene-Isoprene HOMs, Terpene nitrates I, Terpene nitrates II, and Isoprene accretions, exhibited strong correlations with the OA-AMS data, indicating HOMs' tendency to condense into the particle phase. Components primarily composed of accretion products, like Terpene accretions, Sunlit factor, and Sunlit terpenes, displayed weaker correlations. This weak correlation may be attributed to the fact that these molecules were detected at significantly lower levels compared to the first four PCA-derived components, contributing only minimally to the total organic aerosol.

In summary, these analyses provide valuable insights into the complex chemistry of organic compounds in the forest environment, shedding light on various factors influencing their concentrations and formation pathways.

This research work highlighted a number of perspectives intended to expand upon these findings:

- The first part of this work revealed that several factors can influence the NO_3^- ToFCIMS instrument's performance, such as the settings of the APi components voltages, the choice of inlet flows, and temperature. Both laboratory and field observations showed variations in reagent ion signals with changes in relative humidity. Therefore, it is recommended to investigate the impact of humidity on the instrument's sensitivity. If such an effect is confirmed, efforts should be made to develop strategies for minimizing this influence, particularly during field campaigns where humidity exhibits significant diurnal variations.
- The results from the calibration experiments highlighted that the selected organic compounds, particularly small dicarboxylic acids, may not be suitable for determining calibration factors for HOMs quantification. This limitation could be attributed to their specific oxidation state or chemical structure. These findings underscored that the sensitivity of the NO_3^- ToFCIMS is compound-specific, particularly for compounds in the lower mass range of the spectra. To address this challenge, it is essential to identify and explore organic compounds that better represent the properties of HOMs and to serve as a

more dependable and accurate method for quantifying HOMs and compare newly obtained calibration factors with the one obtained by the reference method which uses sulfuric acid as a calibrant. Since such compounds may not be readily available commercially, synthesizing them in the laboratory becomes a necessary step.

- It is advisable to conduct chamber experiments that replicate atmospheric conditions, especially in the context of monoterpene ozonolysis. These experiments should consider the influence of NO_x and the presence of particulate seeds within the chemical reactors. Such an approach may help validate and provide insights into the observed disparity between our chamber experiments and field observations concerning the abundance of accretion products relative to monomer products.
- Expanding the scope of ionization schemes for gas phase measurements in chamber experiments, beyond nitrate, is a logical next step. Utilizing complementary ionization methods like trifluoromethoxy anions (CF₃O⁻) for OVOCs and semi-volatile organic compounds (SVOCs) (Crouse et al., 2006), acetate for organic acids (Bertram et al., 2011), and iodide for a broader range of OVOCs (Lee et al., 2014), can provide a more comprehensive understanding of the evolution of VOC precursors into gas-phase HOMs and subsequently SOA.
- The ambient HOM results presented in Chapter 4 provide valuable insights, but to achieve a comprehensive understanding of HOMs' formation and fate, it is essential to continue investigating once all data from other parameters measured at the top of the tower are available. A PMF analysis on the dataset could also help improve the classification of the different HOMs classes during the campaign and therefore help getting some more insight in the processes responsible for HOMs formation.
- Another perspective would be to further explore the link between HOMs and aerosol formation by utilizing PMF analysis on AMS data, in order to determine if a better correlation and correspondence can be observed for specific factors.
- Exploring the molecular composition of aerosols through the analysis of filters collected at the site, especially employing orbitrap analysis on quartz filters, could provide another perspective. This approach would help us ascertain whether similar compounds are also present in the aerosols, thereby strengthening our findings regarding the role of HOMs in the formation and aging of organic aerosols.
- It has been found that formation and fate of HOMs in the atmosphere are greatly affected by atmospheric dynamics, particularly during nighttime conditions when the decoupling of

air masses below the canopy occur (Zha et al., 2018). Given the presence of another NO_3^- CIMS instrument deployed at ground level, a valuable perspective would be to conduct a comparative analysis between ground-based HOMs measurements and our HOMs measurements from above the canopy. This approach could offer valuable insights into the influence of atmospheric dynamics on HOMs levels. Moreover, this analysis would be valuable insights into the nocturnal chemical processes of HOMs formation.

References

- Ahlberg, E., Falk, J., Eriksson, A., Holst, T., Brune, W.H., Kristensson, A., Roldin, P., Svenningsson, B., 2017. Secondary organic aerosol from VOC mixtures in an oxidation flow reactor. *Atmospheric Environment* 161, 210–220. <https://doi.org/10.1016/j.atmosenv.2017.05.005>
- Airparif, 2022. Emissions de polluants atmosphériques et de gaz à effet de serre - Bilan Île-de-France-2019.
- Airparif, 2021. Inventaire 2018 des émissions atmosphériques en Île-de-France | Airparif [WWW Document]. Airparif. URL <https://www.airparif.asso.fr/actualite/2021/inventaire-2018-des-emissions-atmospheriques-en-ile-de-france> (accessed 11.23.22).
- Ambrose, J., Seinfeld, J., 2008. Chemistry of secondary organic aerosol: Formation and evolution of low-volatility organics in the atmosphere. *Atmospheric Environment* 32.
- Aruffo, E., Wang, J., Ye, J., Ohno, P., Qin, Y., Stewart, M., McKinney, K., Di Carlo, P., Martin, S.T., 2022. Partitioning of Organonitrates in the Production of Secondary Organic Aerosols from α -Pinene Photo-Oxidation. *Environ. Sci. Technol.* 56, 5421–5429. <https://doi.org/10.1021/acs.est.1c08380>
- Atkinson, R., 2000. Atmospheric chemistry of VOCs and NO_x. *Atmospheric Environment* 34, 2063–2101. [https://doi.org/10.1016/S1352-2310\(99\)00460-4](https://doi.org/10.1016/S1352-2310(99)00460-4)
- Atkinson, R., 1997. Gas-Phase Tropospheric Chemistry of Volatile Organic Compounds: 1. Alkanes and Alkenes. *Journal of Physical and Chemical Reference Data* 26, 215–290. <https://doi.org/10.1063/1.556012>
- Atkinson, R., 1995. Gas phase tropospheric chemistry of organic compounds, in: Harrison, R.M., Hester, R.E. (Eds.), *Issues in Environmental Science and Technology*. Royal Society of Chemistry, Cambridge, pp. 65–90. <https://doi.org/10.1039/9781847552310-00065>
- Atkinson, R., Arey, J., 2003a. Gas-phase tropospheric chemistry of biogenic volatile organic compounds: a review. *Atmospheric Environment* 37, 197–219. [https://doi.org/10.1016/S1352-2310\(03\)00391-1](https://doi.org/10.1016/S1352-2310(03)00391-1)
- Atkinson, R., Arey, J., 2003b. Atmospheric Degradation of Volatile Organic Compounds. *Chem. Rev.* 103, 4605–4638. <https://doi.org/10.1021/cr0206420>
- Atkinson, R., Aschmann, S.M., 1993. Hydroxyl radical production from the gas-phase reactions of ozone with a series of alkenes under atmospheric conditions. *Environ. Sci. Technol.* 27, 1357–1363. <https://doi.org/10.1021/es00044a010>
- Atkinson, R., Baulch, D.L., Cox, R.A., Crowley, J.N., Hampson, R.F., Hynes, R.G., Jenkin, M.E., Rossi, M.J., Troe, J., IUPAC Subcommittee, 2006. Evaluated kinetic and photochemical data for atmospheric chemistry: Volume II – gas phase reactions of organic species. *Atmos. Chem. Phys.* 6, 3625–4055. <https://doi.org/10.5194/acp-6-3625-2006>
- Aumont, B., Szopa, S., Madronich, S., 2005. Modelling the evolution of organic carbon during its gas-phase tropospheric oxidation: development of an explicit model based on a self generating approach. *Atmospheric Chemistry and Physics* 5, 2517. <https://doi.org/10.5194/ACP-5-2497-2005>
- Baklanov, A., Lawrence, M., Pandis, S., Mahura, A., Finardi, S., Moussiopoulos, N., Beekmann, M., Laj, P., Gomes, L., Jaffrezo, J.-L., Borbon, A., Coll, I., Gros, V., Sciare, J., Kukkonen, J., Galmarini, S., Giorgi, F., Grimmond, S., Esau, I., Stohl, A., Denby, B., Wagner, T., Butler, T., Baltensperger, U., Builtjes, P., van den Hout, D., van der Gon, H.D., Collins, B., Schluenzen, H., Kulmala, M., Zilitinkevich, S., Sokhi, R., Friedrich, R., Theloke, J., Kummer, U., Jalkanen, L., Halenka, T., Wiedensholer, A., Pyle, J., Rossow, W.B., 2010. MEGAPOLI: concept of multi-scale modelling of megacity impact on air quality and

- climate. *Advances in Science and Research* 4, 115–120. <https://doi.org/10.5194/asr-4-115-2010>
- Baudic, A., Gros, V., Bonsang, B., 2016. Experimental and statistical characterization of Volatile Organic Compounds (VOC) within the Île-de-France region, *Caractérisation expérimentale et statistique des sources de Composés Organiques Volatils (COV) en région Île-de-France*. Université Paris Saclay (COMUE).
- Baudic, A., Gros, V., Sauvage, S., Locoge, N., Sanchez, O., Sarda-Estève, R., Kalogridis, C., Petit, J., Bonnaire, N., Baisnée, D., Favez, O., Albinet, A., Sciare, J., Bonsang, B., 2017. Seasonal variability and source apportionment of volatile organic compounds (VOCs) in the Paris megacity (France).
- Bernal, E., 2014. Limit of Detection and Limit of Quantification Determination in Gas Chromatography. pp. 57–81. <https://doi.org/10.5772/57016>
- Berndt, T., Herrmann, H., Sipilä, M., Kulmala, M., 2016a. Highly Oxidized Second-Generation Products from the Gas-Phase Reaction of OH Radicals with Isoprene. *J. Phys. Chem. A* 120, 10150–10159. <https://doi.org/10.1021/acs.jpca.6b10987>
- Berndt, T., Jokinen, T., Sipilä, M., Mauldin, R.L., Herrmann, H., Stratmann, F., Junninen, H., Kulmala, M., 2014. H₂SO₄ formation from the gas-phase reaction of stabilized Criegee Intermediates with SO₂: Influence of water vapour content and temperature. *Atmospheric Environment* 89, 603–612. <https://doi.org/10.1016/j.atmosenv.2014.02.062>
- Berndt, T., Mentler, B., Scholz, W., Fischer, L., Herrmann, H., Kulmala, M., Hansel, A., 2018a. Accretion Product Formation from Ozonolysis and OH Radical Reaction of α -Pinene: Mechanistic Insight and the Influence of Isoprene and Ethylene. *Environ. Sci. Technol.* 52, 11069–11077. <https://doi.org/10.1021/acs.est.8b02210>
- Berndt, T., Richters, S., Jokinen, T., Hyttinen, N., Kurtén, T., Otkjær, R.V., Kjaergaard, H.G., Stratmann, F., Herrmann, H., Sipilä, M., Kulmala, M., Ehn, M., 2016b. Hydroxyl radical-induced formation of highly oxidized organic compounds. *Nat Commun* 7, 13677. <https://doi.org/10.1038/ncomms13677>
- Berndt, T., Richters, S., Kaethner, R., Voigtländer, J., Stratmann, F., Sipilä, M., Kulmala, M., Herrmann, H., 2015. Gas-Phase Ozonolysis of Cycloalkenes: Formation of Highly Oxidized RO₂ Radicals and Their Reactions with NO, NO₂, SO₂, and Other RO₂ Radicals. *J. Phys. Chem. A* 119, 10336–10348. <https://doi.org/10.1021/acs.jpca.5b07295>
- Berndt, T., Scholz, W., Mentler, B., Fischer, L., Herrmann, H., Kulmala, M., Hansel, A., 2018b. Accretion Product Formation from Self- and Cross-Reactions of RO₂ Radicals in the Atmosphere. *Angewandte Chemie International Edition* 57, 3820–3824. <https://doi.org/10.1002/anie.201710989>
- Bertram, T.H., Kimmel, J.R., Crisp, T.A., Ryder, O.S., Yatavelli, R.L.N., Thornton, J.A., Cubison, M.J., Gonin, M., Worsnop, D.R., 2011. A field-deployable, chemical ionization time-of-flight mass spectrometer. *Atmos. Meas. Tech.* 4, 1471–1479. <https://doi.org/10.5194/amt-4-1471-2011>
- Bianchi, F., Garmash, O., He, X., Yan, C., Iyer, S., Rosendahl, I., Xu, Z., Rissanen, M.P., Riva, M., Taipale, R., Sarnela, N., Petäjä, T., Worsnop, D.R., Kulmala, M., Ehn, M., Junninen, H., 2017. The role of highly oxygenated molecules (HOMs) in determining the composition of ambient ions in the boreal forest. *Atmospheric Chemistry and Physics* 17, 13819–13831. <https://doi.org/10.5194/acp-17-13819-2017>
- Bianchi, F., Kurtén, T., Riva, M., Mohr, C., Rissanen, M.P., Roldin, P., Berndt, T., Crouse, J.D., Wennberg, P.O., Mentel, T.F., Wildt, J., Junninen, H., Jokinen, T., Kulmala, M., Worsnop, D.R., Thornton, J.A., Donahue, N., Kjaergaard, H.G., Ehn, M., 2019. Highly Oxygenated Organic Molecules (HOM) from Gas-Phase Autoxidation Involving Peroxy Radicals: A

- Key Contributor to Atmospheric Aerosol. *Chem. Rev.* 119, 3472–3509. <https://doi.org/10.1021/acs.chemrev.8b00395>
- Bianchi, F., Tröstl, J., Junninen, H., Frege, C., Henne, S., Hoyle, C.R., Molteni, U., Herrmann, E., Adamov, A., Bukowiecki, N., Chen, X., Duplissy, J., Gysel, M., Hutterli, M., Kangasluoma, J., Kontkanen, J., Kürten, A., Manninen, H.E., Münch, S., Peräkylä, O., Petäjä, T., Rondo, L., Williamson, C., Weingartner, E., Curtius, J., Worsnop, D.R., Kulmala, M., Dommen, J., Baltensperger, U., 2016. New particle formation in the free troposphere: A question of chemistry and timing. *Science* 352, 1109–1112. <https://doi.org/10.1126/science.aad5456>
- Bilde, M., Barsanti, K., Booth, M., Cappa, C.D., Donahue, N.M., Emanuelsson, E.U., McFiggans, G., Krieger, U.K., Marcolli, C., Topping, D., Ziemann, P., Barley, M., Clegg, S., Dennis-Smith, B., Hallquist, M., Hallquist, Å.M., Khlystov, A., Kulmala, M., Mogensen, D., Percival, C.J., Pope, F., Reid, J.P., Ribeiro da Silva, M.A.V., Rosenoern, T., Salo, K., Soonsin, V.P., Yli-Juuti, T., Prisle, N.L., Pagels, J., Rarey, J., Zardini, A.A., Riipinen, I., 2015. Saturation Vapor Pressures and Transition Enthalpies of Low-Volatility Organic Molecules of Atmospheric Relevance: From Dicarboxylic Acids to Complex Mixtures. *Chem. Rev.* 115, 4115.
- Bohnenstengel, S.I., Belcher, S.E., Aiken, A., Allan, J.D., Allen, G., Bacak, A., Bannan, T.J., Barlow, J.F., Beddows, D.C.S., Bloss, W.J., Booth, A.M., Chemel, C., Coceal, O., Marco, C.F.D., Dubey, M.K., Faloon, K.H., Fleming, Z.L., Furger, M., Gietl, J.K., Graves, R.R., Green, D.C., Grimmond, C.S.B., Halios, C.H., Hamilton, J.F., Harrison, R.M., Heal, M.R., Heard, D.E., Helfter, C., Herndon, S.C., Holmes, R.E., Hopkins, J.R., Jones, A.M., Kelly, F.J., Kotthaus, S., Langford, B., Lee, J.D., Leigh, R.J., Lewis, A.C., Lidster, R.T., Lopez-Hilfiker, F.D., McQuaid, J.B., Mohr, C., Monks, P.S., Nemitz, E., Ng, N.L., Percival, C.J., Prévôt, A.S.H., Ricketts, H.M.A., Sokhi, R., Stone, D., Thornton, J.A., Tremper, A.H., Valach, A.C., Visser, S., Whalley, L.K., Williams, L.R., Xu, L., Young, D.E., Zotter, P., 2015. Meteorology, Air Quality, and Health in London: The ClearLo Project. *Bulletin of the American Meteorological Society* 96, 779–804. <https://doi.org/10.1175/BAMS-D-12-00245.1>
- Booth, A.M., Barley, M.H., Topping, D.O., McFiggans, G., Garforth, A., Percival, C.J., 2010. Solid state and sub-cooled liquid vapour pressures of substituted dicarboxylic acids using Knudsen Effusion Mass Spectrometry (KEMS) and Differential Scanning Calorimetry. *Atmospheric Chemistry and Physics* 10, 4879–4892. <https://doi.org/10.5194/acp-10-4879-2010>
- Bouvier-Brown, N.C., Goldstein, A.H., Gilman, J.B., Kuster, W.C., de Gouw, J.A., 2009. In-situ ambient quantification of monoterpenes, sesquiterpenes, and related oxygenated compounds during BEARPEX 2007: implications for gas- and particle-phase chemistry. *Atmospheric Chemistry and Physics* 9, 5505–5518. <https://doi.org/10.5194/acp-9-5505-2009>
- Bradley, R.S., Cotson, S., 1953. 347. The vapour pressure and lattice energy of hydrogen-bonded crystals. Part II. α - and β -Anhydrous oxalic acid and tetragonal pentaerythritol. *J. Chem. Soc.* 1684–1688. <https://doi.org/10.1039/JR9530001684>
- Brean, J., Harrison, R.M., Shi, Z., Beddows, D.C.S., Acton, W.J.F., Hewitt, C.N., Squires, F.A., Lee, J., 2019. Observations of highly oxidized molecules and particle nucleation in the atmosphere of Beijing. *Atmospheric Chemistry and Physics* 19, 14933–14947. <https://doi.org/10.5194/acp-19-14933-2019>
- Bridgeman, O.C., Aldrich, E.W., 1964. Vapor Pressure Tables for Water. *Journal of Heat Transfer* 86, 279–286. <https://doi.org/10.1115/1.3687121>

- Brophy, P., Farmer, D.K., 2015. A switchable reagent ion high resolution time-of-flight chemical ionization mass spectrometer for real-time measurement of gas phase oxidized species: characterization from the 2013 southern oxidant and aerosol study. *Atmos. Meas. Tech.* 15.
- Brown, S., Stutz, J., 2012. Nighttime radical observations and chemistry. *Chem. Soc. Rev.* 41, 6405–6447. <https://doi.org/10.1039/C2CS35181A>
- Brown, S.S., deGouw, J.A., Warneke, C., Ryerson, T.B., Dubé, W.P., Atlas, E., Weber, R.J., Peltier, R.E., Neuman, J.A., Roberts, J.M., Swanson, A., Flocke, F., McKeen, S.A., Brioude, J., Sommariva, R., Trainer, M., Fehsenfeld, F.C., Ravishankara, A.R., 2009. Nocturnal isoprene oxidation over the Northeast United States in summer and its impact on reactive nitrogen partitioning and secondary organic aerosol. *Atmospheric Chemistry and Physics* 9, 3027–3042. <https://doi.org/10.5194/acp-9-3027-2009>
- Brown, S.S., Stark, H., Ryerson, T.B., Williams, E.J., Nicks Jr., D.K., Trainer, M., Fehsenfeld, F.C., Ravishankara, A.R., 2003. Nitrogen oxides in the nocturnal boundary layer: Simultaneous in situ measurements of NO₃, N₂O₅, NO₂, NO, and O₃. *Journal of Geophysical Research: Atmospheres* 108. <https://doi.org/10.1029/2002JD002917>
- Brüggemann, M., Poulain, L., Held, A., Stelzer, T., Zuth, C., Richters, S., Mutzel, A., van Pinxteren, D., Iinuma, Y., Katkevica, S., Rabe, R., Herrmann, H., Hoffmann, T., 2017. Real-time detection of highly oxidized organosulfates and BSOA marker compounds during the F-BEACH 2014 field study. *Atmospheric Chemistry and Physics* 17, 1453–1469. <https://doi.org/10.5194/acp-17-1453-2017>
- Cain, K.P., Liangou, A., Davidson, M.L., Pandis, S.N., 2021. α -Pinene, Limonene, and Cyclohexene Secondary Organic Aerosol Hygroscopicity and Oxidation Level as a Function of Volatility. *Aerosol and Air Quality Research* 21, 200511. <https://doi.org/10.4209/aaqr.2020.08.0511>
- Cantrell, C., Michoud, V., 2022. An Experiment to Study Atmospheric Oxidation Chemistry and Physics of Mixed Anthropogenic–Biogenic Air Masses in the Greater Paris Area. *Bulletin of the American Meteorological Society* 103, 599–603. <https://doi.org/10.1175/BAMS-D-21-0115.1>
- Cappa, C.D., Lovejoy, E.R., Ravishankara, A.R., 2008. Evidence for liquid-like and nonideal behavior of a mixture of organic aerosol components. *Proceedings of the National Academy of Sciences* 105, 18687–18691. <https://doi.org/10.1073/pnas.0802144105>
- Carlton, A.G., de Gouw, J., Jimenez, J.L., Ambrose, J.L., Attwood, A.R., Brown, S., Baker, K.R., Brock, C., Cohen, R.C., Edgerton, S., Farkas, C.M., Farmer, D., Goldstein, A.H., Gratz, L., Guenther, A., Hunt, S., Jaeglé, L., Jaffe, D.A., Mak, J., McClure, C., Nenes, A., Nguyen, T.K., Pierce, J.R., de Sa, S., Selin, N.E., Shah, V., Shaw, S., Shepson, P.B., Song, S., Stutz, J., Surratt, J.D., Turpin, B.J., Warneke, C., Washenfelder, R.A., Wennberg, P.O., Zhou, X., 2018. SYNTHESIS OF THE SOUTHEAST ATMOSPHERE STUDIES 22.
- Carlton, A.G., Pinder, R.W., Bhave, P.V., Pouliot, G.A., 2010. To What Extent Can Biogenic SOA be Controlled? *Environ. Sci. Technol.* 44, 3376–3380. <https://doi.org/10.1021/es903506b>
- Carlton, A.G., Wiedinmyer, C., Kroll, J.H., 2009. A review of Secondary Organic Aerosol (SOA) formation from isoprene. *Atmospheric Chemistry and Physics* 9, 4987–5005. <https://doi.org/10.5194/acp-9-4987-2009>
- Carslaw, N., Carslaw, D., 2001. The Gas-Phase Chemistry Of Urban Atmospheres. *Surveys in Geophysics* 22, 31–53. <https://doi.org/10.1023/A:1010601507383>
- Carslaw, N., Plane, J.M.C., Coe, H., Cuevas, E., 1997. Observations of the nitrate radical in the free troposphere at Izaña de Tenerife. *Journal of Geophysical Research: Atmospheres* 102, 10613–10622. <https://doi.org/10.1029/96JD03512>
- Chen, T., Liu, Y., Chu, B., Liu, C., Liu, J., Ge, Y., Ma, Q., Ma, J., He, H., 2019. Differences of the oxidation process and secondary organic aerosol formation at low and high precursor

- concentrations. *Journal of Environmental Sciences* 79, 256–263. <https://doi.org/10.1016/j.jes.2018.11.011>
- Chen, T., Zhang, P., Chu, B., Ma, Q., Ge, Y., Liu, J., He, H., 2022. Secondary organic aerosol formation from mixed volatile organic compounds: Effect of RO₂ chemistry and precursor concentration. *npj Clim Atmos Sci* 5, 1–8. <https://doi.org/10.1038/s41612-022-00321-y>
- Cheng, X., Chen, Q., Jie Li, Y., Zheng, Y., Liao, K., Huang, G., 2021. Highly oxygenated organic molecules produced by the oxidation of benzene and toluene in a wide range of OH exposure and NO_x conditions. *Atmospheric Chemistry and Physics* 21, 12005–12019. <https://doi.org/10.5194/acp-21-12005-2021>
- Cheng, Xi, Chen, Q., Li, Y., Huang, G., Liu, Y., Lu, S., Zheng, Y., Qiu, W., Lu, K., Qiu, X., Bianchi, F., Yan, C., Yuan, B., Shao, M., Wang, Z., Zhu, T., Wu, Y., Zeng, L., 2021. Secondary Production of Gaseous Nitrated Phenols in Polluted Urban Environments. *Environmental Science & Technology* 55. <https://doi.org/10.1021/acs.est.0c07988>
- Cheng, X., Li, Y.J., Zheng, Y., Liao, K., Zhu, T., Ye, C., Qiu, X., Koenig, T.K., Ge, Y., Chen, Q., 2023. Oxygenated organic molecules produced by low-NO_x photooxidation of aromatic compounds and their contributions to secondary organic aerosol. *EGUsphere* 2023, 1–24. <https://doi.org/10.5194/egusphere-2023-1215>
- Cho, H.-J., Kang, J., Kim, D., Seo, A., Park, M., Joo, H., Park, K., 2018. A Study on Elevated Concentrations of Submicrometer Particles in an Urban Atmosphere. *Atmosphere* 9, 393. <https://doi.org/10.3390/atmos9100393>
- Chuong, B., Zhang, J., Donahue, N.M., 2004. Cycloalkene Ozonolysis: Collisionally Mediated Mechanistic Branching. *J. Am. Chem. Soc.* 126, 12363–12373. <https://doi.org/10.1021/ja0485412>
- Comrie, A.C., 1994. A synoptic climatology of rural ozone pollution at three forest sites in Pennsylvania. *Atmospheric Environment* 28, 1601–1614. [https://doi.org/10.1016/1352-2310\(94\)90306-9](https://doi.org/10.1016/1352-2310(94)90306-9)
- Crawford, I., Robinson, N.H., Flynn, M.J., Foot, V.E., Gallagher, M.W., Huffman, J.A., Stanley, W.R., Kaye, P.H., 2014. Characterisation of bioaerosol emissions from a Colorado pine forest: results from the BEACHON-RoMBAS experiment. *Atmospheric Chemistry and Physics* 14, 8559–8578. <https://doi.org/10.5194/acp-14-8559-2014>
- Creasey, D., Heard, D., Lee, J., 2000. Absorption cross-section measurements of water vapour and oxygen at 185 nm. Implications for the calibration of field instruments to measure OH, HO₂ and RO₂ radicals. *Geophysical Research Letters* 27, 1651–1654. <https://doi.org/10.1029/1999GL011014>
- Criegee, R., 1975. Mechanism of Ozonolysis. *Angewandte Chemie International Edition in English* 14, 745–752. <https://doi.org/10.1002/anie.197507451>
- Crouse, J.D., McKinney, K.A., Kwan, A.J., Wennberg, P.O., 2006. Measurement of Gas-Phase Hydroperoxides by Chemical Ionization Mass Spectrometry. *Anal. Chem.* 78, 6726–6732. <https://doi.org/10.1021/ac0604235>
- Crouse, J.D., Nielsen, L.B., Jørgensen, S., Kjaergaard, H.G., Wennberg, P.O., 2013. Autoxidation of Organic Compounds in the Atmosphere. *J. Phys. Chem. Lett.* 4, 3513–3520. <https://doi.org/10.1021/jz4019207>
- Dam, M., Draper, D.C., Marsavin, A., Fry, J.L., Smith, J.N., 2022. Observations of gas-phase products from the nitrate-radical-initiated oxidation of four monoterpenes. *Atmospheric Chemistry and Physics* 22, 9017–9031. <https://doi.org/10.5194/acp-22-9017-2022>
- D'Ambro, E.L., Lee, B.H., Liu, J., Shilling, J.E., Gaston, C.J., Lopez-Hilfiker, F.D., Schobesberger, S., Zaveri, R.A., Mohr, C., Lutz, A., Zhang, Z., Gold, A., Surratt, J.D., Rivera-Rios, J.C., Keutsch, F.N., Thornton, J.A., 2016. Molecular composition and volatility of isoprene photochemical oxidation secondary organic aerosol under low- and

- high-NO_x conditions. *Atmospheric Chemistry and Physics* 17, 159–174. <https://doi.org/10.5194/acp-17-159-2017>
- Darnall, K.R., Carter, W.P.L., Winer, A.M., Lloyd, A.C., Pitts, J.N.Jr., 1976. Importance of RO₂ + nitric oxide in alkyl nitrate formation from C₄-C₆ alkane photooxidations under simulated atmospheric conditions. *J. Phys. Chem.* 80, 1948–1950. <https://doi.org/10.1021/j100558a029>
- Davidson, J.A., Fehsenfeld, F.C., Howard, C.J., 1977. The heats of formation of NO₃⁻ and NO₃⁻-association complexes with HNO₃ and HBr. *International Journal of Chemical Kinetics* 9, 17–29. <https://doi.org/10.1002/kin.550090104>
- DeCarlo, P.F., Kimmel, J.R., Trimborn, A., Northway, M.J., Jayne, J.T., Aiken, A.C., Gonin, M., Fuhrer, K., Horvath, T., Docherty, K.S., Worsnop, D.R., Jimenez, J.L., 2006. Field-Deployable, High-Resolution, Time-of-Flight Aerosol Mass Spectrometer. *Anal. Chem.* 78, 8281–8289. <https://doi.org/10.1021/ac061249n>
- Dement, W.A., Tyson, B.J., Mooney, H.A., 1975. Mechanism of monoterpene volatilization in *Salvia mellifera*. *Phytochemistry* 14, 2555–2557. [https://doi.org/10.1016/0031-9422\(75\)85223-X](https://doi.org/10.1016/0031-9422(75)85223-X)
- Dentener, F.J., Crutzen, P.J., 1993. Reaction of N₂O₅ on tropospheric aerosols: Impact on the global distributions of NO_x, O₃, and OH. *Journal of Geophysical Research: Atmospheres* 98, 7149–7163. <https://doi.org/10.1029/92JD02979>
- Directive 1999/13/CE, Article 2. Directive n° 1999/13/CE du 11/03/99 relative à la réduction des émissions de composés organiques volatils dues à l'utilisation de solvants organiques dans certaines activités et installations | AIDA [WWW Document]. URL https://aida.ineris.fr/consultation_document/1015 (accessed 9.22.20).
- Donahue, N.M., Kroll, J.H., Pandis, S.N., Robinson, A.L., 2012. A two-dimensional volatility basis set – Part 2: Diagnostics of organic-aerosol evolution. *Atmospheric Chemistry and Physics* 12, 615–634. <https://doi.org/10.5194/acp-12-615-2012>
- Doussin, J.-F., Durand-Jolibois, R., Ritz, D., Monod, A., Carlier, P., 1997. Design of an environmental chamber for the study of atmospheric chemistry: New developments in the analytical device. *Analisis* 25, 236. [https://doi.org/10.1016/S0365-4877\(97\)86083-4](https://doi.org/10.1016/S0365-4877(97)86083-4)
- Doussin, J.-F., Fuchs, H., Kiendler-Scharr, A., Seakins, P., Wenger, J. (Eds.), 2023. *A Practical Guide to Atmospheric Simulation Chambers*. Springer International Publishing, Cham. <https://doi.org/10.1007/978-3-031-22277-1>
- Draper, D.C., Myllys, N., Hyttinen, N., Møller, K.H., Kjaergaard, H.G., Fry, J.L., Smith, J.N., Kurtén, T., 2019. Formation of Highly Oxidized Molecules from NO₃ Radical Initiated Oxidation of Δ-3-Carene: A Mechanistic Study. *ACS Earth Space Chem.* 3, 1460–1470. <https://doi.org/10.1021/acsearthspacechem.9b00143>
- Dudareva, N., Negre, F., Nagegowda, D., Orlova, I., 2006. Plant Volatiles: Recent Advances and Future Perspectives. *Critical Reviews in Plant Sciences* 25, 417–440. <https://doi.org/10.1080/07352680600899973>
- Duflot, V., Tulet, P., Flores, O., Barthe, C., Colomb, A., Deguillaume, L., Vaïtilingom, M., Perring, A., Huffman, A., Hernandez, M.T., Sellegri, K., Robinson, E., O'Connor, D.J., Gomez, O.M., Burnet, F., Bourriane, T., Strasberg, D., Rocco, M., Bertram, A.K., Chazette, P., Totems, J., Fournel, J., Stamenoff, P., Metzger, J.-M., Chabasset, M., Rousseau, C., Bourriane, E., Sancelme, M., Delort, A.-M., Wegener, R.E., Chou, C., Elizondo, P., 2019. Preliminary results from the FARCE 2015 campaign: multidisciplinary study of the forest–gas–aerosol–cloud system on the tropical island of La Réunion. *Atmospheric Chemistry and Physics* 19, 10591–10618. <https://doi.org/10.5194/acp-19-10591-2019>
- Duhl, T.R., Helmig, D., Guenther, A., 2008. Sesquiterpene emissions from vegetation: a review. *Biogeosciences* 5, 761–777. <https://doi.org/10.5194/bg-5-761-2008>

- Dusanter, S., Duncianu, M., Tomas, A., Locoge, N., Villenave, E., Perraudin, E., Flaud, P.M., 2018. Deployment of a mobile photochemical reactor during the 2018 CERVOLAND field campaign to investigate BVOC oxidation, in: AGU Fall Meeting Abstracts. pp. A43M-3289.
- Edwards, G.D., Cantrell, C.A., Stephens, S., Hill, B., Goyea, O., Shetter, R.E., Mauldin, R.L., Kosciuch, E., Tanner, D.J., Eisele, F.L., 2003. Chemical Ionization Mass Spectrometer Instrument for the Measurement of Tropospheric HO₂ and RO₂. *Anal. Chem.* 75, 5317–5327. <https://doi.org/10.1021/ac034402b>
- Ehn, M., Berndt, T., Wildt, J., Mentel, T., 2017. Highly Oxygenated Molecules from Atmospheric Autoxidation of Hydrocarbons: A Prominent Challenge for Chemical Kinetics Studies. *International Journal of Chemical Kinetics* 49, 821–831. <https://doi.org/10.1002/kin.21130>
- Ehn, M., Junninen, H., Petäjä, T., Kurtén, T., Kerminen, V.-M., Schobesberger, S., Manninen, H.E., Ortega, I.K., Vehkamäki, H., Kulmala, M., Worsnop, D.R., 2010. Composition and temporal behavior of ambient ions in the boreal forest. *Atmospheric Chemistry and Physics* 10, 8513–8530. <https://doi.org/10.5194/acp-10-8513-2010>
- Ehn, M., Kleist, E., Junninen, H., Petäjä, T., Lönn, G., Schobesberger, S., Dal Maso, M., Trimborn, A., Kulmala, M., Worsnop, D.R., Wahner, A., Wildt, J., Mentel, Th.F., 2012. Gas phase formation of extremely oxidized pinene reaction products in chamber and ambient air. *Atmospheric Chemistry and Physics* 12, 5113–5127. <https://doi.org/10.5194/acp-12-5113-2012>
- Ehn, M., Thornton, J.A., Kleist, E., Sipilä, M., Junninen, H., Pullinen, I., Springer, M., Rubach, F., Tillmann, R., Lee, B., Lopez-Hilfiker, F., Andres, S., Acir, I.-H., Rissanen, M., Jokinen, T., Schobesberger, S., Kangasluoma, J., Kontkanen, J., Nieminen, T., Kurtén, T., Nielsen, L.B., Jørgensen, S., Kjaergaard, H.G., Canagaratna, M., Maso, M.D., Berndt, T., Petäjä, T., Wahner, A., Kerminen, V.-M., Kulmala, M., Worsnop, D.R., Wildt, J., Mentel, T.F., 2014. A large source of low-volatility secondary organic aerosol. *Nature* 506, 476–479. <https://doi.org/10.1038/nature13032>
- Eisele, F., Tanner, D., 1993. Measurement of the gas phase concentration of H₂SO₄ and methane sulfonic acid and estimates of H₂SO₄ production and loss in the atmosphere. *Journal of Geophysical Research* 98, 9001–9010.
- Elshorbany, Y.F., Kurtenbach, R., Wiesen, P., Lissi, E., Rubio, M., Villena, G., Gramsch, E., Rickard, A.R., Pilling, M.J., Kleffmann, J., 2009. Oxidation capacity of the city air of Santiago, Chile. *Atmospheric Chemistry and Physics* 9, 2257–2273. <https://doi.org/10.5194/acp-9-2257-2009>
- Emel'yanenko, V.N., Turovtsev, V.V., Fedina, Y.A., 2018. Thermodynamic properties of pyruvic acid and its methyl ester. *Thermochimica Acta* 665, 70–75. <https://doi.org/10.1016/j.tca.2018.05.009>
- Emmerson, K.M., Carslaw, N., Pilling, M.J., 2005. Urban Atmospheric Chemistry During the PUMA Campaign 2: Radical Budgets for OH, HO₂ and RO₂. *Journal of Atmospheric Chemistry* 52, 165–183. <https://doi.org/10.1007/s10874-005-1323-2>
- Evans, M., Knippertz, P., Aristide, A., Allan, R., Amekudzi, L., Brooks, B., Chiu, J.-Y., Coe, H., Fink, A., Flamant, C., Jegede, O., Lioussé, C., Lohou, F., Kalthoff, N., Mari, C., Marsham, J., Véronique, Y., Reimann, C., Léon, K., Reinares Martínez, I., 2018. Policy-relevant findings of the DACCWA project. <https://doi.org/10.5281/zenodo.1476843>
- Fast, J.D., Berg, L.K., Alexander, L., Bell, D., D'Ambro, E., Hubbe, J., Kuang, C., Liu, J., Long, C., Matthews, A., Mei, F., Newsom, R., Pekour, M., Pinterich, T., Schmid, B., Schobesberger, S., Shilling, J., Smith, J.N., Springston, S., Suski, K., Thornton, J.A., Tomlinson, J., Wang, J., Xiao, H., Zelenyuk, A., 2019. Overview of the HI-SCALE Field

- Campaign: A New Perspective on Shallow Convective Clouds. *Bulletin of the American Meteorological Society* 100, 821–840. <https://doi.org/10.1175/BAMS-D-18-0030.1>
- Faxon, C., Hammes, J., Le Breton, M., Pathak, R.K., Hallquist, M., 2018. Characterization of organic nitrate constituents of secondary organic aerosol (SOA) from nitrate-radical-initiated oxidation of limonene using high-resolution chemical ionization mass spectrometry. *Atmospheric Chemistry and Physics* 18, 5467–5481. <https://doi.org/10.5194/acp-18-5467-2018>
- Fehsenfeld, F., Calvert, J., Fall, R., Goldan, P., Guenther, A.B., Hewitt, C.N., Lamb, B., Liu, S., Trainer, M., Westberg, H., Zimmerman, P., 1992. Emissions of volatile organic compounds from vegetation and the implications for atmospheric chemistry. *Global Biogeochemical Cycles* 6, 389–430. <https://doi.org/10.1029/92GB02125>
- Fenske, J.D., Paulson, S.E., 1999. Human Breath Emissions of VOCs. *Journal of the Air & Waste Management Association* 49, 594–598. <https://doi.org/10.1080/10473289.1999.10463831>
- Ferreira de Brito, J., Riffault, V., Dusanter, S., Jamar, M., 2023. ACROSS_IMTNE_RambForest_AMS_AboveCanopy_L2. <https://doi.org/10.25326/491>
- Field, F.H., 1968. Chemical ionization mass spectrometry. *Acc. Chem. Res.* 1, 42–49. <https://doi.org/10.1021/ar50002a002>
- Finlayson-Pitts, B.J., 2010. Halogens in the Troposphere. *Anal. Chem.* 82, 770–776. <https://doi.org/10.1021/ac901478p>
- Finlayson-Pitts, B.J., Pitts, J.N., 2000. CHAPTER 6 - Rates and Mechanisms of Gas-Phase Reactions in Irradiated Organic – NO_x – Air Mixtures, in: Finlayson-Pitts, B.J., Pitts, J.N. (Eds.), *Chemistry of the Upper and Lower Atmosphere*. Academic Press, San Diego, pp. 179–263. <https://doi.org/10.1016/B978-012257060-5/50008-3>
- Fiore, A.M., Jacob, D.J., Bey, I., Yantosca, R.M., Field, B.D., Fusco, A.C., Wilkinson, J.G., 2002. Background ozone over the United States in summer: Origin, trend, and contribution to pollution episodes. *Journal of Geophysical Research: Atmospheres* 107, ACH 11-1-ACH 11-25. <https://doi.org/10.1029/2001JD000982>
- Fischer, E.V., Jacob, D.J., Yantosca, R.M., Sulprizio, M.P., Millet, D.B., Mao, J., Paulot, F., Singh, H.B., Roiger, A., Ries, L., Talbot, R.W., Dzepina, K., Pandey Deolal, S., 2014. Atmospheric peroxyacetyl nitrate (PAN): a global budget and source attribution. *Atmos Chem Phys* 14, 2679–2698. <https://doi.org/10.5194/acp-14-2679-2014>
- Fiscus, E.L., Booker, F.L., Burkey, K.O., 2005. Crop responses to ozone: uptake, modes of action, carbon assimilation and partitioning. *Plant, Cell & Environment* 28, 997–1011. <https://doi.org/10.1111/j.1365-3040.2005.01349.x>
- Fishman, J., Ramanathan, V., Crutzen, P.J., Liu, S.C., 1979. Tropospheric ozone and climate. *Nature* 282, 818–820. <https://doi.org/10.1038/282818a0>
- Frege, C., Bianchi, F., Molteni, U., Tröstl, J., Junninen, H., Henne, S., Sipilä, M., Herrmann, E., Rossi, M.J., Kulmala, M., Hoyle, C.R., Baltensperger, U., Dommen, J., 2017. Chemical characterization of atmospheric ions at the high altitude research station Jungfraujoch (Switzerland). *Atmospheric Chemistry and Physics* 17, 2613–2629. <https://doi.org/10.5194/acp-17-2613-2017>
- Frege, C., Ortega, I.K., Rissanen, M.P., Praplan, A.P., Steiner, G., Heinritzi, M., Ahonen, L., Amorim, A., Bernhammer, A.-K., Bianchi, F., Brilke, S., Breitenlechner, M., Dada, L., Dias, A., Duplissy, J., Ehrhart, S., El-Haddad, I., Fischer, L., Fuchs, C., Garmash, O., Gonin, M., Hansel, A., Hoyle, C.R., Jokinen, T., Junninen, H., Kirkby, J., Kürten, A., Lehtipalo, K., Leiminger, M., Mauldin, R.L., Molteni, U., Nichman, L., Petäjä, T., Sarnela, N., Schobesberger, S., Simon, M., Sipilä, M., Stolzenburg, D., Tomé, A., Vogel, A.L., Wagner, A.C., Wagner, R., Xiao, M., Yan, C., Ye, P., Curtius, J., Donahue, N.M., Flagan, R.C., Kulmala, M., Worsnop, D.R., Winkler, P.M., Dommen, J., Baltensperger, U., 2018.

- Influence of temperature on the molecular composition of ions and charged clusters during pure biogenic nucleation. *Atmospheric Chemistry and Physics* 18, 65–79. <https://doi.org/10.5194/acp-18-65-2018>
- Freney, E.J., Sellegri, K., Canonaco, F., Colomb, A., Borbon, A., Michoud, V., Doussin, J.-F., Crumeyrolle, S., Amarouche, N., Pichon, J.-M., Bourianne, T., Gomes, L., Prevot, A.S.H., Beekmann, M., Schwarzenböck, A., 2014. Characterizing the impact of urban emissions on regional aerosol particles: airborne measurements during the MEGAPOLI experiment. *Atmospheric Chemistry and Physics* 14, 1397–1412. <https://doi.org/10.5194/acp-14-1397-2014>
- Fry, J.L., Draper, D.C., Barsanti, K.C., Smith, J.N., Ortega, J., Winkler, P.M., Lawler, M.J., Brown, S.S., Edwards, P.M., Cohen, R.C., Lee, L., 2014. Secondary Organic Aerosol Formation and Organic Nitrate Yield from NO₃ Oxidation of Biogenic Hydrocarbons. *Environ. Sci. Technol.* 48, 11944–11953. <https://doi.org/10.1021/es502204x>
- Fry, J.L., Draper, D.C., Zarzana, K.J., Campuzano-Jost, P., Day, D.A., Jimenez, J.L., Brown, S.S., Cohen, R.C., Kaser, L., Hansel, A., Cappellin, L., Karl, T., Hodzic Roux, A., Turnipseed, A., Cantrell, C., Lefer, B.L., Grossberg, N., 2013. Observations of gas- and aerosol-phase organic nitrates at BEACHON-RoMBAS 2011. *Atmospheric Chemistry and Physics* 13, 8585–8605. <https://doi.org/10.5194/acp-13-8585-2013>
- Fuentes, J.D., Lerdau, M., Atkinson, R., Baldocchi, D., Bottenheim, J.W., Ciccioli, P., Lamb, B., Geron, C., Gu, L., Guenther, A., Sharkey, T.D., Stockwell, W., 2000. Biogenic Hydrocarbons in the Atmospheric Boundary Layer: A Review. *Bulletin of the American Meteorological Society* 81, 1537–1575.
- Garmash, O., 2020. Mass Spectrometry Studies on Vapours Forming Atmospheric Aerosol Particles.
- Garmash, O., Rissanen, M.P., Pullinen, I., Schmitt, S., Kausiala, O., Tillmann, R., Zhao, D., Percival, C., Bannan, T.J., Priestley, M., Hallquist, Å.M., Kleist, E., Kiendler-Scharr, A., Hallquist, M., Berndt, T., McFiggans, G., Wildt, J., Mentel, T.F., Ehn, M., 2020. Multi-generation OH oxidation as a source for highly oxygenated organic molecules from aromatics. *Atmospheric Chemistry and Physics* 20, 515–537. <https://doi.org/10.5194/acp-20-515-2020>
- Geyer, A., Aliche, B., Ackermann, R., Martinez, M., Harder, H., Brune, W., di Carlo, P., Williams, E., Jobson, T., Hall, S., Shetter, R., Stutz, J., 2003. Direct observations of daytime NO₃: Implications for urban boundary layer chemistry. *Journal of Geophysical Research: Atmospheres* 108. <https://doi.org/10.1029/2002JD002967>
- Geyer, A., Aliche, B., Konrad, S., Schmitz, T., Stutz, J., Platt, U., 2001. Chemistry and oxidation capacity of the nitrate radical in the continental boundary layer near Berlin. *Journal of Geophysical Research: Atmospheres* 106, 8013–8025. <https://doi.org/10.1029/2000JD900681>
- Gilliam, F.S., Sigmon, J.T., Reiter, M.A., Krovetz, D.O., 1989. Elevational and spatial variation in daytime ozone concentrations in the Virginia Blue Ridge Mountains: implications for forest exposure. *Canadian Journal of Forest Research* 19, 422–426. <https://doi.org/10.1139/x89-066>
- Gilliam, F.S., Turrill, N.L., 1995. Temporal Patterns of Ozone Pollution in West Virginia: Implications for High-Elevation Hardwood Forests. *Journal of the Air & Waste Management Association* 45, 621–626. <https://doi.org/10.1080/10473289.1995.10467392>
- Goldman, M.J., Green, W.H., Kroll, J.H., 2021. Chemistry of Simple Organic Peroxy Radicals under Atmospheric through Combustion Conditions: Role of Temperature, Pressure, and NO_x Level. *The Journal of Physical Chemistry A* 125, 10303–10314. <https://doi.org/10.1021/acs.jpca.1c07203>

- Goldstein, A.H., Galbally, I.E., 2007. Known and Unexplored Organic Constituents in the Earth's Atmosphere. *Environ. Sci. Technol.* 41, 1514–1521. <https://doi.org/10.1021/es072476p>
- Graham, R.A., Johnston, H.S., 1978. The photochemistry of the nitrate radical and the kinetics of the nitrogen pentoxide-ozone system. *J. Phys. Chem.* 82, 254–268. <https://doi.org/10.1021/j100492a002>
- Gryparis, A., Forsberg, B., Katsouyanni, K., Analitis, A., Touloumi, G., Schwartz, J., Samoli, E., Medina, S., Anderson, H.R., Niciu, E.M., Wichmann, H.-E., Kriz, B., Kosnik, M., Skorkovsky, J., Vonk, J.M., Dörtbudak, Z., 2004. Acute Effects of Ozone on Mortality from the “Air Pollution and Health. *Am J Respir Crit Care Med* 170, 1080–1087. <https://doi.org/10.1164/rccm.200403-333OC>
- Guenther, A., 2013. Biological and Chemical Diversity of Biogenic Volatile Organic Emissions into the Atmosphere. *International Scholarly Research Notices* 2013, e786290. <https://doi.org/10.1155/2013/786290>
- Guenther, A., Hewitt, C.N., Erickson, D., Fall, R., Geron, C., Graedel, T., Harley, P., Klinger, L., Lerdau, M., McKay, W.A., Pierce, T., Scholes, B., Steinbrecher, R., Tallamraju, R., Taylor, J., Zimmerman, P., 1995. A global model of natural volatile organic compound emissions. *Journal of geophysical research* 100, 8873–8892. <https://doi.org/10.1029/94JD02950>
- Guenther, A.B., Jiang, X., Heald, C.L., Sakulyanontvittaya, T., Duhl, T., Emmons, L.K., Wang, X., 2012. The Model of Emissions of Gases and Aerosols from Nature version 2.1 (MEGAN2.1): an extended and updated framework for modeling biogenic emissions. *Geoscientific Model Development* 5, 1471–1492. <https://doi.org/10.5194/gmd-5-1471-2012>
- Guo, H., Ecker, J.R., 2004. The ethylene signaling pathway: new insights. *Current Opinion in Plant Biology* 7, 40–49. <https://doi.org/10.1016/j.pbi.2003.11.011>
- Guo, Y., Shen, H., Pullinen, I., Luo, H., Kang, S., Vereecken, L., Fuchs, H., Hallquist, M., Acir, I.-H., Tillmann, R., Rohrer, F., Wildt, J., Kiendler-Scharr, A., Wahner, A., Zhao, D., Mentel, T.F., 2022a. Identification of highly oxygenated organic molecules and their role in aerosol formation in the reaction of limonene with nitrate radical. *Atmospheric Chemistry and Physics* 22, 11323–11346. <https://doi.org/10.5194/acp-22-11323-2022>
- Guo, Y., Yan, C., Liu, Y., Qiao, X., Zheng, F., Zhang, Y., Zhou, Y., Li, C., Fan, X., Lin, Z., Feng, Z., Zhang, Y., Zheng, P., Tian, L., Nie, W., Wang, Z., Huang, D., Daellenbach, K.R., Yao, L., Dada, L., Bianchi, F., Jiang, J., Liu, Y., Kerminen, V.-M., Kulmala, M., 2022b. Seasonal variation in oxygenated organic molecules in urban Beijing and their contribution to secondary organic aerosol. *Atmospheric Chemistry and Physics* 22, 10077–10097. <https://doi.org/10.5194/acp-22-10077-2022>
- Hallquist, M., Wenger, J.C., Baltensperger, U., Rudich, Y., Simpson, D., Claeys, M., Dommen, J., Donahue, N.M., George, C., Goldstein, A.H., Hamilton, J.F., Herrmann, H., Hoffmann, T., Iinuma, Y., Jang, M., Jenkin, M.E., Jimenez, J.L., Kiendler-Scharr, A., Maenhaut, W., McFiggans, G., Mentel, T.F., Monod, A., Prévôt, A.S.H., Seinfeld, J.H., Surratt, J.D., Szmigielski, R., Wildt, J., 2009. The formation, properties and impact of secondary organic aerosol: current and emerging issues. *Atmospheric Chemistry and Physics* 9, 5155–5236. <https://doi.org/10.5194/acp-9-5155-2009>
- Han, Y., Stroud, C.A., Liggió, J., Li, S.-M., 2016. The effect of particle acidity on secondary organic aerosol formation from α -pinene photooxidation under atmospherically relevant conditions. *Atmospheric Chemistry and Physics* 16, 13929–13944. <https://doi.org/10.5194/acp-16-13929-2016>
- Hantschke, L., Novelli, A., Bohn, B., Cho, C., Reimer, D., Rohrer, F., Tillmann, R., Glowania, M., Hofzumahaus, A., Kiendler-Scharr, A., Wahner, A., Fuchs, H., 2021. Atmospheric photooxidation and ozonolysis of Δ^3 -carene and 3-caronaldehyde: rate constants and

- product yields. *Atmospheric Chemistry and Physics* 21, 12665–12685. <https://doi.org/10.5194/acp-21-12665-2021>
- Harb, S., Cirtog, M., Alage, S., Cantrell, C., Michoud, V., Cazaunau, M., Pangui, E., Bergé, A., Giorio, C., Battaglia, F., Picquet-Varrault, B., 2023a. Kinetic and mechanistic experimental study of the reactivity of α -phellandrene with the NO₃ radicals. (in preparation).
- Harb, S., Cirtog, M., Alage, S., Cantrell, C., Michoud, V., Cazaunau, M., Pangui, E., Bergé, A., Giorio, C., Battaglia, F., Picquet-Varrault, B., 2023b. Kinetic and mechanistic experimental study of the reactivity of β -phellandrene with the NO₃ radicals. (in preparation).
- Harrison, M.A.J., Barra, S., Borghesi, D., Vione, D., Arsene, C., Iulian Olariu, R., 2005. Nitrated phenols in the atmosphere: a review. *Atmospheric Environment* 39, 231–248. <https://doi.org/10.1016/j.atmosenv.2004.09.044>
- Harrison, R.M., 2018. Urban atmospheric chemistry: a very special case for study. *npj Clim Atmos Sci* 1, 20175. <https://doi.org/10.1038/s41612-017-0010-8>
- Harrison, R.M., Yin, J., Tilling, R.M., Cai, X., Seakins, P.W., Hopkins, J.R., Lansley, D.L., Lewis, A.C., Hunter, M.C., Heard, D.E., Carpenter, L.J., Creasey, D.J., Lee, J.D., Pilling, M.J., Carslaw, N., Emmerson, K.M., Redington, A., Derwent, R.G., Ryall, D., Mills, G., Penkett, S.A., 2006. Measurement and modelling of air pollution and atmospheric chemistry in the U.K. West Midlands conurbation: Overview of the PUMA Consortium project. *Science of The Total Environment* 360, 5–25. <https://doi.org/10.1016/j.scitotenv.2005.08.053>
- Heard, D.E., Carpenter, L.J., Creasey, D.J., Hopkins, J.R., Lee, J.D., Lewis, A.C., Pilling, M.J., Seakins, P.W., Carslaw, N., Emmerson, K.M., 2004. High levels of the hydroxyl radical in the winter urban troposphere. *Geophysical Research Letters* 31. <https://doi.org/10.1029/2004GL020544>
- Heinritzi, M., Dada, L., Simon, M., Stolzenburg, D., Wagner, A.C., Fischer, L., Ahonen, L.R., Amanatidis, S., Baalbaki, R., Baccarini, A., Bauer, P.S., Baumgartner, B., Bianchi, F., Brilke, S., Chen, D., Chiu, R., Dias, A., Dommen, J., Duplissy, J., Finkenzeller, H., Frege, C., Fuchs, C., Garmash, O., Gordon, H., Granzin, M., El Haddad, I., He, X., Helm, J., Hofbauer, V., Hoyle, C.R., Kangasluoma, J., Keber, T., Kim, C., Kürten, A., Lamkaddam, H., Laurila, T.M., Lampilahti, J., Lee, C.P., Lehtipalo, K., Leiminger, M., Mai, H., Makhmutov, V., Manninen, H.E., Marten, R., Mathot, S., Mauldin, R.L., Mentler, B., Molteni, U., Müller, T., Nie, W., Nieminen, T., Onnela, A., Partoll, E., Passananti, M., Petäjä, T., Pfeifer, J., Pospisilova, V., Quéléver, L.L.J., Rissanen, M.P., Rose, C., Schobesberger, S., Scholz, W., Scholze, K., Sipilä, M., Steiner, G., Stozhkov, Y., Tauber, C., Tham, Y.J., Vazquez-Pufleau, M., Virtanen, A., Vogel, A.L., Volkamer, R., Wagner, R., Wang, M., Weitz, L., Wimmer, D., Xiao, M., Yan, C., Ye, P., Zha, Q., Zhou, X., Amorim, A., Baltensperger, U., Hansel, A., Kulmala, M., Tomé, A., Winkler, P.M., Worsnop, D.R., Donahue, N.M., Kirkby, J., Curtius, J., 2020. Molecular understanding of the suppression of new-particle formation by isoprene. *Atmospheric Chemistry and Physics* 20, 11809–11821. <https://doi.org/10.5194/acp-20-11809-2020>
- Heinritzi, M., Simon, M., Steiner, G., Wagner, A.C., Kürten, A., Hansel, A., Curtius, J., 2016. Characterization of the mass-dependent transmission efficiency of a CIMS. *Atmos. Meas. Tech.* 9, 1449–1460. <https://doi.org/10.5194/amt-9-1449-2016>
- Hildebrandt, L., Henry, K.M., Kroll, J.H., Worsnop, D.R., Pandis, S.N., Donahue, N.M., 2011. Evaluating the Mixing of Organic Aerosol Components Using High-Resolution Aerosol Mass Spectrometry. *Environ. Sci. Technol.* 45, 6329–6335. <https://doi.org/10.1021/es200825g>
- Hodzic, A., Kasibhatla, P.S., Jo, D.S., Cappa, C.D., Jimenez, J.L., Madronich, S., Park, R.J., 2016. Rethinking the global secondary organic aerosol (SOA) budget: stronger production, faster

- removal, shorter lifetime. *Atmospheric Chemistry and Physics* 16, 7917–7941. <https://doi.org/10.5194/acp-16-7917-2016>
- Hoyle, C.R., Boy, M., Donahue, N.M., Fry, J.L., Glasius, M., Guenther, A., Hallar, A.G., Huff Hartz, K., Petters, M.D., Petäjä, T., Rosenoern, T., Sullivan, A.P., 2011. A review of the anthropogenic influence on biogenic secondary organic aerosol. *Atmospheric Chemistry and Physics* 11, 321–343. <https://doi.org/10.5194/acp-11-321-2011>
- Huang, W., Li, H., Sarnela, N., Heikkinen, L., Tham, Y.J., Mikkilä, J., Thomas, S.J., Donahue, N.M., Kulmala, M., Bianchi, F., 2021. Measurement report: Molecular composition and volatility of gaseous organic compounds in a boreal forest – from volatile organic compounds to highly oxygenated organic molecules. *Atmos. Chem. Phys.* 21, 8961–8977. <https://doi.org/10.5194/acp-21-8961-2021>
- Huey, L.G., 2007. Measurement of trace atmospheric species by chemical ionization mass spectrometry: Speciation of reactive nitrogen and future directions. *Mass Spectrometry Reviews* 26, 166–184. <https://doi.org/10.1002/mas.20118>
- Hunter, E.P.L., Lias, S.G., 1998. Evaluated Gas Phase Basicities and Proton Affinities of Molecules: An Update. *Journal of Physical and Chemical Reference Data* 27, 413–656. <https://doi.org/10.1063/1.556018>
- Huszar, P., Belda, M., Halenka, T., 2016. On the long-term impact of emissions from central European cities on regional air quality. *Atmospheric Chemistry and Physics* 16, 1331–1352. <https://doi.org/10.5194/acp-16-1331-2016>
- Hyttinen, N., Kupiainen-Määttä, O., Rissanen, M.P., Muuronen, M., Ehn, M., Kurtén, T., 2015. Modeling the Charging of Highly Oxidized Cyclohexene Ozonolysis Products Using Nitrate-Based Chemical Ionization. *J. Phys. Chem. A* 119, 6339–6345. <https://doi.org/10.1021/acs.jpca.5b01818>
- Hyttinen, N., Otkjær, R.V., Iyer, S., Kjaergaard, H.G., Rissanen, M.P., Wennberg, P.O., Kurtén, T., 2018. Computational Comparison of Different Reagent Ions in the Chemical Ionization of Oxidized Multifunctional Compounds. *J. Phys. Chem. A* 122, 269–279. <https://doi.org/10.1021/acs.jpca.7b10015>
- Im, U., Kanakidou, M., 2012. Impacts of East Mediterranean megacity emissions on air quality. *Atmospheric Chemistry and Physics* 12, 6335–6355. <https://doi.org/10.5194/acp-12-6335-2012>
- Inomata, S., Fushimi, A., Sato, K., Fujitani, Y., Yamada, H., 2015. 4-Nitrophenol, 1-nitropyrene, and 9-nitroanthracene emissions in exhaust particles from diesel vehicles with different exhaust gas treatments. *Atmospheric Environment* 110, 93–102. <https://doi.org/10.1016/j.atmosenv.2015.03.043>
- Isaacman-VanWertz, G., Massoli, P., O'Brien, R., Lim, C., Franklin, J.P., Moss, J.A., Hunter, J.F., Nowak, J.B., Canagaratna, M.R., Misztal, P.K., Arata, C., Roscioli, J.R., Herndon, S.T., Onasch, T.B., Lambe, A.T., Jayne, J.T., Su, L., Knopf, D.A., Goldstein, A.H., Worsnop, D.R., Kroll, J.H., 2018. Chemical evolution of atmospheric organic carbon over multiple generations of oxidation. *Nature Chemistry* 10, 462–468. <https://doi.org/10.1038/s41557-018-0002-2>
- Iyer, S., Rissanen, M.P., Valiev, R., Barua, S., Krechmer, J.E., Thornton, J., Ehn, M., Kurtén, T., 2021. Molecular mechanism for rapid autoxidation in α -pinene ozonolysis. *Nature Communications* 12, 878. <https://doi.org/10.1038/s41467-021-21172-w>
- Jacob, D.J., Field, B.D., Li, Q., Blake, D.R., de Gouw, J., Warneke, C., Hansel, A., Wisthaler, A., Singh, H.B., Guenther, A., 2005. Global budget of methanol: Constraints from atmospheric observations. *Journal of Geophysical Research: Atmospheres* 110. <https://doi.org/10.1029/2004JD005172>

- Jaoui, M., Piletic, I.R., Szmigielski, R., Rudzinski, K.J., Lewandowski, M., Riedel, T.P., Kleindienst, T.E., 2021. Rapid production of highly oxidized molecules in isoprene aerosol via peroxy and alkoxy radical isomerization pathways in low and high NO_x environments: Combined laboratory, computational and field studies. *Science of The Total Environment* 775, 145592. <https://doi.org/10.1016/j.scitotenv.2021.145592>
- Jenkin, M.E., Clemitshaw, K.C., 2000. Ozone and other secondary photochemical pollutants: chemical processes governing their formation in the planetary boundary layer. *Atmospheric Environment* 34, 2499–2527. [https://doi.org/10.1016/S1352-2310\(99\)00478-1](https://doi.org/10.1016/S1352-2310(99)00478-1)
- Johnson, D., Marston, G., 2008. The gas-phase ozonolysis of unsaturated volatile organic compounds in the troposphere. *Chemical Society reviews* 37, 699–716. <https://doi.org/10.1039/b704260b>
- Jokinen, T., 2015. Formation of low-volatility aerosol precursor molecules and clusters in the atmosphere (PhD Thesis). Report series in aerosol science. Finnish Association for Aerosol Research, Finland.
- Jokinen, T., Berndt, T., Makkonen, R., Kerminen, V.-M., Junninen, H., Paasonen, P., Stratmann, F., Herrmann, H., Guenther, A.B., Worsnop, D.R., Kulmala, M., Ehn, M., Sipilä, M., 2015. Production of extremely low volatile organic compounds from biogenic emissions: Measured yields and atmospheric implications. *Proceedings of the National Academy of Sciences* 112, 7123–7128. <https://doi.org/10.1073/pnas.1423977112>
- Jokinen, T., Kausiala, O., Garmash, O., Peräkylä, O., Junninen, H., Schobesberger, S., Yan, C., Sipilä, M., Rissanen, M., 2016. Production of highly oxidized organic compounds from ozonolysis of β -caryophyllene: Laboratory and field measurements 21, 262–273.
- Jokinen, T., Sipilä, M., Junninen, H., Ehn, M., Lönn, G., Hakala, J., Petäjä, T., Mauldin, R.L.I., Kulmala, M., Worsnop, D.R., 2012. Atmospheric sulphuric acid and neutral cluster measurements using CI-APi-TOF. *Atmospheric Chemistry and Physics* 12, 4117–4125. <https://doi.org/10.5194/acp-12-4117-2012>
- Jokinen, T., Sipilä, M., Richters, S., Kerminen, V.-M., Paasonen, P., Stratmann, F., Worsnop, D., Kulmala, M., Ehn, M., Herrmann, H., Berndt, T., 2014. Rapid Autoxidation Forms Highly Oxidized RO₂ Radicals in the Atmosphere. *Angewandte Chemie International Edition* 53, 14596–14600. <https://doi.org/10.1002/anie.201408566>
- Jolliffe, I.T., Cadima, J., 2016. Principal component analysis: a review and recent developments. *Philosophical Transactions of the Royal Society A: Mathematical, Physical and Engineering Sciences* 374, 20150202. <https://doi.org/10.1098/rsta.2015.0202>
- Jonsson, Å.M., Hallquist, M., Ljungström, E., 2006. Impact of Humidity on the Ozone Initiated Oxidation of Limonene, Δ^3 -Carene, and α -Pinene. *Environ. Sci. Technol.* 40, 188–194. <https://doi.org/10.1021/es051163w>
- Jordan, A., Haidacher, S., Hanel, G., Hartungen, E., Märk, L., Seehauser, H., Schotchkowsky, R., Sulzer, P., Märk, T.D., 2009. A high resolution and high sensitivity proton-transfer-reaction time-of-flight mass spectrometer (PTR-TOF-MS). *International Journal of Mass Spectrometry* 286, 122–128. <https://doi.org/10.1016/j.ijms.2009.07.005>
- Junninen, H., Ehn, M., Petäjä, T., Luosujärvi, L., Kotiaho, T., Kostianen, R., Rohner, U., Gonin, M., Fuhrer, K., Kulmala, M., Worsnop, D.R., 2010. A high-resolution mass spectrometer to measure atmospheric ion composition. *Atmospheric Measurement Techniques* 3, 1039–1053. <https://doi.org/10.5194/amt-3-1039-2010>
- Kanakidou, M., Seinfeld, J.H., Pandis, S.N., Barnes, I., Dentener, F.J., Facchini, M.C., Dingenen, R.V., Ervens, B., Nenes, A., Nielsen, C.J., Swietlicki, E., Putaud, J.P., Balkanski, Y., Fuzzi, S., Horth, J., Moortgat, G.K., Winterhalter, R., Myhre, C.E.L., Tsigaridis, K., Vignati, E., Stephanou, E.G., Wilson, J., 2005. Organic aerosol and global climate modelling: a review. *Atmos. Chem. Phys.* 71.

- Kanawade, V.P., Jobson, B.T., Guenther, A.B., Erupe, M.E., Pressley, S.N., Tripathi, S.N., Lee, S.-H., 2011. Isoprene suppression of new particle formation in a mixed deciduous forest. *Atmospheric Chemistry and Physics* 11, 6013–6027. <https://doi.org/10.5194/acp-11-6013-2011>
- Khattatov, T., 2019. Development, calibration and deployment of an airborne chemical ionization mass for trace gas measurements (PhD Thesis). <https://doi.org/10.13140/RG.2.2.35945.03683>
- Kiendler-Scharr, A., Wildt, J., Maso, M.D., Hohaus, T., Kleist, E., Mentel, T.F., Tillmann, R., Uerlings, R., Schurr, U., Wahner, A., 2009. New particle formation in forests inhibited by isoprene emissions. *Nature* 461, 381–384. <https://doi.org/10.1038/nature08292>
- Kirkby, J., Duplissy, J., Sengupta, K., Frege, C., Gordon, H., Williamson, C., Heinritzi, M., Simon, M., Yan, C., Almeida, J., Tröstl, J., Nieminen, T., Ortega, I.K., Wagner, R., Adamov, A., Amorim, A., Bernhammer, A.-K., Bianchi, F., Breitenlechner, M., Brilke, S., Chen, X., Craven, J., Dias, A., Ehrhart, S., Flagan, R.C., Franchin, A., Fuchs, C., Guida, R., Hakala, J., Hoyle, C.R., Jokinen, T., Junninen, H., Kangasluoma, J., Kim, J., Krapf, M., Kürten, A., Laaksonen, A., Lehtipalo, K., Makhmutov, V., Mathot, S., Molteni, U., Onnela, A., Peräkylä, O., Piel, F., Petäjä, T., Praplan, A.P., Pringle, K., Rap, A., Richards, N.A.D., Riipinen, I., Rissanen, M.P., Rondo, L., Sarnela, N., Schobesberger, S., Scott, C.E., Seinfeld, J.H., Sipilä, M., Steiner, G., Stozhkov, Y., Stratmann, F., Tomé, A., Virtanen, A., Vogel, A.L., Wagner, A.C., Wagner, P.E., Weingartner, E., Wimmer, D., Winkler, P.M., Ye, P., Zhang, X., Hansel, A., Dommen, J., Donahue, N.M., Worsnop, D.R., Baltensperger, U., Kulmala, M., Carslaw, K.S., Curtius, J., 2016. Ion-induced nucleation of pure biogenic particles. *Nature* 533, 521–526. <https://doi.org/10.1038/nature17953>
- Koch, S., Winterhalter, R., Uherek, E., Kolloff, A., Neeb, P., Moortgat, G.K., 2000. Formation of new particles in the gas-phase ozonolysis of monoterpenes. *Atmospheric Environment* 34, 4031–4042. [https://doi.org/10.1016/S1352-2310\(00\)00133-3](https://doi.org/10.1016/S1352-2310(00)00133-3)
- Krechmer, J.E., Coggon, M.M., Massoli, P., Nguyen, T.B., Crouse, J.D., Hu, W., Day, D.A., Tyndall, G.S., Henze, D.K., Rivera-Rios, J.C., Nowak, J.B., Kimmel, J.R., Mauldin, R.L., Stark, H., Jayne, J.T., Sipilä, M., Junninen, H., St. Clair, J.M., Zhang, X., Feiner, P.A., Zhang, L., Miller, D.O., Brune, W.H., Keutsch, F.N., Wennberg, P.O., Seinfeld, J.H., Worsnop, D.R., Jimenez, J.L., Canagaratna, M.R., 2015. Formation of Low Volatility Organic Compounds and Secondary Organic Aerosol from Isoprene Hydroxyhydroperoxide Low-NO Oxidation. *Environ. Sci. Technol.* 49, 10330–10339. <https://doi.org/10.1021/acs.est.5b02031>
- Kroll, J., Seinfeld, J., 2008. Chemistry of secondary organic aerosol: Formation and evolution of low-volatility organics in the atmosphere. *Atmospheric Environment* 42, 3593–3624. <https://doi.org/10.1016/j.atmosenv.2008.01.003>
- Kroll, J.H., Donahue, N.M., Cee, V.J., Demerjian, K.L., Anderson, J.G., 2002. Gas-Phase Ozonolysis of Alkenes: Formation of OH from Anti Carbonyl Oxides. *J. Am. Chem. Soc.* 124, 8518–8519. <https://doi.org/10.1021/ja0266060>
- Kroll, J.H., Ng, N.L., Murphy, S.M., Flagan, R.C., Seinfeld, J.H., 2006. Secondary Organic Aerosol Formation from Isoprene Photooxidation. *Environ. Sci. Technol.* 40, 1869–1877. <https://doi.org/10.1021/es0524301>
- Kukui, A., Chartier, M., Wang, J., Chen, H., Dusanter, S., Sauvage, S., Michoud, V., Locoge, N., Gros, V., Bourriane, T., Sellegri, K., Pichon, J.-M., 2021. Role of Criegee intermediates in the formation of sulfuric acid at a Mediterranean (Cape Corsica) site under influence of biogenic emissions. *Atmospheric Chemistry and Physics* 21, 13333–13351. <https://doi.org/10.5194/acp-21-13333-2021>

- Kürten, A., Bergen, A., Heinritzi, M., Leiminger, M., Lorenz, V., Piel, F., Simon, M., Sitals, R., Wagner, A.C., Curtius, J., 2016. Observation of new particle formation and measurement of sulfuric acid, ammonia, amines and highly oxidized organic molecules at a rural site in central Germany. *Atmospheric Chemistry and Physics* 16, 12793–12813. <https://doi.org/10.5194/acp-16-12793-2016>
- Kürten, A., Rondo, L., Ehrhart, S., Curtius, J., 2012. Calibration of a Chemical Ionization Mass Spectrometer for the Measurement of Gaseous Sulfuric Acid. *J. Phys. Chem. A* 116, 6375–6386. <https://doi.org/10.1021/jp212123n>
- Kuwata, K.T., Kujala, B.J., Morrow, Z.W., Tonc, E., 2011. Quantum chemical and RRKM/master equation studies of cyclopropene ozonolysis. *Computational and Theoretical Chemistry* 965, 305–312. <https://doi.org/10.1016/j.comptc.2010.10.019>
- Lai, A.C.K., Nazaroff, W.W., 2000. MODELING INDOOR PARTICLE DEPOSITION FROM TURBULENT FLOW ONTO SMOOTH SURFACES. *Journal of Aerosol Science* 31, 463–476. [https://doi.org/10.1016/S0021-8502\(99\)00536-4](https://doi.org/10.1016/S0021-8502(99)00536-4)
- Lambe, A., Massoli, P., Zhang, X., Canagaratna, M., Nowak, J., Daube, C., Yan, C., Nie, W., Onasch, T., Jayne, J., Kolb, C., Davidovits, P., Worsnop, D., Brune, W., 2017. Controlled nitric oxide production via $O(^1S_D)$, N_2O reactions for use in oxidation flow reactor studies. *Atmospheric Measurement Techniques* 10, 2283–2298. <https://doi.org/10.5194/amt-10-2283-2017>
- Lamkaddam, H., 2017. Study under simulated condition of the secondary organic aerosol from the photooxydation of n-dodecane: Impact of the physical-chemical processes, Etude en atmosphère simulée de la formation d'Aérosol Organique Secondaire issue de la photooxydation du n-dodécane: impact des paramètres environnementaux. Université Paris-Est.
- Laothawornkitkul, J., Taylor, J.E., Paul, N.D., Hewitt, C.N., 2009. Biogenic volatile organic compounds in the Earth system. *New Phytologist* 183, 27–51. <https://doi.org/10.1111/j.1469-8137.2009.02859.x>
- Lee, A., Goldstein, A.H., Kroll, J.H., Ng, N.L., Varutbangkul, V., Flagan, R.C., Seinfeld, J.H., 2006. Gas-phase products and secondary aerosol yields from the photooxidation of 16 different terpenes. *Journal of Geophysical Research: Atmospheres* 111. <https://doi.org/10.1029/2006JD007050>
- Lee, B.H., Lopez-Hilfiker, F.D., Mohr, C., Kurtén, T., Worsnop, D.R., Thornton, J.A., 2014. An Iodide-Adduct High-Resolution Time-of-Flight Chemical-Ionization Mass Spectrometer: Application to Atmospheric Inorganic and Organic Compounds. *Environ. Sci. Technol.* 48, 6309–6317. <https://doi.org/10.1021/es500362a>
- Lee, B.H., Mohr, C., Lopez-Hilfiker, F.D., Lutz, A., Hallquist, M., Lee, L., Romer, P., Cohen, R.C., Iyer, S., Kurtén, T., Hu, W., Day, D.A., Campuzano-Jost, P., Jimenez, J.L., Xu, L., Ng, N.L., Guo, H., Weber, R.J., Wild, R.J., Brown, S.S., Koss, A., de Gouw, J., Olson, K., Goldstein, A.H., Seco, R., Kim, S., McAvey, K., Shepson, P.B., Starn, T., Baumann, K., Edgerton, E.S., Liu, J., Shilling, J.E., Miller, D.O., Brune, W., Schobesberger, S., D'Ambro, E.L., Thornton, J.A., 2016. Highly functionalized organic nitrates in the southeast United States: Contribution to secondary organic aerosol and reactive nitrogen budgets. *Proceedings of the National Academy of Sciences* 113, 1516–1521. <https://doi.org/10.1073/pnas.1508108113>
- Lee, S.-H., Uin, J., Guenther, A.B., de Gouw, J.A., Yu, F., Nadykto, A.B., Herb, J., Ng, N.L., Koss, A., Brune, W.H., Baumann, K., Kanawade, V.P., Keutsch, F.N., Nenes, A., Olsen, K., Goldstein, A., Ouyang, Q., 2016. Isoprene suppression of new particle formation: Potential mechanisms and implications. *Journal of Geophysical Research: Atmospheres* 121, 14,621–14,635. <https://doi.org/10.1002/2016JD024844>

- Lehtipalo, K., Yan, C., Dada, L., Bianchi, F., Xiao, M., Wagner, R., Stolzenburg, D., Ahonen, L.R., Amorim, A., Baccarini, A., Bauer, P.S., Baumgartner, B., Bergen, A., Bernhammer, A.-K., Breitenlechner, M., Brilke, S., Buchholz, A., Mazon, S.B., Chen, D., Chen, X., Dias, A., Dommen, J., Draper, D.C., Duplissy, J., Ehn, M., Finkenzeller, H., Fischer, L., Frege, C., Fuchs, C., Garmash, O., Gordon, H., Hakala, J., He, X., Heikkinen, L., Heinritzi, M., Helm, J.C., Hofbauer, V., Hoyle, C.R., Jokinen, T., Kangasluoma, J., Kerminen, V.-M., Kim, C., Kirkby, J., Kontkanen, J., Kürten, A., Lawler, M.J., Mai, H., Mathot, S., Mauldin, R.L., Molteni, U., Nichman, L., Nie, W., Nieminen, T., Ojdanic, A., Onnela, A., Passananti, M., Petäjä, T., Piel, F., Pospisilova, V., Quéléver, L.L.J., Rissanen, M.P., Rose, C., Sarnela, N., Schallhart, S., Schuchmann, S., Sengupta, K., Simon, M., Sipilä, M., Tauber, C., Tomé, A., Tröstl, J., Väisänen, O., Vogel, A.L., Volkamer, R., Wagner, A.C., Wang, M., Weitz, L., Wimmer, D., Ye, P., Ylisirniö, A., Zha, Q., Carslaw, K.S., Curtius, J., Donahue, N.M., Flagan, R.C., Hansel, A., Riipinen, I., Virtanen, A., Winkler, P.M., Baltensperger, U., Kulmala, M., Worsnop, D.R., 2018. Multicomponent new particle formation from sulfuric acid, ammonia, and biogenic vapors. *Science Advances* 4, eaau5363. <https://doi.org/10.1126/sciadv.aau5363>
- Lelieveld, J., Gromov, S., Pozzer, A., Taraborrelli, D., 2016. Global tropospheric hydroxyl distribution, budget and reactivity. *Atmospheric Chemistry and Physics* 16, 12477–12493. <https://doi.org/10.5194/acp-16-12477-2016>
- Li, K., Zhang, X., Zhao, B., Bloss, W.J., Lin, C., White, S., Yu, H., Chen, L., Geng, C., Yang, W., Azzi, M., George, C., Bai, Z., 2022. Suppression of anthropogenic secondary organic aerosol formation by isoprene. *npj Climate and Atmospheric Science* 5, 12. <https://doi.org/10.1038/s41612-022-00233-x>
- Li, X., Chee, S., Hao, J., Abbatt, J.P.D., Jiang, J., Smith, J.N., 2019. Relative humidity effect on the formation of highly oxidized molecules and new particles during monoterpene oxidation. *Atmospheric Chemistry and Physics* 19, 1555–1570. <https://doi.org/10.5194/acp-19-1555-2019>
- Lightfoot, P.D., Cox, R.A., Crowley, J.N., Destriau, M., Hayman, G.D., Jenkin, M.E., Moortgat, G.K., Zabel, F., 1992. Organic peroxy radicals: Kinetics, spectroscopy and tropospheric chemistry. *Atmospheric Environment. Part A. General Topics, Organic Peroxy Radicals: Kinetics, Spectroscopy and Tropospheric Chemistry* 26, 1805–1961. [https://doi.org/10.1016/0960-1686\(92\)90423-I](https://doi.org/10.1016/0960-1686(92)90423-I)
- Lim, Y.B., Ziemann, P.J., 2009. Effects of Molecular Structure on Aerosol Yields from OH Radical-Initiated Reactions of Linear, Branched, and Cyclic Alkanes in the Presence of NO_x. *Environ. Sci. Technol.* 43, 2328–2334. <https://doi.org/10.1021/es803389s>
- Liu, D., Zhang, Y., Zhong, S., Chen, S., Xie, Q., Zhang, D., Zhang, Q., Hu, W., Deng, J., Wu, L., Ma, C., Tong, H., Fu, P., 2022. Large differences of highly oxygenated organic molecules (HOMs) and low volatile species in SOA formed from ozonolysis of β -pinene and limonene. *Atmospheric Chemistry and Physics Discussions* 2022, 1–29. <https://doi.org/10.5194/acp-2022-636>
- Liu, J., Alexander, L., Fast, J., Lindenmaier, R., Shilling, J., 2021. Aerosol characteristics at the Southern Great Plains site during the HI-SCALE campaign. *Atmospheric Chemistry and Physics* 21, 5101–5116. <https://doi.org/10.5194/acp-21-5101-2021>
- Liu, J., D'Ambro, E.L., Lee, B.H., Lopez-Hilfiker, F.D., Zaveri, R.A., Rivera-Rios, J.C., Keutsch, F.N., Iyer, S., Kurten, T., Zhang, Z., Gold, A., Surratt, J.D., Shilling, J.E., Thornton, J.A., 2016. Efficient Isoprene Secondary Organic Aerosol Formation from a Non-IEPOX Pathway. *Environ. Sci. Technol.* 50, 9872–9880. <https://doi.org/10.1021/acs.est.6b01872>
- Liu, Z., Wang, Y., Gu, D., Zhao, C., Huey, L.G., Stickel, R., Liao, J., Shao, M., Zhu, T., Zeng, L., Amoroso, A., Costabile, F., Chang, C.-C., Liu, S.-C., 2012. Summertime photochemistry

- during CAREBeijing-2007: RO_x budgets and O₃ formation. *Atmospheric Chemistry and Physics* 12, 7737–7752. <https://doi.org/10.5194/acp-12-7737-2012>
- Loreto, F., Schnitzler, J.-P., 2010. Abiotic stresses and induced BVOCs. *Trends in Plant Science, Special Issue: Induced biogenic volatile organic compounds from plants* 15, 154–166. <https://doi.org/10.1016/j.tplants.2009.12.006>
- Loza, C.L., Coggon, M.M., Nguyen, T.B., Zuend, A., Flagan, R.C., Seinfeld, J.H., 2013. On the Mixing and Evaporation of Secondary Organic Aerosol Components. *Environ. Sci. Technol.* 47, 6173–6180. <https://doi.org/10.1021/es400979k>
- Luo, H., Vereecken, L., Shen, H., Kang, S., Pullinen, I., Hallquist, M., Fuchs, H., Wahner, A., Kiendler-Scharr, A., Mentel, T.F., Zhao, D., 2023. Formation of highly oxygenated organic molecules from the oxidation of limonene by OH radical: significant contribution of H-abstraction pathway. *Atmospheric Chemistry and Physics* 23, 7297–7319. <https://doi.org/10.5194/acp-23-7297-2023>
- Maksymiuk, C.S., Gayahtri, C., Gil, R.R., Donahue, N.M., 2009. Secondary organic aerosol formation from multiphase oxidation of limonene by ozone: mechanistic constraints via two-dimensional heteronuclear NMR spectroscopy. *Phys. Chem. Chem. Phys.* 11, 7810–7818. <https://doi.org/10.1039/B820005J>
- Mao, J., Ren, X., Chen, S., Brune, W.H., Chen, Z., Martinez, M., Harder, H., Lefer, B., Rappenglück, B., Flynn, J., Leuchner, M., 2010. Atmospheric oxidation capacity in the summer of Houston 2006: Comparison with summer measurements in other metropolitan studies. *Atmospheric Environment* 44, 4107–4115. <https://doi.org/10.1016/j.atmosenv.2009.01.013>
- Martin, S.T., Artaxo, P., Machado, L., Manzi, A.O., Souza, R.A.F., Schumacher, C., Wang, J., Biscaro, T., Brito, J., Calheiros, A., Jardine, K., Medeiros, A., Portela, B., Sá, S.S. de, Adachi, K., Aiken, A.C., Albrecht, R., Alexander, L., Andreae, M.O., Barbosa, H.M.J., Buseck, P., Chand, D., Comstock, J.M., Day, D.A., Dubey, M., Fan, J., Fast, J., Fisch, G., Fortner, E., Giangrande, S., Gilles, M., Goldstein, A.H., Guenther, A., Hubbe, J., Jensen, M., Jimenez, J.L., Keutsch, F.N., Kim, S., Kuang, C., Laskin, A., McKinney, K., Mei, F., Miller, M., Nascimento, R., Pauliquevis, T., Pekour, M., Peres, J., Petäjä, T., Pöhlker, C., Pöschl, U., Rizzo, L., Schmid, B., Shilling, J.E., Dias, M.A.S., Smith, J.N., Tomlinson, J.M., Tóta, J., Wendisch, M., 2017. The Green Ocean Amazon Experiment (GoAmazon2014/5) Observes Pollution Affecting Gases, Aerosols, Clouds, and Rainfall over the Rain Forest. *Bulletin of the American Meteorological Society* 98, 981–997. <https://doi.org/10.1175/BAMS-D-15-00221.1>
- Massoli, P., Stark, H., Canagaratna, M.R., Krechmer, J.E., Xu, L., Ng, N.L., Mauldin, R.L., Yan, C., Kimmel, J., Misztal, P.K., Jimenez, J.L., Jayne, J.T., Worsnop, D.R., 2018. Ambient Measurements of Highly Oxidized Gas-Phase Molecules during the Southern Oxidant and Aerosol Study (SOAS) 2013. *ACS Earth Space Chem.* 2, 653–672. <https://doi.org/10.1021/acsearthspacechem.8b00028>
- Maurin, N., 2013. Formation et devenir de l'aérosol organique secondaire issu de l'ozonolyse de l'alpha-pinène : étude expérimentale en atmosphère simulée et analyse chimique (PhD Thesis).
- Mayorga, R., Xia, Y., Zhao, Z., Long, B., Zhang, H., 2022. Peroxy Radical Autoxidation and Sequential Oxidation in Organic Nitrate Formation during Limonene Nighttime Oxidation. *Environ. Sci. Technol.* 56, 15337–15346. <https://doi.org/10.1021/acs.est.2c04030>
- McFiggans, G., Mentel, T.F., Wildt, J., Pullinen, I., Kang, S., Kleist, E., Schmitt, S., Springer, M., Tillmann, R., Wu, C., Zhao, D., Hallquist, M., Faxon, C., Le Breton, M., Hallquist, Å.M., Simpson, D., Bergström, R., Jenkin, M.E., Ehn, M., Thornton, J.A., Alfarra, M.R., Bannan, T.J., Percival, C.J., Priestley, M., Topping, D., Kiendler-Scharr, A., 2019. Secondary

- organic aerosol reduced by mixture of atmospheric vapours. *Nature* 565, 587–593. <https://doi.org/10.1038/s41586-018-0871-y>
- McIlveen, R., 1991. *Fundamentals of Weather and Climate*. Psychology Press.
- Meder, M.J.A., Peräkylä, O., Varelas, J.G., Luo, J., Cai, R., Zhang, Y., Kurtén, T., Riva, M., Rissanen, M.P., Geiger, F.M., Thomson, R.J., Ehn, M., 2022. Selective deuteration as a tool for resolving autoxidation mechanisms in α -pinene ozonolysis. *EGU*sphere 1–26. <https://doi.org/10.5194/egusphere-2022-1131>
- Mehra, A., 2021. *Determining Biogenic and Anthropogenic Contributions to Secondary Organic Aerosol*. The University of Manchester.
- Mehra, A., Canagaratna, M., Bannan, T.J., Worrall, S.D., Bacak, A., Priestley, M., Liu, D., Zhao, J., Xu, W., Sun, Y., Hamilton, J.F., Squires, F.A., Lee, J., Bryant, D.J., Hopkins, J.R., Elzein, A., Budisulistiorini, S.H., Cheng, X., Chen, Q., Wang, Y., Wang, L., Stark, H., Krechmer, J.E., Brean, J., Slater, E., Whalley, L., Heard, D., Ouyang, B., Acton, W.J.F., Hewitt, C.N., Wang, X., Fu, P., Jayne, J., Worsnop, D., Allan, J., Percival, C., Coe, H., 2021. Using highly time-resolved online mass spectrometry to examine biogenic and anthropogenic contributions to organic aerosol in Beijing. *Faraday Discuss.* 226, 382–408. <https://doi.org/10.1039/D0FD00080A>
- Mellouki, A., Wallington, T.J., Chen, J., 2015. Atmospheric Chemistry of Oxygenated Volatile Organic Compounds: Impacts on Air Quality and Climate. *Chem. Rev.* 115, 3984–4014. <https://doi.org/10.1021/cr500549n>
- Mentel, T.F., Springer, M., Ehn, M., Kleist, E., Pullinen, I., Kurtén, T., Rissanen, M., Wahner, A., Wildt, J., 2015. Formation of highly oxidized multifunctional compounds: autoxidation of peroxy radicals formed in the ozonolysis of alkenes – deduced from structure–product relationships. *Atmospheric Chemistry and Physics* 15, 6745–6765. <https://doi.org/10.5194/acp-15-6745-2015>
- Menut, L., Vautard, R., Flamant, C., Abonnel, C., Beekmann, M., Chazette, P., Flamant, P.H., Gombert, D., Guédalia, D., Kley, D., Lefebvre, M.P., Lossec, B., Martin, D., Mégie, G., Perros, P., Sicard, M., Toupance, G., 2000. Measurements and modelling of atmospheric pollution over the Paris area: an overview of the ESQUIF Project. *Annales Geophysicae* 18, 1467–1481. <https://doi.org/10.1007/s00585-000-1467-y>
- Mermet, K., Perraudin, E., Dusanter, S., Sauvage, S., Léonardis, T., Flaud, P.-M., Bsaibes, S., Kammer, J., Michoud, V., Gratien, A., Cirtog, M., Al Ajami, M., Truong, F., Batut, S., Hecquet, C., Doussin, J.-F., Schoemaeker, C., Gros, V., Locoge, N., Villenave, E., 2021. Atmospheric reactivity of biogenic volatile organic compounds in a maritime pine forest during the LANDEX episode 1 field campaign. *Science of The Total Environment* 756, 144129. <https://doi.org/10.1016/j.scitotenv.2020.144129>
- Michoud, V., Kukui, A., Camredon, M., Colomb, A., Borbon, A., Miet, K., Aumont, B., Beekmann, M., Durand-Jolibois, R., Perrier, S., Zapf, P., Siour, G., Ait-Helal, W., Locoge, N., Sauvage, S., Afif, C., Gros, V., Furger, M., Ancellet, G., Doussin, J.F., 2012. Radical budget analysis in a suburban European site during the MEGAPOLI summer field campaign. *Atmospheric Chemistry and Physics* 12, 11951–11974. <https://doi.org/10.5194/acp-12-11951-2012>
- Michoud, V., Sciare, J., Sauvage, S., Dusanter, S., Léonardis, T., Gros, V., Kalogridis, C., Zannoni, N., Féron, A., Petit, J.-E., Crenn, V., Baisnée, D., Sarda-Estève, R., Bonnaire, N., Marchand, N., DeWitt, H.L., Pey, J., Colomb, A., Gheusi, F., Szidat, S., Stavroulas, I., Borbon, A., Locoge, N., 2017. Organic carbon at a remote site of the western Mediterranean Basin: sources and chemistry during the ChArMEx SOP2 field experiment. *Atmospheric Chemistry and Physics* 17, 8837–8865. <https://doi.org/10.5194/acp-17-8837-2017>

- Millet, D.B., Alwe, H.D., Chen, X., Deventer, M.J., Griffis, T.J., Holzinger, R., Bertman, S.B., Rickly, P.S., Stevens, P.S., Léonardis, T., Locoge, N., Dusanter, S., Tyndall, G.S., Alvarez, S.L., Erickson, M.H., Flynn, J.H., 2018. Bidirectional Ecosystem–Atmosphere Fluxes of Volatile Organic Compounds Across the Mass Spectrum: How Many Matter? *ACS Earth Space Chem.* 2, 764–777. <https://doi.org/10.1021/acsearthspacechem.8b00061>
- Mohr, C., Lopez-Hilfiker, F.D., Yli-Juuti, T., Heitto, A., Lutz, A., Hallquist, M., D'Ambro, E.L., Rissanen, M.P., Hao, L., Schobesberger, S., Kulmala, M., Mauldin III, R.L., Makkonen, U., Sipilä, M., Petäjä, T., Thornton, J.A., 2017. Ambient observations of dimers from terpene oxidation in the gas phase: Implications for new particle formation and growth. *Geophysical Research Letters* 44, 2958–2966. <https://doi.org/10.1002/2017GL072718>
- Mohr, C., Lopez-Hilfiker, F.D., Zotter, P., Prévôt, A.S.H., Xu, L., Ng, N.L., Herndon, S.C., Williams, L.R., Franklin, J.P., Zahniser, M.S., Worsnop, D.R., Knighton, W.B., Aiken, A.C., Gorkowski, K.J., Dubey, M.K., Allan, J.D., Thornton, J.A., 2013. Contribution of Nitrated Phenols to Wood Burning Brown Carbon Light Absorption in Detling, United Kingdom during Winter Time. *Environ. Sci. Technol.* 47, 6316–6324. <https://doi.org/10.1021/es400683v>
- Mohr, C., Weimer, S., Richter, R., DeCarlo, P., Chirico, R., Heringa, M., Prevot, A., Baltensperger, U., 2009. Source apportionment of ambient aerosol applying PMF on AMS mobile and stationary data 11, 12006.
- Molhave, L., Clausen, G., Berglund, B., Ceaurriz, J., Kettrup, A., Lindvall, T., Maroni, M., Pickering, A.C., Risse, U., Rothweiler, H., Seifert, B., Younes, M., 1997. Total Volatile Organic Compounds (TVOC) in Indoor Air Quality Investigations*. *Indoor Air* 7, 225–240. <https://doi.org/10.1111/j.1600-0668.1997.00002.x>
- Molina, L.T., Madronich, S., Gaffney, J.S., Apel, E., de Foy, B., Fast, J., Ferrare, R., Herndon, S., Jimenez, J.L., Lamb, B., Osornio-Vargas, A.R., Russell, P., Schauer, J.J., Stevens, P.S., Volkamer, R., Zavala, M., 2010. An overview of the MILAGRO 2006 Campaign: Mexico City emissions and their transport and transformation. *Atmos. Chem. Phys.* 10, 8697–8760. <https://doi.org/10.5194/acp-10-8697-2010>
- Møller, K.H., Bates, K.H., Kjaergaard, H.G., 2019. The Importance of Peroxy Radical Hydrogen-Shift Reactions in Atmospheric Isoprene Oxidation. *J. Phys. Chem. A* 123, 920–932. <https://doi.org/10.1021/acs.jpca.8b10432>
- Molteni, U., Bianchi, F., Klein, F., El Haddad, I., Frege, C., Rossi, M.J., Dommen, J., Baltensperger, U., 2018. Formation of highly oxygenated organic molecules from aromatic compounds. *Atmospheric Chemistry and Physics* 18, 1909–1921. <https://doi.org/10.5194/acp-18-1909-2018>
- Molteni, U., Simon, M., Heinritzi, M., Hoyle, C.R., Bernhammer, A.-K., Bianchi, F., Breitenlechner, M., Brilke, S., Dias, A., Duplissy, J., Frege, C., Gordon, H., Heyn, C., Jokinen, T., Kürten, A., Lehtipalo, K., Makhmutov, V., Petäjä, T., Pieber, S.M., Praplan, A.P., Schobesberger, S., Steiner, G., Stozhkov, Y., Tomé, A., Tröstl, J., Wagner, A.C., Wagner, R., Williamson, C., Yan, C., Baltensperger, U., Curtius, J., Donahue, N.M., Hansel, A., Kirkby, J., Kulmala, M., Worsnop, D.R., Dommen, J., 2019. Formation of Highly Oxygenated Organic Molecules from α -Pinene Ozonolysis: Chemical Characteristics, Mechanism, and Kinetic Model Development. *ACS Earth Space Chem.* 3, 873–883. <https://doi.org/10.1021/acsearthspacechem.9b00035>
- Monks, P.S., 2005. Gas-phase radical chemistry in the troposphere. *Chem. Soc. Rev.* 34, 376–395. <https://doi.org/10.1039/B307982C>
- Monks, P.S., Archibald, A.T., Colette, A., Cooper, O., Coyle, M., Derwent, R., Fowler, D., Granier, C., Law, K.S., Mills, G.E., Stevenson, D.S., Tarasova, O., Thouret, V., von Schneidemesser, E., Sommariva, R., Wild, O., Williams, M.L., 2015. Tropospheric ozone

- and its precursors from the urban to the global scale from air quality to short-lived climate forcer. *Atmos. Chem. Phys.* 15, 8889–8973. <https://doi.org/10.5194/acp-15-8889-2015>
- Müller, M., Mikoviny, T., Wisthaler, A., 2014. Detector aging induced mass discrimination and non-linearity effects in PTR-ToF-MS. *International Journal of Mass Spectrometry* 365–366, 93–97. <https://doi.org/10.1016/j.ijms.2013.12.008>
- Mutzel, A., Poulain, L., Berndt, T., Iinuma, Y., Rodigast, M., Böge, O., Richters, S., Spindler, G., Sipilä, M., Jokinen, T., Kulmala, M., Herrmann, H., 2015. Highly Oxidized Multifunctional Organic Compounds Observed in Tropospheric Particles: A Field and Laboratory Study. *Environ. Sci. Technol.* 49, 7754–7761. <https://doi.org/10.1021/acs.est.5b00885>
- Nagori, J., Janssen, R.H.H., Fry, J.L., Krol, M., Jimenez, J.L., Hu, W., de Arellano, J.V.-G., 2019. Biogenic emissions and land–atmosphere interactions as drivers of the daytime evolution of secondary organic aerosol in the southeastern US. *Atmos. Chem. Phys.* 29.
- Nascimento, J.P., Bela, M.M., Meller, B.B., Banducci, A.L., Rizzo, L.V., Vara-Vela, A.L., Barbosa, H.M.J., Gomes, H., Rafee, S.A.A., Franco, M.A., Carbone, S., Cirino, G.G., Souza, R.A.F., McKeen, S.A., Artaxo, P., 2021. Aerosols from anthropogenic and biogenic sources and their interactions – modeling aerosol formation, optical properties, and impacts over the central Amazon basin. *Atmospheric Chemistry and Physics* 21, 6755–6779. <https://doi.org/10.5194/acp-21-6755-2021>
- National Research Council, 1991. VOCs and NO_x: Relationship to Ozone and Associated Pollutants, in: *Rethinking the Ozone Problem in Urban and Regional Air Pollution*. The National Academies Press, Washington, DC. <https://doi.org/10.17226/1889>
- Ng, N.L., Brown, S.S., Archibald, A.T., Atlas, E., Cohen, R.C., Crowley, J.N., Day, D.A., Donahue, N.M., Fry, J.L., Fuchs, H., Griffin, R.J., Guzman, M.I., Herrmann, H., Hodzic, A., Iinuma, Y., Jimenez, J.L., Kiendler-Scharr, A., Lee, B.H., Luecken, D.J., Mao, J., McLaren, R., Mutzel, A., Osthoff, H.D., Ouyang, B., Picquet-Varrault, B., Platt, U., Pye, H.O.T., Rudich, Y., Schwantes, R.H., Shiraiwa, M., Stutz, J., Thornton, J.A., Tilgner, A., Williams, B.J., Zaveri, R.A., 2017. Nitrate radicals and biogenic volatile organic compounds: oxidation, mechanisms, and organic aerosol. *Atmos. Chem. Phys.* 60.
- Ng, N.L., Chhabra, P.S., Chan, A.W.H., Surratt, J.D., Kroll, J.H., Kwan, A.J., McCabe, D.C., Wennberg, P.O., Sorooshian, A., Murphy, S.M., Dalleska, N.F., Flagan, R.C., Seinfeld, J.H., 2007. Effect of NO_x level on secondary organic aerosol (SOA) formation from the photooxidation of terpenes. *Atmospheric Chemistry and Physics* 7, 5159–5174. <https://doi.org/10.5194/acp-7-5159-2007>
- Ng, N.L., Kwan, A.J., Surratt, J.D., Chan, A.W.H., Chhabra, P.S., Sorooshian, A., Pye, H.O.T., Crouse, J.D., Wennberg, P.O., Flagan, R.C., Seinfeld, J.H., 2008. Secondary organic aerosol (SOA) formation from reaction of isoprene with nitrate radicals (NO₃). *Atmospheric Chemistry and Physics* 8, 4117–4140. <https://doi.org/10.5194/acp-8-4117-2008>
- Noyes, W.A.Jr., Wobbe, D.E., 1926. THE VAPOR PRESSURE OF ANHYDROUS OXALIC ACID. *J. Am. Chem. Soc.* 48, 1882–1887. <https://doi.org/10.1021/ja01418a012>
- Nozière, B., Kalberer, M., Claeys, M., Allan, J., D’Anna, B., Decesari, S., Finessi, E., Glasius, M., Grgić, I., Hamilton, J.F., Hoffmann, T., Iinuma, Y., Jaoui, M., Kahnt, A., Kampf, C.J., Kourtev, I., Maenhaut, W., Marsden, N., Saarikoski, S., Schnelle-Kreis, J., Surratt, J.D., Szidat, S., Szmigielski, R., Wisthaler, A., 2015. The Molecular Identification of Organic Compounds in the Atmosphere: State of the Art and Challenges. *Chem. Rev.* 115, 3919–3983. <https://doi.org/10.1021/cr5003485>
- ONF, O.N. des F., 2006. Milieux naturels et peuplements forestiers [WWW Document]. URL http://www1.onf.fr/enforet/rambouillet/comprendre/diagnostic_enjeux/20120521-132157-503304/@@index.html (accessed 3.6.23).

- Orlando, J.J., Tyndall, G.S., Calvert, J.G., 1992. Thermal decomposition pathways for peroxyacetyl nitrate (PAN): Implications for atmospheric methyl nitrate levels. *Atmospheric Environment. Part A. General Topics* 26, 3111–3118. [https://doi.org/10.1016/0960-1686\(92\)90468-Z](https://doi.org/10.1016/0960-1686(92)90468-Z)
- Pagonis, D., Algrim, L.B., Price, D.J., Day, D.A., Handschy, A.V., Stark, H., Miller, S.L., de Gouw, J.A., Jimenez, J.L., Ziemann, P.J., 2019. Autoxidation of Limonene Emitted in a University Art Museum. *Environ. Sci. Technol. Lett.* 6, 520–524. <https://doi.org/10.1021/acs.estlett.9b00425>
- Panda, S.K., Jana, P.K., 2015. Efficient task scheduling algorithms for heterogeneous multi-cloud environment. *The Journal of Supercomputing* 71, 1505–1533. <https://doi.org/10.1007/s11227-014-1376-6>
- Parrish, D.D., Allen, D.T., Bates, T.S., Estes, M., Fehsenfeld, F.C., Feingold, G., Ferrare, R., Hardesty, R.M., Meagher, J.F., Nielsen-Gammon, J.W., Pierce, R.B., Ryerson, T.B., Seinfeld, J.H., Williams, E.J., 2009. Overview of the Second Texas Air Quality Study (TexAQS II) and the Gulf of Mexico Atmospheric Composition and Climate Study (GoMACCS). *J. Geophys. Res.* 114, D00F13. <https://doi.org/10.1029/2009JD011842>
- Peñuelas, J., Llusià, J., 2003. BVOCs: plant defense against climate warming? *Trends in Plant Science* 8, 105–109. [https://doi.org/10.1016/S1360-1385\(03\)00008-6](https://doi.org/10.1016/S1360-1385(03)00008-6)
- Peñuelas, J., Llusià, J., 2002. Linking photorespiration, monoterpenes and thermotolerance in *Quercus*. *New Phytologist* 155, 227–237. <https://doi.org/10.1046/j.1469-8137.2002.00457.x>
- Petäjä, T., Mauldin, R.L., III, Kosciuch, E., McGrath, J., Nieminen, T., Paasonen, P., Boy, M., Adamov, A., Kotiaho, T., Kulmala, M., 2009. Sulfuric acid and OH concentrations in a boreal forest site. *Atmospheric Chemistry and Physics* 9, 7435–7448. <https://doi.org/10.5194/acp-9-7435-2009>
- Petäjä, T., Moisseev, D., Sinclair, V., O'Connor, E., Manninen, A., Levula, J., Väänänen, R., Heikkinen, L., Äijälä, M., Aalto, J., Thornton, J., 2016. Biogenic Aerosols—Effects on Clouds and Climate (BAECC) Final Campaign Summary (No. DOE/SC-ARM--15-051, 1242990). <https://doi.org/10.2172/1242990>
- Pichersky, E., Gershenzon, J., 2002. The formation and function of plant volatiles: perfumes for pollinator attraction and defense. *Current Opinion in Plant Biology* 5, 237–243. [https://doi.org/10.1016/S1369-5266\(02\)00251-0](https://doi.org/10.1016/S1369-5266(02)00251-0)
- Picquet-Varrault, B., Orphal, J., Doussin, J.-F., Carlier, P., Flaud, J.-M., 2005. Laboratory Intercomparison of the Ozone Absorption Coefficients in the Mid-infrared (10 μm) and Ultraviolet (300–350 nm) Spectral Regions. *J. Phys. Chem. A* 109, 1008–1014. <https://doi.org/10.1021/jp0405411>
- Poulain, L., Tilgner, A., Brüggemann, M., Mettke, P., He, L., Anders, J., Böge, O., Mutzel, A., Herrmann, H., 2022. Particle-Phase Uptake and Chemistry of Highly Oxygenated Organic Molecules (HOMs) From α -Pinene OH Oxidation. *Journal of Geophysical Research: Atmospheres* 127, e2021JD036414. <https://doi.org/10.1029/2021JD036414>
- Praplan, A.P., Schobesberger, S., Bianchi, F., Rissanen, M.P., Ehn, M., Jokinen, T., Junninen, H., Adamov, A., Amorim, A., Dommen, J., Duplissy, J., Hakala, J., Hansel, A., Heinritzi, M., Kangasluoma, J., Kirkby, J., Krapf, M., Kürten, A., Lehtipalo, K., Riccobono, F., Rondo, L., Sarnela, N., Simon, M., Tomé, A., Tröstl, J., Winkler, P.M., Williamson, C., Ye, P., Curtius, J., Baltensperger, U., Donahue, N.M., Kulmala, M., Worsnop, D.R., 2015. Elemental composition and clustering behaviour of α -pinene oxidation products for different oxidation conditions. *Atmospheric Chemistry and Physics* 15, 4145–4159. <https://doi.org/10.5194/acp-15-4145-2015>

- Presto, A.A., Huff Hartz, K.E., Donahue, N.M., 2005. Secondary Organic Aerosol Production from Terpene Ozonolysis. 2. Effect of NO_x Concentration. *Environ. Sci. Technol.* 39, 7046–7054. <https://doi.org/10.1021/es050400s>
- Priestley, M., Bannan, T.J., Le Breton, M., Worrall, S.D., Kang, S., Pullinen, I., Schmitt, S., Tillmann, R., Kleist, E., Zhao, D., Wildt, J., Garmash, O., Mehra, A., Bacak, A., Shallcross, D.E., Kiendler-Scharr, A., Hallquist, Å.M., Ehn, M., Coe, H., Percival, C.J., Hallquist, M., Mentel, T.F., McFiggans, G., 2021. Chemical characterisation of benzene oxidation products under high- and low-NO_x conditions using chemical ionisation mass spectrometry. *Atmospheric Chemistry and Physics* 21, 3473–3490. <https://doi.org/10.5194/acp-21-3473-2021>
- Pullinen, I., Schmitt, S., Kang, S., Sarrafzadeh, M., Schlag, P., Andres, S., Kleist, E., Mentel, T.F., Rohrer, F., Springer, M., Tillmann, R., Wildt, J., Wu, C., Zhao, D., Wahner, A., Kiendler-Scharr, A., 2020. Impact of NO_x on secondary organic aerosol (SOA) formation from α -pinene and β -pinene photooxidation: the role of highly oxygenated organic nitrates. *Atmos. Chem. Phys.* 23.
- Quéléver, L.L.J., Kristensen, K., Normann Jensen, L., Rosati, B., Teiwes, R., Daellenbach, K.R., Peräkylä, O., Roldin, P., Bossi, R., Pedersen, H.B., Glasius, M., Bilde, M., Ehn, M., 2019. Effect of temperature on the formation of highly oxygenated organic molecules (HOMs) from alpha-pinene ozonolysis. *Atmospheric Chemistry and Physics* 19, 7609–7625. <https://doi.org/10.5194/acp-19-7609-2019>
- Ramírez, N., Cuadras, A., Rovira, E., Borrull, F., Marcé, R.M., 2012. Chronic risk assessment of exposure to volatile organic compounds in the atmosphere near the largest Mediterranean industrial site. *Environment International* 39, 200–209. <https://doi.org/10.1016/j.envint.2011.11.002>
- Reimann, S., Lewis, A.C., 2007. Anthropogenic VOCs, in: *Volatile Organic Compounds in the Atmosphere*. John Wiley & Sons, Ltd, pp. 33–81. <https://doi.org/10.1002/9780470988657.ch2>
- Ren, X., Brune, W.H., Oligier, A., Metcalf, A.R., Simpas, J.B., Shirley, T., Schwab, J.J., Bai, C., Roychowdhury, U., Li, Y., Cai, C., Demerjian, K.L., He, Y., Zhou, X., Gao, H., Hou, J., 2006. OH, HO₂, and OH reactivity during the PMTACS–NY Whiteface Mountain 2002 campaign: Observations and model comparison. *Journal of Geophysical Research: Atmospheres* 111. <https://doi.org/10.1029/2005JD006126>
- Ren, X., Harder, H., Martinez, M., Leshner, R.L., Oligier, A., Simpas, J.B., Brune, W.H., Schwab, J.J., Demerjian, K.L., He, Y., Zhou, X., Gao, H., 2003. OH and HO₂ Chemistry in the urban atmosphere of New York City. *Atmospheric Environment* 37, 3639–3651. [https://doi.org/10.1016/S1352-2310\(03\)00459-X](https://doi.org/10.1016/S1352-2310(03)00459-X)
- Ribeiro da Silva, M.A.V., Monte, M.J.S., Ribeiro, J.R., 1999. Vapour pressures and the enthalpies and entropies of sublimation of five dicarboxylic acids. *The Journal of Chemical Thermodynamics* 31, 1093–1107. <https://doi.org/10.1006/jcht.1999.0522>
- Riccobono, F., Schobesberger, S., Scott, C.E., Dommen, J., Ortega, I.K., Rondo, L., Almeida, J., Amorim, A., Bianchi, F., Breitenlechner, M., David, A., Downard, A., Dunne, E.M., Duplissy, J., Ehrhart, S., Flagan, R.C., Franchin, A., Hansel, A., Junninen, H., Kajos, M., Keskinen, H., Kupc, A., Kürten, A., Kvashin, A.N., Laaksonen, A., Lehtipalo, K., Makhmutov, V., Mathot, S., Nieminen, T., Onnela, A., Petäjä, T., Praplan, A.P., Santos, F.D., Schallhart, S., Seinfeld, J.H., Sipilä, M., Spracklen, D.V., Stozhkov, Y., Stratmann, F., Tomé, A., Tsagkogeorgas, G., Vaattovaara, P., Viisanen, Y., Vrtala, A., Wagner, P.E., Weingartner, E., Wex, H., Wimmer, D., Carslaw, K.S., Curtius, J., Donahue, N.M., Kirkby, J., Kulmala, M., Worsnop, D.R., Baltensperger, U., 2014. Oxidation products of biogenic

- emissions contribute to nucleation of atmospheric particles. *Science* 344, 717–721. <https://doi.org/10.1126/science.1243527>
- Richters, S., Herrmann, H., Berndt, T., 2016. Highly Oxidized RO₂ Radicals and Consecutive Products from the Ozonolysis of Three Sesquiterpenes. *Environ. Sci. Technol.* 50, 2354–2362. <https://doi.org/10.1021/acs.est.5b05321>
- Riipinen, I., Pierce, J.R., Yli-Juuti, T., Nieminen, T., Häkkinen, S., Ehn, M., Junninen, H., Lehtipalo, K., Petäjä, T., Slowik, J., Chang, R., Shantz, N.C., Abbatt, J., Leitch, W.R., Kerminen, V.-M., Worsnop, D.R., Pandis, S.N., Donahue, N.M., Kulmala, M., 2011. Organic condensation: a vital link connecting aerosol formation to cloud condensation nuclei (CCN) concentrations. *Atmospheric Chemistry and Physics* 11, 3865–3878. <https://doi.org/10.5194/acp-11-3865-2011>
- Rissanen, M., 2021. Anthropogenic Volatile Organic Compound (AVOC) Autoxidation as a Source of Highly Oxygenated Organic Molecules (HOM). *J. Phys. Chem. A* 125, 9027–9039. <https://doi.org/10.1021/acs.jpca.1c06465>
- Rissanen, M.P., 2018. NO₂ Suppression of Autoxidation–Inhibition of Gas-Phase Highly Oxidized Dimer Product Formation. *ACS Earth Space Chem.* 2, 1211–1219. <https://doi.org/10.1021/acsearthspacechem.8b00123>
- Rissanen, M.P., Kurtén, T., Sipilä, M., Thornton, J.A., Kangasluoma, J., Sarnela, N., Junninen, H., Jørgensen, S., Schallhart, S., Kajos, M.K., Taipale, R., Springer, M., Mentel, T.F., Ruuskanen, T., Petäjä, T., Worsnop, D.R., Kjaergaard, H.G., Ehn, M., 2014. The Formation of Highly Oxidized Multifunctional Products in the Ozonolysis of Cyclohexene. *J. Am. Chem. Soc.* 136, 15596–15606. <https://doi.org/10.1021/ja507146s>
- Riva, M., Rantala, P., Krechmer, J.E., Peräkylä, O., Zhang, Y., Heikkinen, L., Garmash, O., Yan, C., Kulmala, M., Worsnop, D., Ehn, M., 2019. Evaluating the performance of five different chemical ionization techniques for detecting gaseous oxygenated organic species. *Atmos. Meas. Tech.* 12, 2403–2421. <https://doi.org/10.5194/amt-12-2403-2019>
- Roberts, J.M., 1990. The atmospheric chemistry of organic nitrates. *Atmospheric Environment. Part A. General Topics* 24, 243–287. [https://doi.org/10.1016/0960-1686\(90\)90108-Y](https://doi.org/10.1016/0960-1686(90)90108-Y)
- Roser, M., Ritchie, H., Ortiz-Ospina, E., 2013. World Population Growth. *Our World in Data*.
- Ryerson, T.B., Andrews, A.E., Angevine, W.M., Bates, T.S., Brock, C.A., Cairns, B., Cohen, R.C., Cooper, O.R., Gouw, J.A. de, Fehsenfeld, F.C., Ferrare, R.A., Fischer, M.L., Flagan, R.C., Goldstein, A.H., Hair, J.W., Hardesty, R.M., Hostetler, C.A., Jimenez, J.L., Langford, A.O., McCauley, E., McKeen, S.A., Molina, L.T., Nenes, A., Oltmans, S.J., Parrish, D.D., Pederson, J.R., Pierce, R.B., Prather, K., Quinn, P.K., Seinfeld, J.H., Senff, C.J., Sorooshian, A., Stutz, J., Surratt, J.D., Trainer, M., Volkamer, R., Williams, E.J., Wofsy, S.C., 2013. The 2010 California Research at the Nexus of Air Quality and Climate Change (CalNex) field study. *Journal of Geophysical Research: Atmospheres* 118, 5830–5866. <https://doi.org/10.1002/jgrd.50331>
- Ryerson, T.B., Trainer, M., Angevine, W.M., Brock, C.A., Dissly, R.W., Fehsenfeld, F.C., Frost, G.J., Goldan, P.D., Holloway, J.S., Hübler, G., Jakoubek, R.O., Kuster, W.C., Neuman, J.A., Nicks Jr., D.K., Parrish, D.D., Roberts, J.M., Sueper, D.T., Atlas, E.L., Donnelly, S.G., Flocke, F., Fried, A., Potter, W.T., Schauffler, S., Stroud, V., Weinheimer, A.J., Wert, B.P., Wiedinmyer, C., Alvarez, R.J., Banta, R.M., Darby, L.S., Senff, C.J., 2003. Effect of petrochemical industrial emissions of reactive alkenes and NO_x on tropospheric ozone formation in Houston, Texas. *Journal of Geophysical Research: Atmospheres* 108. <https://doi.org/10.1029/2002JD003070>
- Sarrafzadeh, M., Wildt, J., Pullinen, I., Springer, M., Kleist, E., Tillmann, R., Schmitt, S.H., Wu, C., Mentel, T.F., Zhao, D., Hastie, D.R., Kiendler-Scharr, A., 2016. Impact of NO_x and OH

- on secondary organic aerosol formation from β -pinene photooxidation. *Atmospheric Chemistry and Physics* 16, 11237–11248. <https://doi.org/10.5194/acp-16-11237-2016>
- Saunders, S.M., Jenkin, M.E., Derwent, R.G., Pilling, M.J., 2003. Protocol for the development of the Master Chemical Mechanism, MCM v3 (Part A): tropospheric degradation of non-aromatic volatile organic compounds. *Atmospheric Chemistry and Physics* 3, 161–180. <https://doi.org/10.5194/acp-3-161-2003>
- Schervish, M., Donahue, N.M., 2020. Peroxy radical chemistry and the volatility basis set. *Atmospheric Chemistry and Physics* 20, 1183–1199. <https://doi.org/10.5194/acp-20-1183-2020>
- Schobesberger, S., Junninen, H., Bianchi, F., Lönn, G., Ehn, M., Lehtipalo, K., Dommen, J., Ehrhart, S., Ortega, I.K., Franchin, A., Nieminen, T., Riccobono, F., Hutterli, M., Duplissy, J., Almeida, J., Amorim, A., Breitenlechner, M., Downard, A.J., Dunne, E.M., Flagan, R.C., Kajos, M., Keskinen, H., Kirkby, J., Kupc, A., Kürten, A., Kurtén, T., Laaksonen, A., Mathot, S., Onnela, A., Praplan, A.P., Rondo, L., Santos, F.D., Schallhart, S., Schnitzhofer, R., Sipilä, M., Tomé, A., Tsagkogeorgas, G., Vehkamäki, H., Wimmer, D., Baltensperger, U., Carslaw, K.S., Curtius, J., Hansel, A., Petäjä, T., Kulmala, M., Donahue, N.M., Worsnop, D.R., 2013. Molecular understanding of atmospheric particle formation from sulfuric acid and large oxidized organic molecules. *Proc Natl Acad Sci U S A* 110, 17223–17228. <https://doi.org/10.1073/pnas.1306973110>
- Seco, R., Peñuelas, J., Filella, I., 2007. Short-chain oxygenated VOCs: Emission and uptake by plants and atmospheric sources, sinks, and concentrations. *Atmospheric Environment* 41, 2477–2499. <https://doi.org/10.1016/j.atmosenv.2006.11.029>
- Seinfeld, John H, Pandis, S.N., 2016. *Atmospheric Chemistry and Physics: From Air Pollution to Climate Change*, 3rd ed, Third edition. John Wiley & Sons, Inc., Hoboken, New Jersey.
- Sharkey, T.D., Wiberley, A.E., Donohue, A.R., 2008. Isoprene Emission from Plants: Why and How. *Ann Bot* 101, 5–18. <https://doi.org/10.1093/aob/mcm240>
- Shen, H., Vereecken, L., Kang, S., Pullinen, I., Fuchs, H., Zhao, D., Mentel, T.F., 2022. Unexpected significance of a minor reaction pathway in daytime formation of biogenic highly oxygenated organic compounds. *Science Advances* 8, eabp8702. <https://doi.org/10.1126/sciadv.abp8702>
- Shen, H., Zhao, D., Pullinen, I., Kang, S., Vereecken, L., Fuchs, H., Acir, I.-H., Tillmann, R., Rohrer, F., Wildt, J., Kiendler-Scharr, A., Wahner, A., Mentel, T.F., 2021. Highly Oxygenated Organic Nitrates Formed from NO₃ Radical-Initiated Oxidation of β -Pinene. *Environ. Sci. Technol.* 55, 15658–15671. <https://doi.org/10.1021/acs.est.1c03978>
- Shilling, J.E., Zaveri, R.A., Fast, J.D., Kleinman, L., Alexander, M.L., Canagaratna, M.R., Fortner, E., Hubbe, J.M., Jayne, J.T., Sedlacek, A., Setyan, A., Springston, S., Worsnop, D.R., Zhang, Q., 2013. Enhanced SOA formation from mixed anthropogenic and biogenic emissions during the CARES campaign. *Atmospheric Chemistry and Physics* 13, 2091–2113. <https://doi.org/10.5194/acp-13-2091-2013>
- Shrivastava, M., Andreae, M.O., Artaxo, P., Barbosa, H.M.J., Berg, L.K., Brito, J., Ching, J., Easter, R.C., Fan, J., Fast, J.D., Feng, Z., Fuentes, J.D., Glasius, M., Goldstein, A.H., Alves, E.G., Gomes, H., Gu, D., Guenther, A., Jathar, S.H., Kim, S., Liu, Y., Lou, S., Martin, S.T., McNeill, V.F., Medeiros, A., de Sá, S.S., Shilling, J.E., Springston, S.R., Souza, R. a. F., Thornton, J.A., Isaacman-VanWertz, G., Yee, L.D., Ynoue, R., Zaveri, R.A., Zelenyuk, A., Zhao, C., 2019. Urban pollution greatly enhances formation of natural aerosols over the Amazon rainforest. *Nat Commun* 10, 1046. <https://doi.org/10.1038/s41467-019-08909-4>
- Silva, M.D.M.C.R. da, Silva, M.A.V.R. da, Pilcher, G., 1986. Enthalpies of combustion of the three trihydroxybenzenes and of 3-methoxycatechol and 4-nitrocatechol. *The Journal of Chemical Thermodynamics* 18, 295–300. [https://doi.org/10.1016/0021-9614\(86\)90058-3](https://doi.org/10.1016/0021-9614(86)90058-3)

- Sindelarova, K., Granier, C., Bouarar, I., Guenther, A., Tilmes, S., Stavrakou, T., Müller, J.-F., Kuhn, U., Stefani, P., Knorr, W., 2014. Global data set of biogenic VOC emissions calculated by the MEGAN model over the last 30 years. *Atmospheric Chemistry and Physics* 14, 9317–9341. <https://doi.org/10.5194/acp-14-9317-2014>
- Sindelarova, K., Markova, J., Simpson, D., Huszar, P., Karlicky, J., Darras, S., Granier, C., 2022. High-resolution biogenic global emission inventory for the time period 2000–2019 for air quality modelling. *Earth System Science Data* 14, 251–270. <https://doi.org/10.5194/essd-14-251-2022>
- Skelly, J.M., 2000. Tropospheric Ozone and Its Importance to Forests and Natural Plant Communities of the Northeastern United States. *Northeastern Naturalist* 7, 221–236.
- Smith, J., McMurry, P., 2015. New Particle Formation Study Final Campaign Report 15.
- Sofowote, U.M., Su, Y., Dabek-Zlotorzynska, E., Rastogi, A.K., Brook, J., Hopke, P.K., 2015. Sources and temporal variations of constrained PMF factors obtained from multiple-year receptor modeling of ambient PM_{2.5} data from five speciation sites in Ontario, Canada. *Atmospheric Environment* 108, 140–150. <https://doi.org/10.1016/j.atmosenv.2015.02.055>
- Spicer, C.W., Villa, Alberto., Wiebe, H.A., Heicklen, Julian., 1973. Reactions of methylperoxy radicals with nitric oxide and nitrogen dioxide. *J. Am. Chem. Soc.* 95, 13–20. <https://doi.org/10.1021/ja00782a003>
- Stark, H., Yatavelli, R.L.N., Thompson, S.L., Kimmel, J.R., Cubison, M.J., Chhabra, P.S., Canagaratna, M.R., Jayne, J.T., Worsnop, D.R., Jimenez, J.L., 2015. Methods to extract molecular and bulk chemical information from series of complex mass spectra with limited mass resolution. *International Journal of Mass Spectrometry* 389, 26–38. <https://doi.org/10.1016/j.ijms.2015.08.011>
- Stavrakou, T., Guenther, A., Razavi, A., Clarisse, L., Clerbaux, C., Coheur, P.-F., Hurtmans, D., Karagulian, F., De Mazière, M., Vigouroux, C., Amelynck, C., Schoon, N., Laffineur, Q., Heinesch, B., Aubinet, M., Rinsland, C., Müller, J.-F., 2011. First space-based derivation of the global atmospheric methanol emission fluxes. *Atmospheric Chemistry and Physics* 11, 4873–4898. <https://doi.org/10.5194/acp-11-4873-2011>
- Stein, A.F., Draxler, R.R., Rolph, G.D., Stunder, B.J.B., Cohen, M.D., Ngan, F., 2015. NOAA's HYSPLIT Atmospheric Transport and Dispersion Modeling System. *Bulletin of the American Meteorological Society* 96, 2059–2077. <https://doi.org/10.1175/BAMS-D-14-00110.1>
- Steiner, A.H., Goldstein, A.L., 2007. Biogenic VOCs, in: *Volatile Organic Compounds in the Atmosphere*. John Wiley & Sons, Ltd, pp. 82–128. <https://doi.org/10.1002/9780470988657.ch3>
- Steiner, A.L., Pressley, S.N., Botros, A., Jones, E., Chung, S.H., Edburg, S.L., 2011. Analysis of coherent structures and atmosphere-canopy coupling strength during the CABINEX field campaign. *Atmospheric Chemistry and Physics* 11, 11921–11936. <https://doi.org/10.5194/acp-11-11921-2011>
- Stolzenburg, D., Fischer, L., Vogel, A.L., Heinritzi, M., Schervish, M., Simon, M., Wagner, A.C., Dada, L., Ahonen, L.R., Amorim, A., Baccarini, A., Bauer, P.S., Baumgartner, B., Bergen, A., Bianchi, F., Breitenlechner, M., Brilke, S., Mazon, S.B., Chen, D., Dias, A., Draper, D.C., Duplissy, J., Haddad, I.E., Finkenzeller, H., Frege, C., Fuchs, C., Garmash, O., Gordon, H., He, X., Helm, J., Hofbauer, V., Hoyle, C.R., Kim, C., Kirkby, J., Kontkanen, J., Kürten, A., Lampilahti, J., Lawler, M., Lehtipalo, K., Leiminger, M., Mai, H., Mathot, S., Mentler, B., Molteni, U., Nie, W., Nieminen, T., Nowak, J.B., Ojdanic, A., Onnela, A., Passananti, M., Petäjä, T., Quéléver, L.L.J., Rissanen, M.P., Sarnela, N., Schallhart, S., Tauber, C., Tomé, A., Wagner, R., Wang, M., Weitz, L., Wimmer, D., Xiao, M., Yan, C., Ye, P., Zha, Q., Baltensperger, U., Curtius, J., Dommen, J., Flagan, R.C., Kulmala, M.,

- Smith, J.N., Worsnop, D.R., Hansel, A., Donahue, N.M., Winkler, P.M., 2018. Rapid growth of organic aerosol nanoparticles over a wide tropospheric temperature range. *Proceedings of the National Academy of Sciences* 115, 9122–9127. <https://doi.org/10.1073/pnas.1807604115>
- Stone, D., Whalley, L.K., Heard, D.E., 2012. Tropospheric OH and HO₂ radicals: field measurements and model comparisons. *Chem. Soc. Rev.* 41, 6348–6404. <https://doi.org/10.1039/C2CS35140D>
- Stroud, C., Makar, P., Karl, T., Guenther, A., Geron, C., Turnipseed, A., Nemitz, E., Baker, B., Potosnak, M., Fuentes, J.D., 2005. Role of canopy-scale photochemistry in modifying biogenic-atmosphere exchange of reactive terpene species: Results from the CELTIC field study. *Journal of Geophysical Research: Atmospheres* 110. <https://doi.org/10.1029/2005JD005775>
- Stull, R.B., 1988. *An Introduction to Boundary Layer Meteorology*. Springer Science & Business Media.
- Stutz, J., Alicke, B., Ackermann, R., Geyer, A., White, A., Williams, E., 2004. Vertical profiles of NO₃, N₂O₅, O₃, and NO_x in the nocturnal boundary layer: 1. Observations during the Texas Air Quality Study 2000. *Journal of Geophysical Research: Atmospheres* 109. <https://doi.org/10.1029/2003JD004209>
- Stutz, J., Wong, K.W., Lawrence, L., Ziemba, L., Flynn, J.H., Rappenglück, B., Lefer, B., 2010. Nocturnal NO₃ radical chemistry in Houston, TX. *Atmospheric Environment* 44, 4099–4106. <https://doi.org/10.1016/j.atmosenv.2009.03.004>
- Taatjes, C.A., 2006. Uncovering the Fundamental Chemistry of Alkyl + O₂ Reactions via Measurements of Product Formation. *J. Phys. Chem. A* 110, 4299–4312. <https://doi.org/10.1021/jp056997f>
- Timonen, H., Cubison, M., Aurela, M., Brus, D., Lihavainen, H., Hillamo, R., Canagaratna, M., Nekat, B., Weller, R., Worsnop, D., Saarikoski, S., 2016. Applications and limitations of constrained high-resolution peak fitting on low resolving power mass spectra from the ToF-ACSM. *Atmospheric Measurement Techniques* 9, 3263–3281. <https://doi.org/10.5194/amt-9-3263-2016>
- Tingey, D.T., Evans, R., Gumpertz, M., 1981. Effects of environmental conditions on isoprene emission from live oak. *Planta* 152, 565–570. <https://doi.org/10.1007/BF00380829>
- Tingey, D.T., Evans, R.C., Bates, E.H., Gumpertz, M.L., 1987. Isoprene emissions and photosynthesis in three ferns – The influence of light and temperature. *Physiologia Plantarum* 69, 609–616. <https://doi.org/10.1111/j.1399-3054.1987.tb01974.x>
- Tofwerk, A., 2016. *Getting Started Guide TOF-CIMS Instrument*.
- Tomaz, S., Wang, D., Zabalegui, N., Li, D., Lamkaddam, H., Bachmeier, F., Vogel, A., Monge, M.E., Perrier, S., Baltensperger, U., George, C., Rissanen, M., Ehn, M., El Haddad, I., Riva, M., 2021. Structures and reactivity of peroxy radicals and dimeric products revealed by online tandem mass spectrometry. *Nature Communications* 12, 300. <https://doi.org/10.1038/s41467-020-20532-2>
- Topol, I.A., Tawa, G.J., Caldwell, R.A., Eissenstat, M.A., Burt, S.K., 2000. Acidity of Organic Molecules in the Gas Phase and in Aqueous Solvent. *J. Phys. Chem. A* 104, 9619–9624. <https://doi.org/10.1021/jp001938h>
- Tröstl, J., Chuang, W.K., Gordon, H., Heinritzi, M., Yan, C., Molteni, U., Ahlm, L., Frege, C., Bianchi, F., Wagner, R., Simon, M., Lehtipalo, K., Williamson, C., Craven, J.S., Duplissy, J., Adamov, A., Almeida, J., Bernhammer, A.-K., Breitenlechner, M., Brilke, S., Dias, A., Ehrhart, S., Flagan, R.C., Franchin, A., Fuchs, C., Guida, R., Gysel, M., Hansel, A., Hoyle, C.R., Jokinen, T., Junninen, H., Kangasluoma, J., Keskinen, H., Kim, J., Krapf, M., Kürten, A., Laaksonen, A., Lawler, M., Leiminger, M., Mathot, S., Möhler, O., Nieminen, T.,

- Onnela, A., Petäjä, T., Piel, F.M., Miettinen, P., Rissanen, M.P., Rondo, L., Sarnela, N., Schobesberger, S., Sengupta, K., Sipilä, M., Smith, J.N., Steiner, G., Tomè, A., Virtanen, A., Wagner, A.C., Weingartner, E., Wimmer, D., Winkler, P.M., Ye, P., Carslaw, K.S., Curtius, J., Dommen, J., Kirkby, J., Kulmala, M., Riipinen, I., Worsnop, D.R., Donahue, N.M., Baltensperger, U., 2016. The role of low-volatility organic compounds in initial particle growth in the atmosphere. *Nature* 533, 527–531. <https://doi.org/10.1038/nature18271>
- Tsiligiannis, E., Hammes, J., Salvador, C.M., Mentel, T.F., Hallquist, M., 2019. Effect of NO_x on 1,3,5-trimethylbenzene (TMB) oxidation product distribution and particle formation. *Atmospheric Chemistry and Physics* 19, 15073–15086. <https://doi.org/10.5194/acp-19-15073-2019>
- UCAR, C. for S.E., 2015. Layers of Earth's Atmosphere [WWW Document]. URL <https://scied.ucar.edu/atmosphere-layers> (accessed 9.30.20).
- UNCTAD, 2022. Total and urban population. Handbook of Statistics 2022. URL <https://hbs.unctad.org/total-and-urban-population/> (accessed 3.3.23).
- US EPA, 1990. Air Emissions Species Manual Volume I: Volatile Organic Compound Species Profiles [WWW Document]. URL <https://nepis.epa.gov/Exe/ZyPDF.cgi/00001VFS.PDF?Dockey=00001VFS.PDF> (accessed 11.18.22).
- Vallat, A., Gu, H., Dorn, S., 2005. How rainfall, relative humidity and temperature influence volatile emissions from apple trees in situ. *Phytochemistry* 66, 1540–1550. <https://doi.org/10.1016/j.phytochem.2005.04.038>
- Velikova, V., Pinelli, P., Pasqualini, S., Reale, L., Ferranti, F., Loreto, F., 2005. Isoprene decreases the concentration of nitric oxide in leaves exposed to elevated ozone. *New Phytologist* 166, 419–426. <https://doi.org/10.1111/j.1469-8137.2005.01409.x>
- Venkat Ratnam, M., Patra, A.K., Krishna Murthy, B.V., 2010. Tropical mesopause: Is it always close to 100 km? *Journal of Geophysical Research: Atmospheres* 115. <https://doi.org/10.1029/2009JD012531>
- Vereecken, L., Francisco, J.S., 2012. Theoretical studies of atmospheric reaction mechanisms in the troposphere. *Chem. Soc. Rev.* 41, 6259–6293. <https://doi.org/10.1039/C2CS35070J>
- Vereecken, L., Nozière, B., 2020. H migration in peroxy radicals under atmospheric conditions. *Atmospheric Chemistry and Physics* 20, 7429–7458. <https://doi.org/10.5194/acp-20-7429-2020>
- Vestenius, M., Hellén, H., Levula, J., Kuronen, P., Helminen, K.J., Nieminen, T., Kulmala, M., Hakola, H., 2014. Acidic reaction products of monoterpenes and sesquiterpenes in atmospheric fine particles in a boreal forest. *Atmospheric Chemistry and Physics* 14, 7883–7893. <https://doi.org/10.5194/acp-14-7883-2014>
- Vickers, C., Gershenson, J., Lerdau, M., Loreto, F., 2009. A unified mechanism of action for volatile isoprenoids in plant abiotic stress. *Nature chemical biology* 5, 283–91. <https://doi.org/10.1038/nchembio.158>
- Vickers, C.E., Bongers, M., Liu, Q., Delatte, T., Bouwmeester, H., 2014. Metabolic engineering of volatile isoprenoids in plants and microbes. *Plant, Cell & Environment* 37, 1753–1775. <https://doi.org/10.1111/pce.12316>
- Villanueva-Fierro, I., Popp, C.J., Martin, R.S., 2004. Biogenic emissions and ambient concentrations of hydrocarbons, carbonyl compounds and organic acids from ponderosa pine and cottonwood trees at rural and forested sites in Central New Mexico. *Atmospheric Environment* 38, 249–260. <https://doi.org/10.1016/j.atmosenv.2003.09.051>
- Vivone, G., D'Amico, G., Summa, D., Lolli, S., Amodeo, A., Bortoli, D., Pappalardo, G., 2021. Atmospheric boundary layer height estimation from aerosol lidar: a new approach based on

- morphological image processing techniques. *Atmos. Chem. Phys.* 21, 4249–4265. <https://doi.org/10.5194/acp-21-4249-2021>
- Voliotis, A., Du, M., Wang, Y., Shao, Y., Alfarra, M.R., Bannan, T.J., Hu, D., Pereira, K.L., Hamilton, J.F., Hallquist, M., Mentel, T.F., McFiggans, G., 2022. Chamber investigation of the formation and transformation of secondary organic aerosol in mixtures of biogenic and anthropogenic volatile organic compounds. *Atmospheric Chemistry and Physics* 22, 14147–14175. <https://doi.org/10.5194/acp-22-14147-2022>
- Wallace, J.M., Hobbs, P.V., 2006. *Atmospheric Science: An Introductory Survey*. Elsevier.
- Wang, J., Doussin, J.F., Perrier, S., Perraudin, E., Katrib, Y., Pangui, E., Picquet-Varrault, B., 2011. Design of a new multi-phase experimental simulation chamber for atmospheric photo-smog, aerosol and cloud chemistry research. *Atmospheric Measurement Techniques* 4, 2465–2494. <https://doi.org/10.5194/amt-4-2465-2011>
- Wang, Lingyu, Liu, Y., Wang, Liming, 2019. Ozonolysis of 3-carene in the atmosphere. Formation mechanism of hydroxyl radical and secondary ozonides. *Phys. Chem. Chem. Phys.* 21, 8081–8091. <https://doi.org/10.1039/C8CP07195K>
- Wang, M., Chen, D., Xiao, M., Ye, Q., Stolzenburg, D., Hofbauer, V., Ye, P., Vogel, A.L., Mauldin, R.L.I., Amorim, A., Baccarini, A., Baumgartner, B., Brilke, S., Dada, L., Dias, A., Duplissy, J., Finkenzeller, H., Garmash, O., He, X.-C., Hoyle, C.R., Kim, C., Kvashnin, A., Lehtipalo, K., Fischer, L., Molteni, U., Petäjä, T., Pospisilova, V., Quéléver, L.L.J., Rissanen, M., Simon, M., Tauber, C., Tomé, A., Wagner, A.C., Weitz, L., Volkamer, R., Winkler, P.M., Kirkby, J., Worsnop, D.R., Kulmala, M., Baltensperger, U., Dommen, J., El-Haddad, I., Donahue, N.M., 2020. Photo-oxidation of Aromatic Hydrocarbons Produces Low-Volatility Organic Compounds. *Environ. Sci. Technol.* 54, 7911–7921. <https://doi.org/10.1021/acs.est.0c02100>
- Wang, S., Wu, R., Berndt, T., Ehn, M., Wang, L., 2017. Formation of Highly Oxidized Radicals and Multifunctional Products from the Atmospheric Oxidation of Alkylbenzenes. *Environ. Sci. Technol.* 51, 8442–8449. <https://doi.org/10.1021/acs.est.7b02374>
- Wang, S., Zhang, Q., Wang, G., Wei, Y., Wang, W., Wang, Q., 2023. The neglected autoxidation pathways for the formation of highly oxygenated organic molecules (HOMs) and the nucleation of the HOMs generated by limonene. *Atmospheric Environment* 304, 119727. <https://doi.org/10.1016/j.atmosenv.2023.119727>
- Wang, T., Nie, W., Gao, J., Xue, L.K., Gao, X.M., Wang, X.F., Qiu, J., Poon, C.N., Meinardi, S., Blake, D., Wang, S.L., Ding, A.J., Chai, F.H., Zhang, Q.Z., Wang, W.X., 2010. Air quality during the 2008 Beijing Olympics: secondary pollutants and regional impact. *Atmos. Chem. Phys.* 10, 7603–7615. <https://doi.org/10.5194/acp-10-7603-2010>
- Wang, Y., Jacob, D.J., Logan, J.A., 1998. Global simulation of tropospheric O₃-NO_x-hydrocarbon chemistry: 3. Origin of tropospheric ozone and effects of nonmethane hydrocarbons. *Journal of Geophysical Research: Atmospheres* 103, 10757–10767. <https://doi.org/10.1029/98JD00156>
- Wang, Y., Riva, M., Xie, H., Heikkinen, L., Schallhart, S., Zha, Q., Yan, C., He, X.C., Peräkylä, O., Ehn, M., 2020. Formation of Highly Oxygenated Organic Molecules from Chlorine-Atom-Initiated Oxidation of Alpha-Pinene. *Atmos. Chem. Phys.* 20, 5145.
- Wang, Yonghong, Clusius, P., Yan, C., Dällenbach, K., Yin, R., Wang, M., He, X.-C., Chu, B., Lu, Y., Dada, L., Kangasluoma, J., Rantala, P., Deng, C., Lin, Z., Wang, W., Yao, L., Fan, X., Du, W., Cai, J., Heikkinen, L., Tham, Y.J., Zha, Q., Ling, Z., Junninen, H., Petäjä, T., Ge, M., Wang, Yuesi, He, H., Worsnop, D.R., Kerminen, V.-M., Bianchi, F., Wang, L., Jiang, J., Liu, Y., Boy, M., Ehn, M., Donahue, N.M., Kulmala, M., 2022. Molecular Composition of Oxygenated Organic Molecules and Their Contributions to Organic

- Aerosol in Beijing. *Environ. Sci. Technol.* 56, 770–778. <https://doi.org/10.1021/acs.est.1c05191>
- Wang, Z., Ehn, M., Rissanen, M.P., Garmash, O., Quéléver, L., Xing, L., Monge-Palacios, M., Rantala, P., Donahue, N.M., Berndt, T., Sarathy, S.M., 2021. Efficient alkane oxidation under combustion engine and atmospheric conditions. *Commun Chem* 4, 1–8. <https://doi.org/10.1038/s42004-020-00445-3>
- Wayne, R.P., Barnes, I., Biggs, P., Burrows, J.P., Canosa-Mas, C.E., Hjorth, J., Bras, G.L., Moortgat, G.K., Perner, D., Poulet, G., Restelli, G., Sidebottom, H., 1991. The nitrate radical: Physics, chemistry, and the atmosphere. *Atmospheric Environment. Part A. General Topics* 25, 1–203. [https://doi.org/10.1016/0960-1686\(91\)90192-A](https://doi.org/10.1016/0960-1686(91)90192-A)
- Weber, R.J., Sullivan, A.P., Peltier, R.E., Russell, A., Yan, B., Zheng, M., de Gouw, J., Warneke, C., Brock, C., Holloway, J.S., Atlas, E.L., Edgerton, E., 2007. A study of secondary organic aerosol formation in the anthropogenic-influenced southeastern United States. *Journal of Geophysical Research: Atmospheres* 112. <https://doi.org/10.1029/2007JD008408>
- Williams, J., Crowley, J., Fischer, H., Harder, H., Martinez, M., Petäjä, T., Rinne, J., Bäck, J., Boy, M., Dal Maso, M., Hakala, J., Kajos, M., Keronen, P., Rantala, P., Aalto, J., Aaltonen, H., Paatero, J., Vesala, T., Hakola, H., Levula, J., Pohja, T., Herrmann, F., Auld, J., Mesarchaki, E., Song, W., Yassaa, N., Nölscher, A., Johnson, A.M., Custer, T., Sinha, V., Thieser, J., Pouvesle, N., Taraborrelli, D., Tang, M.J., Bozem, H., Hosaynali-Beygi, Z., Axinte, R., Oswald, R., Novelli, A., Kubistin, D., Hens, K., Javed, U., Trawny, K., Breitenberger, C., Hidalgo, P.J., Ebben, C.J., Geiger, F.M., Corrigan, A.L., Russell, L.M., Ouwersloot, H.G., Vilà-Guerau de Arellano, J., Ganzeveld, L., Vogel, A., Beck, M., Bayerle, A., Kampf, C.J., Bertelmann, M., Köllner, F., Hoffmann, T., Valverde, J., González, D., Riekkola, M.-L., Kulmala, M., Lelieveld, J., 2011. The summertime Boreal forest field measurement intensive (HUMPPA-COPEC-2010): an overview of meteorological and chemical influences. *Atmospheric Chemistry and Physics* 11, 10599–10618. <https://doi.org/10.5194/acp-11-10599-2011>
- Wit, H., Bouwstra, J., Blok, J., De Kruif, C.G. (Kees), 1983. Vapor pressures and lattice energies of oxalic acid, mesotartaric acid, phloroglucinol, myoinositol, and their hydrates. *The Journal of Chemical Physics* 78, 1470–1475. <https://doi.org/10.1063/1.444836>
- Wolfe, G.M., Kaiser, J., Hanisco, T.F., Keutsch, F.N., de Gouw, J.A., Gilman, J.B., Graus, M., Hatch, C.D., Holloway, J., Horowitz, L.W., Lee, B.H., Lerner, B.M., Lopez-Hilifiker, F., Mao, J., Marvin, M.R., Peischl, J., Pollack, I.B., Roberts, J.M., Ryerson, T.B., Thornton, J.A., Veres, P.R., Warneke, C., 2016. Formaldehyde production from isoprene oxidation across NO_x regimes. *Atmospheric Chemistry and Physics* 16, 2597–2610. <https://doi.org/10.5194/acp-16-2597-2016>
- Wolfe, G.M., Thornton, J.A., Bouvier-Brown, N.C., Goldstein, A.H., Park, J.-H., McKay, M., Matross, D.M., Mao, J., Brune, W.H., LaFranchi, B.W., Browne, E.C., Min, K.-E., Wooldridge, P.J., Cohen, R.C., Crouse, J.D., Faloona, I.C., Gilman, J.B., Kuster, W.C., de Gouw, J.A., Huisman, A., Keutsch, F.N., 2011. The Chemistry of Atmosphere-Forest Exchange (CAFE) Model – Part 2: Application to BEARPEX-2007 observations. *Atmospheric Chemistry and Physics* 11, 1269–1294. <https://doi.org/10.5194/acp-11-1269-2011>
- World Health Organization (WHO), 2020. Air pollution [WWW Document]. URL <https://www.who.int/westernpacific/health-topics/air-pollution> (accessed 4.17.20).
- World Population Review, 2023. Paris Population 2023 [WWW Document]. URL <https://worldpopulationreview.com/world-cities/paris-population> (accessed 3.6.23).
- Wu, R., Vereecken, L., Tsiligiannis, E., Kang, S., Albrecht, S.R., Hantschke, L., Zhao, D., Novelli, A., Fuchs, H., Tillmann, R., Hohaus, T., Carlsson, P.T.M., Shenolikar, J., Bernard, F.,

- Crowley, J.N., Fry, J.L., Brownwood, B., Thornton, J.A., Brown, S.S., Kiendler-Scharr, A., Wahner, A., Hallquist, M., Mentel, T.F., 2021. Molecular composition and volatility of multi-generation products formed from isoprene oxidation by nitrate radical. *Atmospheric Chemistry and Physics* 21, 10799–10824. <https://doi.org/10.5194/acp-21-10799-2021>
- Xu, L., Guo, H., Boyd, C.M., Klein, M., Bougiatioti, A., Cerully, K.M., Hite, J.R., Isaacman-VanWertz, G., Kreisberg, N.M., Knote, C., Olson, K., Koss, A., Goldstein, A.H., Hering, S.V., de Gouw, J., Baumann, K., Lee, S.-H., Nenes, A., Weber, R.J., Ng, N.L., 2015. Effects of anthropogenic emissions on aerosol formation from isoprene and monoterpenes in the southeastern United States. *Proc. Natl. Acad. Sci. U.S.A.* 112, 37–42. <https://doi.org/10.1073/pnas.1417609112>
- Xu, L., Kollman, M.S., Song, C., Shilling, J.E., Ng, N.L., 2014. Effects of NO_x on the Volatility of Secondary Organic Aerosol from Isoprene Photooxidation. *Environ. Sci. Technol.* 48, 2253–2262. <https://doi.org/10.1021/es404842g>
- Xu, Z.N., Nie, W., Liu, Y.L., Sun, P., Huang, D.D., Yan, C., Krechmer, J., Ye, P.L., Xu, Z., Qi, X.M., Zhu, C.J., Li, Y.Y., Wang, T.Y., Wang, L., Huang, X., Tang, R.Z., Guo, S., Xiu, G.L., Fu, Q.Y., Worsnop, D., Chi, X.G., Ding, A.J., 2021. Multifunctional Products of Isoprene Oxidation in Polluted Atmosphere and Their Contribution to SOA. *Geophysical Research Letters* 48, e2020GL089276. <https://doi.org/10.1029/2020GL089276>
- Yan, C., Nie, W., Äijälä, M., Rissanen, M.P., Canagaratna, M.R., Massoli, P., Junninen, H., Jokinen, T., Sarnela, N., Häme, S.A.K., Schobesberger, S., Canonaco, F., Yao, L., Prévôt, A.S.H., Petäjä, T., Kulmala, M., Sipilä, M., Worsnop, D.R., Ehn, M., 2016. Source characterization of highly oxidized multifunctional compounds in a boreal forest environment using positive matrix factorization. *Atmospheric Chemistry and Physics* 16, 12715–12731. <https://doi.org/10.5194/acp-16-12715-2016>
- Yatavelli, R.L.N., Stark, H., Thompson, S.L., Kimmel, J.R., Cubison, M.J., Day, D.A., Campuzano-Jost, P., Palm, B.B., Hodzic, A., Thornton, J.A., Jayne, J.T., Worsnop, D.R., Jimenez, J.L., 2014. Semicontinuous measurements of gas–particle partitioning of organic acids in a ponderosa pine forest using a MOVI-HRTof-CIMS. *Atmospheric Chemistry and Physics* 14, 1527–1546. <https://doi.org/10.5194/acp-14-1527-2014>
- Ye, C., Yuan, B., Lin, Y., Wang, Z., Hu, W., Li, T., Chen, W., Wu, C., Wang, C., Huang, S., Qi, J., Wang, B., Wang, C., Song, W., Wang, X., Zheng, E., Krechmer, J.E., Ye, P., Zhang, Z., Wang, X., Worsnop, D.R., Shao, M., 2021. Chemical characterization of oxygenated organic compounds in the gas phase and particle phase using iodide CIMS with FIGAERO in urban air. *Atmospheric Chemistry and Physics* 21, 8455–8478. <https://doi.org/10.5194/acp-21-8455-2021>
- Yi, H., Cazaunau, M., Gratien, A., Michoud, V., Pangui, E., Doussin, J.-F., Chen, W., 2021. Intercomparison of IBBCEAS, NitroMAC and FTIR analyses for HONO, NO₂ and CH₂O measurements during the reaction of NO₂ with H₂O vapour in the simulation chamber CESAM. *Atmospheric Measurement Techniques* 14, 5701–5715. <https://doi.org/10.5194/amt-14-5701-2021>
- Youssefi, S., Waring, M.S., 2014. Transient Secondary Organic Aerosol Formation from Limonene Ozonolysis in Indoor Environments: Impacts of Air Exchange Rates and Initial Concentration Ratios. *Environ. Sci. Technol.* 48, 7899–7908. <https://doi.org/10.1021/es5009906>
- Yuan, B., Koss, A., Warneke, C., Gilman, J.B., Lerner, B.M., Stark, H., de Gouw, J.A., 2016. A high-resolution time-of-flight chemical ionization mass spectrometer utilizing hydronium ions (H₃O⁺ ToF-CIMS) for measurements of volatile organic compounds in the atmosphere. *Atmospheric Measurement Techniques* 9, 2735–2752. <https://doi.org/10.5194/amt-9-2735-2016>

- Yuan, B., Liggió, J., Wentzell, J., Li, S.-M., Stark, H., Roberts, J.M., Gilman, J., Lerner, B., Warneke, C., Li, R., Leithead, A., Osthoff, H.D., Wild, R., Brown, S.S., de Gouw, J.A., 2015. Secondary formation of nitrated phenols: insights from observations during the Uintah Basin Winter Ozone Study (UBWOS) 2014 (preprint). *Gases/Field Measurements/Troposphere/Chemistry* (chemical composition and reactions). <https://doi.org/10.5194/acpd-15-28659-2015>
- Zaveri, R.A., Shaw, W.J., Cziczo, D.J., Schmid, B., Ferrare, R.A., Alexander, M.L., Alexandrov, M., Alvarez, R.J., Arnott, W.P., Atkinson, D.B., Baidar, S., Banta, R.M., Barnard, J.C., Beranek, J., Berg, L.K., Brechtel, F., Brewer, W.A., Cahill, J.F., Cairns, B., Cappa, C.D., Chand, D., China, S., Comstock, J.M., Dubey, M.K., Easter, R.C., Erickson, M.H., Fast, J.D., Floerchinger, C., Flowers, B.A., Fortner, E., Gaffney, J.S., Gilles, M.K., Gorkowski, K., Gustafson, W.I., Gyawali, M., Hair, J., Hardesty, R.M., Harworth, J.W., Herndon, S., Hiranuma, N., Hostetler, C., Hubbe, J.M., Jayne, J.T., Jeong, H., Jobson, B.T., Kassianov, E.I., Kleinman, L.I., Kluzek, C., Knighton, B., Kolesar, K.R., Kuang, C., Kubátová, A., Langford, A.O., Laskin, A., Laulainen, N., Marchbanks, R.D., Mazzoleni, C., Mei, F., Moffet, R.C., Nelson, D., Obland, M.D., Oetjen, H., Onasch, T.B., Ortega, I., Ottaviani, M., Pekour, M., Prather, K.A., Radney, J.G., Rogers, R.R., Sandberg, S.P., Sedlacek, A., Senff, C.J., Senum, G., Setyan, A., Shilling, J.E., Shrivastava, M., Song, C., Springston, S.R., Subramanian, R., Suski, K., Tomlinson, J., Volkamer, R., Wallace, H.W., Wang, J., Weickmann, A.M., Worsnop, D.R., Yu, X.-Y., Zelenyuk, A., Zhang, Q., 2012. Overview of the 2010 Carbonaceous Aerosols and Radiative Effects Study (CARES). *Atmospheric Chemistry and Physics* 12, 7647–7687. <https://doi.org/10.5194/acp-12-7647-2012>
- Zehnder, C., Manoylov, K., Mutiti, S., Mutiti, C., VandeVoort, A., Bennett, D., 2018. Composition and Structure of the Atmosphere, in: *Introduction to Environmental Science: 2nd Edition*. Biological Sciences Open Textbooks.
- Zha, Q., Yan, C., Junninen, H., Riva, M., Sarnela, N., Aalto, J., Quéléver, L., Schallhart, S., Dada, L., Heikkinen, L., Peräkylä, O., Zou, J., Rose, C., Wang, Y., Mammarella, I., Katul, G., Vesala, T., Worsnop, D.R., Kulmala, M., Petäjä, T., Bianchi, F., Ehn, M., 2018. Vertical characterization of highly oxygenated molecules (HOMs) below and above a boreal forest canopy. *Atmospheric Chemistry and Physics* 18, 17437–17450. <https://doi.org/10.5194/acp-18-17437-2018>
- Zhang, Y., Li, D., Ma, Y., Dubois, C., Wang, X., Perrier, S., Chen, H., Wang, H., Jing, S., Lu, Y., Lou, S., Yan, C., Nie, W., Chen, J., Huang, C., George, C., Riva, M., 2022. Field Detection of Highly Oxygenated Organic Molecules in Shanghai by Chemical Ionization–Orbitrap. *Environ. Sci. Technol.* 56, 7608–7617. <https://doi.org/10.1021/acs.est.1c08346>
- Zhang, Y., Morris, J.R., 2015. Hydrogen Abstraction Probability in Reactions of Gas-Phase NO₃ with an OH-Functionalized Organic Surface. *J. Phys. Chem. C* 119, 14742–14747. <https://doi.org/10.1021/acs.jpcc.5b00562>
- Zhao, D., Pullinen, I., Fuchs, H., Schrade, S., Wu, R., Acir, I.-H., Tillmann, R., Rohrer, F., Wildt, J., Guo, Y., Kiendler-Scharr, A., Wahner, A., Kang, S., Vereecken, L., Mentel, T.F., 2021. Highly oxygenated organic molecule (HOM) formation in the isoprene oxidation by NO₃ radical. *Atmospheric Chemistry and Physics* 21, 9681–9704. <https://doi.org/10.5194/acp-21-9681-2021>
- Zhao, D., Schmitt, S.H., Wang, M., Acir, I.-H., Tillmann, R., Tan, Z., Novelli, A., Fuchs, H., Pullinen, I., Wegener, R., Rohrer, F., Wildt, J., Kiendler-Scharr, A., Wahner, A., Mentel, T.F., 2018. Effects of NO_x and SO₂ on the secondary organic aerosol formation from photooxidation of α -pinene and limonene. *Atmospheric Chemistry and Physics* 18, 1611–1628. <https://doi.org/10.5194/acp-18-1611-2018>

- Zhao, J., Häkkinen, E., Graeffe, F., Krechmer, J.E., Canagaratna, M.R., Worsnop, D.R., Kangasluoma, J., Ehn, M., 2023. A combined gas- and particle-phase analysis of highly oxygenated organic molecules (HOMs) from α -pinene ozonolysis. *Atmospheric Chemistry and Physics* 23, 3707–3730. <https://doi.org/10.5194/acp-23-3707-2023>
- Zhao, Y., Thornton, J.A., Pye, H.O.T., 2018. Quantitative constraints on autoxidation and dimer formation from direct probing of monoterpene-derived peroxy radical chemistry. *Proceedings of the National Academy of Sciences* 115, 12142–12147. <https://doi.org/10.1073/pnas.1812147115>
- Zhou, L., Gierens, R., Sogachev, A., Mogensen, D., Ortega, J., Smith, J.N., Harley, P.C., Prenni, A.J., Levin, E.J.T., Turnipseed, A., Rusanen, A., Smolander, S., Guenther, A.B., Kulmala, M., Karl, T., Boy, M., 2015. Contribution from biogenic organic compounds to particle growth during the 2010 BEACHON-ROCS campaign in a Colorado temperate needleleaf forest. *Atmospheric Chemistry and Physics* 15, 8643–8656. <https://doi.org/10.5194/acp-15-8643-2015>
- Zhu, Y., Zhang, J., Wang, J., Chen, W., Han, Y., Ye, C., Li, Y., Liu, J., Zeng, L., Wu, Y., Wang, X., Wang, W., Chen, J., Zhu, T., 2016. Distribution and sources of air pollutants in the North China Plain based on non-road mobile measurements. *Atmos. Chem. Phys.* 16, 12551–12565. <https://doi.org/10.5194/acp-16-12551-2016>

Appendix

Supplement–Chapter 2

S.2.1. Effect of ion trajectory guiding voltages

S.2.1.1. Thuner derived set of voltages initially obtained by Aerodyne

Table S.2.1. Initial voltage configuration setting derived from using the Thuner software method.

Components	Voltages (V)
Nozzle	0.1
SSQ	
SSQ Entr Plate	0.1
SSQ front	0.5
SSQ back	0.7
Lens skimmer	2.1
Skimmer	2.1
BSQ	
BSQ front	6.597
BSQ back	5.655
Skimmer 2	7.726
PB	
Reference	62.35
Ion lens 2	163.908997
Deflector Flange	24.6
Deflector	22.4
TOF chamber	
Pulse	700
Reference	10
Extraction 1	30
Extraction 2	700
Lens	2724
Drift	3000
Reflectron Grid	648.9
Reflectron Back	
Detector	2040
Post acceleration	2700

S.2.1.2. Oxalic acid sensitivities with different sets of voltages

The oxalic acid ($C_2H_2O_4$) investigation was repeated using the 4 sets of voltages (Table 2.3 and Table S.2.2).

Table S.2.2. Different Set of Voltage configuration

Component s	Set 1(V)	Set 2 (V)	Set 3 (V)	Set 4 (V)
Skimmer	2.1	2.1	4	4
BSQ front	6.2	7	6.2	5.7
BSQ back	5.7	7	5.7	6.2

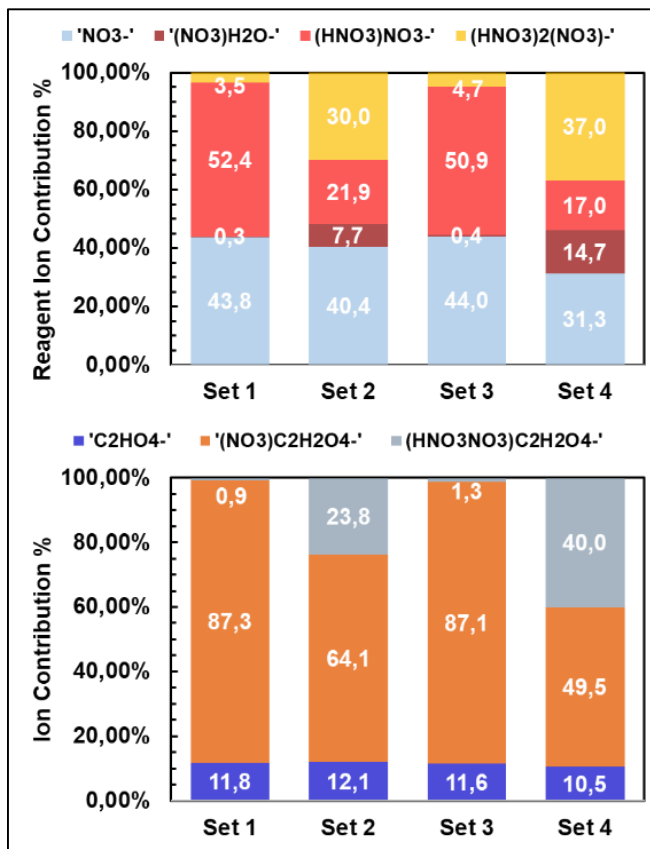


Figure S.2.1. a. Contribution in percentage of the reagent ions $(\text{HNO}_3)_{n-0.2}\text{NO}_3^-$ and $(\text{NO}_3)\text{H}_2\text{O}^-$ to the total reagent ions. b. Ion contribution in percentage of the deprotonated form C_2HO_4^- and the two clusters $(\text{NO}_3)\text{C}_2\text{H}_2\text{O}_4^-$ and $(\text{HNO}_3\text{NO}_3)\text{C}_2\text{H}_2\text{O}_4^-$ to the total $\text{C}_2\text{H}_2\text{O}_4$ ion products.

Figure S.2.1.a. displays the reagent ion signal patterns with the change between the 4 sets. One can conclude a quite similar reagent ion contribution as discussed in sub-section 2.2.2.b.

As shown in Figure S.2.1.b, Set 2 and Set 4 significantly increased the abundance of the $(\text{HNO}_3\text{NO}_3)\text{C}_2\text{H}_2\text{O}_4^-$ cluster (m/z 214.97) with a contribution of 24% and 40% of the total $\text{C}_2\text{H}_2\text{O}_4$ signals compared to about 1% and 1.3%, respectively for Set 1 and Set 3. C_2HO_4^- (m/z 88.98) bare ion signals remains unchanged with an average of 12% of total $\text{C}_2\text{H}_2\text{O}_4$ signals whereas $(\text{NO}_3)\text{C}_2\text{H}_2\text{O}_4^-$ (m/z 151.98) decreased in Set 2 and Set 4 to 64% and 50% compared to 87% in Set 1 and Set 3, respectively. Hence, the increase in the presence of $(\text{HNO}_3)_2\text{NO}_3^-$ cluster is correlated with the greater formation of $(\text{HNO}_3\text{NO}_3)\text{C}_2\text{H}_2\text{O}_4^-$ cluster.

Table S.2.3. Calibration factors obtained for succinic acid from experiments with varied sets of applied voltages.

Set of voltages	Calibration factor (molecules.cm ⁻³)
1	1.26×10 ¹³
2	1.49×10 ¹³
3	1.32×10 ¹³
4	1.44×10 ¹³

The sensitivities of the ToFCIMS towards total C₂H₂O₄ ion signals are summarized in Table S.2.3.

Again, to obtain a less complex mass spectrum, C_{C₂H₂O₄} obtained from Set 1 and Set 3 were compared and showed a better sensitivity when using Set 1, although with a small relative difference of about 5%. Hence a slightly better sensitivity and a less complex mass spectrum are the keys to choosing Set 1.

S.2.1.3. Tartaric acid sensitivities with different sets of voltages

Investigations were performed using the various voltage sets 1, 2 and 4 with a concentration of tartaric acid C₄H₆O₆ of about 5 ppb. Comparable reagent ion contributions were obtained that were similar to those discussed in sub-section 2.2.2.b and S.2.1.2, which shows the reproducibility of the instrument response. However, in the case of C₄H₆O₆, whichever set is employed, about one-half of the ions from C₄H₆O₆ were in the deprotonated form C₄H₅O₆⁻ (m/z 149.01) and the first cluster (NO₃)·C₄H₆O₆⁻ (m/z 212.005). Briefly, the contribution of (NO₃)·C₄H₆O₆⁻ was slightly higher for Set 2 (54.3%) and Set 4 (53%) compared to Set 1 (49.3%). In addition, the contribution of C₄H₅O₆⁻ was slightly lower for Set 2 (44.6%) and Set 4 (43.5%) compared to Set 1 (50.6%). A much smaller contribution of the second cluster was also observed (HNO₃NO₃)·C₄H₆O₆⁻ (m/z 275.001). For instance, the highest contribution of the latter using Set 4 was only 3% while hardly any was formed using Set 1 (Figure S.2.2.b). The variations in the proportion of the different ion products may impact the sensitivity of the ToFCIMS toward C₄H₆O₆ when employing each set of voltages.

The performance of the three sets tested were assessed and the optimum was found to be Set 1 (C_{C₄H₆O₆} = 4.5×10¹² molecule.cm⁻³) showing lower values than with Set 2 (C_{C₄H₆O₆} = 4.9×10¹² molecule.cm⁻³) (9% RD) and about 15% RD with Set 4 (C_{C₄H₆O₆} = 5.21×10¹² molecule.cm⁻³).

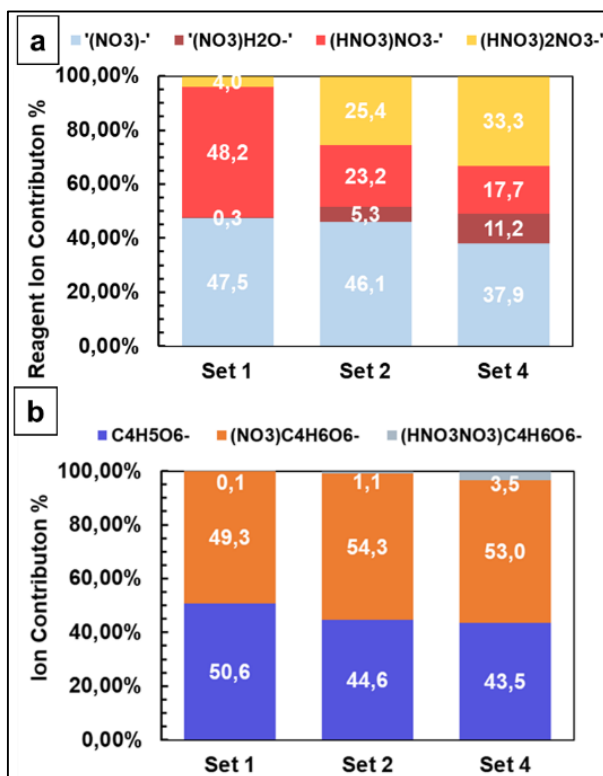


Figure S.2.2.a. Contribution in percentage of the reagent ions $(\text{HNO}_3)_{n=0-2}\text{NO}_3^-$ and $(\text{NO}_3)\text{H}_2\text{O}^-$ to the total reagent ions. b. Percentage contribution of the deprotonated form $\text{C}_4\text{H}_5\text{O}_6^-$ and the two clusters $(\text{NO}_3)\text{C}_4\text{H}_6\text{O}_6^-$ and $(\text{HNO}_3\text{NO}_3)\text{C}_4\text{H}_6\text{O}_6^-$ for measurements of tartaric acid. Numbers represent the ion contribution (%) for the various ions.

S.2.1.4. Pyruvic acid sensitivities with different sets of voltages

Sets 1 and 2 were applied to the instrument during measurement of pyruvic acid ($\text{C}_3\text{H}_4\text{O}_3$). As obtained with succinic acid, the larger voltages applied to the BSQF and BSQB induced larger reagent ion cluster formation. Unlike the acids $\text{C}_2\text{H}_2\text{O}_4$, $\text{C}_4\text{H}_6\text{O}_4$, and $\text{C}_4\text{H}_6\text{O}_6$, $\text{C}_3\text{H}_4\text{O}_3$ only ionizes via deprotonation ($\text{C}_3\text{H}_3\text{O}_3^-$) and cluster formation with bare nitrate ($\text{NO}_3\cdot\text{C}_3\text{H}_4\text{O}_3^-$) for both settings, with a 36% $\text{C}_3\text{H}_3\text{O}_3^-$ and 64% $\text{NO}_3\cdot\text{C}_3\text{H}_4\text{O}_3^-$ ion contribution with Set 1, and 17% $\text{C}_3\text{H}_3\text{O}_3^-$ and 83% $\text{NO}_3\cdot\text{C}_3\text{H}_4\text{O}_3^-$ ion contribution using Set 2. Set 1 resulted in better sensitivity ($C_{\text{C}_3\text{H}_4\text{O}_3}=4.64\times 10^{15}$ molecule. cm^{-3}) compared to Set 2 ($C_{\text{C}_3\text{H}_4\text{O}_3}=6.82\times 10^{15}$ molecule. cm^{-3}) with 32% RD.

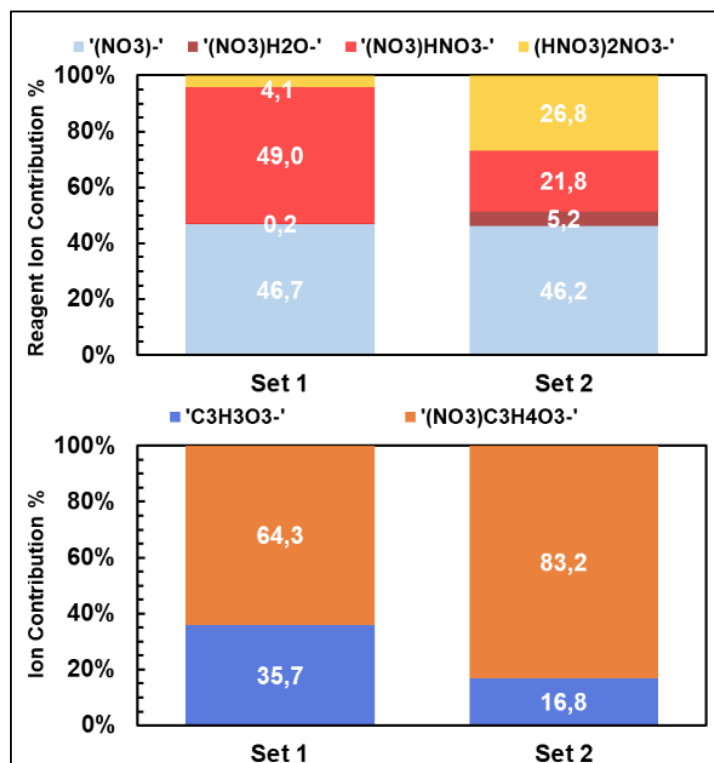
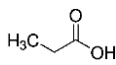
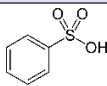
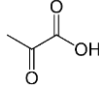
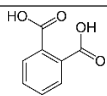
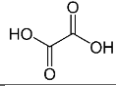
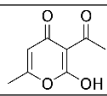
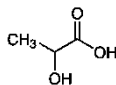
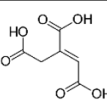
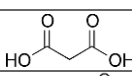
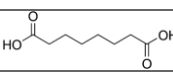
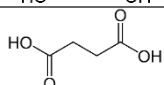
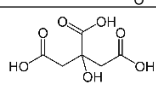
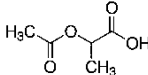
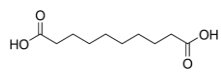
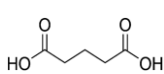
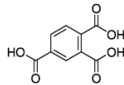
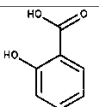
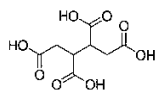
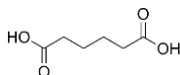
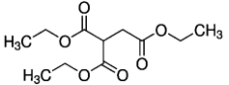
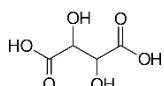
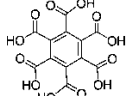
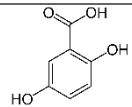
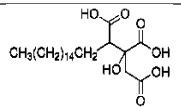
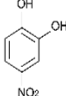
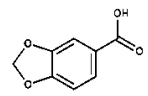
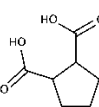


Figure S.2.3. Contribution in percentage of the reagent ions $(\text{HNO}_3)_{n=0-2}\text{NO}_3^-$ and $(\text{NO}_3)\text{H}_2\text{O}^-$ to the total reagent ions. b. Percentage contribution of the deprotonated form $\text{C}_3\text{H}_3\text{O}_3^-$ and the two clusters $(\text{NO}_3)\text{C}_3\text{H}_4\text{O}_3^-$ for measurements of pyruvic acid. Numbers represent the ion contribution (%) for the various ions.

S.2.2. Chemical Structures of Organic Compounds Reviewed in Chapter 2, Section 2.3

Table S.2.4. The chemical formulas of the organic compounds listed in Table 2.6. Candidate organic compounds used to evaluate the sensitivity of the instrument. The yielding response (+ = detected, - = not detected) is based on the appropriate heating

Compound	Chemical Formula	Compound	Chemical Formula
Propanoic acid		Benzenesulfonic Acid	
Pyruvic Acid		Phthalic Acid	
Oxalic Acid		Dehydroacetic Acid	
Lactic acid		T-aconitic Acid	
Malonic Acid		Suberic Acid	
Succinic Acid		Citric Acid	
2-acetoxypropionic Acid		Sebacic Acid	
Glutaric Acid		1,2,4-benzenetricarboxylic Acid	
Salicylic Acid		1,2,3,4-butanetetracarboxylic Acid	
Adipic Acid		1,1,2 Ethane Triethylcarboxylate	
Tartaric Acid		Mellitic Acid	
2,5-dihydroxy Benzoic Acid		Agaric Acid	
4-nitrocatechol		Piperonylic Acid	
Cis-cyclopentane-1,2-dicarboxylic Acid			

S.2.3. Data Analysis: Tofware

The Tofware (Tofware AG, version 3.2.5) software is used to process the HDF5 data files from the instrument. It runs within the data analysis software environment called Igor Pro (version 8.04 64-

bit, Wavemetrics, Lake Oswego, OR, USA) (Stark et al., 2015). As mentioned in section 2.1.5, pre-averaging raw data was done on a one-minute basis for laboratory experiments and on a ten-minute basis for field measurements. Averaging is an important step to improve the signal-to-noise ratio (S/N) and the precision of the measurements, and therefore achieves a lower detection limit (LOD). This latter parameter is defined as the smallest concentration of analyte that can be distinguished from the baseline with a given level of confidence (Bernal, 2014).

S.2.3.1. Mass calibration

Mass (m/z) calibration is the first task to prepare data for subsequent analysis. Using the method detailed in section 2.1.5, a reference mass spectrum must then be defined as being representative of the whole data set. It is usually the region with the best mass accuracy, in ppm, which is defined as the difference between the measured and the calculated m/z values as a fraction of the calculated m/z value, multiplied by 10^6 (Equation S.2.1).

$$\text{Mass accuracy (ppm)} = ((m/z)_{\text{meas}} - (m/z)_{\text{calc}})/(m/z)_{\text{calc}} \times 10^6 \quad \text{Equation S.2.1}$$

S.2.3.2. Baseline determination

The baseline is defined as the detector signal in the absence of an analyte. For a precise determination of peak area, height or width, the baseline signal needs to be determined and subtracted from the sample signal. For baselines that are comparable to the sample signals, this can significantly improve the accuracy of the method. The method includes a low-pass filter for noise removal, a moving average using a window defined by the width parameter, in arbitrary units, (typically set to 5-6) with the lowest point taken as the baseline. Multi-peak signals, defined as the presence of one or more overlapping peaks at the same or nearly the same nominal m/z value may exist in the spectrum. A multi-peak fitting is thereby needed to determine the individual peak intensities.

S.2.3.3. Peak shape and width

As previously mentioned, a preliminary mass calibration is usually performed assuming a Gaussian peak shape. However, the latter would be observed in a mass spectrometer in an ideal situation, whereas in reality, potential non-linear effects within the instrument, e.g. the ions interaction and changes in tuning resulting from user input, can result in asymmetric peak shapes (DeCarlo et al., 2006; Stark et al., 2015).

The actual peak shape is initially obtained from the average of individual ion peak shapes, which are included in the mass calibration list along with the most intense peaks present in the mass spectrum. The shape is optimized by eliminating individual peak shapes that are clearly not good matches to the nominal Gaussian shape, which can be seen in the figure where the normalized peaks (colored traces in the “Before” plot) are compared to the Gaussian shape (Figure S.2.4).

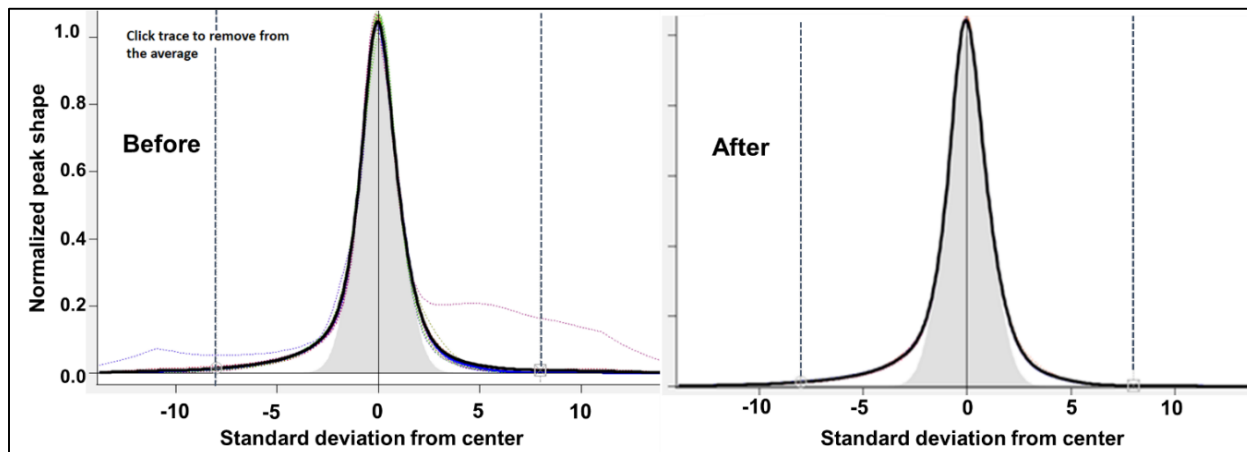


Figure S.2.4. Example of a normalized peak shape before and after removal of noisy and asymmetric individual peaks. The dashed colored lines represent the shapes of individual peaks. The average of selected peaks is shown by the thick black line. The light grey filled area depicts the Gaussian peak shape.

Once the peak shape is optimized, one needs to refine the peak shape as a function of m/z . An example of this is illustrated in Figure S.2.5. In the left graph, the FWHM shows a linear relationship with m/Q (the red line), that is processed in an iterative fashion by keeping peaks located on this line while those significantly off the line are manually removed. The same iterative process applies for the non-linear relation between the mass resolution and the m/Q (lower right plot in Figure S.2.5).

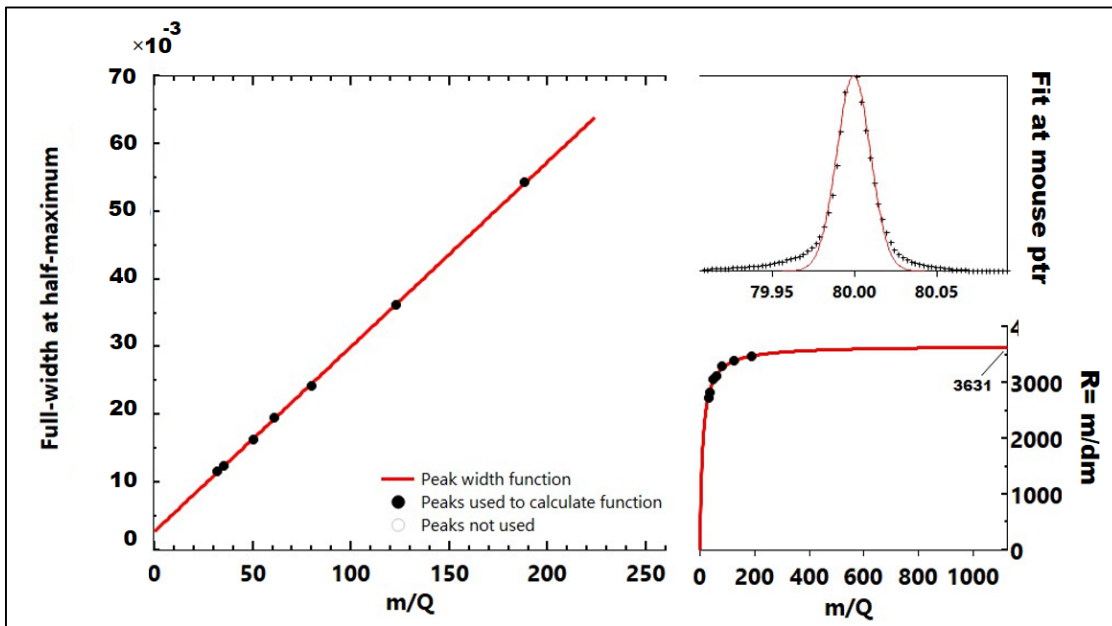


Figure S.2.5. An example of a tuned relationship between the peak width (left plot) and the mass resolution (lower right plot) as a function of the mass-to-charge ratio.

Having completed these steps, the mass calibration must be repeated by using the refined peak shape (Figure S.2.6).

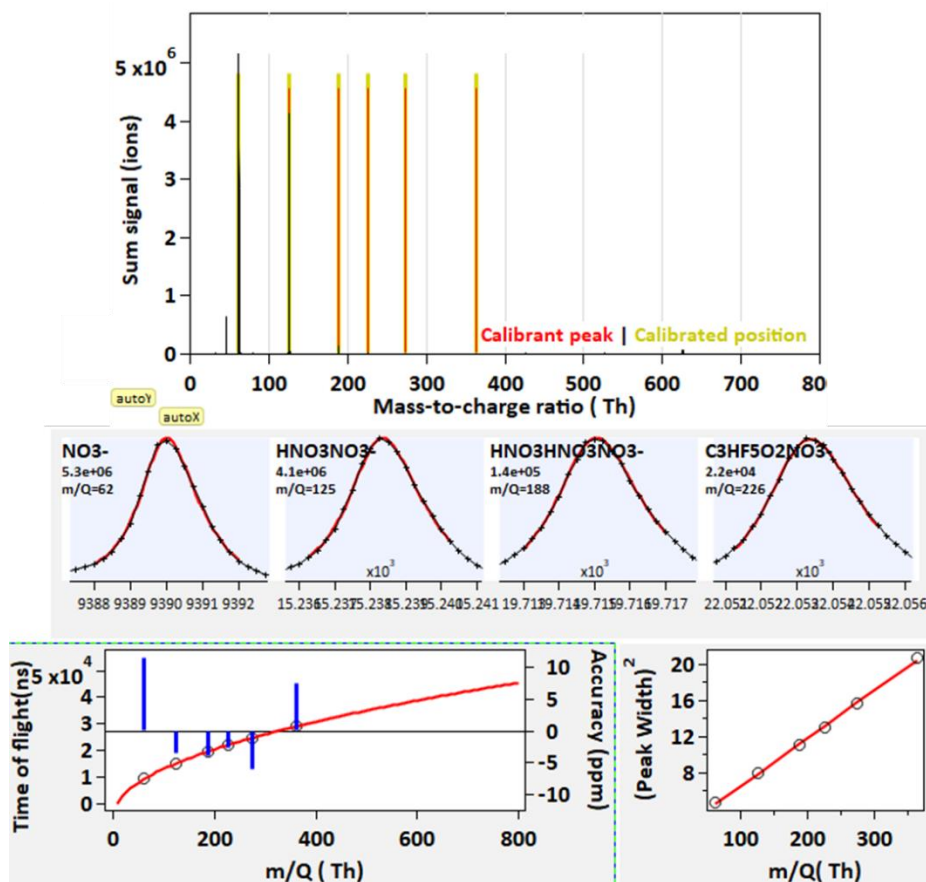


Figure S.2.6. Optimized mass calibration based on the same data used in Figure 2.4.

S.2.3.4. High resolution peak identification

Once these tasks are complete, the exploration of the mass spectrum can begin to identify peaks of interest. This is possible within Tofware through the use of 'HR peak fit' function and by simply browsing and selecting the peaks to be identified. In brief, this function is based on the multi-peak fitting algorithm that determines the signal as a function of the m/z for individual or overlapping peaks. Hence, as shown in Equation S.2.2, this can be described as a linear combination of individual peaks of the same peak shape but at different locations (m/z) and amplitude (intensity) (Stark et al., 2015; Timonen et al., 2016).

$$I(m/z) = \sum_{i=1}^n A_i \times S_i(m/z) \quad \text{Equation S.2.2}$$

Where, $I(m/z)$ is the signal at m/z , n is the number of overlapping peaks at that m/z , A_i is the amplitude of the peak I , and $S_i(m/z)$ is the peak shape function, centered on peak i , normalized to the single peak height.

Prior to peak identification the user-defined data range was extracted from single or multiple files. For instance, in the case of the experiments conducted in the simulation chamber, spectra were processed for the chamber composition measurements and for background measurements. One may subsequently browse the two averaged mass spectrum on the same panel, so the background peaks can be directly located and excluded from the identification. Within this thesis work, the identification of the peaks in the mass spectra was done manually to guarantee the peaks used represented a reliable set. In simulation chamber experiments and other optimization tests, the time series of the selected peak was simultaneously browsed to ensure that this is not associated with a contaminant molecule, primarily fluorinated organic acids.

Peaks, including overlapping ones, were assigned one by one starting with the lowest m/z using the automatic 'Composition finder' tool, by defining the name of the element, which can be an atom or a neutral/ion molecule, e.g., C, H, O if only OVOCs are the target compounds and other atoms like N, S, etc., or ions like NO_3^- since HOMs are expected to form stable clusters with these. This tool gives a list of possible peak formulas with their exact masses and mass accuracies along with the related isotopes, including their exact masses and abundances, which is a percentage of the amplitude of the monoisotopic peak. By analyzing the higher m/z values, we can identify whether they are a result of isotopic patterns. This helps us decide whether to exclude them from the list of peaks or utilize the information to evaluate the contribution of isotopes to the overlapping peaks.

In conclusion, to assign the correct peak formula, one should verify that the molecular formula is reasonable and chemically feasible, if its theoretical (exact) mass falls within the instrumental mass accuracy range, and how well the formula conforms to isotopic constraints. This process allows us to make accurate determinations and select appropriate peak formulas. To illustrate this procedure involved in determining peak formulas, Figure S.2.7 provides an example depicting the error between the fitted peak and the exact mass of the defined formula.

One should also note that, in the case of two or more overlapping peaks, the assignment starts with the largest peak and determining its elemental composition. Unknown peaks were subsequently removed and refitted and this is repeated until all the peaks of reasonable size have been identified Mehra (2021).

An illustration of the combined use of isotopic distribution and chemical composition finder approach is shown in Figure S.2.7. This figure showcases an example of an ion product detected at m/z 342 Th during a limonene plus O_3 experiment. The green dashed lines indicate the mass region under study, the blue peak represents the peak fit and the green lines depict the calculated isotopes corresponding to the 342 Th peak. It is important to note that the mass accuracy in this experiment was within ± 20 ppm.

Two examples of possible chemical formulas are taken from the composition finder table within the range of the mass accuracy: $(NO_3) \cdot C_{10}H_{16}O_9^-$, shown in blue, and $(NO_3) \cdot C_{15}H_{10}N_3O_3^-$, shown in red color. The $(NO_3) \cdot C_{10}H_{16}O_9^-$ formula demonstrates a closely matching isotopic ratio with the observed signal. However, for $(NO_3) \cdot C_{15}H_{10}N_3O_3^-$, the calculated isotopic fit exceeds the actual signal observed, suggesting a mismatch. Furthermore, it is peculiar that the hydrogen numbers are so low in $C_{15}H_{10}N_3O_3$ and 3 nitrogen atoms are proposed while no NO_x was added nor existed in the chemical system. On the other hand, $C_{10}H_{16}O_9$ is a reasonable choice especially since limonene has the molecular formula $C_{10}H_{16}$.

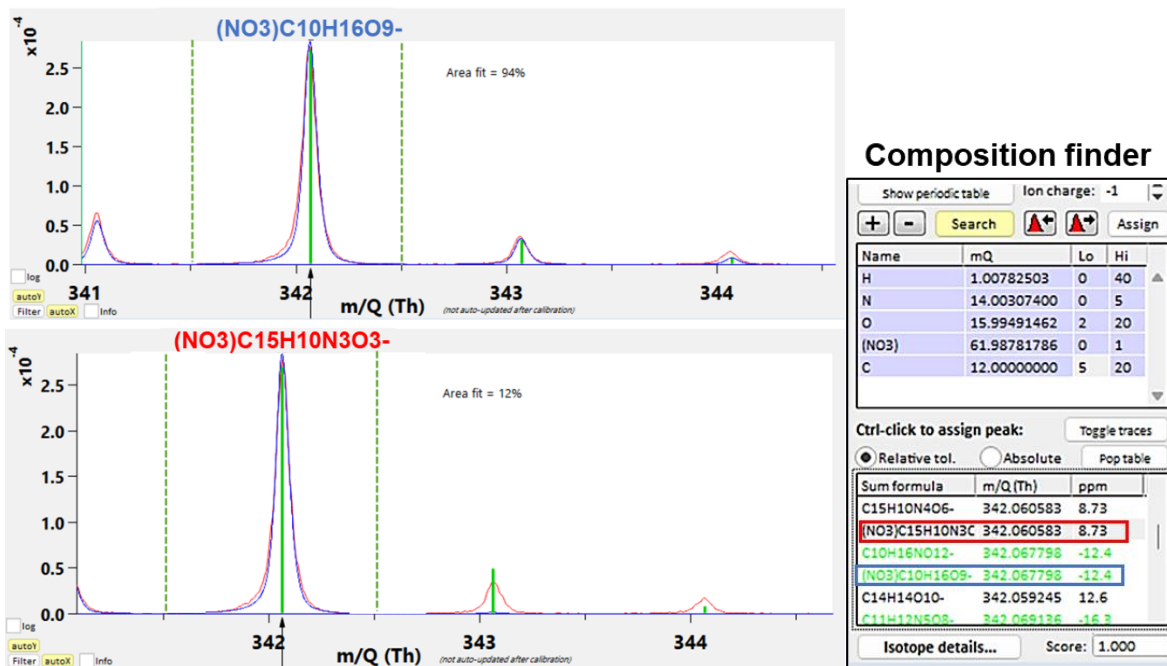


Figure S.2.7. Example of chemical composition identification procedure of peak 342 Th.

Supplement–Chapter 3

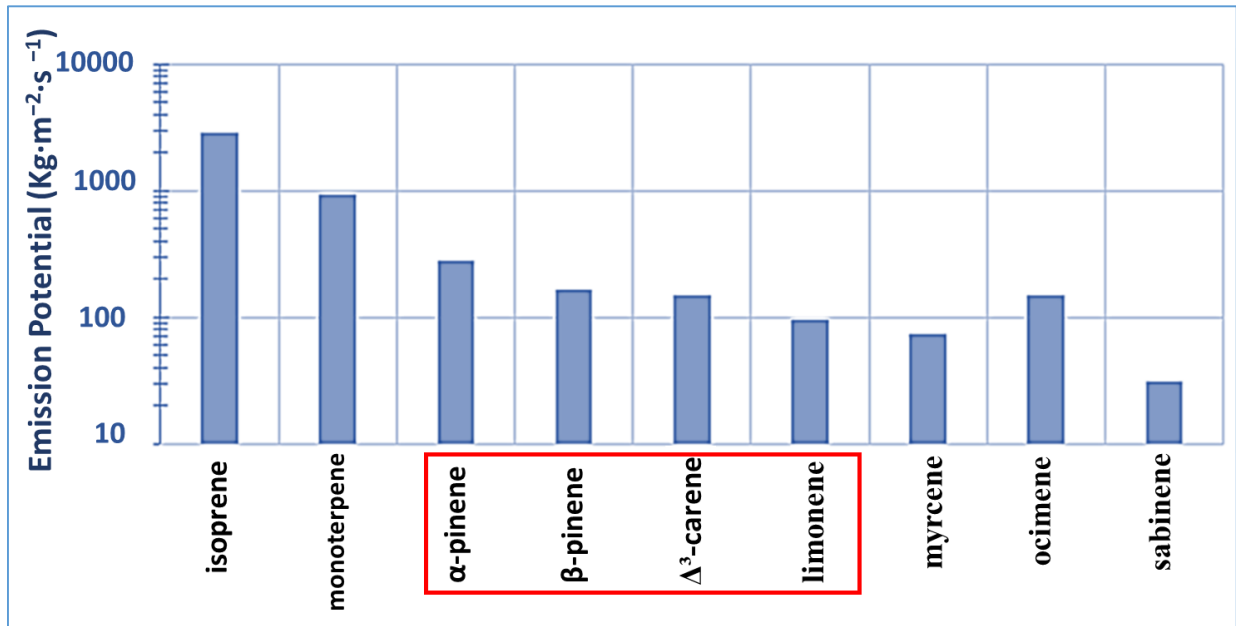


Figure S.3.1. The average emission potentials of terpenes centered on the Rambouillet supersite as extracted from MEGAN emissions database (Guenther et al., 2012).

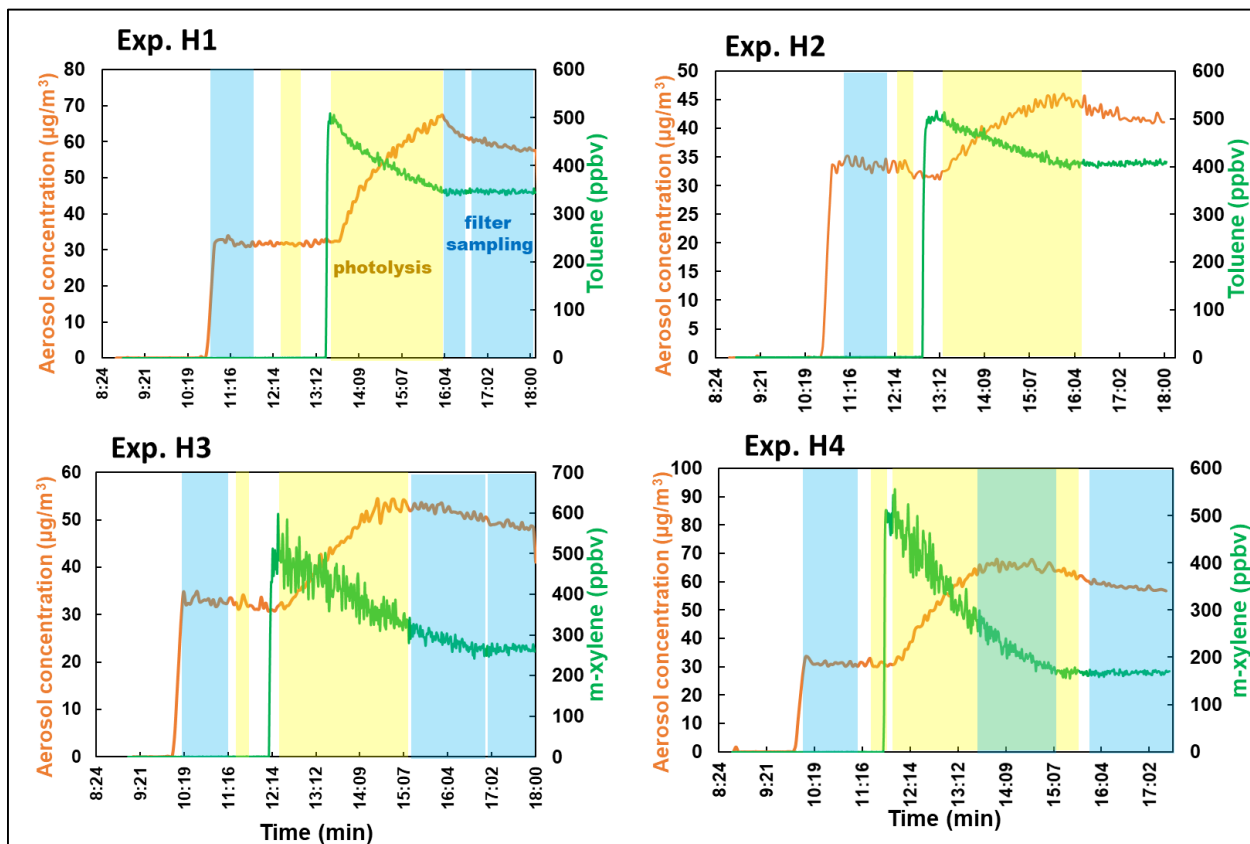


Figure S.3.2. Experiment H1-H4-time series of VOC precursors (in green) and the aerosol mass concentrations (in orange). The seed injection is done and shown prior to the injection of VOCs into the chamber. Aerosol mass concentrations were determined using the SMPS (with a density of 1.4 g/cm³), as described in section 3.3.2. The yellow shaded region indicates the photolysis period, while the blue shaded region corresponds to the filter sampling period.

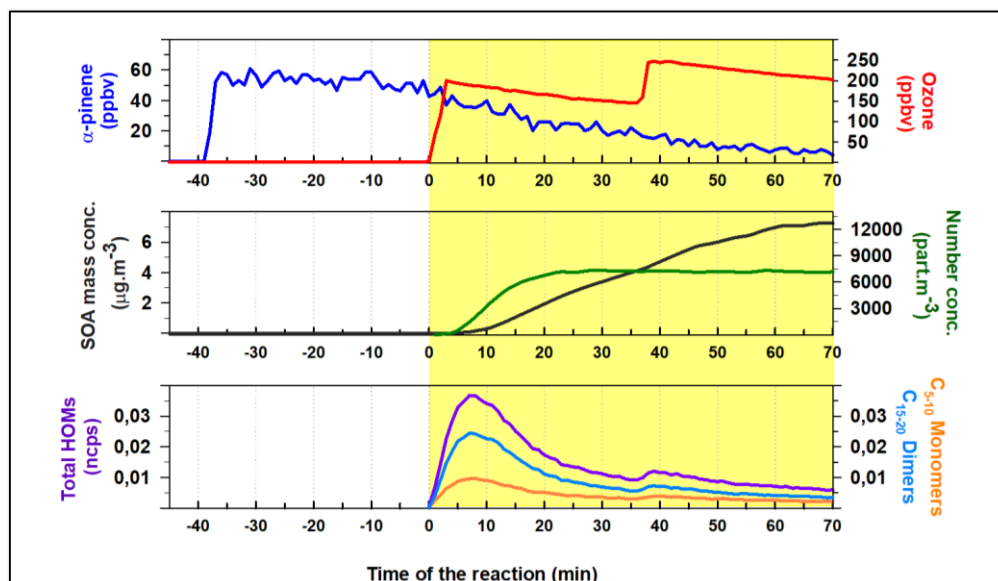


Figure S.3.3. Experiment O2-time series of gas phase precursors (top panel), α -pinene (in blue) and O₃ (in red), along with the SOA mass and number concentrations (second panel) (in black and green, respectively), the gas phase normalized HOM products (bottom panel): total HOMs (in purple), the sum of C₅₋₁₀ monomers (in orange) and C₁₅₋₂₀ dimers (in light blue).

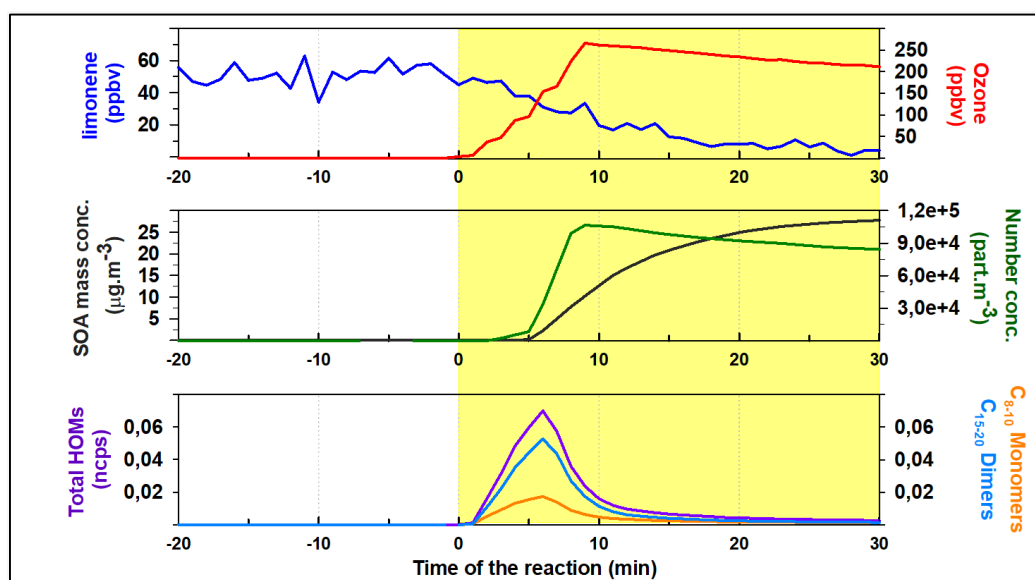


Figure S.3.4. Experiment O4-time series of gas phase precursors (top panel), limonene (in blue) and O₃ (in red), along with the SOA mass and number concentrations (second panel) (in black and green, respectively), the gas phase normalized HOM products (bottom panel): total HOMs (in purple), the sum of C₈₋₁₀ monomers (in orange) and C₁₅₋₂₀ dimers (in light blue).

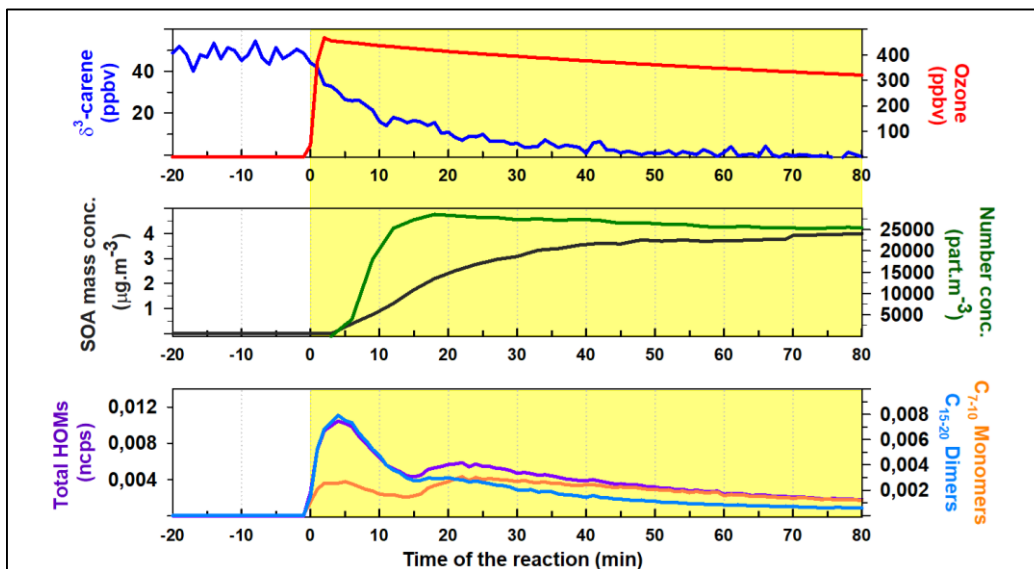


Figure S.3.5. Experiment O6-time series of gas phase precursors (top panel, 3-carene (in blue) and O₃ (in red), along with their SOA mass and number concentrations (second panel) (in black and green, respectively), the gas phase normalized HOM products (bottom panel): total HOMs (in purple), the sum of C₇₋₁₀ monomers (in orange) and C₁₅₋₂₀ dimers (in light blue).

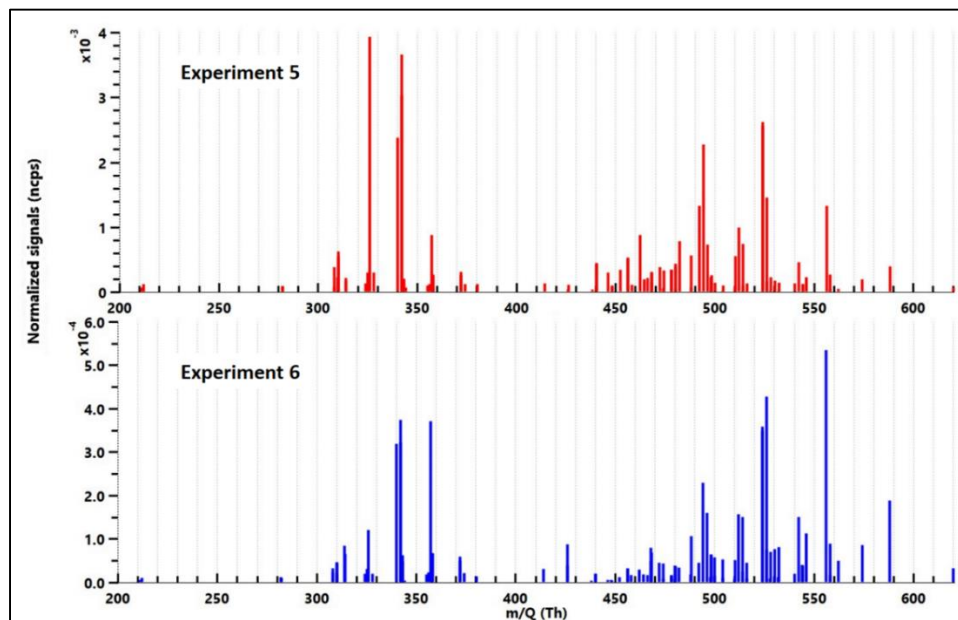


Figure S.3.6. Comparison of the average mass spectra obtained from Experiments O5 (red bars) and O6 (blue bars).

Table S.3.1. Peaks identified in the average mass spectrum from α -pinene ozonolysis experiments using NO_3^- ToF-CIMS. The m/z values correspond to the HOM mass to charge ratios in Thomson (Th), while O/C and H/C denote the elemental ratios, representing the oxygen-to-carbon and hydrogen-to-carbon ratios, respectively.

Formula	m/z Th	O/C	H/C	Formula	m/z Th	O/C	H/C
C₄H₄O₄	116.01	1.00	1.00	C₁₀H₁₆O₁₁	312.07	1.10	1.60
C₅H₆O₆	162.02	1.20	1.20	C₁₁H₁₄O₁₄	370.04	1.27	1.27
C₅H₆O₇	178.01	1.40	1.20	C₁₂H₁₆O₁₃	368.06	1.08	1.33
C₆H₆O₈	206.01	1.33	1.00	C₁₂H₁₈O₁₂	354.08	1.00	1.50
C₆H₈O₉	224.02	1.50	1.33	C₁₂H₁₈O₁₃	370.07	1.08	1.50
C₇H₈O₇	204.03	1.00	1.14	C₁₂H₂₆O₁₃	378.14	1.08	2.17
C₇H₈O₈	220.02	1.14	1.14	C₁₃H₂₀O₁₁	352.10	0.85	1.54
C₇H₁₀O₇	206.04	1.00	1.43	C₁₃H₂₀O₁₂	368.10	0.92	1.54
C₇H₁₀O₈	222.04	1.14	1.43	C₁₃H₂₆O₁₂	374.14	0.92	2.00
C₇H₁₀O₉	238.03	1.29	1.43	C₁₄H₂₀O₉	332.11	0.64	1.43
C₈H₁₂O₇	220.06	0.88	1.50	C₁₄H₂₀O₁₀	348.11	0.71	1.43
C₈H₁₂O₈	236.05	1.00	1.50	C₁₄H₂₀O₁₁	364.10	0.79	1.43
C₈H₁₂O₉	252.05	1.13	1.50	C₁₄H₂₀O₁₂	380.10	0.86	1.43
C₈H₁₂O₁₀	268.04	1.25	1.50	C₁₄H₂₀O₁₃	396.09	0.93	1.43
C₈H₁₂O₁₁	284.04	1.38	1.50	C₁₄H₂₀O₁₅	428.08	1.07	1.43
C₈H₁₄O₈	238.07	1.00	1.75	C₁₄H₂₂O₈	318.13	0.57	1.57
C₉H₁₀O₁₀	278.03	1.11	1.11	C₁₄H₂₂O₁₀	350.12	0.71	1.57
C₉H₁₀O₁₁	294.02	1.22	1.11	C₁₄H₂₈O₁₁	372.16	0.79	2.00
C₉H₁₀O₁₂	310.02	1.33	1.11	C₁₅H₁₈O₉	342.10	0.60	1.20
C₉H₁₀O₁₅	358.00	1.67	1.11	C₁₅H₂₂O₁₀	362.12	0.67	1.47
C₉H₁₂O₈	248.05	0.89	1.33	C₁₅H₂₂O₁₂	394.11	0.80	1.47
C₉H₁₂O₉	264.05	1.00	1.33	C₁₅H₂₂O₁₃	410.11	0.87	1.47
C₉H₁₂O₁₁	296.04	1.22	1.33	C₁₅H₂₂O₁₄	426.10	0.93	1.47
C₉H₁₂O₁₂	312.03	1.33	1.33	C₁₅H₂₂O₁₅	442.10	1.00	1.47
C₉H₁₂O₁₃	328.03	1.44	1.33	C₁₅H₂₂O₁₆	458.09	1.07	1.47
C₉H₁₄O₈	250.07	0.89	1.56	C₁₆H₂₂O₁₂	406.11	0.75	1.38
C₉H₁₄O₉	266.06	1.00	1.56	C₁₆H₂₂O₁₃	422.11	0.81	1.38
C₉H₁₆O₈	252.08	0.89	1.78	C₁₆H₂₄O₁₁	392.13	0.69	1.50
C₉H₁₆O₉	268.08	1.00	1.78	C₁₆H₂₄O₁₃	424.12	0.81	1.50
C₁₀H₁₄O₇	246.07	0.70	1.40	C₁₆H₂₄O₁₅	456.11	0.94	1.50
C₁₀H₁₄O₈	262.07	0.80	1.40	C₁₆H₂₆O₁₂	410.14	0.75	1.63
C₁₀H₁₄O₉	278.06	0.90	1.40	C₁₆H₂₆O₁₄	442.13	0.88	1.63
C₁₀H₁₄O₁₀	294.06	1.00	1.40	C₁₆H₂₆O₁₅	458.13	0.94	1.63
C₁₀H₁₄O₁₁	310.05	1.10	1.40	C₁₇H₂₂O₁₁	402.12	0.65	1.29
C₁₀H₁₄O₁₂	326.05	1.20	1.40	C₁₇H₂₄O₁₀	388.14	0.59	1.41
C₁₀H₁₄O₁₄	358.04	1.40	1.40	C₁₇H₂₄O₁₁	404.13	0.65	1.41
C₁₀H₁₅O₈	263.08	0.80	1.50	C₁₇H₂₄O₁₃	436.12	0.76	1.41
C₁₀H₁₅O₁₀	295.07	1.00	1.50	C₁₇H₂₄O₁₄	452.12	0.82	1.41
C₁₀H₁₅O₁₂	327.06	1.20	1.50	C₁₇H₂₄O₁₆	484.11	0.94	1.41
C₁₀H₁₆O₇	248.09	0.70	1.60	C₁₇H₂₄O₁₇	500.10	1.00	1.41
C₁₀H₁₆O₈	264.08	0.80	1.60	C₁₇H₂₄O₁₈	516.10	1.06	1.41
C₁₀H₁₆O₉	280.08	0.90	1.60	C₁₇H₂₆O₁₁	406.15	0.65	1.53
C₁₀H₁₆O₁₀	296.07	1.00	1.60	C₁₇H₂₆O₁₂	422.14	0.71	1.53

Table S.3.1 (continued). Peaks identified in the mass spectrum from α -pinene ozonolysis experiments using NO_3^- -ToF-CIMS. The m/z values correspond to the HOM mass to charge ratios in Thomson (Th), while O/C and H/C denote the elemental ratios, representing the oxygen-to-carbon and hydrogen-to-carbon ratios, respectively.

Formula	m/z Th	O/C	H/C	Formula	m/z Th	O/C	H/C
C₁₇H₂₆O₁₃	438.14	0.76	1.53	C₁₉H₂₆O₁₉	558.11	1.00	1.37
C₁₇H₂₆O₁₄	454.13	0.82	1.53	C₁₉H₂₈O₉	400.17	0.47	1.47
C₁₇H₂₈O₁₃	440.15	0.76	1.65	C₁₉H₂₈O₁₀	416.17	0.53	1.47
C₁₇H₂₈O₁₄	456.15	0.82	1.65	C₁₉H₂₈O₁₁	432.16	0.58	1.47
C₁₇H₂₈O₁₅	472.14	0.88	1.65	C₁₉H₂₈O₁₂	448.16	0.63	1.47
C₁₈H₂₂O₁₁	414.12	0.61	1.22	C₁₉H₂₈O₁₃	464.15	0.68	1.47
C₁₈H₂₄O₁₀	400.14	0.56	1.33	C₁₉H₂₈O₁₄	480.15	0.74	1.47
C₁₈H₂₄O₁₁	416.13	0.61	1.33	C₁₉H₂₈O₁₅	496.14	0.79	1.47
C₁₈H₂₄O₁₂	432.13	0.67	1.33	C₁₉H₂₈O₁₆	512.14	0.84	1.47
C₁₈H₂₆O₉	386.16	0.50	1.44	C₁₉H₃₀O₈	386.19	0.42	1.58
C₁₈H₂₆O₁₀	402.15	0.56	1.44	C₁₉H₃₀O₉	402.19	0.47	1.58
C₁₈H₂₆O₁₁	418.15	0.61	1.44	C₁₉H₃₀O₁₀	418.18	0.53	1.58
C₁₈H₂₆O₁₂	434.14	0.67	1.44	C₁₉H₃₀O₁₁	434.18	0.58	1.58
C₁₈H₂₆O₁₃	450.14	0.72	1.44	C₁₉H₃₀O₁₂	450.17	0.63	1.58
C₁₈H₂₆O₁₅	482.13	0.83	1.44	C₁₉H₃₀O₁₃	466.17	0.68	1.58
C₁₈H₂₆O₁₆	498.12	0.89	1.44	C₁₉H₃₀O₁₄	482.16	0.74	1.58
C₁₈H₂₈O₉	388.17	0.50	1.56	C₁₉H₃₀O₁₅	498.16	0.79	1.58
C₁₈H₂₈O₁₀	404.17	0.56	1.56	C₁₉H₃₂O₈	388.21	0.42	1.68
C₁₈H₂₈O₁₁	420.16	0.61	1.56	C₁₉H₃₂O₁₆	516.17	0.84	1.68
C₁₈H₂₈O₁₂	436.16	0.67	1.56	C₁₉H₃₆O₂₀	584.18	0.00	1.89
C₁₈H₂₈O₁₃	452.15	0.72	1.56	C₂₀H₃₀O₈	398.19	0.40	1.50
C₁₈H₂₈O₁₄	468.15	0.78	1.56	C₂₀H₃₀O₉	414.19	0.45	1.50
C₁₈H₂₈O₁₅	484.14	0.83	1.56	C₂₀H₃₀O₁₀	430.18	0.50	1.50
C₁₈H₂₈O₁₆	500.14	0.89	1.56	C₂₀H₃₀O₁₁	446.18	0.55	1.50
C₁₈H₂₈O₁₇	516.13	0.94	1.56	C₂₀H₃₀O₁₂	462.17	0.60	1.50
C₁₈H₂₈O₁₈	532.13	1.00	1.56	C₂₀H₃₀O₁₃	478.17	0.65	1.50
C₁₈H₃₀O₁₀	406.18	0.56	1.67	C₂₀H₃₀O₁₄	494.16	0.70	1.50
C₁₉H₂₆O₁₀	414.15	0.53	1.37	C₂₀H₃₀O₁₅	510.16	0.75	1.50
C₁₉H₂₆O₁₁	430.15	0.58	1.37	C₂₀H₃₀O₁₆	526.15	0.80	1.50
C₁₉H₂₆O₁₂	446.14	0.63	1.37	C₂₀H₃₀O₁₇	542.15	0.85	1.50
C₁₉H₂₆O₁₃	462.14	0.68	1.37	C₂₀H₃₀O₁₈	558.14	0.90	1.50
C₁₉H₂₆O₁₄	478.13	0.74	1.37	C₂₀H₃₂O₉	416.20	0.45	1.60
C₁₉H₂₆O₁₅	494.13	0.79	1.37	C₂₀H₃₂O₁₁	448.19	0.55	1.60
C₁₉H₂₆O₁₆	510.12	0.84	1.37	C₂₀H₃₂O₁₂	464.19	0.60	1.60
C₁₉H₂₆O₁₇	526.12	0.89	1.37	C₂₀H₃₂O₁₃	480.18	0.65	1.60
C₁₉H₂₆O₁₈	542.11	0.95	1.37	C₂₀H₃₂O₁₅	512.17	0.75	1.60

Table S.3.2. Peaks identified in the mass spectrum from limonene ozonolysis experiments using NO_3^- -ToF-CIMS. The m/z values correspond to the HOM mass to charge ratios in Thomson (Th), while O/C and H/C denote the elemental ratios, representing the oxygen-to-carbon and hydrogen-to-carbon ratios, respectively.

Formula	m/z Th	O/C	H/C	Formula	m/z Th	O/C	H/C
C₈H₁₂O₇	220.06	0.88	1.50	C₁₈H₃₀O₁₀	406.18	0.56	1.67
C₁₀H₁₄O₇	246.07	0.70	1.40	C₁₈H₃₀O₁₁	422.18	0.61	1.67
C₁₀H₁₄O₈	262.07	0.80	1.40	C₁₈H₃₀O₁₂	438.17	0.67	1.67
C₁₀H₁₄O₉	278.06	0.90	1.40	C₁₉H₂₈O₉	400.17	0.47	1.47
C₁₀H₁₄O₁₀	294.06	1.00	1.40	C₁₉H₂₈O₁₁	432.16	0.58	1.47
C₁₀H₁₄O₁₁	310.05	1.10	1.40	C₁₉H₂₈O₁₂	448.16	0.63	1.47
C₁₀H₁₅O₈	263.08	0.80	1.50	C₁₉H₂₈O₁₃	464.15	0.68	1.47
C₁₀H₁₅O₁₀	295.07	1.00	1.50	C₁₉H₂₈O₁₄	480.15	0.74	1.47
C₁₀H₁₆O₇	248.09	0.70	1.60	C₁₉H₃₀O₁₀	418.18	0.53	1.58
C₁₀H₁₆O₈	264.08	0.80	1.60	C₁₉H₃₀O₁₁	434.18	0.58	1.58
C₁₀H₁₆O₉	280.08	0.90	1.60	C₁₉H₃₀O₁₂	450.17	0.63	1.58
C₁₀H₁₆O₁₀	296.07	1.00	1.60	C₁₉H₃₀O₁₃	466.17	0.68	1.58
C₁₀H₁₆O₁₁	312.07	1.10	1.60	C₁₉H₃₀O₁₄	482.16	0.74	1.58
C₁₆H₂₆O₁₀	378.15	0.63	1.63	C₂₀H₃₀O₁₀	430.18	0.50	1.50
C₁₆H₂₆O₁₁	394.15	0.69	1.63	C₂₀H₃₀O₁₂	462.17	0.60	1.50
C₁₆H₂₆O₁₂	410.14	0.75	1.63	C₂₀H₃₀O₁₃	478.17	0.65	1.50
C₁₈H₂₈O₁₀	404.17	0.56	1.56	C₂₀H₃₀O₁₄	494.16	0.70	1.50
C₁₈H₂₈O₁₁	420.16	0.61	1.56	C₂₀H₃₀O₁₅	510.16	0.75	1.50
C₁₈H₂₈O₁₂	436.16	0.67	1.56	C₂₀H₃₀O₁₆	526.15	0.80	1.50
C₁₈H₂₈O₁₃	452.15	0.72	1.56	C₂₀H₃₂O₁₄	496.18	0.70	1.60
C₁₈H₂₈O₁₄	468.15	0.78	1.56				

Table S.3.3. Peaks identified in the mass spectrum from 3-carene ozonolysis experiments using NO₃⁻-ToF-CIMS. The m/z values correspond to the HOM mass to charge ratios in Thomson (Th), while O/C and H/C denote the elemental ratios, representing the oxygen-to-carbon and hydrogen-to-carbon ratios, respectively.

Formula	m/z Th	O/C	H/C	Formula	m/z Th	O/C	H/C
C ₇ H ₈ O ₈	220.02	1.14	1.14	C ₁₆ H ₂₆ O ₁₄	442.13	0.88	1.63
C ₇ H ₈ O ₁₀	252.01	1.43	1.14	C ₁₇ H ₂₆ O ₁₀	390.15	0.59	1.53
C ₈ H ₁₂ O ₇	220.06	0.88	1.50	C ₁₇ H ₂₆ O ₁₁	406.15	0.65	1.53
C ₈ H ₁₂ O ₉	252.05	1.13	1.50	C ₁₇ H ₂₆ O ₁₄	454.13	0.82	1.53
C ₉ H ₁₀ O ₁₂	310.02	1.33	1.11	C ₁₇ H ₂₆ O ₁₅	470.13	0.88	1.53
C ₉ H ₁₂ O ₈	248.05	0.89	1.33	C ₁₈ H ₂₆ O ₉	386.16	0.50	1.44
C ₉ H ₁₂ O ₉	264.05	1.00	1.33	C ₁₈ H ₂₆ O ₁₀	402.15	0.56	1.44
C ₉ H ₁₂ O ₁₀	280.04	1.11	1.33	C ₁₈ H ₂₆ O ₁₁	418.15	0.61	1.44
C ₉ H ₁₂ O ₁₁	296.04	1.22	1.33	C ₁₈ H ₂₆ O ₁₂	434.14	0.67	1.44
C ₉ H ₁₃ O ₁₀	281.05	1.11	1.44	C ₁₈ H ₂₆ O ₁₃	450.14	0.72	1.44
C ₉ H ₁₄ O ₉	266.06	1.00	1.56	C ₁₈ H ₂₆ O ₁₅	482.13	0.83	1.44
C ₉ H ₁₄ O ₁₀	282.06	1.11	1.56	C ₁₈ H ₂₈ O ₁₀	404.17	0.56	1.56
C ₁₀ H ₁₃ O ₁₀	293.05	1.00	1.30	C ₁₈ H ₂₈ O ₁₁	420.16	0.61	1.56
C ₁₀ H ₁₄ O ₇	246.07	0.70	1.40	C ₁₈ H ₂₈ O ₁₂	436.16	0.67	1.56
C ₁₀ H ₁₄ O ₈	262.07	0.80	1.40	C ₁₈ H ₂₈ O ₁₃	452.15	0.72	1.56
C ₁₀ H ₁₄ O ₉	278.06	0.90	1.40	C ₁₈ H ₂₈ O ₁₄	468.15	0.78	1.56
C ₁₀ H ₁₄ O ₁₀	294.06	1.00	1.40	C ₁₈ H ₂₈ O ₁₅	484.14	0.83	1.56
C ₁₀ H ₁₄ O ₁₁	310.05	1.10	1.40	C ₁₈ H ₂₈ O ₁₆	500.14	0.89	1.56
C ₁₀ H ₁₅ O ₈	263.08	0.80	1.50	C ₁₉ H ₂₆ O ₁₃	462.14	0.68	1.37
C ₁₀ H ₁₅ O ₁₀	295.07	1.00	1.50	C ₁₉ H ₂₈ O ₉	400.17	0.47	1.47
C ₁₀ H ₁₆ O ₇	248.09	0.70	1.60	C ₁₉ H ₂₈ O ₁₀	416.17	0.53	1.47
C ₁₀ H ₁₆ O ₉	280.08	0.90	1.60	C ₁₉ H ₂₈ O ₁₁	432.16	0.58	1.47
C ₁₀ H ₁₆ O ₁₀	296.07	1.00	1.60	C ₁₉ H ₂₈ O ₁₂	448.16	0.63	1.47
C ₁₀ H ₁₆ O ₁₁	312.07	1.10	1.60	C ₁₉ H ₂₈ O ₁₃	464.15	0.68	1.47
C ₁₀ H ₁₇ O ₉	281.09	0.90	1.70	C ₁₉ H ₂₈ O ₁₄	480.15	0.74	1.47
C ₁₀ H ₂₀ O ₁₄	364.09	1.40	2.00	C ₁₉ H ₂₈ O ₁₅	496.14	0.79	1.47
C ₁₃ H ₁₈ O ₉	318.10	0.69	1.38	C ₁₉ H ₂₈ O ₁₆	512.14	0.84	1.47
C ₁₃ H ₂₀ O ₁₁	352.10	0.85	1.54	C ₁₉ H ₃₀ O ₈	386.19	0.42	1.58
C ₁₅ H ₂₂ O ₁₁	378.12	0.73	1.47	C ₁₉ H ₃₀ O ₁₀	418.18	0.53	1.58
C ₁₅ H ₂₂ O ₁₂	394.11	0.80	1.47	C ₁₉ H ₃₀ O ₁₃	466.17	0.68	1.58
C ₁₅ H ₂₄ O ₁₂	396.13	0.80	1.60	C ₁₉ H ₃₀ O ₁₄	482.16	0.74	1.58
C ₁₅ H ₂₄ O ₁₃	412.12	0.87	1.60	C ₂₀ H ₃₀ O ₁₀	430.18	0.50	1.50
C ₁₆ H ₂₀ O ₁₄	436.09	0.88	1.25	C ₂₀ H ₃₀ O ₁₂	462.17	0.60	1.50
C ₁₆ H ₂₂ O ₁₂	406.11	0.75	1.38	C ₂₀ H ₃₀ O ₁₃	478.17	0.65	1.50
C ₁₆ H ₂₂ O ₁₄	438.10	0.88	1.38	C ₂₀ H ₃₀ O ₁₄	494.16	0.70	1.50
C ₁₆ H ₂₄ O ₁₀	376.14	0.63	1.50	C ₂₀ H ₃₀ O ₁₆	526.15	0.80	1.50
C ₁₆ H ₂₆ O ₁₀	378.15	0.63	1.63	C ₂₀ H ₃₀ O ₁₈	558.14	0.90	1.50
C ₁₆ H ₂₆ O ₁₁	394.15	0.69	1.63	C ₂₀ H ₃₂ O ₇	384.21	0.35	1.60
C ₁₆ H ₂₆ O ₁₂	410.14	0.75	1.63	C ₂₀ H ₃₂ O ₉	416.20	0.45	1.60
C ₁₆ H ₂₆ O ₁₃	426.14	0.81	1.63				

Table S.3.4. Peaks identified in the mass spectrum from 3-carene plus limonene ozonolysis experiments using NO_3^- -ToF-CIMS. The m/z values correspond to the HOM mass to charge ratios in Thomson (Th), while O/C and H/C denote the elemental ratios, representing the oxygen-to-carbon and hydrogen-to-carbon ratios, respectively.

Formula	m/z Th	O/C	H/C	Formula	m/z Th	O/C	H/C
$\text{C}_8\text{H}_{10}\text{O}_8$	234.04	1.00	1.25	$\text{C}_{18}\text{H}_{28}\text{O}_{10}$	404.17	0.56	1.56
$\text{C}_8\text{H}_{12}\text{O}_7$	220.06	0.88	1.50	$\text{C}_{18}\text{H}_{28}\text{O}_{11}$	420.16	0.61	1.56
$\text{C}_8\text{H}_{12}\text{O}_8$	236.05	1.00	1.50	$\text{C}_{18}\text{H}_{28}\text{O}_{12}$	436.16	0.67	1.56
$\text{C}_8\text{H}_{14}\text{O}_7$	222.07	0.88	1.75	$\text{C}_{18}\text{H}_{28}\text{O}_{13}$	452.15	0.72	1.56
$\text{C}_9\text{H}_{10}\text{O}_8$	246.04	0.89	1.11	$\text{C}_{18}\text{H}_{28}\text{O}_{14}$	468.15	0.78	1.56
$\text{C}_9\text{H}_{10}\text{O}_{10}$	278.03	1.11	1.11	$\text{C}_{18}\text{H}_{30}\text{O}_{10}$	406.18	0.56	1.67
$\text{C}_9\text{H}_{10}\text{O}_{11}$	294.02	1.22	1.11	$\text{C}_{18}\text{H}_{30}\text{O}_{11}$	422.18	0.61	1.67
$\text{C}_9\text{H}_{12}\text{O}_8$	248.05	0.89	1.33	$\text{C}_{18}\text{H}_{30}\text{O}_{12}$	438.17	0.67	1.67
$\text{C}_9\text{H}_{12}\text{O}_9$	264.05	1.00	1.33	$\text{C}_{19}\text{H}_{26}\text{O}_7$	366.17	0.37	1.37
$\text{C}_9\text{H}_{12}\text{O}_{10}$	280.04	1.11	1.33	$\text{C}_{19}\text{H}_{26}\text{O}_{13}$	462.14	0.68	1.37
$\text{C}_9\text{H}_{14}\text{O}_7$	234.07	0.78	1.56	$\text{C}_{19}\text{H}_{28}\text{O}_9$	400.17	0.47	1.47
$\text{C}_9\text{H}_{14}\text{O}_8$	250.07	0.89	1.56	$\text{C}_{19}\text{H}_{28}\text{O}_{10}$	416.17	0.53	1.47
$\text{C}_9\text{H}_{14}\text{O}_9$	266.06	1.00	1.56	$\text{C}_{19}\text{H}_{28}\text{O}_{11}$	432.16	0.58	1.47
$\text{C}_9\text{H}_{16}\text{O}_7$	236.09	0.78	1.78	$\text{C}_{19}\text{H}_{28}\text{O}_{12}$	448.16	0.63	1.47
$\text{C}_{10}\text{H}_{14}\text{O}_7$	246.07	0.70	1.40	$\text{C}_{19}\text{H}_{28}\text{O}_{13}$	464.15	0.68	1.47
$\text{C}_{10}\text{H}_{14}\text{O}_8$	262.07	0.80	1.40	$\text{C}_{19}\text{H}_{28}\text{O}_{14}$	480.15	0.74	1.47
$\text{C}_{10}\text{H}_{14}\text{O}_9$	278.06	0.90	1.40	$\text{C}_{19}\text{H}_{28}\text{O}_{16}$	512.14	0.84	1.47
$\text{C}_{10}\text{H}_{14}\text{O}_{10}$	294.06	1.00	1.40	$\text{C}_{19}\text{H}_{30}\text{O}_8$	386.19	0.42	1.58
$\text{C}_{10}\text{H}_{14}\text{O}_{11}$	310.05	1.10	1.40	$\text{C}_{19}\text{H}_{30}\text{O}_9$	402.19	0.47	1.58
$\text{C}_{10}\text{H}_{14}\text{O}_{12}$	326.05	1.20	1.40	$\text{C}_{19}\text{H}_{30}\text{O}_{10}$	418.18	0.53	1.58
$\text{C}_{10}\text{H}_{15}\text{O}_8$	263.08	0.80	1.50	$\text{C}_{19}\text{H}_{30}\text{O}_{12}$	450.17	0.63	1.58
$\text{C}_{10}\text{H}_{15}\text{O}_{10}$	295.07	1.00	1.50	$\text{C}_{19}\text{H}_{30}\text{O}_{13}$	466.17	0.68	1.58
$\text{C}_{10}\text{H}_{16}\text{O}_7$	248.09	0.70	1.60	$\text{C}_{19}\text{H}_{30}\text{O}_{14}$	482.16	0.74	1.58
$\text{C}_{10}\text{H}_{16}\text{O}_8$	264.08	0.80	1.60	$\text{C}_{19}\text{H}_{30}\text{O}_{15}$	498.16	0.79	1.58
$\text{C}_{10}\text{H}_{16}\text{O}_9$	280.08	0.90	1.60	$\text{C}_{19}\text{H}_{30}\text{O}_{16}$	514.15	0.84	1.58
$\text{C}_{10}\text{H}_{16}\text{O}_{10}$	296.07	1.00	1.60	$\text{C}_{20}\text{H}_{30}\text{O}_8$	398.19	0.40	1.50
$\text{C}_{10}\text{H}_{16}\text{O}_{11}$	312.07	1.10	1.60	$\text{C}_{20}\text{H}_{30}\text{O}_{10}$	430.18	0.50	1.50
$\text{C}_{16}\text{H}_{24}\text{O}_{13}$	424.12	0.81	1.50	$\text{C}_{20}\text{H}_{30}\text{O}_{11}$	446.18	0.55	1.50
$\text{C}_{16}\text{H}_{26}\text{O}_8$	346.16	0.50	1.63	$\text{C}_{20}\text{H}_{30}\text{O}_{12}$	462.17	0.60	1.50
$\text{C}_{16}\text{H}_{26}\text{O}_9$	362.16	0.56	1.63	$\text{C}_{20}\text{H}_{30}\text{O}_{13}$	478.17	0.65	1.50
$\text{C}_{16}\text{H}_{26}\text{O}_{10}$	378.15	0.63	1.63	$\text{C}_{20}\text{H}_{30}\text{O}_{14}$	494.16	0.70	1.50
$\text{C}_{16}\text{H}_{26}\text{O}_{11}$	394.15	0.69	1.63	$\text{C}_{20}\text{H}_{30}\text{O}_{15}$	510.16	0.75	1.50
$\text{C}_{16}\text{H}_{26}\text{O}_{12}$	410.14	0.75	1.63	$\text{C}_{20}\text{H}_{30}\text{O}_{16}$	526.15	0.80	1.50
$\text{C}_{16}\text{H}_{26}\text{O}_{13}$	426.14	0.81	1.63	$\text{C}_{20}\text{H}_{30}\text{O}_{17}$	542.15	0.85	1.50
$\text{C}_{17}\text{H}_{24}\text{O}_{10}$	388.14	0.59	1.41	$\text{C}_{20}\text{H}_{32}\text{O}_9$	416.20	0.45	1.60
$\text{C}_{17}\text{H}_{26}\text{O}_9$	374.16	0.53	1.53	$\text{C}_{20}\text{H}_{32}\text{O}_{10}$	432.20	0.50	1.60
$\text{C}_{17}\text{H}_{28}\text{O}_9$	376.17	0.53	1.65	$\text{C}_{20}\text{H}_{32}\text{O}_{11}$	448.19	0.55	1.60
$\text{C}_{17}\text{H}_{28}\text{O}_{10}$	392.17	0.59	1.65	$\text{C}_{20}\text{H}_{32}\text{O}_{12}$	464.19	0.60	1.60
$\text{C}_{17}\text{H}_{28}\text{O}_{12}$	424.16	0.71	1.65	$\text{C}_{20}\text{H}_{32}\text{O}_{14}$	496.18	0.70	1.60
$\text{C}_{18}\text{H}_{28}\text{O}_8$	372.18	0.44	1.56	$\text{C}_{20}\text{H}_{32}\text{O}_{15}$	512.17	0.75	1.60
$\text{C}_{18}\text{H}_{28}\text{O}_9$	388.17	0.50	1.56				

Table S.3.5. Peaks identified in the mass spectrum from α -pinene plus limonene ozonolysis experiments using NO_3^- -ToF-CIMS. The m/z values correspond to the HOM mass to charge ratios in Thomson (Th), while O/C and H/C denote the elemental ratios, representing the oxygen-to-carbon and hydrogen-to-carbon ratios, respectively.

Formula	m/z Th	O/C	H/C	Formula	m/z Th	O/C	H/C
C₅H₆O₆	162.02	1.20	1.20	C₁₅H₂₂O₁₀	362.12	0.67	1.47
C₅H₆O₇	178.01	1.40	1.20	C₁₅H₂₄O₁₁	380.13	0.73	1.60
C₆H₈O₉	224.02	1.50	1.33	C₁₅H₂₄O₁₃	412.12	0.87	1.60
C₇H₈O₇	204.03	1.00	1.14	C₁₅H₂₆O₁₀	366.15	0.67	1.73
C₇H₈O₈	220.02	1.14	1.14	C₁₆H₂₄O₁₀	376.14	0.63	1.50
C₇H₉O₉	237.02	1.29	1.29	C₁₆H₂₄O₁₁	392.13	0.69	1.50
C₇H₁₀O₉	238.03	1.29	1.43	C₁₆H₂₄O₁₃	424.12	0.81	1.50
C₈H₁₂O₇	220.06	0.88	1.50	C₁₆H₂₆O₈	346.16	0.50	1.63
C₈H₁₂O₈	236.05	1.00	1.50	C₁₆H₂₆O₁₀	378.15	0.63	1.63
C₈H₁₂O₉	252.05	1.13	1.50	C₁₆H₂₆O₁₁	394.15	0.69	1.63
C₉H₁₀O₁₀	278.03	1.11	1.11	C₁₆H₂₆O₁₂	410.14	0.75	1.63
C₉H₁₂O₇	232.06	0.78	1.33	C₁₆H₂₆O₁₃	426.14	0.81	1.63
C₉H₁₂O₈	248.05	0.89	1.33	C₁₆H₂₆O₁₄	442.13	0.88	1.63
C₉H₁₄O₇	234.07	0.78	1.56	C₁₆H₂₆O₁₅	458.13	0.94	1.63
C₉H₁₄O₈	250.07	0.89	1.56	C₁₆H₃₂O₁₂	416.19	0.75	2.00
C₉H₁₄O₉	266.06	1.00	1.56	C₁₇H₂₆O₉	374.16	0.53	1.53
C₉H₁₄O₁₀	282.06	1.11	1.56	C₁₇H₂₆O₁₀	390.15	0.59	1.53
C₉H₁₆O₇	236.09	0.78	1.78	C₁₇H₂₆O₁₂	422.14	0.71	1.53
C₉H₁₆O₈	252.08	0.89	1.78	C₁₇H₂₆O₁₅	470.13	0.88	1.53
C₁₀H₁₄O₇	246.07	0.70	1.40	C₁₇H₂₈O₁₁	408.16	0.65	1.65
C₁₀H₁₄O₈	262.07	0.80	1.40	C₁₇H₂₈O₁₂	424.16	0.71	1.65
C₁₀H₁₄O₉	278.06	0.90	1.40	C₁₇H₂₈O₁₄	456.15	0.82	1.65
C₁₀H₁₄O₁₀	294.06	1.00	1.40	C₁₈H₂₂O₁₁	414.12	0.61	1.22
C₁₀H₁₄O₁₁	310.05	1.10	1.40	C₁₈H₂₆O₁₀	402.15	0.56	1.44
C₁₀H₁₄O₁₂	326.05	1.20	1.40	C₁₈H₂₈O₈	372.18	0.44	1.56
C₁₀H₁₄O₁₃	342.04	1.30	1.40	C₁₈H₂₈O₉	388.17	0.50	1.56
C₁₀H₁₅O₈	263.08	0.80	1.50	C₁₈H₂₈O₁₁	420.16	0.61	1.56
C₁₀H₁₅O₉	279.07	0.90	1.50	C₁₈H₂₈O₁₂	436.16	0.67	1.56
C₁₀H₁₅O₁₀	295.07	1.00	1.50	C₁₈H₂₈O₁₃	452.15	0.72	1.56
C₁₀H₁₅O₁₂	327.06	1.20	1.50	C₁₈H₂₈O₁₄	468.15	0.78	1.56
C₁₀H₁₆O₇	248.09	0.70	1.60	C₁₈H₂₈O₁₅	484.14	0.83	1.56
C₁₀H₁₆O₈	264.08	0.80	1.60	C₁₈H₂₈O₁₆	500.14	0.89	1.56
C₁₀H₁₆O₉	280.08	0.90	1.60	C₁₈H₃₀O₁₀	406.18	0.56	1.67
C₁₀H₁₆O₁₀	296.07	1.00	1.60	C₁₈H₃₀O₁₂	438.17	0.67	1.67
C₁₀H₁₆O₁₁	312.07	1.10	1.60	C₁₈H₃₀O₁₄	470.16	0.78	1.67
C₁₁H₁₆O₁₁	324.07	1.00	1.45	C₁₈H₃₀O₁₅	486.16	0.83	1.67
C₁₁H₁₆O₁₂	340.06	1.09	1.45	C₁₉H₂₆O₉	398.16	0.47	1.37
C₁₂H₁₈O₁₃	370.07	1.08	1.50	C₁₉H₂₆O₁₂	446.14	0.63	1.37
C₁₃H₂₀O₁₁	352.10	0.85	1.54	C₁₉H₂₈O₉	400.17	0.47	1.47
C₁₃H₂₀O₁₂	368.10	0.92	1.54	C₁₉H₂₈O₁₁	432.16	0.58	1.47
C₁₄H₂₀O₁₁	364.10	0.79	1.43	C₁₉H₂₈O₁₂	448.16	0.63	1.47
C₁₄H₂₀O₁₃	396.09	0.93	1.43	C₁₉H₂₈O₁₄	480.15	0.74	1.47
C₁₄H₂₂O₁₂	382.11	0.86	1.57	C₁₉H₂₈O₁₆	512.14	0.84	1.47

Table S.3.5 (continued). Peaks identified in the mass spectrum from α -pinene plus limonene ozonolysis experiments using NO_3^- -ToF-CIMS. The m/z values correspond to the HOM mass to charge ratios in Thomson (Th), while O/C and H/C denote the elemental ratios, representing the oxygen-to-carbon and hydrogen-to-carbon ratios, respectively.

Formula	m/z Th	O/C	H/C
C₁₉H₃₀O₈	386.19	0.42	1.58
C₁₉H₃₀O₁₀	418.18	0.53	1.58
C₁₉H₃₀O₁₁	434.18	0.58	1.58
C₁₉H₃₀O₁₂	450.17	0.63	1.58
C₁₉H₃₀O₁₃	466.17	0.68	1.58
C₁₉H₃₀O₁₄	482.16	0.74	1.58
C₁₉H₃₀O₁₅	498.16	0.79	1.58
C₁₉H₃₀O₁₆	514.15	0.84	1.58
C₂₀H₂₈O₁₆	524.14	0.80	1.40
C₂₀H₃₀O₁₀	430.18	0.50	1.50
C₂₀H₃₀O₁₁	446.18	0.55	1.50
C₂₀H₃₀O₁₂	462.17	0.60	1.50
C₂₀H₃₀O₁₃	478.17	0.65	1.50
C₂₀H₃₀O₁₄	494.16	0.70	1.50
C₂₀H₃₀O₁₅	510.16	0.75	1.50
C₂₀H₃₀O₁₆	526.15	0.80	1.50
C₂₀H₃₀O₁₈	558.14	0.90	1.50
C₂₀H₃₂O₁₄	496.18	0.70	1.60
C₂₀H₃₂O₁₆	528.17	0.80	1.60

Table S.3.6. Peaks identified in the mass spectrum from α -phellandrene ozonolysis experiments using NO_3^- -ToF-CIMS. The m/z values correspond to the HOM mass to charge ratios in Thomson (Th), while O/C and H/C denote the elemental ratios, representing the oxygen-to-carbon and hydrogen-to-carbon ratios, respectively.

Formula	m/z Th	O/C	H/C	N/C
Unidentified	267.02	-	-	-
C₉H₁₄N₂O₉	294.07	1	1.56	0.22
C₉H₁₄N₂O₁₀	310.06	1.11	1.56	0.22
C₁₀H₁₅NO₈	277.08	0.8	1.5	0.1
C₁₀H₁₅NO₉	293.07	0.9	1.5	0.1
C₁₀H₁₅NO₁₁	325.03	1.33	1.22	0.11
C₁₀H₁₇NO₈	279.1	0.8	1.7	0.1
C₁₀H₁₇NO₉	295.09	0.9	1.7	0.1
C₁₀H₁₇NO₁₀	311.09	1	1.7	0.1
C₁₇H₂₆N₂O₁₂	450.12	0.76	1.41	0.06
C₁₇H₂₆N₂O₁₃	466.14	0.76	1.53	0.12
C₁₇H₂₆N₂O₁₄	482.14	0.82	1.53	0.12
C₁₇H₂₆N₂O₁₅	498.13	0.88	1.53	0.12
C₁₇H₂₆N₂O₁₆	514.13	0.94	1.53	0.12
C₂₀H₃₂N₂O₁₀	460.21	0.5	1.6	0.1
C₂₀H₃₂N₂O₁₁	476.2	0.55	1.6	0.1
C₂₀H₃₂N₂O₁₂	492.2	0.6	1.6	0.1
C₂₀H₃₂N₂O₁₃	508.19	0.65	1.6	0.1
C₂₀H₃₂N₂O₁₄	524.19	0.7	1.6	0.1
C₂₀H₃₂N₂O₁₅	540.18	0.75	1.6	0.1
C₂₀H₃₂N₂O₁₆	556.18	0.8	1.6	0.1
C₂₀H₃₂N₂O₁₇	572.17	0.85	1.6	0.1
C₂₀H₃₂N₂O₁₈	588.17	0.9	1.6	0.1
C₂₀H₃₃N₃O₁₉	619.17	0.95	1.65	0.15

Table S.3.7. Peaks identified in the mass spectrum from α -phellandrene plus trans-2-butene ozonolysis experiments using NO_3^- -ToF-CIMS. The m/z values correspond to the HOM mass to charge ratio in Thomson (Th), while O/C and H/C denote the elemental ratios, representing the oxygen-to-carbon and hydrogen-to-carbon ratios, respectively.

Formula	m/z Th	O/C	H/C	N/C
Unidentified	267.01	-	-	-
C₉H₁₄N₂O₁₀	310.06	1	1.6	0.1
C₁₀H₁₄N₂O₁₃	370.05	1.3	1.4	0.2
C₁₀H₁₄N₂O₁₄	386.04	1.4	1.4	0.2
C₁₀H₁₄N₂O₁₅	402.04	1.5	1.4	0.2
C₁₀H₁₅NO₈	277.08	0.8	1.5	0.1
C₁₀H₁₅NO₁₀	309.07	1	1.5	0.1
C₁₀H₁₅NO₁₁	325.03	1.33	1.22	0.11
C₁₀H₁₇NO₈	279.10	0.8	1.7	0.1
C₁₀H₁₇NO₁₀	311.09	1	1.7	0.1
C₁₇H₂₆N₂O₁₂	450.12	0.76	1.41	0.06
C₁₇H₂₆N₂O₁₃	466.14	0.76	1.53	0.12
C₁₇H₂₆N₂O₁₄	482.14	0.82	1.53	0.12
C₁₇H₂₆N₂O₁₅	498.13	0.88	1.53	0.12
C₁₇H₂₆N₂O₁₆	514.13	0.94	1.53	0.12
C₂₀H₃₂N₂O₁₁	476.20	0.55	1.6	0.1
C₂₀H₃₂N₂O₁₂	492.20	0.6	1.6	0.1
C₂₀H₃₂N₂O₁₃	508.19	0.65	1.6	0.1
C₂₀H₃₂N₂O₁₄	524.19	0.7	1.6	0.1
C₂₀H₃₂N₂O₁₅	540.18	0.75	1.6	0.1
C₂₀H₃₂N₂O₁₆	556.18	0.8	1.6	0.1
C₂₀H₃₂N₂O₁₇	572.17	0.85	1.6	0.1
C₂₀H₃₂N₂O₁₈	588.17	0.9	1.6	0.1
C₂₀H₃₃N₃O₁₉	619.17	0.95	1.65	0.15

Table S.3.8. Peaks identified in the mass spectrum from β -phellandrene plus nitrate radical experiments using NO_3^- -ToF-CIMS. The m/z values correspond to the HOM mass to charge ratio in Thomson (Th), while O/C and H/C denote the elemental ratios, representing the oxygen-to-carbon and hydrogen-to-carbon ratios, respectively.

Formula	m/z Th	O/C	H/C	N/C
C₉H₁₄N₂O₉	294.07	1.00	1.56	0.22
C₉H₁₄N₂O₁₀	310.10	1.11	1.56	0.22
C₁₀H₁₅NO₈	277.08	0.80	1.50	0.10
C₁₀H₁₅NO₁₀	309.07	1.00	1.50	0.10
C₁₀H₁₅NO₁₁	325.06	1.10	1.50	0.10
C₁₀H₁₇NO₈	279.10	0.80	1.70	0.10
C₁₀H₁₇NO₉	295.09	0.90	1.70	0.10
C₁₀H₁₇NO₁₀	311.09	1.00	1.70	0.10
C₁₀H₁₆N₂O₁₀	324.08	1.00	1.60	0.20
C₁₇H₂₆N₂O₁₂	450.15	0.71	1.53	0.12
C₁₇H₂₆N₂O₁₄	482.14	0.82	1.53	0.12
C₁₇H₂₆N₂O₁₅	498.13	0.88	1.53	0.12
C₁₇H₂₆N₂O₁₆	514.13	0.94	1.53	0.12
C₁₇H₂₆N₂O₁₈	546.12	1.06	1.53	0.12
C₂₀H₃₂N₂O₁₀	460.21	0.50	1.60	0.10
C₂₀H₃₂N₂O₁₁	476.20	0.55	1.60	0.10
C₂₀H₃₂N₂O₁₂	492.20	0.60	1.60	0.10
C₂₀H₃₂N₂O₁₃	508.19	0.65	1.60	0.10
C₂₀H₃₂N₂O₁₄	524.19	0.70	1.60	0.10
C₂₀H₃₂N₂O₁₅	540.18	0.75	1.60	0.10
C₂₀H₃₂N₂O₁₆	556.18	0.80	1.60	0.10
C₂₀H₃₂N₂O₁₇	572.17	0.85	1.60	0.10
C₂₀H₃₂N₂O₁₈	588.17	0.90	1.60	0.10
C₂₀H₃₃NO₁₀	447.20	0.50	1.65	0.05
C₂₀H₃₃NO₁₄	511.19	0.70	1.65	0.05

Table S.3.9. Peaks identified in the mass spectrum from β -phellandrene plus trans-2-butene and nitrate radical experiments using NO_3^- -ToF-CIMS. The m/z values correspond to the HOM mass to charge ratio in Thomson (Th), while O/C and H/C denote the elemental ratios, representing the oxygen-to-carbon and hydrogen-to-carbon ratios, respectively.

Formula	m/z Th	O/C	H/C	N/C
C₉H₁₄N₂O₉	294.07	1.00	1.56	0.22
C₁₀H₁₅NO₈	277.08	0.80	1.50	0.10
C₁₀H₁₅NO₉	293.07	0.90	1.50	0.10
C₁₀H₁₅NO₁₀	309.07	1.00	1.50	0.10
C₁₀H₁₅NO₁₁	325.06	1.10	1.50	0.10
C₁₀H₁₆NO₉	294.08	0.90	1.60	0.10
C₁₀H₁₇NO₈	279.10	0.80	1.70	0.10
C₁₀H₁₇NO₉	295.09	0.90	1.70	0.10
C₁₀H₁₇NO₁₀	311.09	1.00	1.70	0.10
C₁₀H₁₄N₂O₁₅	402.04	1.5	1.4	0.2
C₁₀H₁₆N₂O₁₀	324.08	1.00	1.60	0.20
C₁₄H₂₄N₂O₁₂	412.13	1.07	1.71	0.14
C₁₇H₂₆N₂O₁₂	450.15	0.71	1.53	0.12
C₁₇H₂₆N₂O₁₃	466.14	0.76	1.53	0.12
C₁₇H₂₆N₂O₁₄	482.14	0.82	1.53	0.12
C₁₇H₂₆N₂O₁₅	498.13	0.88	1.53	0.12
C₁₇H₂₆N₂O₁₆	514.13	0.94	1.53	0.12
C₁₇H₂₆N₂O₁₈	546.12	1.06	1.53	0.12
C₂₀H₃₂N₂O₁₀	460.21	0.50	1.60	0.10
C₂₀H₃₂N₂O₁₁	476.20	0.55	1.60	0.10
C₂₀H₃₂N₂O₁₂	492.20	0.60	1.60	0.10
C₂₀H₃₂N₂O₁₃	508.19	0.65	1.60	0.10
C₂₀H₃₂N₂O₁₄	524.19	0.70	1.60	0.10
C₂₀H₃₂N₂O₁₅	540.18	0.75	1.60	0.10
C₂₀H₃₂N₂O₁₆	556.18	0.80	1.60	0.10
C₂₀H₃₂N₂O₁₇	572.17	0.85	1.60	0.10
C₂₀H₃₂N₂O₁₈	588.17	0.90	1.60	0.10
C₂₀H₃₂N₂O₁₉	604.16	0.95	1.60	0.10
C₂₀H₃₃NO₁₄	511.19	0.70	1.65	0.05

Supplement–Chapter 4

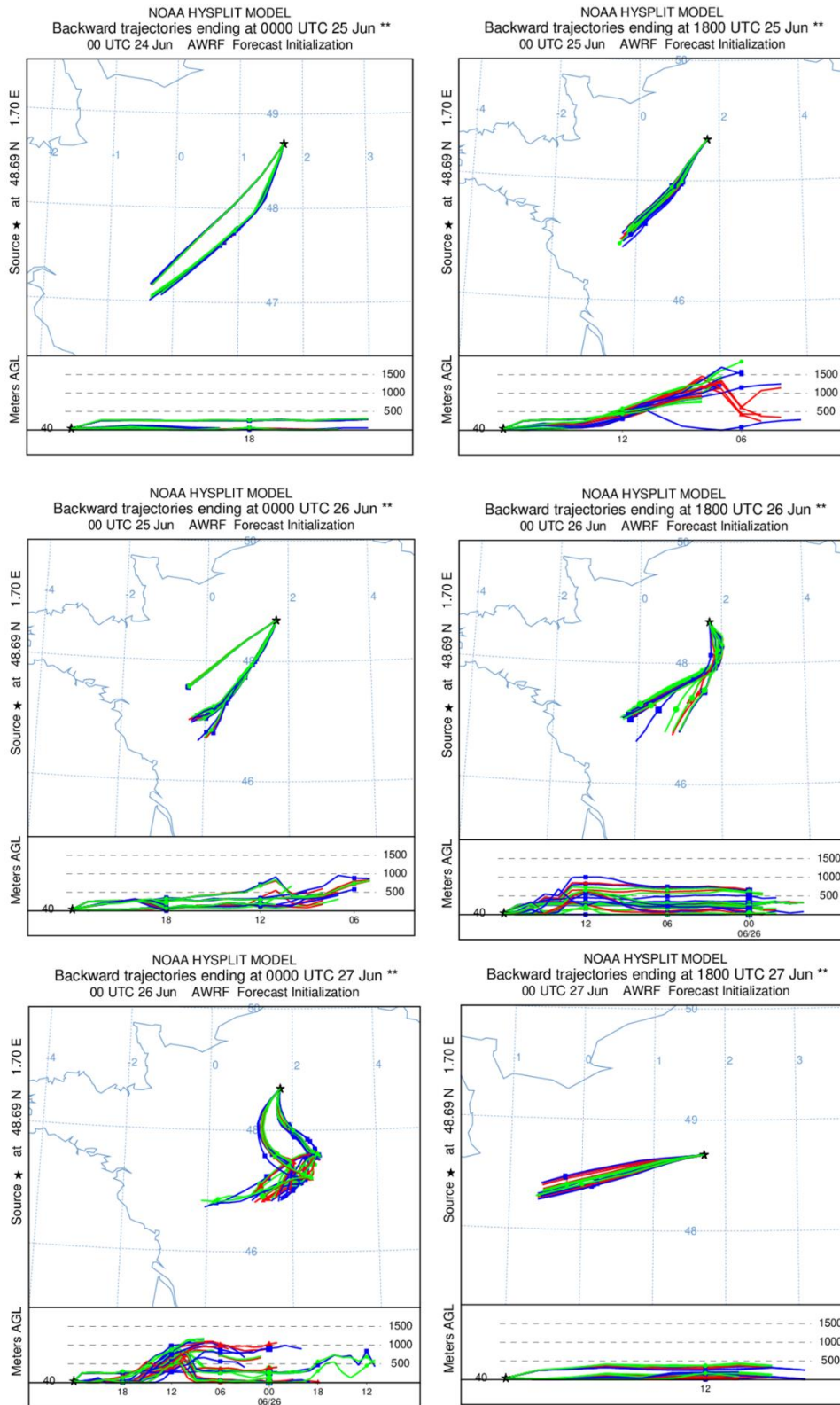


Figure S.4.1. ACROSS Backward trajectory calculations using the Hysplit model, with the source point located at the Rambouillet supersite at a height of 40 m Above Ground Level (AGL). Backward trajectories calculations ended at midnight of for the left panels and at 18:00 for the right panels on each respective day, spanning the period from June 25th to June 27th.

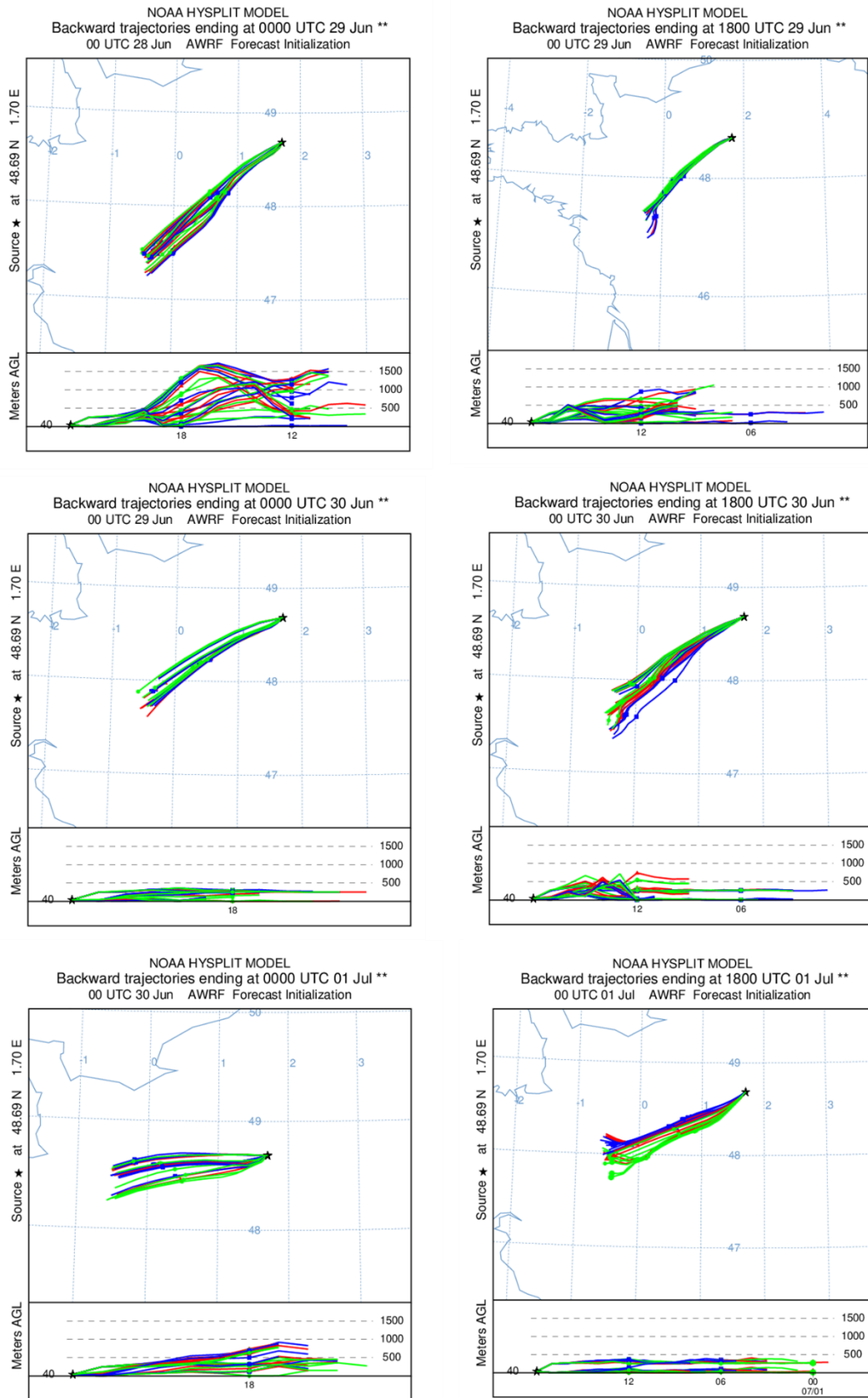


Figure S.4.2. ACROSS Backward trajectory calculations using the Hysplit model, with the source point located at the Rambouillet supersite at a height of 40 m Above Ground Level (AGL). Backward trajectories calculations ended at midnight of for the left panels and at 18:00 for the right panels on each respective day, spanning the period from June 29th to July 1st.

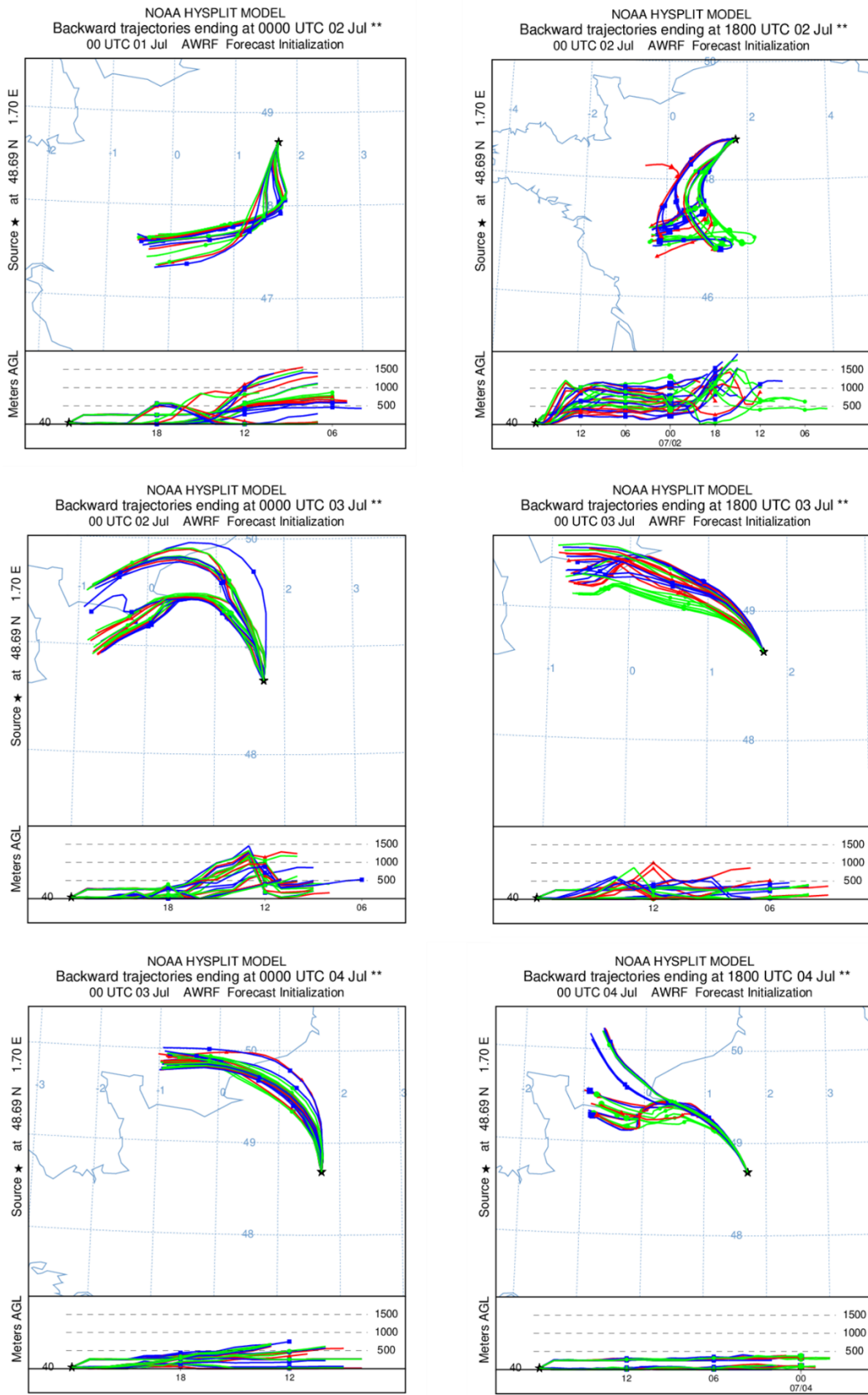


Figure S.4.3. ACROSS Backward trajectory calculations using the Hysplit model, with the source point located at the Rambouillet supersite at a height of 40 m Above Ground Level (AGL). Backward trajectories calculations ended at midnight of for the left panels and at 18:00 for the right panels on each respective day, spanning the period from July 2nd to July 4th.

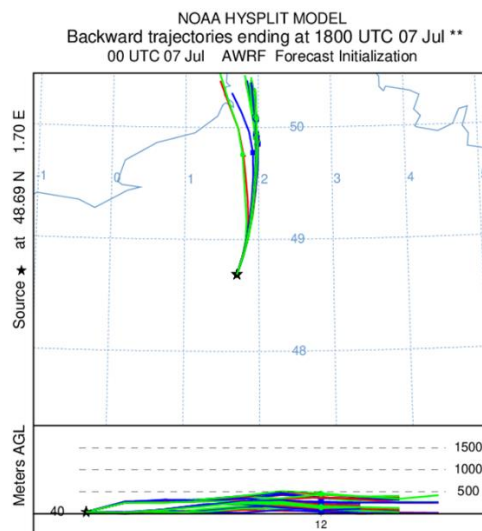
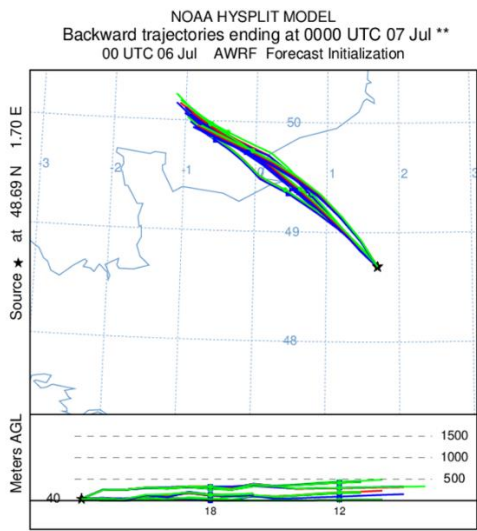
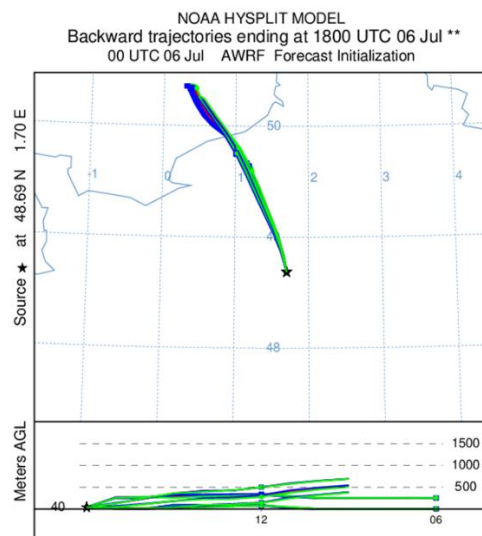
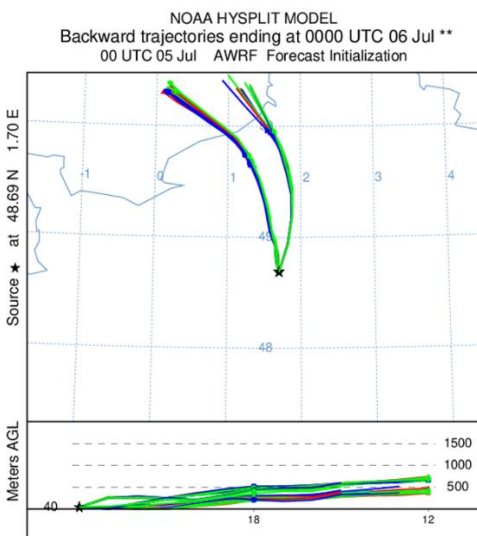
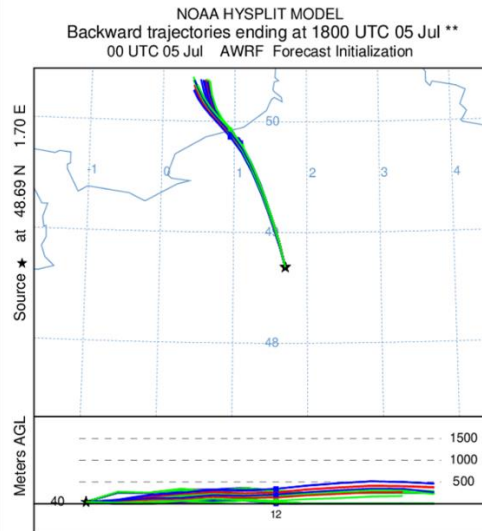
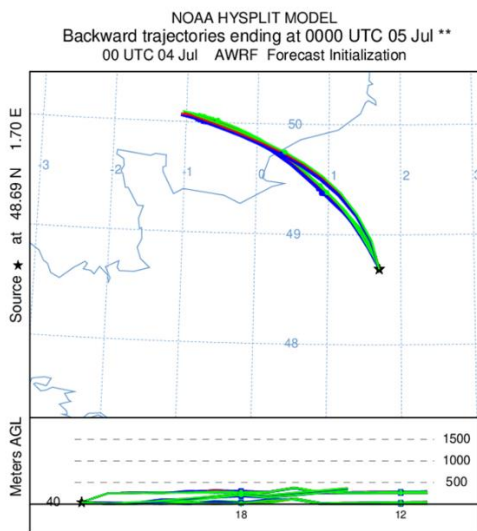


Figure S.4.4. ACROSS Backward trajectory calculations using the Hysplit model, with the source point located at the Rambouillet supersite at a height of 40 m Above Ground Level (AGL). Backward trajectories calculations ended at midnight of for the left panels and at 18:00 for the right panels on each respective day, spanning the period from July 5th to July 7th.

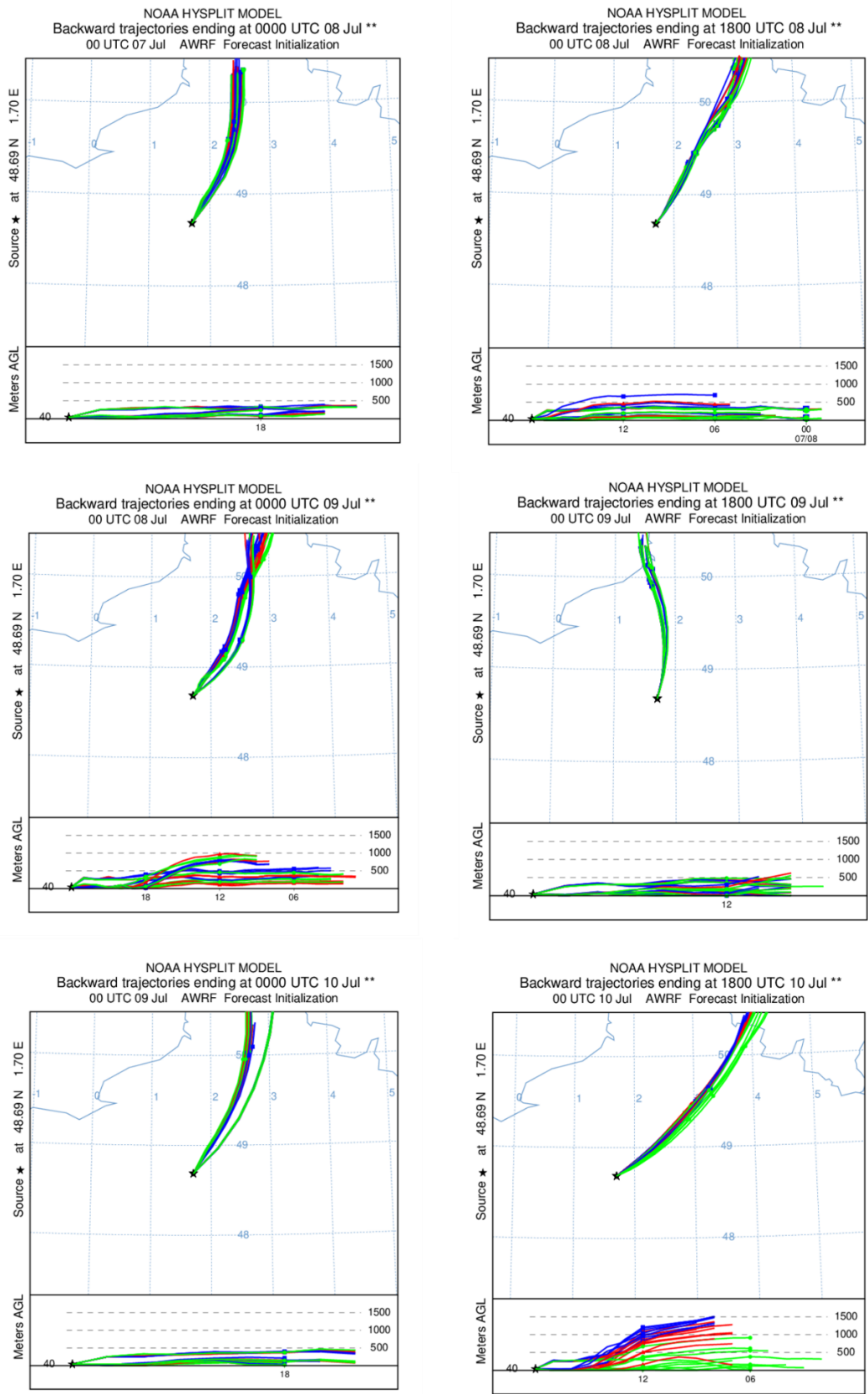


Figure S.4.5. ACROSS Backward trajectory calculations using the Hysplit model, with the source point located at the Rambouillet supersite at a height of 40 m Above Ground Level (AGL). Backward trajectories calculations ended at midnight of for the left panels and at 18:00 for the right panels on each respective day, spanning the period from July 8th to July 10th.

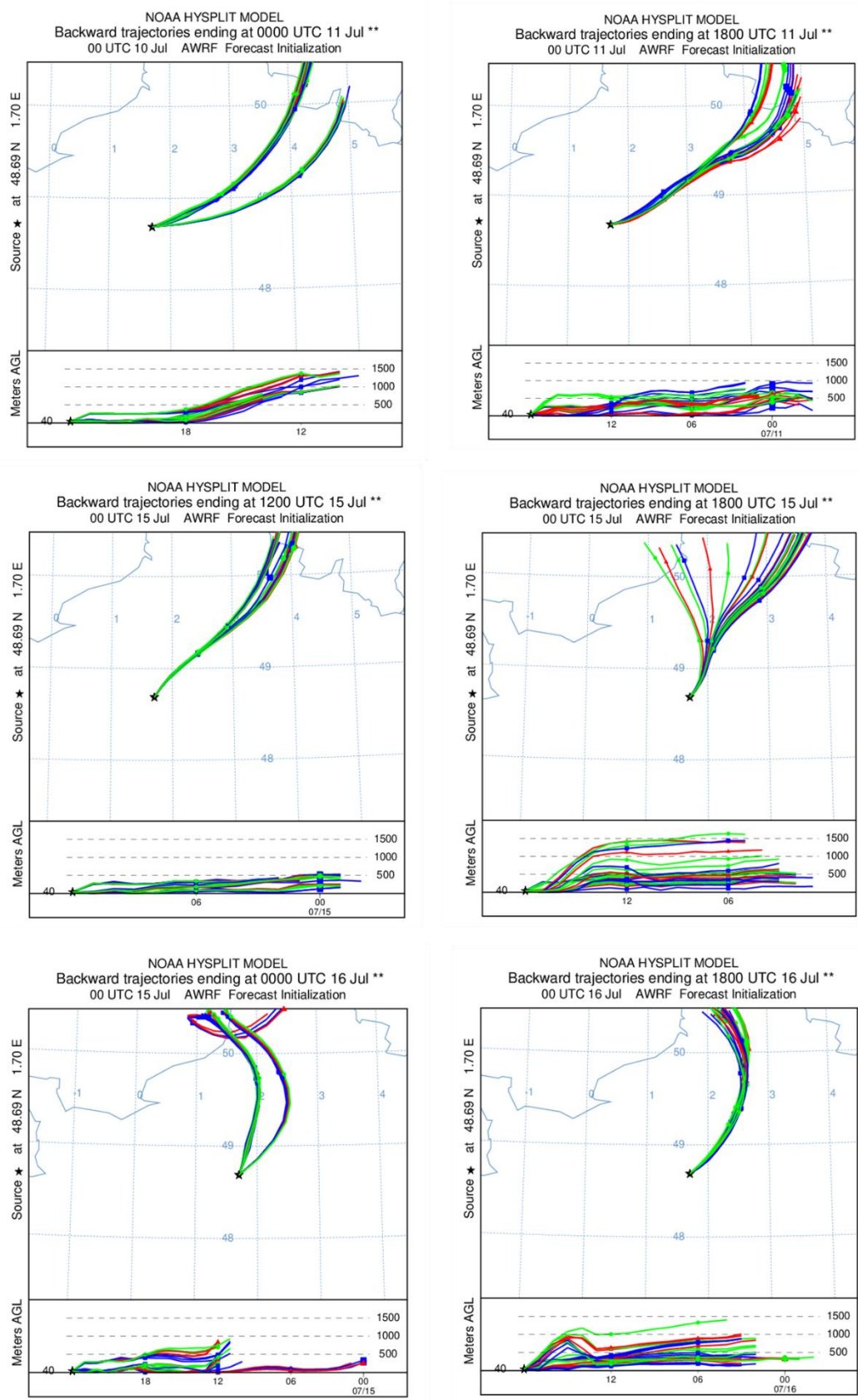


Figure S.4.6. ACROSS Backward trajectory calculations using the Hysplit model, with the source point located at the Rambouillet supersite at a height of 40 m Above Ground Level (AGL). Backward trajectories calculations ended at midnight of for the left panels and at 18:00 for the right panels on each respective day, spanning the period from July 15th to July 16th and July 11th.

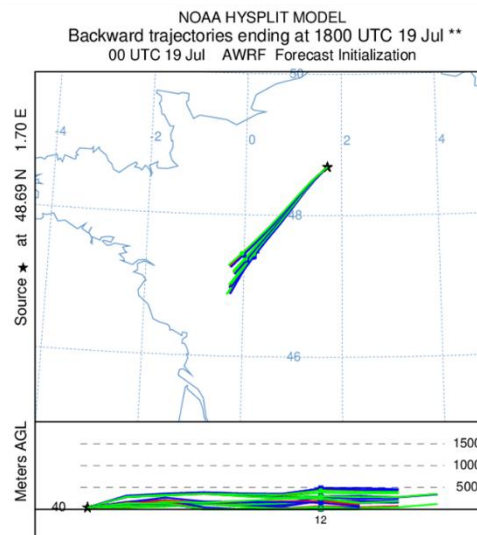
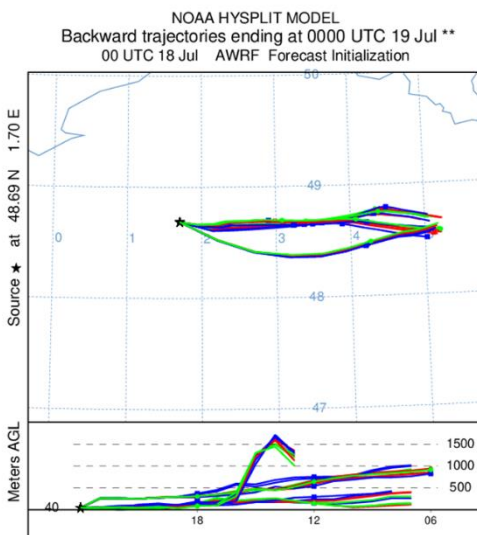
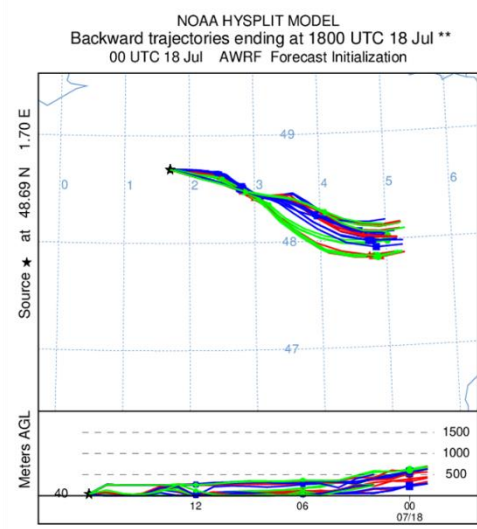
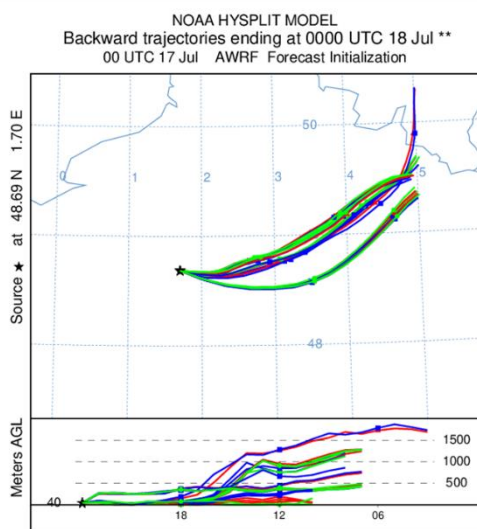
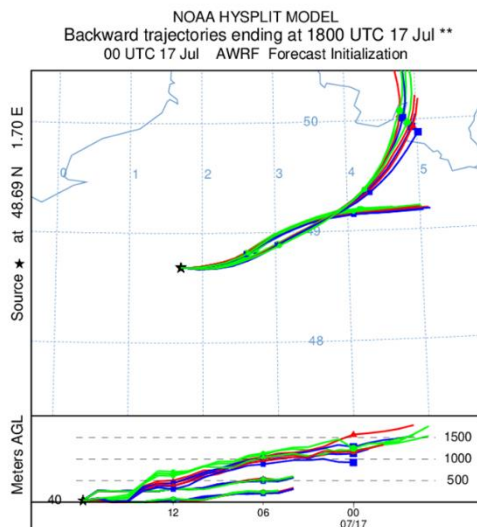
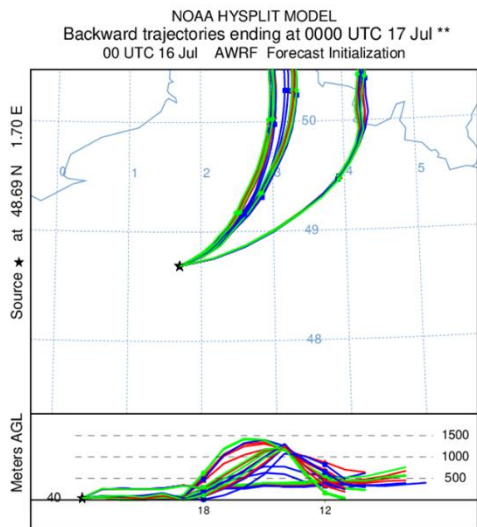


Figure S.4.7. ACROSS Backward trajectory calculations using the Hysplit model, with the source point located at the Rambouillet supersite at a height of 40 m Above Ground Level (AGL). Backward trajectories calculations ended at midnight of for the left panels and at 18:00 for the right panels on each respective day, spanning the period from July 17th to July 19th.

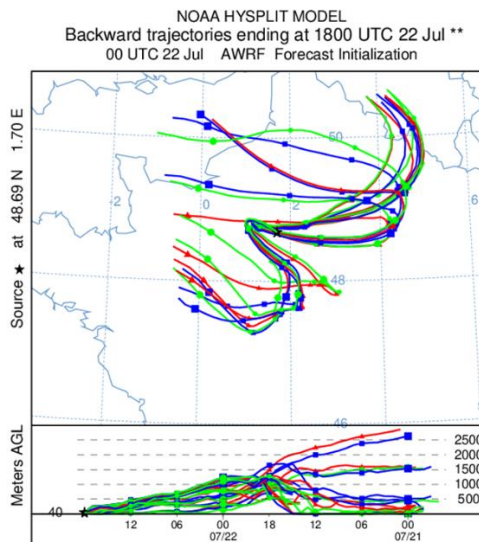
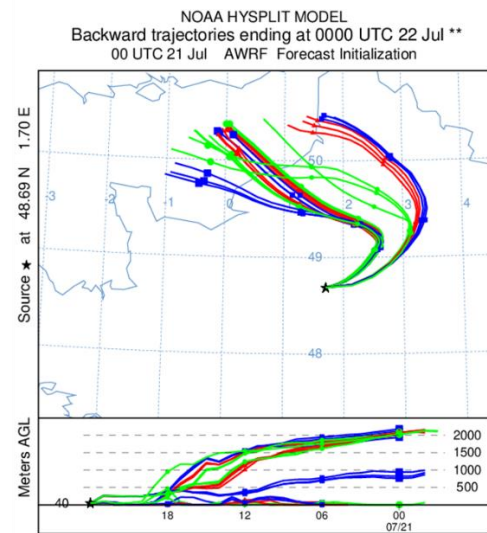
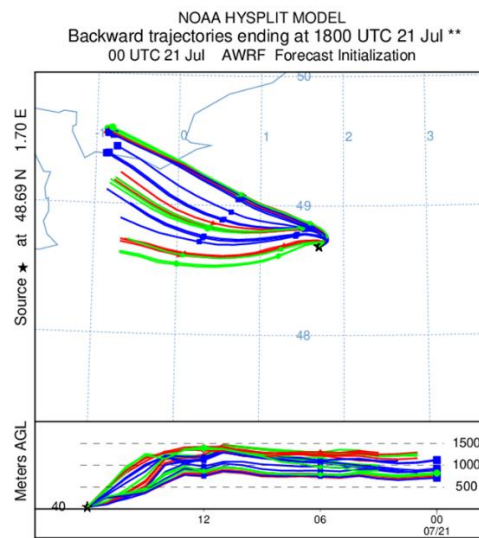
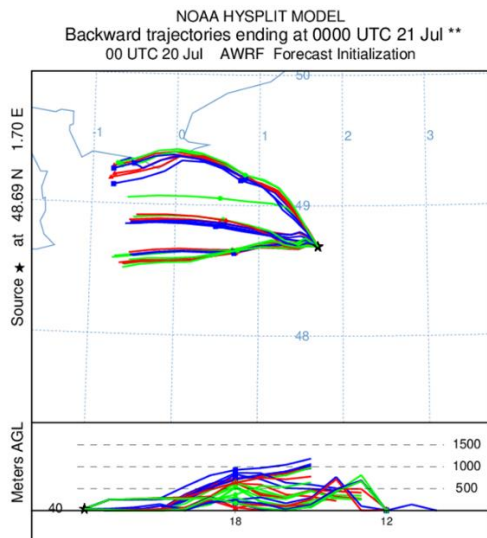
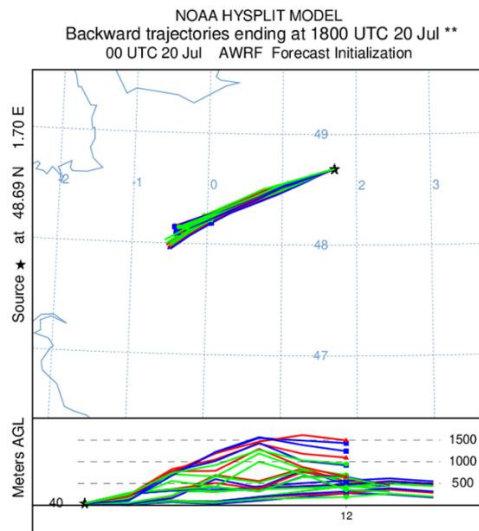
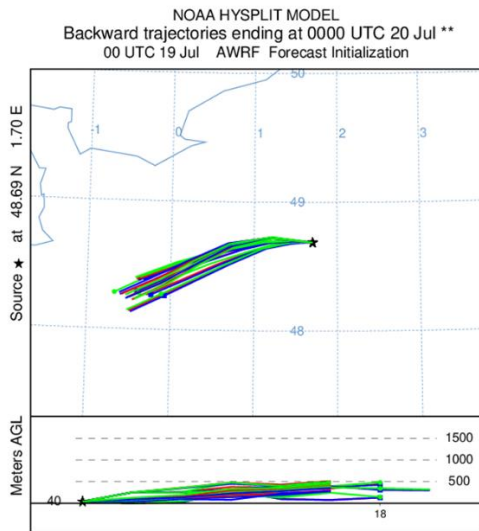


Figure S.4.8. ACROSS Backward trajectory calculations using the Hysplit model, with the source point located at the Rambouillet supersite at a height of 40 m Above Ground Level (AGL). Backward trajectories calculations ended at midnight of for the left panels and at 18:00 for the right panels on each respective day, spanning the period from July 20th to July 22th.

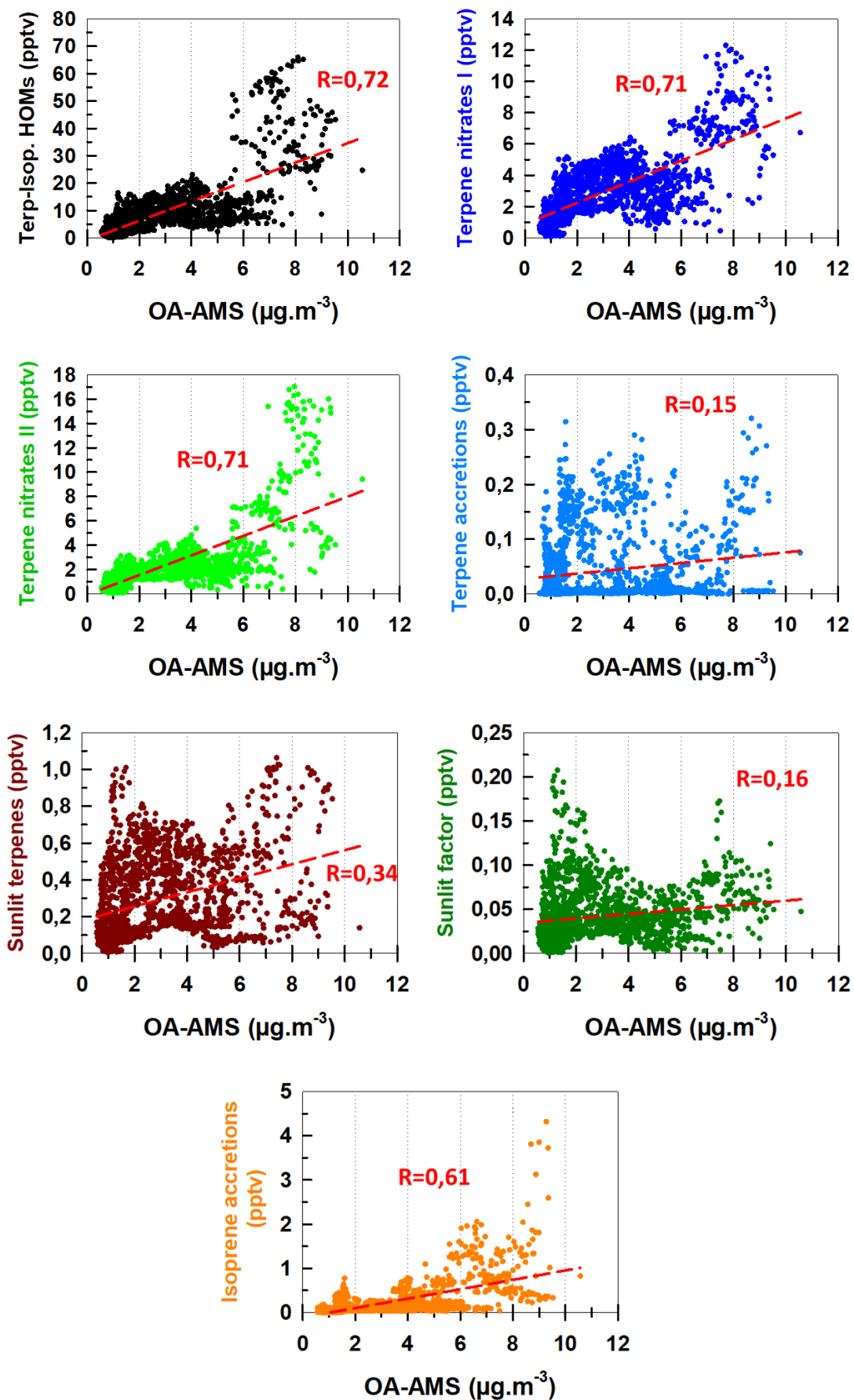


Figure S.4.9. Correlations of the various PCA-derived HOM components with OA-AMS.

Abstract

Volatile organic compounds (VOCs) from both natural and anthropogenic sources play crucial roles in tropospheric chemistry, producing byproducts such as secondary organic aerosols (SOA) and ozone, which can have adverse impacts on human health and the ecosystem.

This PhD thesis focuses on gas-phase products of low volatility, highly oxygenated organic molecules (HOMs), first identified in ambient air in 2010. HOMs rapidly form from the autoxidation of peroxy radicals (RO_2) formed from VOC oxidation. Due to their low volatilities, HOMs significantly contribute to SOA formation and growth. Measuring HOMs in ambient air was made possible by a NO_3^- ToFCIMS. The objectives of this thesis are thus to optimize the instrument in the laboratory, develop a direct calibration protocol, and study HOMs in the Rambouillet forest during ACROSS 2022 summer field campaign, under different conditions, especially during the mixing of urban plume and air masses containing forest emissions.

To achieve these objectives, controlled laboratory experiments were conducted to find the optimum instrument settings. Multiple calibration methods were tested using organic acids to evaluate the sensitivity of the instrument. These results were compared to conventional H_2SO_4 calibration methods. Simulation chamber experiments were conducted involving the oxidation of BVOCs and AVOCs to help identify potential HOMs products encountered in the atmosphere. Finally, Principal Component Analysis (PCA) was applied to the HOMs measurements dataset from the NO_3^- ToFCIMS deployed during ACROSS. This analysis identified seven principal components, each characterized by unique temporal profiles, most likely linked to the BVOCs, isoprene and monoterpenes.

Keywords: Highly oxygenated organic molecules, forest, field campaign, simulation chamber, ToFCIMS

Résumé

Les composés organiques volatils (COV) provenant de sources naturelles et anthropogéniques jouent un rôle crucial dans la chimie de la troposphère, produisant des sous-produits tels que les aérosols organiques secondaires (AOS) et l'ozone, qui peuvent avoir des effets néfastes sur la santé humaine et l'écosystème.

Cette thèse de doctorat se concentre sur des molécules organiques hautement oxygénées (HOMs), identifiées en phase gazeuse pour la première fois dans l'air ambiant en 2010. Les HOMs se forment rapidement à partir de l'autoxydation des radicaux peroxy (RO_2) formés lors de l'oxydation des COV. En raison de leur faible volatilité, les HOMs contribuent de manière significative à la formation et à la croissance des AOS. La mesure des HOMs dans l'air ambiant a été rendue possible par un NO_3^- ToFCIMS.

Les objectifs de cette thèse sont donc d'optimiser l'instrument en laboratoire, de développer un protocole d'étalonnage direct, ainsi que d'étudier les HOMs dans la forêt de Rambouillet lors de la campagne estivale ACROSS 2022. Pour atteindre ces objectifs, des essais en laboratoire ont été menés pour trouver les réglages optimaux de l'instrument. Des méthodes d'étalonnage ont été testées avec des acides organiques pour évaluer la sensibilité de l'instrument, comparées à l'étalonnage classique avec H_2SO_4 . Des expériences en chambre de simulation ont été menées impliquant l'oxydation de COV biogéniques et anthropogéniques, pour aider à identifier les produits potentiels des HOMs dans l'air. Enfin, une analyse en composantes principales (ACP) a été appliquée aux mesures de HOMs obtenus par le NO_3^- ToFCIMS déployé pendant ACROSS. Cette analyse a identifié sept composantes principales, chacune caractérisée par des profils temporels uniques, liés aux deux principaux COV biogéniques, l'isoprène et les monoterpènes.

Mot-clés : Composés organiques hautement oxygénés, forêt, campagne de terrain, chambre de simulation ToFCIMS